Reverse-Engineering, Performance and Aerodynamic Modelling and Redesign of a Single Stage Micro Gas Turbine

Qiming Yu

A thesis submitted in partial fulfilment of the requirements for the degree of

Doctor of Philosophy

The University of Sheffield

Faculty of Engineering

Department of mechanical engineering

Submission Date

December 2023

To my girlfriend and parents, who always believed in me.

Acknowledgements

I would like to extend my heartfelt gratitude to my supervisor, Dr. Robert Howell, for his unwavering guidance, invaluable counsel, and consistent encouragement throughout my PhD journey. His profound expertise and mentorship have been instrumental in honing my capabilities, allowing me to meticulously plan, execute, and assess my research endeavours. Experiencing research cultures beyond the familiar confines of my homeland, China, has been both enlightening and enriching.

Special thanks are due to Sam Lyon for his invaluable assistance in 3D printing and constructing the T106 and the scaled Wren100 stator vane cascades essential for our wind tunnel tests. My appreciation also goes out to Paul from Turbine Solutions for generously providing the Wren100 MGT units.

Lastly, I owe a deep debt of gratitude to my parents and my friends. Their unwavering support, particularly during the challenges posed by the COVID pandemic, has been the bedrock upon which I could complete this extensive research. Their belief in me has been the driving force behind every milestone I achieved.

Abstract

Micro gas turbines (MGTs) have been pivotal in sectors such as electricity generation, military applications, and commercial uses over the past five decades. With increasing global concerns about climate change, there is a pressing need to reduce emissions, including CO_2 and NO_x, from power generation mechanisms like aircraft engines. In alignment with the ACARE (Advisory Council for Aviation Research and Innovation in Europe) goals, there is a mandate to reduce NO_x emissions by 75% per passage kilometre for aircraft engines by 2050, using the year 2000 as the baseline. MGTs, representing scaled models of larger gas turbines, offer a cost-effective platform for aerodynamic exploration and technological advancements in gas turbines at large.

This study utilised both numerical and experimental methodologies to explore the aerodynamics within MGT blade passages, specifically using the Wren44 and Wren100 models supplied by Turbine Power Solutions Ltd. The research was aimed at developing and comparing different reverse-engineering (RE) strategies to enhance the aerodynamic efficiency of the main gas flow paths of the micro turbomachinery. Two unique RE strategies based on laser-scanning and iterative CFD techniques were evaluated. The discrete ("what the part really is") approach proved superior for detailed aerodynamics analysis, while the parametric ("what the part could be") was more suited for rapid design modifications, capturing overall blade performance with fewer parameters.

The entire MGT gas path was simulated using the renowned CFX software suite, employing both RANS and LES modelling techniques. The fidelity of these models was rigorously verified and validated against empirical data from jet engine tests and wind tunnel cascade experiments. The baseline performance of the MGT under various RPMs is documented

with an error margin of 4.45%, as derived from thrust sensor specifications. Subsequent design enhancements and parametric evaluations offered invaluable insights into the intricate physics governing flow dynamics within turbomachinery. For the Wren100 stator, modifications including reducing one vane, halving trailing edge thickness, and increasing the aspect ratio by 11% resulted in a thrust increase from 24.25N to 29.95N and an improvement in rotor isentropic efficiency from 80.1% to 81.1%. Additionally, halving the tip clearance of the rotor, coupled with the redesigned stator, potentially further enhanced isentropic efficiency to 83.4% while maintaining higher thrust levels.

The investigation into varying surface roughness levels through wind tunnel cascade experiments and LES WALE model simulations extended from normal (120,000RPM) to peak (160,000RPM) operational conditions for the Wren100 MGT. These studies culminated in actionable recommendations for optimal surface roughness maintenance. It was observed that surface roughness could eliminate laminar separation bubbles on the suction side near the leading edge of the Wren100 stator under different operational conditions, potentially delaying transition onset and enhancing turbulence intensity in the main flow, thereby reducing secondary losses. For the MGT rotor blade tip, increased surface roughness not only reduced the size of separation bubbles but also delayed their onset, potentially lower secondary effects like tip leakage flows and corner vortices.

This research stands as a pioneering analysis into the different blade characteristics and the effects of surface roughness on boundary layer evolution in MGTs under relatively low Reynolds number conditions, emphasising the importance of tailored roughness maintenance alongside other parameters to maximise thrust and aerodynamic efficiency.

Scholarly Contributions

0.1 Publications

1. Q. Yu, R. J. Howell, *CFD Modelling of Micro Turbomachinery Blade: Integrating Surface Roughness with Novel Reverse-Engineering Strategies*. The Aeronautical Journal (In Progress).

0.2 Conference Presentations

1. Q. Yu, *Study of Different Turbulence Models In Predicting 3D Flow And Impact of Surface Roughness Inside A Single Stage Micro Gas Turbine*. UK Fluids Conference, Sheffield, 2022.

Nomenclature

α	Flow Inlet Angle
β	Flow Exit Angle
Δv	Velocity Deficit
δ	Angle Deviation
δ_{bl}	Boundary Layer Thickness
δ_{wake}	Wake Thickness
$\dot{m}$	Mass Flow Rate
η	Isentropic Efficiency
Λ	Reaction
ϕ	Flow Coefficient
ψ	Stage Loading Coefficient
ρ	Density
τ	Shear Stress
θ	Blade Wedge Angle
ξ	Blade Stagger
C	Absolute Velocity
c	Blade Chord
C_a	Flow Axial Velocity
C_f	Skin Friction Coefficient
C_p	Pressure Coefficient
d	Diameter

F	Thrust
h	Enthalpy
k_s	Sand Grain (SG) Roughness
P	Static Pressure
P_0	Total Pressure
Pr	Pressure Ratio
R_a	Average Roughness Height
R_z	Mean Peak-to-Valley Height
Re	Reynolds Number
Re_k	Roughness Reynolds Number
s	Entropy
T	Temperature
U	Blade Speed
V	Relative Velocity
v_∞	Freestream Velocity
w	Two Dimensional Vorticity
y^+	Dimensionless Wall Distance
Y_p	Stagnation (Total) Pressure Loss Coefficient
AR	Aspect Ratio
CAD	Computer-Aided Design
CFD	Computational Fluid Dynamics
LE	Leading Edge
MGT	Micro Gas Turbine
RE	Reverse-Engineering
TE	Trailing Edge

Contents

List of Figures

Chapter 1

Introduction

1.1 Micro Gas Turbine Development Overview

In the realm of turbomachinery, the Micro Gas Turbine (MGT) represents a relatively recent innovation. Over the past two decades, its significance and application have grown markedly. Originating as a solution for civilian needs, its versatility has since been recognised in defence sectors as well. This widespread adaptability is captured in Figure 1.1, which delineates various contemporary uses of these compact turbines.

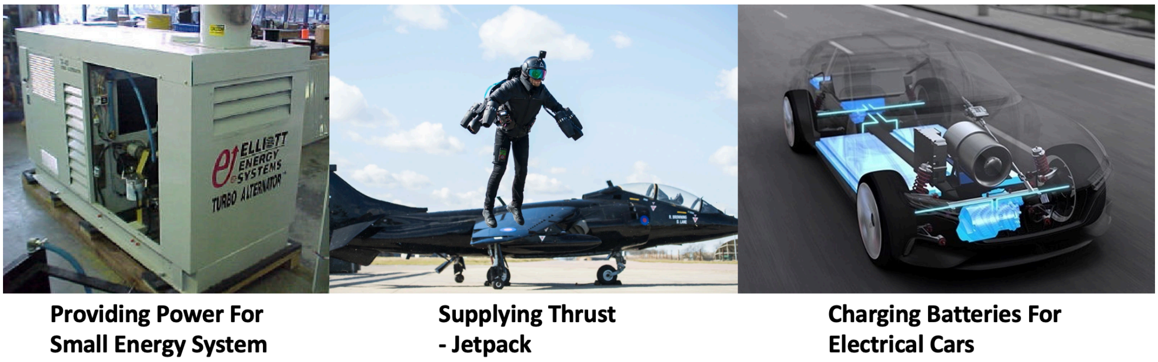

Figure 1.1: Micro Gas Turbine Typical Applications[1, 2, 3]

Compared to their full-sized counterparts turbomachines, the MGTs stand out due to their distinct attributes: they typically lack blade cooling and exhibit comparatively higher aerodynamic losses. By definition, an MGT can be characterised as a turbomachine with a power output ranging from roughly 15 to 300 kW [4]. With years of dedicated technical advancements and accumulating expertise, a variety of MGT models have come to the fore. Presently, several commercial versions of MGTs are available, with companies like Turbine Power Solutions Ltd. leading the way in innovation. Notably, under moderate pressure ratios, contemporary MGTs can achieve impressively high rotational speeds, approximately spanning from 50,000 to 160,000 RPM [5].

Table 1.1 shows some examples of modern MGTs and their specifications.

Turbine	Developer	Turbine Type	Max. Pressure Ratio (P_r)	Max. RPM ($\times 10^3$)	Max. Thrust (N)
Wren44	Wren Power	Single Stage Axial	2.9	195	44
Wren100	Wren Power	Single Stage Axial	2.3	160	100
Mercury HP	AMT	Single Stage Axial	2.8	151.9	88
B100F	BF	Single Stage Axial	3.0	125	120
P100-RX	Jetcat	Single Stage Axial	2.9	154	100
Hawk-100	Hawk	Single Stage Axial	3.8	175	110

Table 1.1: Specifications of Modern MGTs With Similar Thrust Capability [5, 6, 7, 8, 9]

Table 1.1 highlights that MGTs generally operate at low-pressure ratios while achieving high rotational speeds. A prime example of contemporary MGTs is the Wren series turbines, developed by Wren Power Systems Ltd. These turbines employ a myriad of existing technologies, with operational principles outlined as follows.

1. **Air Intake:** Initially, the airflow is directed through an intake component, which guides the air towards the compressor.

2. **Compression:** Within the compressor, the air undergoes compression, leading to a notable increase in both pressure and temperature.

3. **Combustion:** The high-pressure air then exits the compressor and mixes with atomised fuel within the combustion chamber. Concurrently, the ignitor generates electrical sparks or other ignition mechanisms, instigating the deflagration process. This process transforms the chemical energy stored in the fuel into heat, substantially increasing the air temperature.
4. **Turbine Conversion:** The high-enthalpy air then flows into the turbine, where its energy is harnessed and converted into shaft power.
5. **Power Output:** Finally, this shaft power is further transformed into kinetic energy in the turbine stator-rotor stages. This kinetic energy serves dual purposes: driving the compressor and providing the thrust or power output.

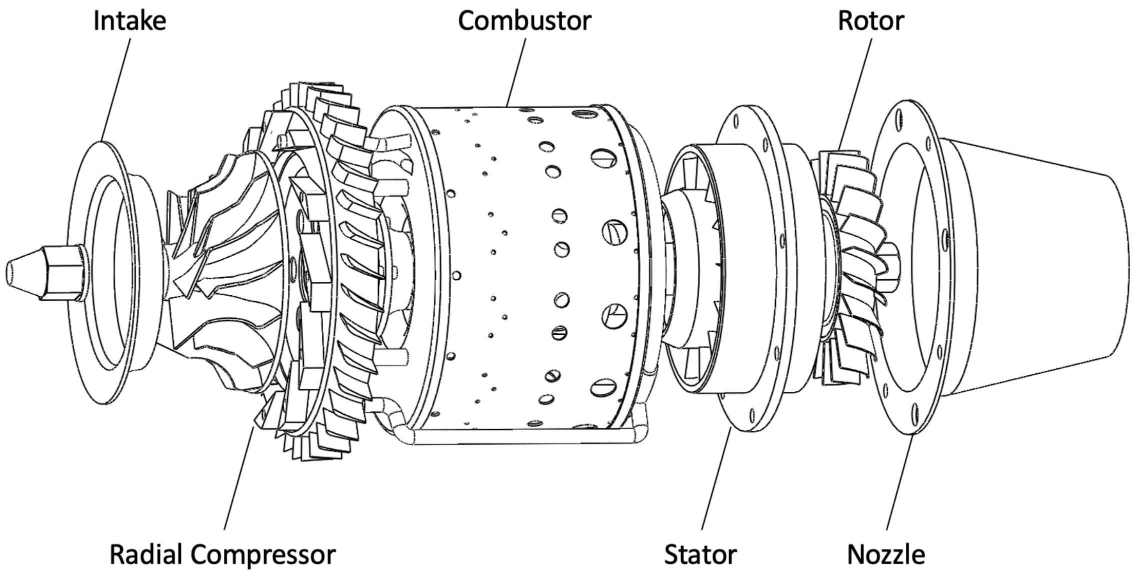

Figure 1.2: The Core Components of Wren Series Engines (CAD Drawing)

In Figure 1.2, the fundamental components of the Wren series engine are delineated. Among these, the Wren44 serves as the foundational model, boasting a peak thrust of 44N. In contrast, its successor, the Wren100, is an enhanced version with an elevated maximum thrust capacity of 100N.

1.2 Aerodynamic Loss in Micro Gas Turbine

Micro Gas Turbines (MGTs) have been observed to generally exhibit lower efficiency when juxtaposed with their larger gas turbine counterparts. The main causes for this differential in efficiency are summarised as follows.

1. **Aspect Ratio Concerns:** One primary consideration is the aspect ratio. MGTs characteristically have a smaller aspect ratio compared to larger turbomachines, predominantly in the 0.5-1.5 range. Due to this distinction, secondary flows in MGTs can capture a major fraction of the blade span. This, in turn, affects the overall aerodynamic performance, as secondary flows can induce loss mechanisms not as prevalent in larger turbines.

2. **Challenges with Tip Clearance:** As engineers miniaturise turbines to the scale of MGTs, there emerges a pronounced difficulty in sustaining minimal tip clearance. Factors contributing to this include the inherently viscous working environment and the reduced blade height. As portrayed in Figure 1.3, the magnified tip clearance in MGTs can result in significant performance deterioration. This is primarily attributed to escalated leakage losses, where the clearance allows a greater volume of working fluid to bypass the turbine's main flow path, causing efficiency penalties.

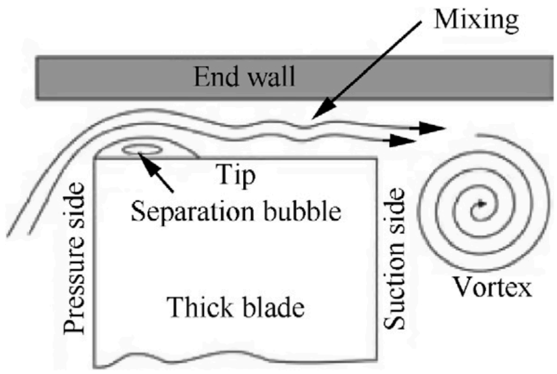

Figure 1.3: Turbo-machine Tip Leakage Flow Schematic Diagram [10]

3. **Reynolds Number Discrepancies:** Historically, studies have illuminated that MGTs predominantly operate under a relatively low Reynolds number spectrum, specifically from 4×10^4 to 5×10^5. This stands in contrast to larger turbines that operate at Reynolds numbers generally spanning from 4.2×10^5 to 8.2×10^5 [13]. It is an established fact in turbomachinery that, at reduced Reynolds numbers, transitional boundary layers become more prominent. These layers, which form a considerable portion of the blade surface boundary layer, are notorious for inducing significant aerodynamic losses. The complexity inherent to these transitional regions has led to the development of many correlations

that are semi-empirical in nature. Thus, it is of paramount importance to conduct experimental validations to accurately assess the aerodynamic performance of MGT blades under these conditions.

In summation, the mechanisms contributing to inefficiencies within MGTs starkly differ from those observed in larger turbomachines. To pave the way for advancements in the aerodynamic performance of MGTs, it is essential to delve deeply into the nuanced interplay between blade design attributes and the prevailing flow conditions, particularly focusing on how they orchestrate the various loss categories.

1.3 Flow Over Rough Surfaces of Turbine Blades

It is widely acknowledged that the presence of rough surfaces can profoundly influence the dynamics of the boundary layer flow, primarily by heightening flow instability proximal to the wall. As depicted in Figure 1.4, surface roughness can disrupt the cohesive viscous sublayer, catalyzing an accelerated transition from a laminar to a turbulent flow regime.

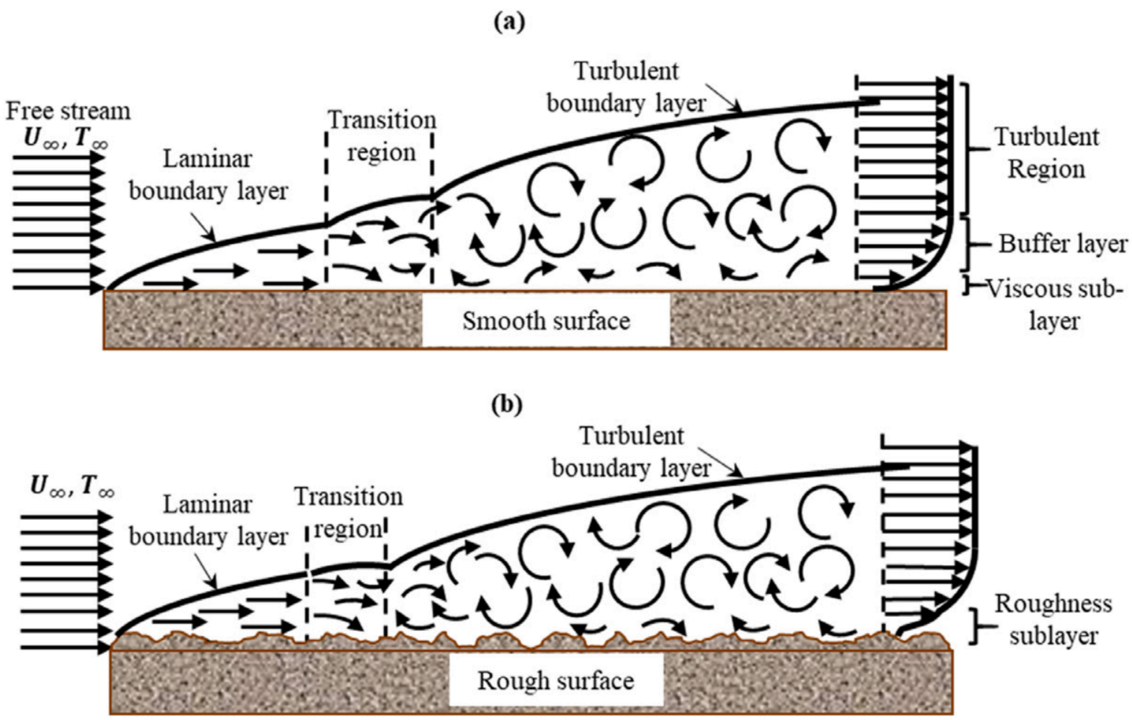

Figure 1.4: Boundary Layer Flow Over (a) Smooth and (b) Rough Surfaces

When this phenomenon is extrapolated to the realm of turbomachinery, the research by Taylor in 1990 illuminates that in-service turbine blades of considerable dimensions can exhibit appreciable roughness. Empirical data demonstrated that the roughness height on the suction side, proximate to the leading edge of the F-100 blade, peaked at 79 μm [12]. Now, when juxtaposing blades of varying scales but manufactured through analogous techniques, this consistent roughness height can potentially wield a disproportionately adverse influence on the aerodynamic performance of micro gas turbines relative to their larger counterparts. In the comprehensive study conducted by Alqallaf, a detailed examination of the impact of surface roughness on the aerodynamics within the turbine section is meticulously showcased. This research highlights how variations in surface roughness, significantly alter the flow dynamics across turbine blades. As shown in Figure 1.5, the visualisations clearly demonstrate that increased roughness leads to heightened turbulence and disrupted flow patterns. These changes are crucial as they affect the overall efficiency of the turbine by increasing the wall shear stress and potentially leading to higher energy dissipation and decreased aerodynamic performance. The findings are pivotal for understanding how even minor alterations in blade surface conditions can profoundly influence turbine aerodynamics, emphasising the need for precise control over surface finish in turbine design and maintenance [11].

However, it is imperative to recognise, as elaborated in Section 1.2, that the Reynolds numbers typical for MGTs are considerably attenuated compared to conventional turbo-machines. Given the propensity of MGTs to manifest relatively pronounced boundary layers, there exists an ambiguity regarding the tangible influence of surface roughness on the comprehensive performance metrics of the engine. Consequently, a pivotal objective of this research endeavour is to demystify the intricate interplay between surface roughness and the flow dynamics characteristic of MGTs.

1.4 Reverse-Engineering of Turbomachinery Parts

Over the years, extensive research efforts have been dedicated to refining the design of turbomachinery components. Often, such endeavours necessitate engineers to reverse-engineer existing 3D CAD models. While traditional design methodologies embark on a functional requirement and progress towards the final product, reverse engineering (RE) adopts an inverse approach. It begins with an extant product and

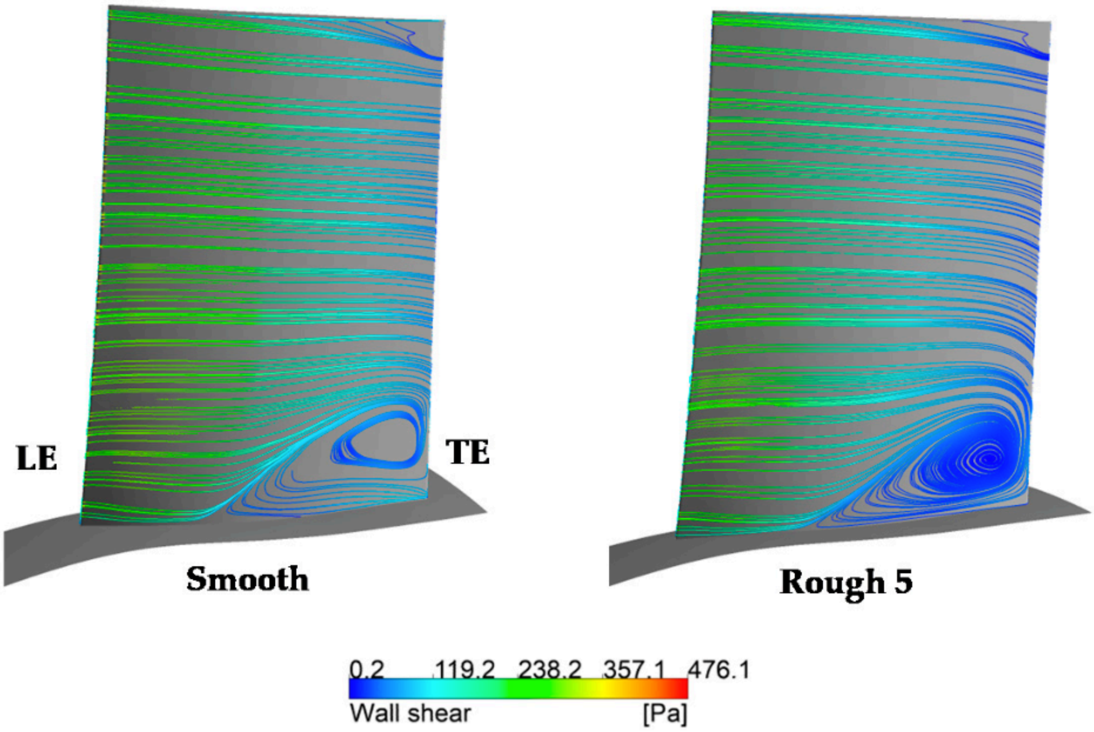

Figure 1.5: Impact of Surface Roughness on Turbine Blade SS Wall Shear Stress (Rough 5: $k_s = 150\mu m$) [11]

meticulously retraces its developmental path to reconstruct its geometry [92]. Various techniques, both contact-based and non-contact, are at the disposal of engineers to recapture the product geometry. Each method strives for a singular objective: to replicate the geometry with utmost fidelity. However, it is paramount to judiciously select an RE method that strikes a balance between achieving impeccable geometric accuracy and optimising resource expenditure in terms of time and cost.

For the RE of intricate geometries, such as micro turbine blades, the choice of digitising technique be it contact or non-contact is pivotal [93, 94]. Interestingly, the RE procedures for both contact and non-contact methods exhibit considerable similarities, with the primary divergence rooted in the data cloud acquisition approach. A noteworthy study by Mahboubkhah et al. (2016) elucidated that technical specifications proclaimed by digitising equipment manufacturers do not always mirror real-world accuracy [95]. This underscores the indispensable nature of experimental validation for RE models. To that end, in this research, both Computational Fluid Dynamics (CFD) simulations and empirical data based on the jet engine and wind tunnel cascade tests were harnessed to critically assess the veracity of RE models.

1.5 Impact of the COVID-19 Pandemic on the Research Project

The unprecedented onset of the COVID-19 pandemic significantly impacted the progression and methodology of this PhD project. The following paragraphs outline the key challenges and adaptations made to ensure the continuation and eventual success of the research.

Initially, the project faced significant delays in receiving parts for the Wren100 MGT from Turbine Solutions Ltd., crucial for the planned investigations. This situation necessitated a shift in focus to the Wren44 stator vanes for reverse engineering (RE) and Computational Fluid Dynamics (CFD) studies during the first one and a half years. Although similar, the Wren44 components were not fully representative of the Wren100 MGT, introducing certain limitations to the initial phase of the research.

The pandemic also imposed restrictions on the operational capacity of the Wren100 engine testing rig. Limited to a maximum of 120,000 RPM for the first two years, this constraint significantly affected the experimental scope and depth of data that could be gathered. Furthermore, the impact of the pandemic on campus operations severely restricted access to vital facilities such as the propulsion lab, tribology lab, and wind tunnel lab. The transition to remote work and the inability to access these labs hindered hands-on experimentation and delayed critical stages of the project.

Another significant challenge was the delayed availability of the wind tunnel facilities, which only became accessible in the third year of the project. The necessity for 3D printing and the use of iForge equipment for creating wind tunnel cascades added to these delays, as these resources were not available during the pandemic-induced lockdowns.

Finally, personal health was also impacted, as contracting COVID-19 necessitated a period of bed rest, directly affecting work efficiency and progress. Despite these challenges, the project adapted and advanced. The use of Wren44 components provided valuable preliminary insights, and virtual meetings, though less ideal than in-person interactions, maintained continuous communication with the supervisor and fellow researchers. This adaptability, resilience, and commitment to the research objectives enabled the successful achievement of most of the goals of this PhD project, despite the extraordinary circumstances imposed by the COVID-19 pandemic.

1.6 Thesis Overview

In this section, a concise overview of each chapter in the thesis is provided:

Chapter 1 provides an overview of MGTs, setting the context for the research by highlighting the intricacies of their aerodynamic behaviours and the ensuing motivations for a detailed analysis.

Chapter 2 presents a comprehensive literature review. It covers MGT performance metrics, loss classifications and their underlying principles, prevailing reverse-engineering approaches, and computational strategies for analysing turbine blade aerodynamics.

Chapter 3 outlines the experimental methodologies and equipment employed throughout the research. It also introduces a novel approach to estimating engine test errors via iterative CFD methods.

Chapter 4 details the development and comparison of varied MGT blade reverse-engineering techniques. It also showcases the reverse-engineered components in preparation for performance assessments in Chapter 5.

Chapter 5 explores the different computational parameters and models vital for the performance analysis and redesign of the MGT stator and rotor. It presents a thorough CFD verification and validation process anchored in jet engine tests and wind tunnel cascade data, with recommendations for selecting reverse-engineered models stemming from two distinct strategies (discrete or parametric).

Chapter 6 provides a comprehensive analysis of the aerodynamic performance of the Wren100 stator and rotor and their interplay. It also includes potential design recommendations aimed at improving the MGT stator and rotor efficacy and thrust.

Chapter 7 undertakes a meticulous study of the influence of varying surface roughness levels on the aerodynamic performance of the MGT, supplemented with potential maintenance recommendations for the MGT stator and rotor.

Chapter 8 incorporates the design enhancements proposed in Chapter 6, offering a comparative analysis of parametric studies and the redesigned performance of the MGT stator and rotor. It also details the manufacture of the redesigned components of the Wren100 MGT in anticipation of future engine tests.

Chapter 9 encapsulates the conclusions drawn from the accumulated research and forwards recommendations for future inquiries geared towards a more profound comprehension of the intricate aerodynamics within MGT blade passages.

Chapter 2

Literature Review

2.1 Introduction

As previously noted, the development and optimisation of micro gas turbines (MGTs) are faced with various challenges, including limitations in size, intricate flow conditions, and the absence of three-dimensional computer-aided design (CAD) data. This chapter provides an outline of existing literature on reverse-engineering of MGT components, recent research on enhancing the prediction and optimisation of turbine blade performance, as well as a comprehensive review of prior studies on the influence of surface roughness on gas turbine performance to enhance comprehension of flow dynamics within MGT blade passages.

2.2 Micro Turbomachinery Blades Fundamentals

2.2.1 Turbine Blade Characteristics

Turbine blades generally comprise two fundamental components, namely, the stator (NGV) and the rotor. The stator is designed to accelerate the flow in the absolute frame, thereby enhancing the tangential momentum, while the rotor serves the purpose of accelerating the flow in the relative frame, thereby generating power and thrust. Presently, gas turbines typically utilise solid or hollow blades, the latter of which facilitate the passage of cooling air within the blade to ensure that the metal temperature is within acceptable levels. The use of hollow blades made of Nickel-based superalloys has become widespread in Turbofan gas turbines with a high thrust-to-weight ratio since the 1990s, leading to a substantial increase in engine performance[14]. In the case of modern high-performance turbines, air-cooled blades are preferred due to the extremely high operating temperature. For example, the

Rolls-Royce Spey Gas Turbine employs triple-pass air cooling blades that have been specially treated to enhance their resistance to oxidation and high temperatures[15]. In this project, studies were only concerned with micro gas turbines, which normally do not have cooling passages due to the tiny blade sizes. Thus, the selection of an appropriate blade shape and its characteristics is of utmost importance in providing an efficient power supply.

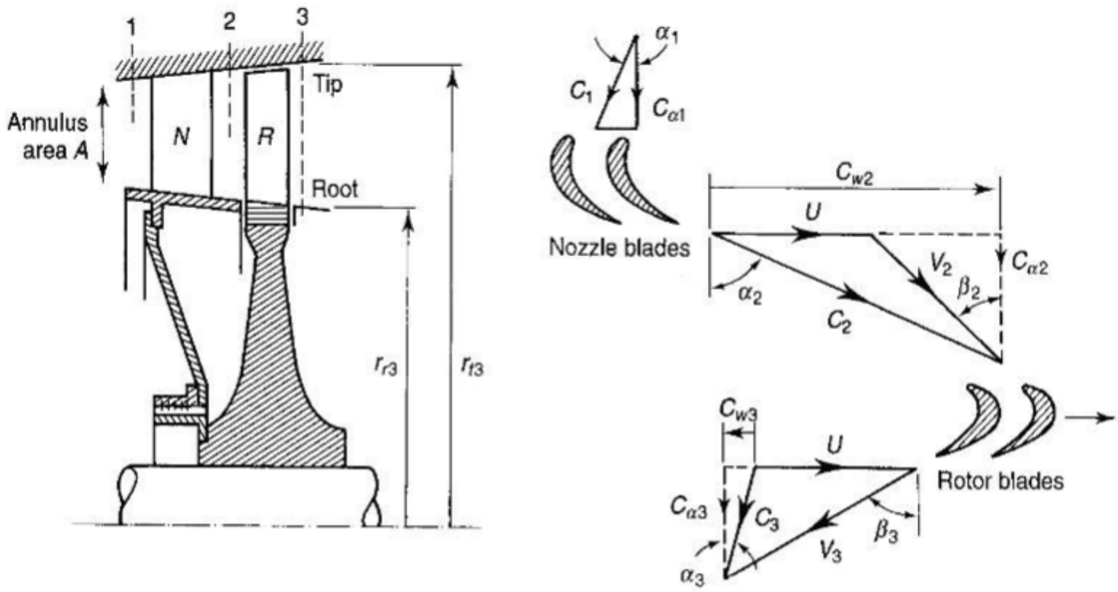

Figure 2.1: Axial Flow Turbine Velocity Triangles [17]

Drawn in a frame of reference that is attached to the rotating blades, the velocity triangles (as shown in Figure 2.1) are useful graphical representations and design tools to analyse fluid motions within the MGT passages. Studies have shown that many important parameters such as the blade design, inlet angle, and rotational speed can be optimised through the analysis of velocity triangles. For turbine velocity triangles, there are three main types of angles, which are the blade angle, relative velocity angle and exit angle. The detailed descriptions of those angles are listed in Table 2.1. The blade angle is the geometric orientation of the blade fixed in the turbine design, whereas the flow angle represents the actual angle at which the working fluid approaches or leaves the blade under dynamic conditions. Deviations between these angles often occur due to the dynamic response to the operation conditions of the turbine that leads to the pressure and velocity changes around the blade. Adjusting the blade angle to maintain optimal design incidence reduces the probability of flow separation and enhances performance, particularly in variable-speed gas turbine engines [18, 19].

Angle Type	Description
Blade Angle	Between the inlet velocity vector and the blade velocity vector
Relative Velocity Angle	Between the inlet velocity vector and the relative velocity vector
Exit Angle	Between the blade velocity vector and the outlet velocity vector

Table 2.1: Angles in Turbine Velocity Triangles [17]

Based on the different velocity triangles, there are two main categories of turbine blades, which are Impulse and Reaction turbines. According to textbook definitions, for the Impulse type of blading, all the pressure drop in the turbine comes from the momentum effect in the nozzle. Therefore, the reaction (Λ) is zero, meaning the gas angle β remain constant after the impulse blade ($\beta_2 \simeq \beta_3$). For the reaction turbine, the pressure change in the turbine would come from both the nozzle and the rotor [21]. During the design of blade profiles, it is significant to understand that the velocity triangles in Figure 2.1 represent the gas angles, not the turbine blade angles.

The design and optimisation of turbine blades involve many blade parameters. Figure 2.2 shows the cascade of turbomachinery blades with the notation of some essential design parameters.
As shown in Figure 2.2, the stagger angle (ξ) is the angle between the reference direction (the line perpendicular to the cascade front) and the chord line. Based on the parameters, several useful blade characteristics could be calculated. The first one is the blade solidity (σ), which is the ratio of the chord (c) and the pitch (s) as shown in Equation 2.1.

$$\sigma = \frac{c}{s} \tag{2.1}$$

Blade solidity is a crucial parameter in determining the pressure drop and mass flow rate across the turbine stage. In practice, the space-chord ratio (s/c) can also be used instead of the solidity. Higher solidity usually means a large blade chord length relative to its circumference or more blade number. Studies have shown that a higher pressure drop that leads to higher power output could be achieved by increasing the

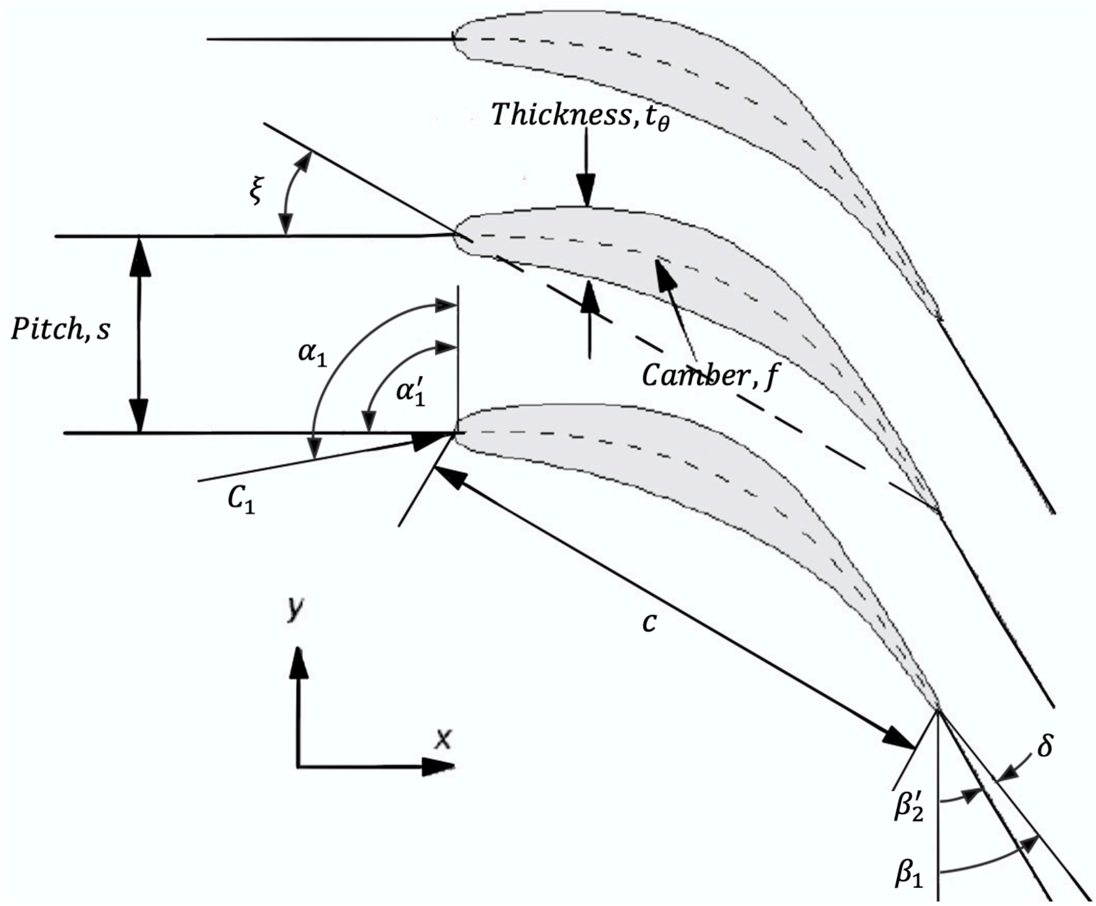

Figure 2.2: Turbomachinery Blades Cascade With Parameters Notations

blade solidity. However, high solidity would often result in too many blades, which could cause higher profile loss due to increased surface area and higher manufacturing and maintenance costs. In addition to impacting the loss and power output of the turbine, blade solidity can also influence the stability of the turbine. A high blade solidity can result in increased vibrational forces, which can cause mechanical stress on the turbine components and reduce its lifespan [17, 20].

Secondly, as the blade outlet angle and the flow outlet angles are expressed by β_2' and β_2, the deviation (δ) can be calculated to represent the difference between the blade exit angle and the flow exit angle:

$$\delta = \beta_2 - \beta_2' \tag{2.2}$$

As the deviation (δ) arises due to the viscous and inviscid effects; therefore it is nearly impossible for the flow to follow the blade angle precisely, meaning the flow will leave the trailing edge at a slightly different angle to the blade exit angle. Thus, for the designed turbine blade to achieve the desired aerodynamics, the designer will need to assume a velocity distribution and a proper computational method to determine different blade characteristics. In addition, it is known that the Reynolds number and the flow boundary layer are interrelated with the deviation. As the Reynolds number decreases, the boundary layer would grow thicker and the deviation would be larger, which could lead to lower turbine stability and efficiency. To justify the computational results and gain a further understanding of unsteady flow phenomena, the design will also be backed up by cascade results.

The third important blade characteristic is the aspect ratio (AR), which refers to the blade height to its chord and can be calculated with Equation 2.3.

$$AR = \frac{h}{c} \tag{2.3}$$

Generally, it is known the higher aspect ratio leads to a lower secondary loss, which is a term used to describe the reduction in efficiency due to losses in the blade wake, such as turbulence and mixing. Reducing secondary loss normally results in higher power outputs and efficiency. However, increased mechanical stress and manufacturing difficulty can be caused by high aspect ratio blades due to their higher vibrational force and deflection. Thus, the value of the optimal aspect ratio is a trade-off between aerodynamic performance and other design considerations and must be carefully decided based on numerical or experimental analysis. Several pieces of previous research have studied the impact of different aspect ratios on the aerodynamic performance of turbomachinery blade channels. Choi et al. compared the effect of three different aspect ratios of 1:0.5, 1:1 and 1:2, and they discovered the 1.1 aspect ratio would have the highest aerodynamic performance ratio [16]. Pullan et al. conducted the experimental and numerical study with three low aspect ratio NGVs, in which extremely strong secondary flows were discovered that resulted in high secondary loss. More details about turbine blade loss are explained in Section 2.3.

2.2.1.1 Micro Gas Turbine Performance Parameters

In contemporary turbomachinery research, the aerodynamic design of blade profiles has been shown to significantly influence turbine performance. For effective design outcomes, a comprehensive understanding of specific performance parameters is paramount prior to delving into intricate details about blade aerodynamics [17]. Utilising velocity triangles for a single axial turbine stage, and integrating the nomenclature presented in Figure 2.1, there are three primary dimensionless variables instrumental for microturbine design: the stage loading coefficient (ψ), the reaction (Λ), and the flow coefficient (ϕ).

The stage loading coefficient (ψ) acts as a representative dimensionless quantity, elucidating the work potential of an individual stage within a turbine system. A judicious choice of ψ during the preliminary design phase of a turbomachine is pivotal, as it influences both efficiency and power output. Currently, the consensus in the field dictates that this coefficient can be ascertained using Equation 2.4, considering the angles outlined in Figure 2.1 [17].

$$\psi = \frac{2C_p\Delta T_{0s}}{U^2} = \frac{2C_a}{U}(tan\beta_2 + tan\beta_3) \tag{2.4}$$

For enhancing the turbine power output and efficiency, optimisation of the stage loading coefficient is possible through various methodologies. Notably, considerations include blade design, inlet conditions (temperature and pressure), the number of stages, and overall turbine dimensions.

Another vital performance metric is the degree of reaction (Λ). Rather than focusing on pressure drops, this dimensionless parameter predominantly considers the reduction in static temperature or enthalpy.

$$\Lambda = \frac{C_a}{2U}(tan\beta_3 - tan\beta_2) \tag{2.5}$$

The reaction (Λ) plays a decisive role in turbine performance, quantifying the fraction of stage expansion occurring within the turbine rotor. A heightened reaction implies a larger segment of the working flow energy being transformed into mechanical energy. Analogous to the stage loading coefficient, prudent selection of the reaction is crucial during the preliminary stages of turbine design. Factors influencing this include inlet conditions, blade design, and turbine dimensions [22]. Empirical investigations, such as the study by Lee et al. on a 10-stage steam turbine, revealed robust correlations between the stage reaction and resultant efficiency [23].

In addition to these parameters, understanding the intricacies of physical expansions, specifically pressure and temperature drops, is of paramount importance. These expansions play a pivotal role in defining the thermodynamic performance of turbines. A pressure drop across the turbine stage signifies the conversion of potential energy (in the form of pressure) into kinetic energy, which is then harnessed as useful work. Conversely, a temperature drop represents the isentropic expansion of the working fluid, leading to an associated decrease in its enthalpy. Both these phenomena, intricately linked with the fundamental principles of energy conservation, directly influence the efficiency and output power of a turbine. Furthermore, they serve as vital benchmarks when evaluating the aerodynamic and thermodynamic efficacy of blade profiles and other design parameters. An optimal balance between pressure and temperature drops, achieved through meticulous design and operational practices, ensures maximised turbine performance while mitigating potential inefficiencies and mechanical stresses.

Last but not least, the Smith chart, drawing from the flow coefficient and stage loading coefficient, has frequently been employed as an initial design instrument to critically assess and design gas turbine performance.

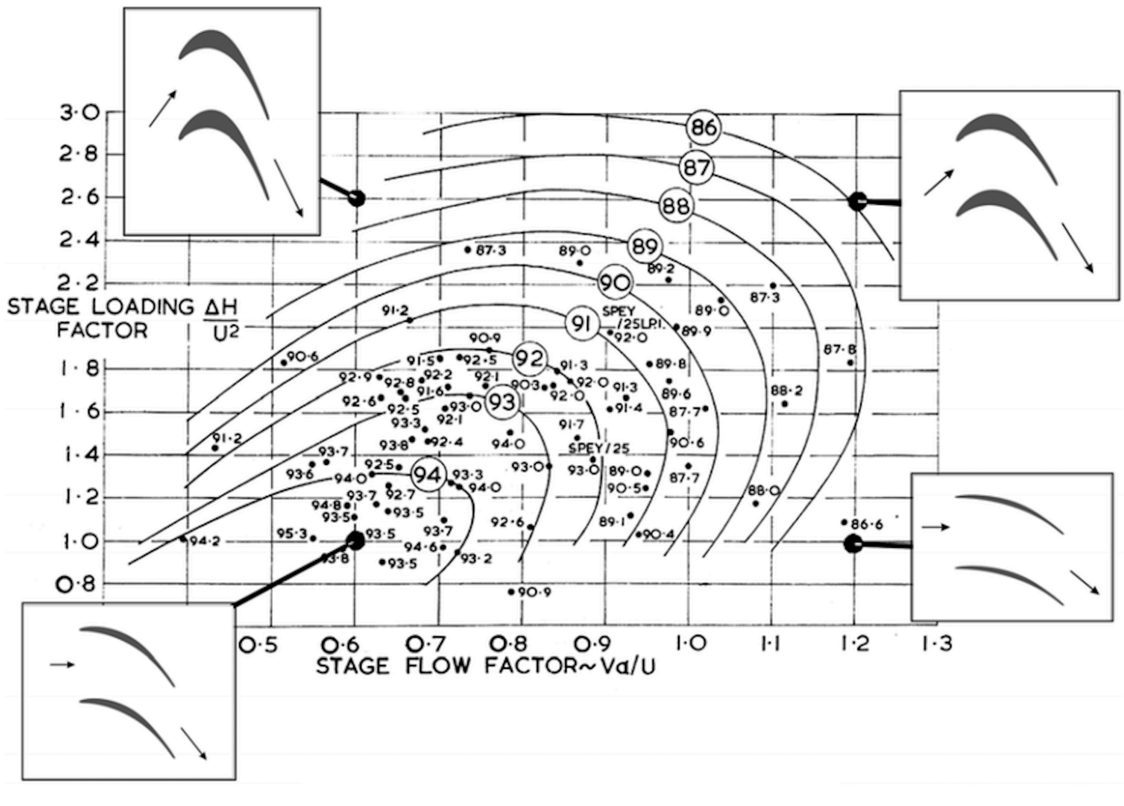

Figure 2.3: Smith Chart For Turbine Stage Efficiency [24, 25]

As shown in Figure 2.3, the Smith chart provides a graphical representation of the turbine complex admittance. By mapping the flow coefficient against the stage loading coefficient, the Smith chart allows engineers to quickly gauge performance characteristics and make informed decisions about modifications or optimisations needed for enhancing turbine efficiency. This tool is particularly beneficial in analysing the influence of diverse design parameters on gas turbine performance. Critical parameters include blade characteristics, such as height, pitch, and angle. Another integral application of the Smith chart is its capability to visually convey the implications of flow angle deviations. Such deviations can potentially result in diminished thrust and efficiency, underscoring the importance of precision in design considerations.

2.3 Micro Turbomachinery Blade Loss Categories

As previously noted, the small scale of Micro Gas Turbines (MGTs) often means they lack features commonly found in larger counterparts, such as internal or film-cooled blades. In contrast, conventional-sized gas turbines frequently employ film cooling to enhance operational efficiency. This technique involves injecting a protective sheath of cooler air between the blade surface and the high-temperature external flow. While film cooling is invaluable in maintaining blade integrity and extending component life under elevated temperature conditions, it is not devoid of challenges. Specifically, the introduction of this cooler layer can lead to the development of a thicker boundary layer on the blade surface, subsequently inducing aerodynamic losses. The experimental research by Day et al. elucidates this phenomenon, illustrating the correlation between film cooling and efficiency losses. Their findings, specifically pertaining to the efficiency loss experienced in a nozzle guide vane due to film cooling, are graphically represented in Figure 2.4.

Ito et al. have extensively documented the impact of film cooling on the mid-span total pressure loss, particularly when cylindrical holes are employed on the pressure side (PS) and suction side (SS) of an airfoil cascade [27]. With this in perspective, non-air-cooled micro turbines stand to benefit significantly by sidestepping these cooling-related losses. In the absence of factors related to blade cooling, the cumulative efficiency degradation for MGTs can be systematically segmented into three principal components: profile loss, secondary loss, and tip leakage loss. Each of these components has its distinct implications on the overall turbine performance and has been the subject of myriad research endeavours. The succeeding subsections delve into existing studies that shed light on these disparate turbine blade loss mechanisms.

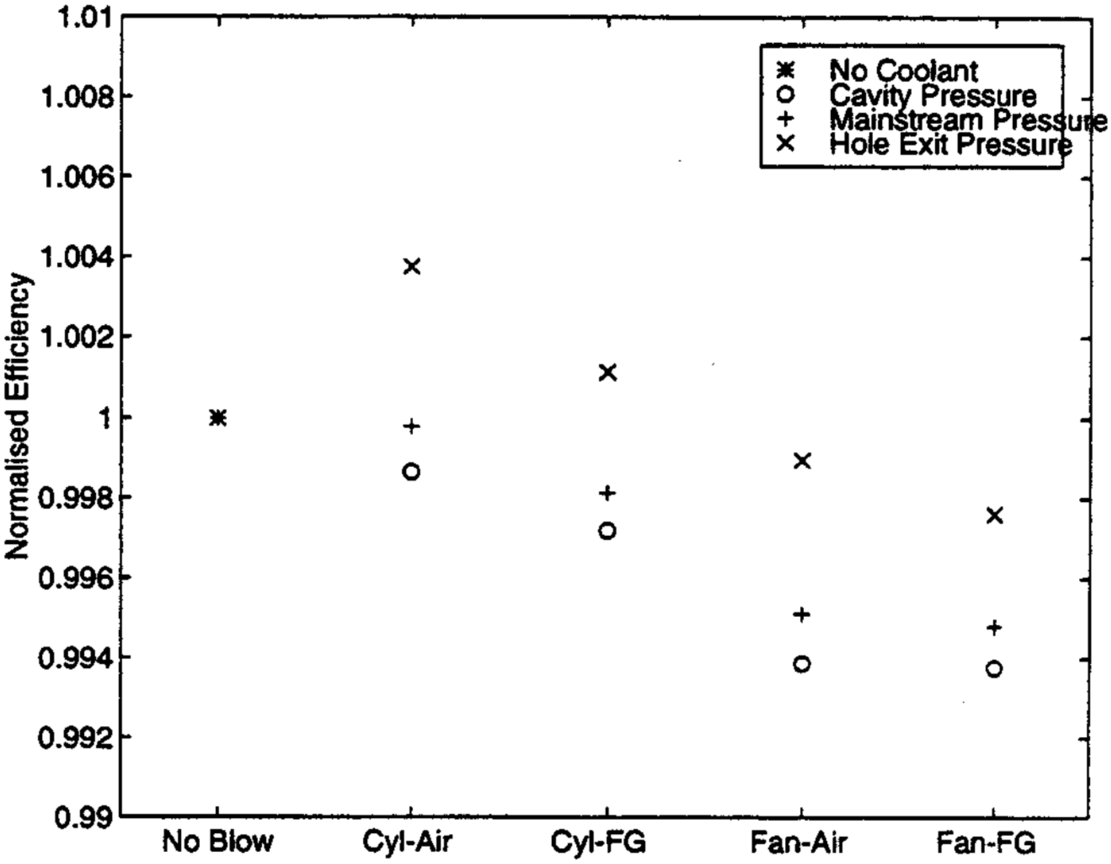

Figure 2.4: NGV Mid-span Efficiency Loss: Cooled Vs. Uncooled [26]

2.3.1 Profile Loss

Across the spectrum of modern turbomachinery, spanning various scales and applications, profile loss stands out as a pivotal determinant of performance. It acts as a critical metric guiding the design and optimisation of stator vanes and rotor blades. Due to the existence of high-velocity regions and flow diffusion near the suction side of turbine blades, the strong adverse pressure gradient is likely to cause the flow boundary layer separation, which could lead to high profile loss and significant reduction of the turbine efficiency [28]. As shown in Figure 2.5, the pressure coefficient distribution diagram shows the typical flow separation within turbine blades due to the low Reynolds number, which could lead to an increased aerodynamic loss [29].
MGTs are particularly susceptible to the repercussions of high profile loss. One notable consequence of such losses is the heightened propensity for the accumulation of dust, debris, and other particulate contaminants on the turbine blades. This accumulation can lower the overall turbine efficiency, leading to tangible reductions in its

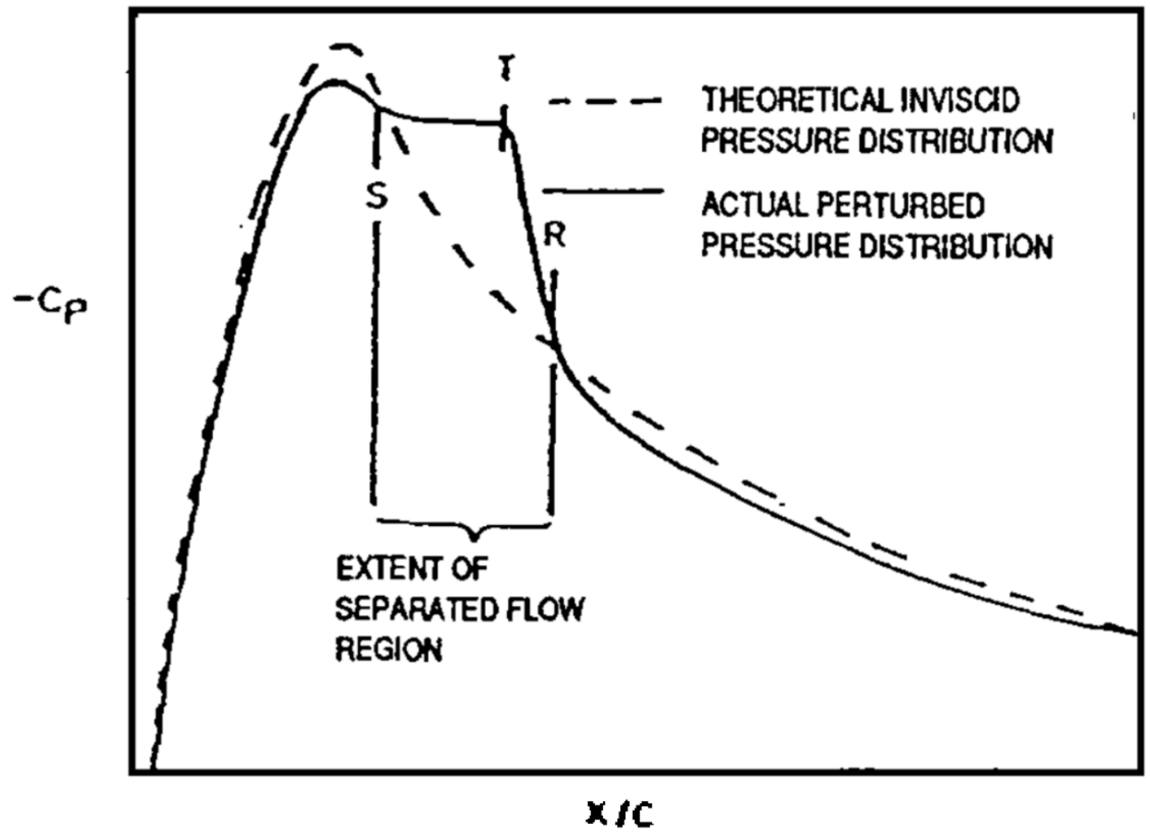

Figure 2.5: Schematic Diagram of a Separation Bubble & Pressure Distribution [29]

overall power output [30].

Extensive research has been conducted to decipher the intricate relationship between profile loss and gas turbine performance. In a seminal experimental study spanning Reynolds number flows from 80,000 to 200,000, LaGraff and Ashpis noted an efficiency decrement of approximately 2% attributable to augmented profile losses. Such losses were traced back to flow separations occurring on the suction side of the turbine blade [31, 32]. Profile loss multifaceted nature stems from its sensitivity to a plethora of factors, including blade shape, surface roughness, Reynolds number, inlet turbulence intensity, and upstream wakes, among others [33]. For transonic turbines, blade shape, specifically the trailing edge configuration, commands paramount significance. As elucidated by Rossiter, Pullan, and Melzer, trailing edge losses can account for nearly a third of total profile losses. Through Large Eddy Simulations (LES), their research spotlighted the inherent connection between trailing edge loss, base pressure, and trailing edge wedge angle. A mere alteration in the trailing edge wedge angle, from 8 to 14 degrees, was documented to slash aerodynamic losses by a substantial

29% [34].

Addressing and reducing profile losses in modern turbines presents a formidable technical challenge. Despite strides in understanding, the complicated flow dynamics within blade passages remain shrouded in mystery. Moreover, mitigation efforts occasionally demand design trade-offs, with solutions for profile loss occasionally exacerbating other types of losses. Given that profile loss is intrinsically linked with separation bubble-related losses, researchers have concentrated their efforts on demystifying the flow dynamics within turbine passages and devising loss control strategies. Pioneering computational studies employing high-fidelity numerical methods, such as Large Eddy Simulations LES and Direct Numerical Simulations (DNS), by Rao et al. and Michelassi et al. revealed that upstream periodically passing wakes, alongside unsteady flow behaviourslike free stream turbulence within blade passagescould be instrumental in curtailing losses like profile loss [35, 36]. These insights were also corroborated experimentally by the work of Opoka and Hodson on the T106 LP turbine blade cascade. Their findings underscored efficiency enhancements to the tune of 0.25%, achieved by optimising the upstream wake and downstream potential flow fields, subsequently leading to diminished suction side boundary layer losses [37].

2.3.1.1 Flow Transition Within Turbo-machines

The role of the boundary layer in shaping blade profile loss cannot be overemphasised. Specifically, the state of the boundary layer proximate to the suction side of a turbine blade profoundly impacts profile loss. The progression of flow transition can precipitate alterations in pressure distribution and augment skin friction drag, making the investigation of transitional dynamics crucial in turbine blade design and optimisation endeavours.

Different Transition Mechanisms

Conventionally, flow transition is characterised as the metamorphosis from laminar to turbulent flow over a finite span. Historically, turbomachinery research often oversimplified the intricacies of this transition. By predominantly employing fully turbulent models, these early studies rendered the transition process as a sudden event, neglecting the nuanced transitional phases in between. Yet, with the advancement of computational capabilities and deeper insights into fluid dynamics, there has been a paradigm shift. A noteworthy example is the modular Reynolds-averaged Navier-Stokes (RANS) methodology. This approach was architected specifically to model the laminar-turbulent transition in turbomachinery flows, signifying a concerted effort to more accurately encapsulate the gradations of the transition process [49]. As delineated in Figure 2.6, turbines can manifest a triad of typical transition mechanisms. These mechanisms encompass:

- **Natural Transition:** This is an inherent process, often instigated by minute perturbations in the flow or surface imperfections, which gradually escalate and culminate in turbulence.
- **Bypass Transition:** This mode is typically expedited by high levels of external turbulence, effectively "bypassing" some of the intermediate phases inherent to the natural transition process.
- **Separation-Induced Transition:** Here, an adverse pressure gradient forces the flow to separate, with the separated laminar boundary layer undergoing a rapid transition to turbulence before reattaching to the surface.

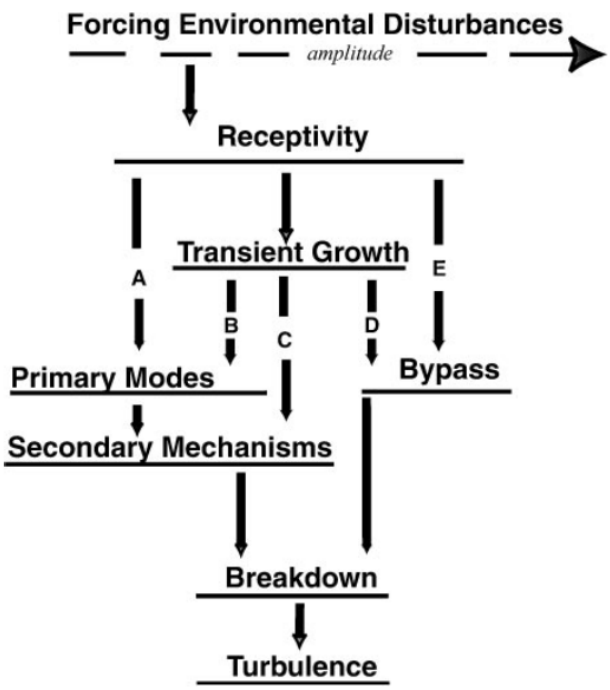

Figure 2.6: The Path from Laminar to Turbulence Transition [50]

The first transition mechanism is known as the natural transition, which is caused by the "Tollmien-Schlichting waves" and occurs typically when the turbulence intensity level is relatively low. For the natural transition flows, the intermittency would be produced slowly, meaning the point of fully turbulent flow can be far from the transition point. Linear instability waves can be found to grow inside the laminar boundary layer and then nonlinear break down into turbulence. Nature transition could be incurred by many small disturbances, including acoustic noise and surface roughness. For turbine blades, nature transition usually happens near the trailing edge region, where exists high adverse pressure gradients and local peak of skin friction coefficients [51, 52].

The second flow transition mechanism is called the bypass transition, which is a rapid process and usually occurs when the turbulence intensity is high. Klebanoff first identified this mechanism during his experimental research on the free-stream turbulent flow, in which he discovered that the turbulence spots or streaks could be developed directly within the boundary layer caused by the free-stream disturbances, meaning the first stage of the transition mechanism is bypassed [53]. Due to the high-intensity level of turbulent flow, the transition process would be forced upstream, leading to a bypass transition instead of a natural transition [54].

The third mechanism is the separation-induced transition. As the name suggests, laminar separation bubbles (LSB) are caused by the separation of the laminar boundary layer due to strong adverse pressure gradients or geometric discontinuities. The separated shear layer then becomes unstable and rolls up to vortices. Afterwards, the vortices interact with the wall and reattach to generate a separation bubble. Finally, the instability of the LSB would increase and break down into turbulence [54, 55]. According to the detailed research by Gaster, during the separation-induced transition process, the bursting phenomenon could be observed, which shows a short separation bubble transfer into a long separation bubble. Gaster also discovered that the flow inside the bubble is mostly laminar with TollmienSchlichting instabilities under low free-stream turbulence conditions [56]. For turbomachinery applications, LSB would naturally be formed near the leading edge of the blade leads to the reduction in the aerodynamic performance. Previous studies have shown that the size of LSB depends on the Reynolds number, the free-stream turbulence intensity and the Reynolds number. Hatman and Wang conducted experimental research on the separation-induced transition under constant free-stream turbulence intensity and adverse pressure gradient, and they found that the size of LSB increases as the Reynolds number reduces. Also, the research by Hatman and Wang shows that under extremely low Reynolds number flow, the boundary layer does not reattach due to massive separation, meaning the LSB is open [57]. Thus, lowering the Reynolds number in turbomachinery would generally lead to higher losses and lower efficiency. To study the separation-induced transition on a highly loaded low-pressure turbine blade profile, Minot et al. carried out RANS simulations based on the four-equations transitional turbulence model. It was found that the use of correlation by Langtry et al. would generate the best compromise between precision and trends for transition Reynolds numbers [58]. Based on the spectral study of a low-pressure blade by Graveline, a method was developed by Graveline and Sjolander to identify frequency peaks according to the empirical relations between flow velocity, boundary layer thickness and the state of the free shear layer on the peak frequency locations. The presence of Kelvin-Helmholtz instability and Tollmien-Schlichting waves were also identified by the above method, which the results suggest that both Reynolds number and turbulence intensity can influence the waves and instabilities [59]. By adopting the LES turbulence model to study the boundary layer transition mechanism, Segui et al. found that the Kelvin-Helmholtz instability is the main cause of the transition mechanisms [60].

Flow Transition Triggering Factors

The transition process, a pivotal element in the study of turbomachinery, has a complex nature, with multiple factors influencing its occurrence and progression. Paramount among these factors are listed as follows [48].

- Incidence angle, which can induce local flow separation.
- Blade surface roughness, affecting the laminar flow stability.
- Free-stream turbulence, inducing disturbances in the flow.
- Surface curvature, altering the pressure distribution.
- Reynolds number, reflecting the flow inertial forces relative to viscous forces.
- Pressure gradient, which can accelerate or decelerate the flow.

Several past studies have delved into understanding this process; however, not all have succeeded in rendering accurate predictions of boundary layer performance. The challenge arises predominantly because, in specific turbo-machines, the transitional region length can be considerably large, demanding keen attention to achieve trustworthy predictions regarding boundary layer behaviour [38]. The cascade study by Walker provides a notable insight into this area. For turbine blades subjected to a Reynolds number of 2×10^5 with a turbulence intensity of 0.2%, the transition zone was found to account for roughly 10% of the chord length. Notably, the experimental observations by Turner and Hodson, made under a free-stream turbulence intensity of 0.5%, echoed the findings by Walker [39, 40, 41]. Moreover, Walker proposed a model, aiming to predict the length of the transitional zone, considering the continuous breakdown of laminar instability waves. This model is expressed as:

$$L_T = 5.6 \frac{C_r}{u_e} \frac{\nu}{u_e} Re_{\delta^*}^{\frac{3}{2}} \tag{2.6}$$

The complex phenomenon of laminar-turbulent transition, especially under varying turbulence levels, has also been the subject of extensive literature. For instance, a study highlighted the transition processes within turbine blades, specifically, when the Free-Stream Turbulence Intensity (FSTI) exceeds the 0.51% range, [43]. Another experimental study shed light on transitions occurring amid high free-stream turbulence in boundary layers affected by pressure gradients [44]. Furthermore, high turbulence levels were observed to greatly influence boundary and shear layer stability, often promoting premature transitions [45].

The interaction between pressure gradients and transitions has also garnered academic attention. A specific experimental study underscored how naturally occurring transitions in boundary layers, combined with turbulence and pressure gradient effects, play a pivotal role, especially in supersonic boundary layers [46]. On the other hand, a simulation-based investigation delved into modelling transitions in boundary layers of roughened turbine blades, emphasising the impacts of both turbulence and pressure gradients [47].

Additionally, a comprehensive research effort elucidated the role of the laminar-turbulent transition in dictating aerodynamics and heat transfer dynamics in both contemporary and next-generation gas turbine engines. This research married both theoretical and experimental approaches to offer a multifaceted perspective on transition phenomena in gas turbines [13].

In conclusion, the intricacy of the transition process, combined with multifactorial influences and occasional disparities in experimental data, makes a universal analytical solution elusive. The contemporary approach often marries numerical simulations with experimental and semi-empirical findings to navigate these challenges. This combination underscores the need for engineers to develop a profound grasp of the diverse physical phenomena at play. The following subsection delves into turbine cascades, a conventional experimental method adopted by engineers to probe into the profile loss of the turbine blades.

2.3.1.2 Axial Turbine Profile Loss Prediction - Cascade Test

As reviewed earlier, gas turbine profile loss primarily results from diffusion and the adverse pressure region near the blade suction side. One prevalent methodology to forecast profile loss involves the execution of two-dimensional cascade tests, facilitated through experimental setups or numerical simulations. The primary goal of these tests is data accumulation to ascertain the aerodynamic viability of the blade profiles in question. Given this backdrop, grasping the intricacies of cascade performance parameters becomes paramount.

In the context of the discussion in subchapter 2.2.1, a multitude of research efforts has pinpointed that deviations (δ) manifest predominantly because of viscous and inviscid phenomena. This renders it an uphill task for the flow to meticulously adhere to the blade angle, inevitably causing the flow to deviate from the blade exit angle as it departs from the trailing edge. This understanding underscores the need for designers to hypothesise a pertinent velocity distribution, and to harness an appropriate computational methodology to delineate the blade various characteristics. It is quintessential that these computational findings are corroborated with cascade results to ensure a holistic understanding of unsteady flow dynamics. Figure 2.7 captures a visual representation of turbine cascade tests undertaken by earlier researchers, emphasising the importance of understanding the deviation angle and its impact on losses.

Past investigations indicate that the main culprits behind losses in blade cascades are the boundary layers forming on both the suction and pressure sides of blades. These layers tend to amalgamate at the blade trailing edge, resulting in a localised defect in stagnation pressure known as blade wake. In a comprehensive review, Curtis et al. distilled a vast array of experimental data concerning loss localisations. The succinct breakdown of these findings can be observed in Figure 2.8.

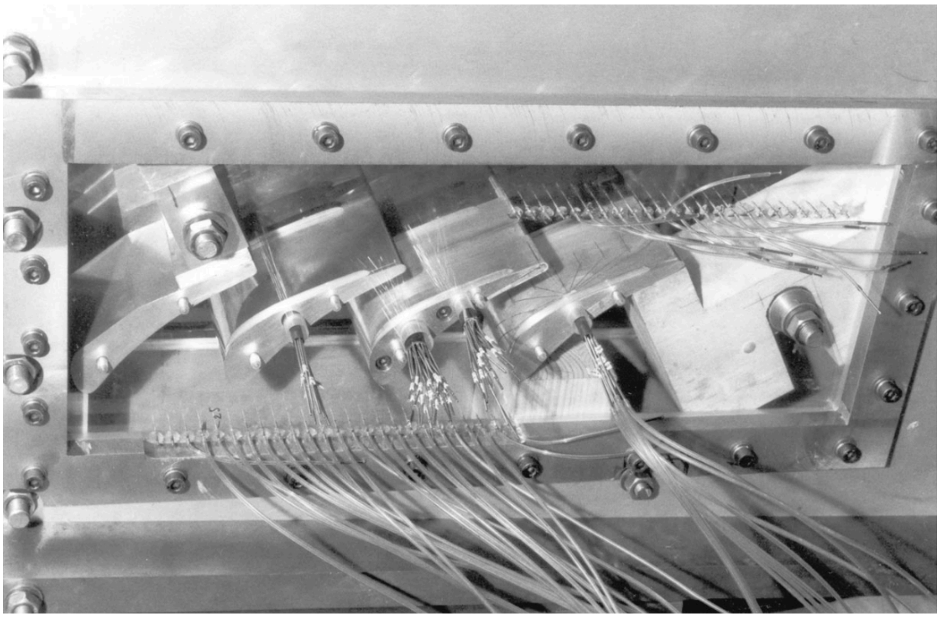

Figure 2.7: Photograph of the Cascade Tests Section [61]

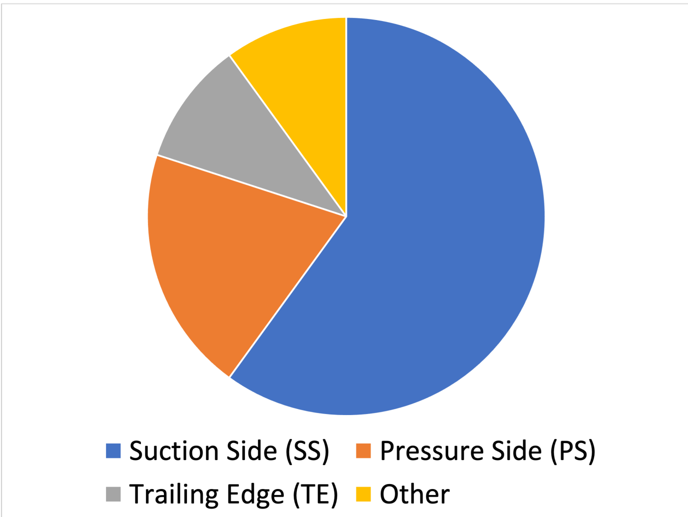

Figure 2.8: Approximate Breakdown of Loss Locations [63]

A cursory glance at Figure 2.8 reveals that most of the loss is attributed to the suction side. In alignment with earlier research, the reduction in stagnation pressure tends to reduce in intensity as the flow moves further from the turbine blades. However, overall losses amplify as the flow mixes out downstream of the trailing edge. Curtis pointed out potential performance enhancements by reducing the thickness of the trailing edge [63]. Moreover, when cascade tests operate under elevated Mach numbers, other contributory loss factors, like shock waves, come into play. The design blueprints for both stator and rotor components can be informed by these cascade tests. Prior research focusing on the two-dimensional cascade model has elucidated the presence of three-dimensional flow patterns, primarily instigated by secondary flow from viscous effects. This phenomenon is typically characterised by the axial velocity density ratio.

2.3.1.3 Performance Parameters of Turbine Cascades

This subsection elucidates various performance parameters employed to assess the performance of turbine blade cascades. Among these parameters, the non-dimensional total pressure loss and flow deflection have gained prominence as performance metrics in turbine blade cascade studies. With a pre-defined Axial Velocity Density Ratio (AVDR) set for the designed turbine blade cascade, essential flow conditions requisite for cascade testing are tabulated in Table 2.2.

Table 2.2: Primary Input Data - Flow Conditions

Required Input Data	**Symbol**
Flow Angle (Inlet)	α_1
Mach Number (Inlet)	M_1
Blade Reynolds Number	Re

Once the primary input data is ascertained, the turbine blade design and performance can be improved by evaluating or computing several parameters, notably the exit flow angle (α_2), stagnation pressure loss (Y_p), and the energy loss coefficient (ζ). These performance parameters are associated with similar functional relationships, as represented by Equation 2.7:

$$\alpha_2 = fn(M_1, \alpha_1, Re); \quad Y_p = fn(M_1, \alpha_1, Re); \quad \zeta = fn(M_1, \alpha_1, Re) \tag{2.7}$$

The exit flow angle (α_2) is a pivotal parameter as it reflects the quantum of work transferred across the turbomachine stage. Another vital metric is the pressure loss coefficient, an aggregate representation of work losses within the blade row due to various aerodynamic intricacies such as boundary layers, flow separation, and shock waves. For turbines, the total pressure loss coefficient can be ascertained based on the blade's reference exit conditions, detailed in Equation 2.8 [17].

$$Y_p = \frac{P_{01} - P_{02}}{P_{01} - P_2} = \frac{P_{01} - P_{02}}{0.5\rho U_2^2} \tag{2.8}$$

Equation 2.8 delineates the stagnation pressure loss coefficient, a metric that gains its significance due to the ease of obtaining variables from cascade test datasets. Another constructive approach to discern the loss coefficient is through the computation of the energy or enthalpy loss coefficient, as expressed in Equation 2.9:

$$\zeta_e = \frac{h_2 - h_{2s}}{h_{02} - h_2} \tag{2.9}$$

In this equation, h_{2s} signifies the terminal isentropic enthalpy in the turbine system. This enthalpy corresponds to isentropic expansion leading to the same static pressure similar to the actual process. The research by Brown in 1972 posits that the energy loss coefficient remains impervious to flow Mach numbers. While these blade row loss coefficients serve as practical tools in cascade flow tests, multiple variables, such as relative stagnation enthalpy and pressure, might undergo transformations without noticeably impacting turbine efficiency [65]. Notably, at subsonic velocities, the energy loss coefficient closely mirrors the stagnation pressure loss coefficient. However, as Mach numbers escalate, the two coefficients deviate, with Y_p surpassing ζ. Within the scope of this PhD research, the aerodynamic comportment of the Wren100 MGT stator vanes and rotor blades will be critically examined, which are operating predominantly with relatively low Reynolds number flows at subsonic speeds. Hence, the stagnation pressure loss coefficient will be the metric of choice for assessing blade performance in cascade tests in this thesis.

2.3.2 Secondary Loss

Secondary losses in gas turbines arise from complex flow structures and interactions within the turbomachinery. Their origin can be traced back to various factors, often a confluence of elements such as tip leakage, endwall effects, and vortex shedding. The implications of these losses are far-reaching, with the potential to critically reduce the overall efficiency and aerodynamic performance of gas turbines. Recognising the importance of secondary losses, significant research endeavours have been channelled towards their precise prediction, understanding, and subsequent mitigation. The following subsections present a meticulous review of key findings, breakthroughs, and methodologies developed over the years in addressing secondary losses in gas turbines.

2.3.2.1 Tip Leakage

It is widely known that the mechanically necessary gap between the rotor blade tip and the stationary casing would lead to leakage flows that increase the secondary loss.

Due to the gap, the flow at the tip does not follow the intended path, which could result in boundary layer interaction and power output reduction, as shown in Figure 2.9.

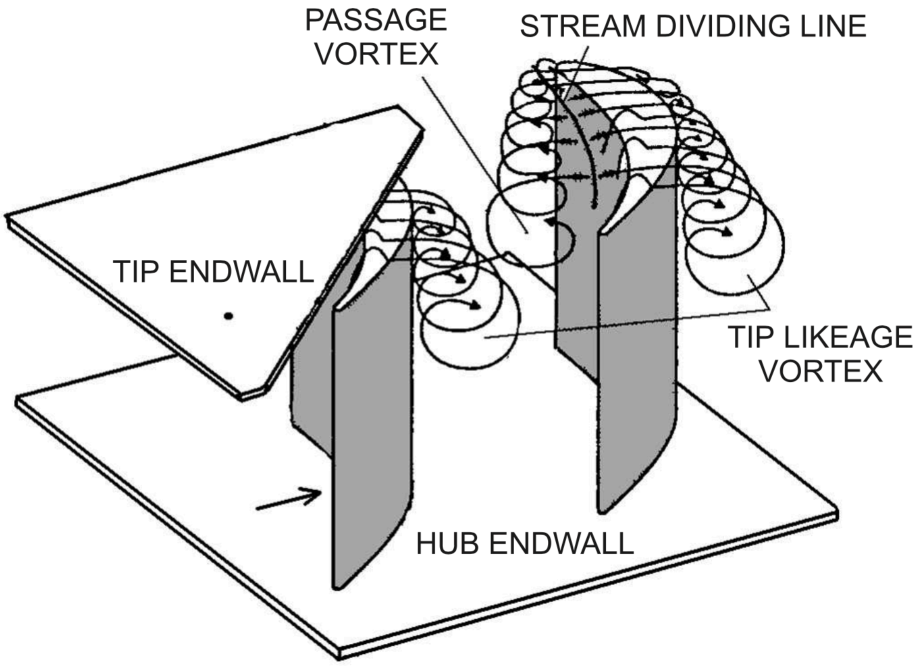

Figure 2.9: Tip Gap Vortex & Blade Passage Vortex Schematic Diagram [64]

According to studies by Denton, it was indicated that the tip leakage loss could account for approximately 1/3 of the total aerodynamic loss [65]. Other vortexes, such as the passage vortex, could interact strongly with the tip leakage vortex. As the flow turning angle and tip clearance increase, the interaction between the leakage and tip-side passage vortex grows stronger [66]. Bringhenti and Barbosa also researched the influence of tip gaps based on a turbine tip clearance model. With higher tip clearance, they discovered an increase in fuel consumption and performance deterioration [67]. Lampart carried out the numerical study to describe the mechanisms of the formation of tip leakages over shrouded and unshrouded rotor blades, in which loss diagrams were presented for two types of leakages in different inlet and outlet flow angles [68].

There have been many researches on minimising the loss caused by tip leakage in gas turbines through active or passive flow control approaches. Wei et al. tried to apply axisymmetric-casing contouring to a two-stage unshrouded HP turbine casing, as shown in Figure 2.10, in which the overall efficiency was improved by 0.14%. It was also found the new design reduces the generation of entropy near the rotor tip region caused by the complex vortex structure [69].

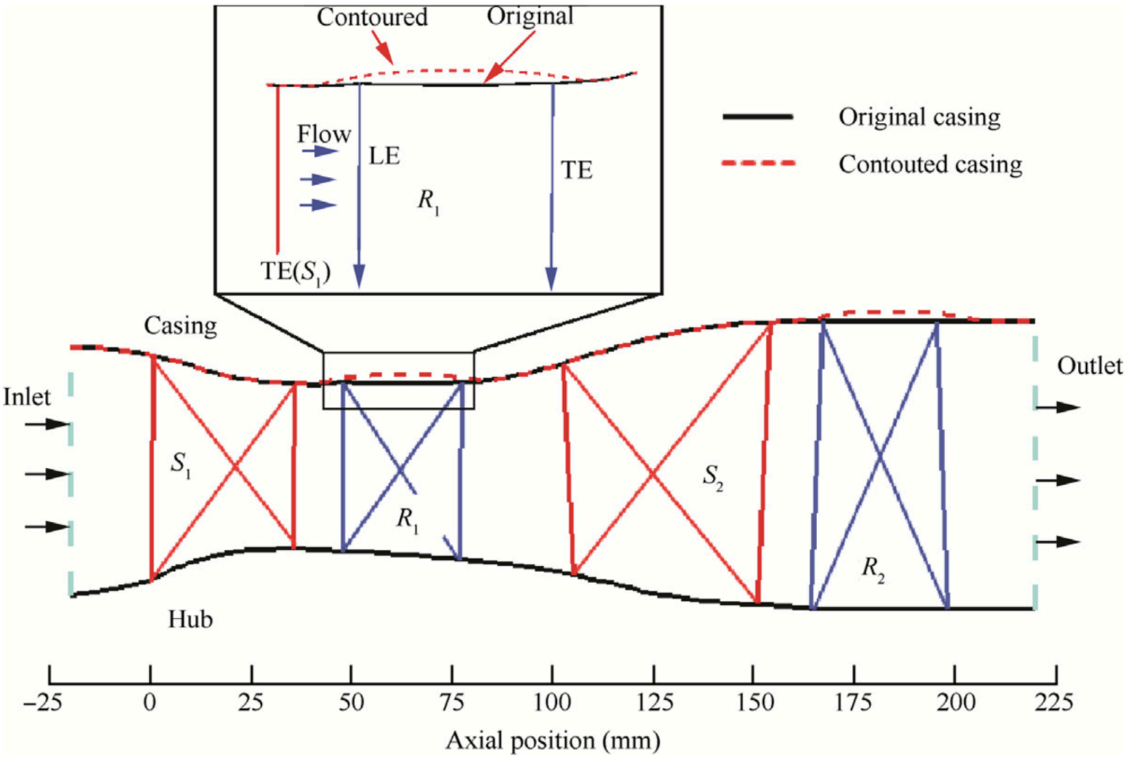

Figure 2.10: Blade Casing: Contoured Vs. Original [69]

Key and Arts experimentally compared the tip gap leakage flow characteristics for flat squealer tip geometries with different Reynolds and Mach number conditions. It was found that the squealer tip is relatively insensitive to the change of Reynolds number would lead to the flow velocity drop within the tip gap compared to the flat tip [70].

By carrying out numerical studies based on different turbulence models, Kirshnababu et al. also discovered that it is advantageous for a gas turbine with the cavity tip as shown in Figure 2.11, which the squealer tip has better aerodynamic and heat transfer performance [71].

2.3.2.2 Endwall

Endwall loss in turbo-machineries is normally caused by the interaction between the endwall boundary layer and the passage vortices formed at the LE and TE of the turbine blade [73]. By conducting cascade experiments in axial turbines, Langston

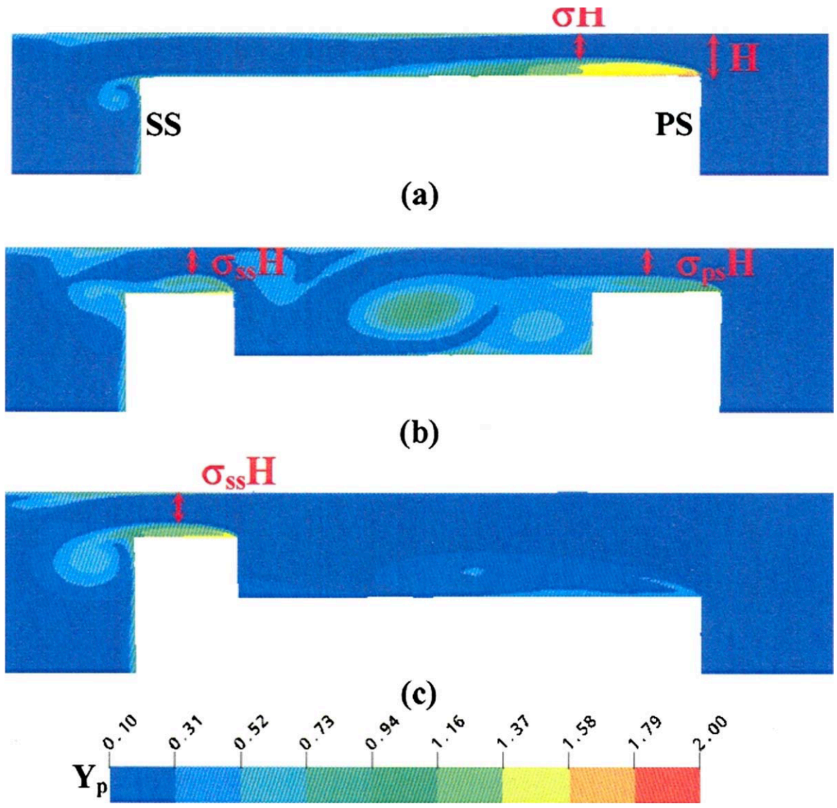

Figure 2.11: Stagnation Pressure Loss Contour Plots Near Blade Tip (a) flat tip, (b) cavity tip, (c) SSS tip with H/C of 1.6% [71]

et al. and Gregory-Smith et al. visualised the complex flow pattern on the endwall, in which the existence of counter vortex on the suction side (SS) and the endwall corner displaced the separation line by a small distance [74, 75]. Adrian et al. further elucidated the vortex structures by employing an eigenvalue method based on RANS simulations, as depicted in Figure 2.12. The formation of the horseshoe vortex (HSV) arises from the inlet boundary layer. The suction side (SS) leg of the vortex remains in close proximity to the blade surface, while the pressure side (PS) leg migrates toward the adjacent blade. Downstream of the suction side, flow separation is instigated by the incoming pressure side leg, subsequently separates and forms into the main passage vortex [76].

To gain a detailed understanding of the endwall loss mechanisms, Denton and Pullan carried out a validated CFD study to identify the sources of endwall loss in axial turbines. It was discovered that the endwall flow for the stator and rotor are completely different. They stated that the optimisation of endwall loss should include the whole turbine stage, instead of one blade row. Although extremely difficult, it was also shown that the endwall loss could be potentially reduced by several approaches, such

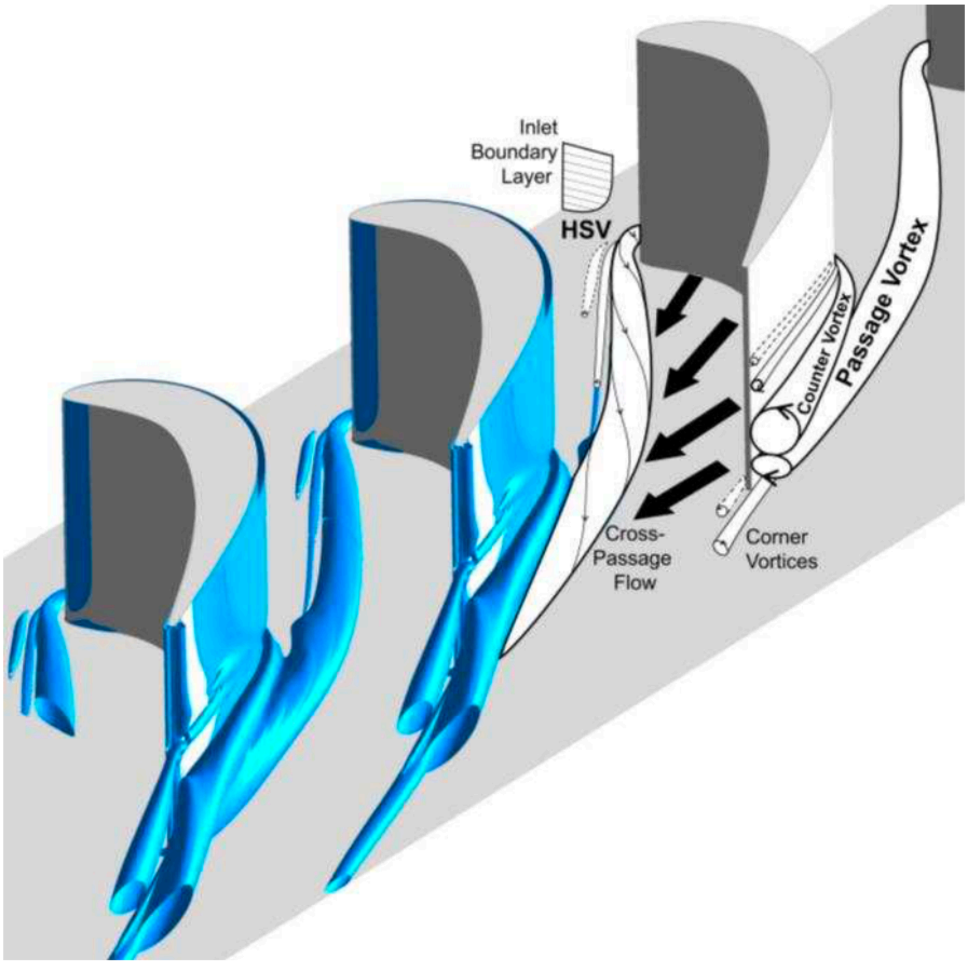

Figure 2.12: Endwall Flow Visualisation CFD [76]

as localised blade twisting and thicking, stacking and endwall profiling [77]. Harrison conducted cascade tests to investigate the effect of blade stacking. It was found that the blade stacking could reduce the strength of secondary flows, which would lead to the drop of downstream flow unsteadiness and mixing loss [78]. Benner et al. examined the influence of the leading edge (LE) geometry on secondary loss in a turbine cascade, illustrating the minor impact of the LE geometry. It was found the loading distribution could largely affect the passage vortex, which result in a change in loss behaviour and downstream flow field [79].

2.3.3 Trailing Edge Loss

Trailing edge loss in gas turbines and micro gas turbines has been an important topic of research for several decades. According to Denton, trailing edge loss could contribute one-third of the total loss in transonic turbine blades, and the reduction of such losses is critical for improving turbine efficiency, reducing fuel consumption, and minimising environmental impacts. By carrying out theoretical and inviscid predictions, it was shown by Denton that the turbine blades featuring a suction surface curvature downstream of the throat exhibit reduced trailing edge loss in comparison to blades that possess a straight suction surface configuration [80].

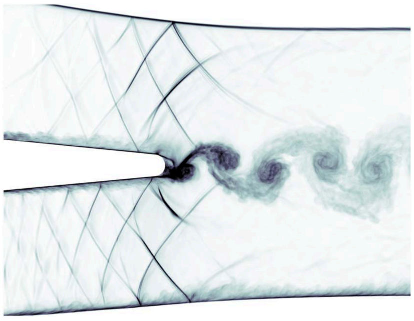

Figure 2.13: Trailing Edge Vortex Shedding Visualisation (Ma=0.85) [61]

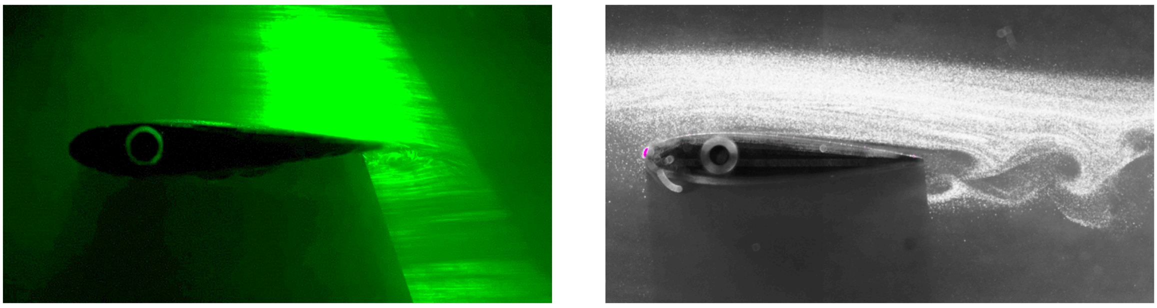

(a) **(b)**

Figure 2.14: Low Reynolds Number (Re=5500) NACA0018 Trailing Edge Vortex Shedding Visualisation [62]

It was also explained by Denton that the trailing edge could be treated as a strong function of the base pressure, meaning low base pressure would lead to higher loss if the vortex shedding was not present [65]. Sieverding et al. experimentally visualised the trailing edge vortex shedding with a high-speed Schlieren camera as shown in Figure 2.13, which non-uniform and unsteady flow with low base pressure ($C_{pb} \approx -0.3$) was discovered [61]. While this diagram occurs at a Mach number (0.85) higher than the normal operational speed of the MGTs in focus for this study, it serves as a valuable extreme-case scenario (eg. peak RPM) that helps describe the flow behaviour which could potentially occur. Additionally, recent studies have enhanced the understanding of these phenomena at extremely low Reynolds numbers, providing clearer visualisations of vortex shedding using advanced flow visualisation techniques, as shown in Figure 2.14, which they discovered the effects of low base pressure on vortex behaviour [62].

Numerous investigations have been undertaken to enhance gas turbine efficiency through the optimisation of trailing edge loss. This typically encompasses modifications to parameters such as surface curvature, trailing edge geometry, boundary layer thickness and state at the trailing edge, trailing edge thickness, and trailing edge wedge angle. Rossiter et al. studied the impact of trailing edge wedge angle based on the LES approach, in which a higher wedge angle (from 8deg to 14deg) was found to be beneficial to the turbine performance (29% reduction of total loss) [81]. Melzer and Pullan experimentally assessed square, round and elliptical geometries of the turbine blade trailing edge. When under transonic conditions, the ability to suppress vortex shedding for the elliptical geometry was discovered. They also found the round trailing edge could have a significantly lower loss at the same Mach number and below a critical Reynolds number, in which the shear layer roll-up would be delayed around a single trailing edge diameter downstream of the trailing edge (detached vortex shedding). As shown in Figure 2.15, the transition of the boundary layer could be linked to the flow behaviour with the change of Reynolds number and the switch of flow regime [82].

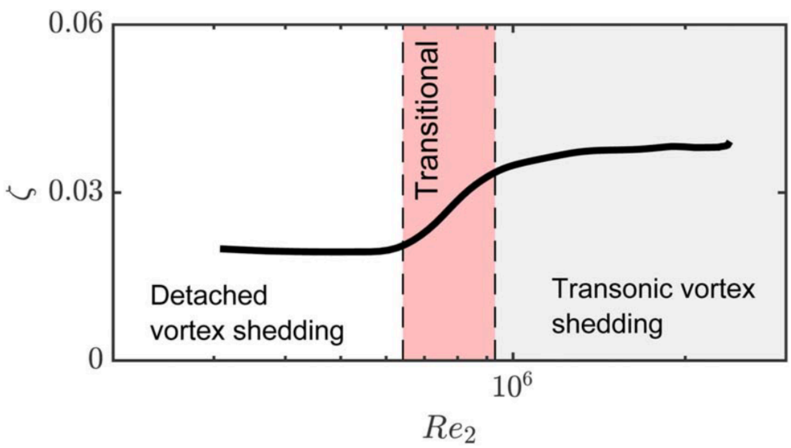

Figure 2.15: Trailing Edge Significant Higher Loss With Onset of Transonic Vortex Shedding [81]

The impact of the state of the boundary layer was researched by Sieverding and

Heinemann based on the flat plate model and blade cascade tests. It was discovered that the boundary layer state has a small influence on the base pressure when the flow is under Mach number of 0.4 before the onset of transonic vortex shedding [83]. Sieverding et al. also investigated several bundled design parameters of the turbine, including surface curvature downstream of the blade throat and trailing edge wedge angle, which increased based pressure was noticed when either of the parameters rises [84].

2.4 Mean Line Performance Prediction for Turbomachinery Blades

In recent advancements, mean line performance modelling has become integral to the design of gas turbine blades, driven by the need for quick and accurate performance predictions. This section builds on the fundamental loss types in turbomachinery, as outlined in Section 2.3, by examining how common loss correlations have evolved. The focus is on the development of these correlations, essential for predicting and minimising losses in turbomachinery. This analysis is crucial for improving blade design efficiency and reliability. The current methods in mean line performance modelling will be reviewed, discussing their strengths and limitations, and how they fit into the broader context of turbomachinery design challenges such as environmental sustainability and economic viability.

This section aims to connect the theoretical aspects of loss mechanisms with practical design considerations, providing a useful guide for designers and engineers in the field. The goal is to highlight the importance of mean line performance prediction in modern turbomachinery blade design and set the stage for further discussions on design optimisation in subsequent chapters.

2.4.1 Ainley and Mathieson Loss Model

The Ainley and Mathieson (A&M) empirical loss model was first introduced in 1951 and has been widely used in mean line modelling for gas turbine aerodynamic performance predictions due to its simplicity and effectiveness. Equation 2.10 displays the total loss coefficient by the A&M loss model [85].

$$Y_t = (Y_p + Y_s + Y_k)X_{Te} \tag{2.10}$$

2.4.1.1 Profile Loss

The profile loss estimated by the A&M loss model is based on the cascade data of the total pressure loss against the ratio of pitch and chord. Figure 2.16 shows the Y_p plots of the nozzle and impulse blades, in which the blade thickness to chord ratio is within 0.15-0.25.

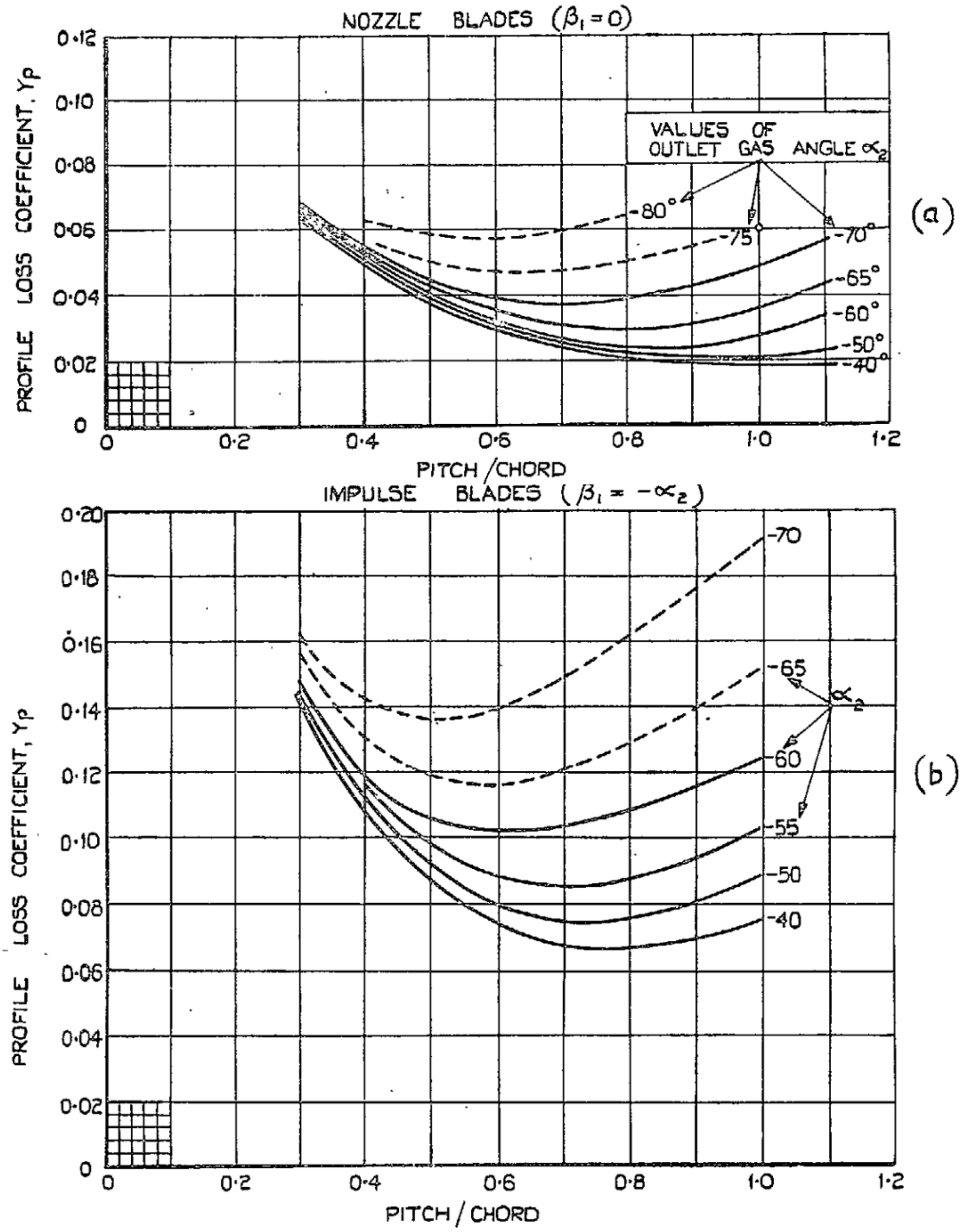

Figure 2.16: Cascade Data of Profile Loss Coefficient At Zero Incidence [85]

With the cascade data shown in Figure 2.16, the mean line prediction of the profile loss for the two types of blading can be calculated by Equation 2.11 and 2.12.

$$Y_p = X_i Y_{p(i=0)} \tag{2.11}$$

$$Y_{p(i=0)} = \{Y_{\beta_1=0} + (\frac{\beta_1}{\alpha_2})^2 [Y_{(\beta_1=-\alpha_2)} - Y_{(\beta_1=0)}]\}(\frac{t/c}{0.2})^{\frac{-\beta_1}{\alpha_2}} \tag{2.12}$$

Ainley and Mathieson also correlated the profile loss at any incidence (Y_p) to the zero incidence ($Y_{p(i=0)}$), which was plotted against the ratio of blade incidence to stalling incidence as shown in Figure 2.17.

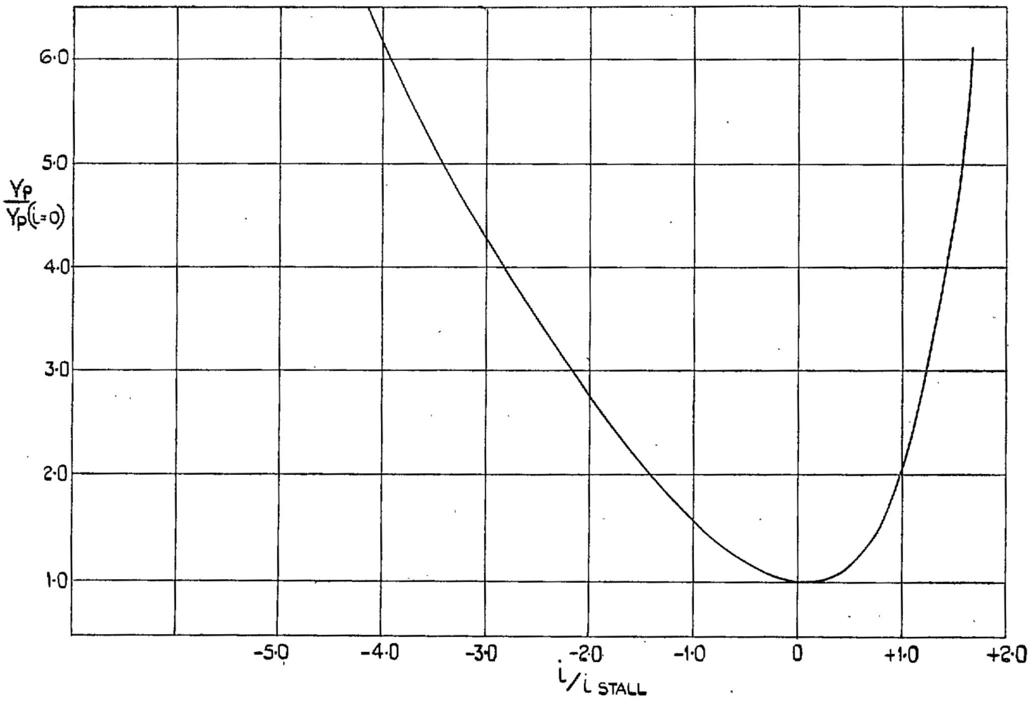

Figure 2.17: Variation of Profile Loss For Typical Turbine Blade [85]

2.4.1.2 Secondary Loss

As mentioned before, secondary loss of gas turbines arises due to the complicated 3D flow phenomena caused by the interaction between the blade passage vortex, the endwall boundary layer and tip leakage loss. The A&M loss model expresses the secondary loss and tip leakage loss based on an empirical factor, λ, the degree of acceleration of flow as it goes through the blade passages.

$$Y_s = \lambda[\frac{C_L}{(s/c)}]^2(\frac{cos^2\alpha_2}{cos^3\alpha_m}) \tag{2.13}$$

$$\lambda = f\{\frac{(A_2/A_1)}{(1 + I.D./O.D.)}\} \tag{2.14}$$

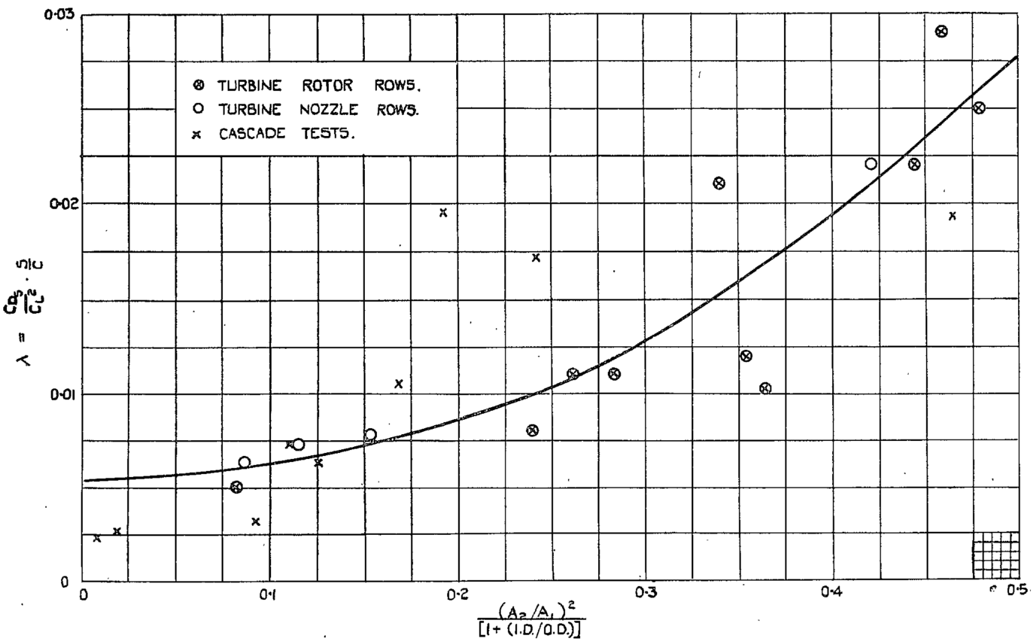

Figure 2.18: Typical Turbine Blade Row Secondary Loss [85]

For tip leakage loss, the A&M loss model expresses it as a function of the ratio of the tip clearance to the blade height with the blade loading coefficient.

$$Y_k = B\frac{\tau}{h}4(tan\alpha_1 - tan\alpha_2)^2(\frac{cos\alpha_2^2}{com\alpha_m}) \tag{2.15}$$

Based on experimental data, the dimensionless factor B in Equation 2.15 is 0.5 for unshroud blades and 0.25 for shroud blades.

2.4.1.3 Trailing Edge Loss

According to the seminal experimental study by Ainley and Mathieson, the effects of trailing edge thickness on turbine performance are quantitatively captured and illustrated in Figure 2.19. This figure plots the normalised trailing edge loss coefficient, as a function of the trailing edge thickness to span ratio. The graph shows a clear linear relationship, with loss coefficients increasing as the trailing edge thickness increases. This trend demonstrates that thicker trailing edges are potentially associated with higher aerodynamic losses, likely due to increased turbulence and drag at the blade trailing edge. This relationship is critical for turbomachinery blade design, emphasising the need to reduce trailing edge thickness to minimise aerodynamic losses and enhance overall turbine efficiency.

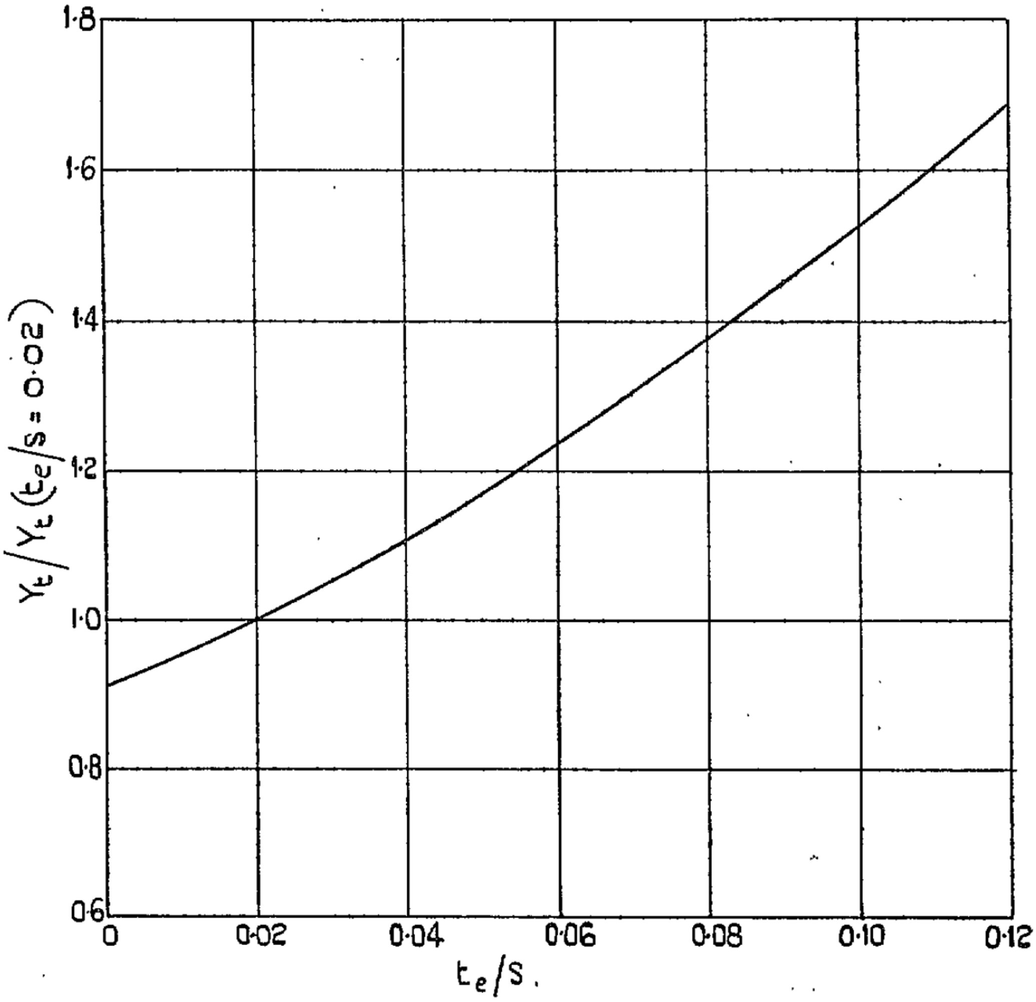

Figure 2.19: Typical Turbine Blade Row Trailing Edge Loss [85]

2.4.2 Dunham and Came Loss Model

The Dunham and Came (D&C) loss model was first introduced in 1970 and is another empirical method for predicting profile different types of aerodynamic loss in axial flow turbines. Compared to the A&M model, the D&C is not as widely used. However, several recent studies have still utilised the D&C model in order to refine and extend its applicability. The D&C model expresses the total loss coefficient as shown in Equation 2.16, which involves the influence of the Reynolds number on the profile loss and secondary loss [86].

$$Y_t = [(Y_p + Y_s)(\frac{Re}{2 \times 10^5})^{-0.2} + Y_k]X_{Te} \tag{2.16}$$

2.4.2.1 Profile Loss

Based on the profile loss equation by the A&M model, the D&C model includes the additional loss component caused by the development of shockwaves as shown in Equation 2.17 [86].

$$Y_p = [1 + 60(M_{out} - 1)^2]X_i Y_{p(i=0)} \tag{2.17}$$

2.4.2.2 Secondary Loss & Tip Clearance Loss

A new blade loading parameter was proposed by the D&C model based on the cascade test data, which was also an improvement based on the A&M model. For the tip leakage loss predictions, power law was replaced by linear independence by the D&C model as it suits better with the experimental data [86].

$$Y_s = 0.0334(\frac{c}{h})4(tan\alpha_1 - tan\alpha_2)^2(\frac{cos^2\alpha_2}{cos^3\alpha_m})(\frac{cos\alpha_2}{cos\beta_1}) \tag{2.18}$$

$$Y_k = B(\frac{c}{h})(\frac{\tau}{c})^{0.78}4(tan\alpha_1 - tan\alpha_2)^2(\frac{cos^2\alpha_2}{cos\alpha_m}) \tag{2.19}$$

2.4.3 Kacker and Okapuu Loss Model

Similar to the D&C model, the Kacker and Okapuu (K&O) loss model was also developed based on the A&M model, which was first introduced in 1982. The empirical functions were validated against the design point efficiencies of 33 turbine stages. Although the original work by Kacker and Okapuu was focused on compressors, the underlying principles can be adapted for axial turbines. For typical gas turbine blades, the total loss coefficient can be estimated by Equation 2.20 and 2.21, in which the profile loss is corrected to account for the effect of Reynolds numbers.

$$Y_t = Y_p f_{Re} + Y_s + Y_{TET} + Y_k \tag{2.20}$$

$$f_{Re} = \begin{cases} (\frac{Re}{2\times10^5})^{-0.4} & \text{if } Re \leq 2\times10^5 \\ 1 & \text{if } 2\times10^5 < Re < 10^6 \\ (\frac{Re}{10^6})^{-0.2} & \text{if } Re \geq 10^6 \end{cases} \tag{2.21}$$

2.4.3.1 Profile Loss

Built upon the A&M loss model, the K&O model shows the relationship between the Mach number and the profile loss as shown in Equation 2.22 and 2.23. Figure 2.20 also shows the experimental data for the channel acceleration and exit Mach number, which can then be used to calculate the correction factor K_p.

$$Y_p = 0.914(Y_{p,A\&M}K_p + Y_{shock}) \tag{2.22}$$

$$K_p = 1 - K_2(1 - K_1) \tag{2.23}$$

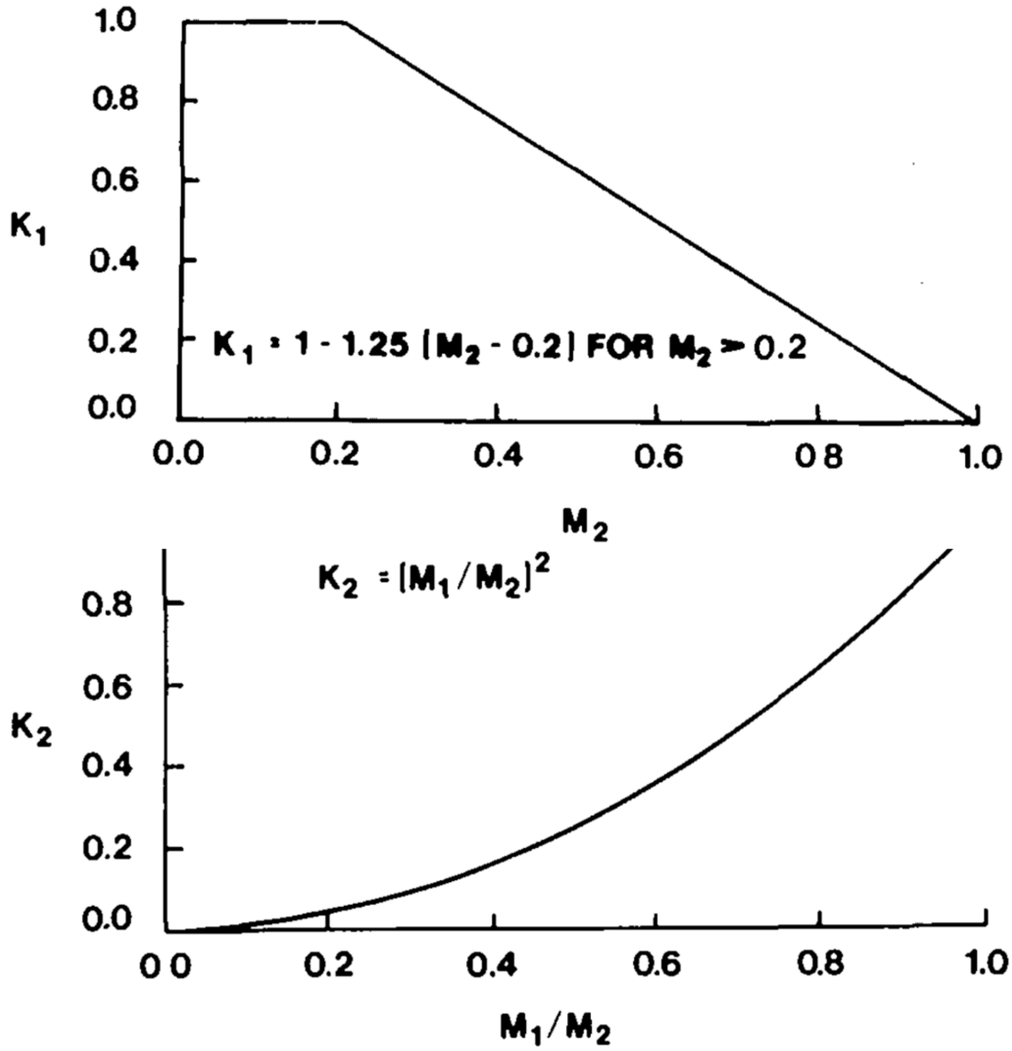

Figure 2.20: Mach Number Empirical Correlation Factors

The K&O model also includes the shock loss as shown in Equation 2.24, in which the turbine blade hub-to-tip ratio is expressed as the exit dynamic pressure head.

$$Y_{shock} = 0.75(M_{1,HUB} - 0.4)^{1.75}(\frac{R_H}{R_T})(\frac{P_1}{P_2})(\frac{1-(1+\frac{\gamma-1}{2}M_1^2)^{\frac{\gamma}{\gamma-1}}}{1-(1+\frac{\gamma-1}{2}M_2^2)^{\frac{\gamma}{\gamma-1}}}) \tag{2.24}$$

2.4.3.2 Secondary Loss & Tip Leakage Loss

The secondary loss estimated by the K&O model is quite similar to the D&C model (Equation 2.18), with the only difference being the correction factor that relates to the aspect ratio. A rapid increase in aerodynamic loss was discovered and confirmed by D&C and K&O as the aspect ratio decreases based on experimental data. Equation 2.25 expresses the new correction factor f_{AR}.

$$f_{AR} = \begin{cases} \frac{1-0.25\sqrt{2-h/c}}{h/c} & \text{if } h/c \leq 2 \\ \frac{1}{h/c} & \text{if } h/c > 2 \end{cases} \tag{2.25}$$

To account for the compressibility factor, as displayed in Equation 2.26, another correction factor was defined in therms of the factor for aspect ratio and profile loss.

$$K_s = 1 - K_3(1 - K_p) \tag{2.26}$$

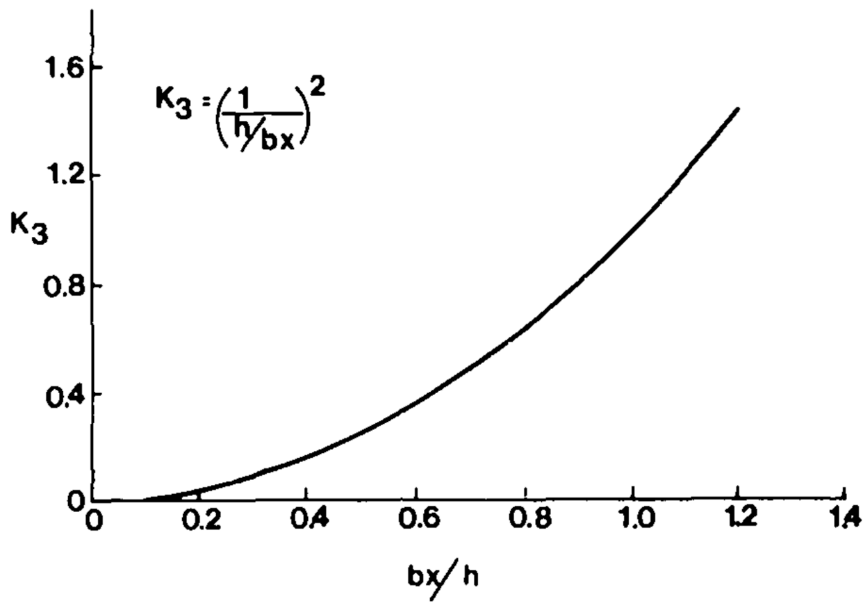

Figure 2.21: Mach Number Correlation Factor K_3

Based on the empirical correction factor K_3 plotted in Figure 2.21, the final function to predict the secondary loss is expressed in Equation 2.27.

$$Y_s = 1.2 Y_{s,D\&C} K_s \tag{2.27}$$

Kacker and Okapuu proposed an iterative method for estimating the tip leakage loss in axial turbines. The initial step entails calculating the efficiency of a turbine with no tip clearance. Subsequently, the efficiency loss attributable to tip clearance is determined using Equation 2.28. Throughout the process, the rotor loss coefficient would experience several increments, necessitating the re-calculation of velocity triangles. The ultimate tip leakage loss is computed once the efficiency converges.

$$\Delta\eta = 0.93\left(\frac{R_{Tip}}{R_{Mean}}\right)\left(\frac{1}{H cos\alpha_2}\right)\eta_{tt,0}\Delta k \tag{2.28}$$

2.4.3.3 Trailing Edge Loss

In terms of the throat opening and the trailing edge thickness, the K&O model plots the trailing edge loss for typical gas turbine blades in Figure 2.22 based on cascade data.

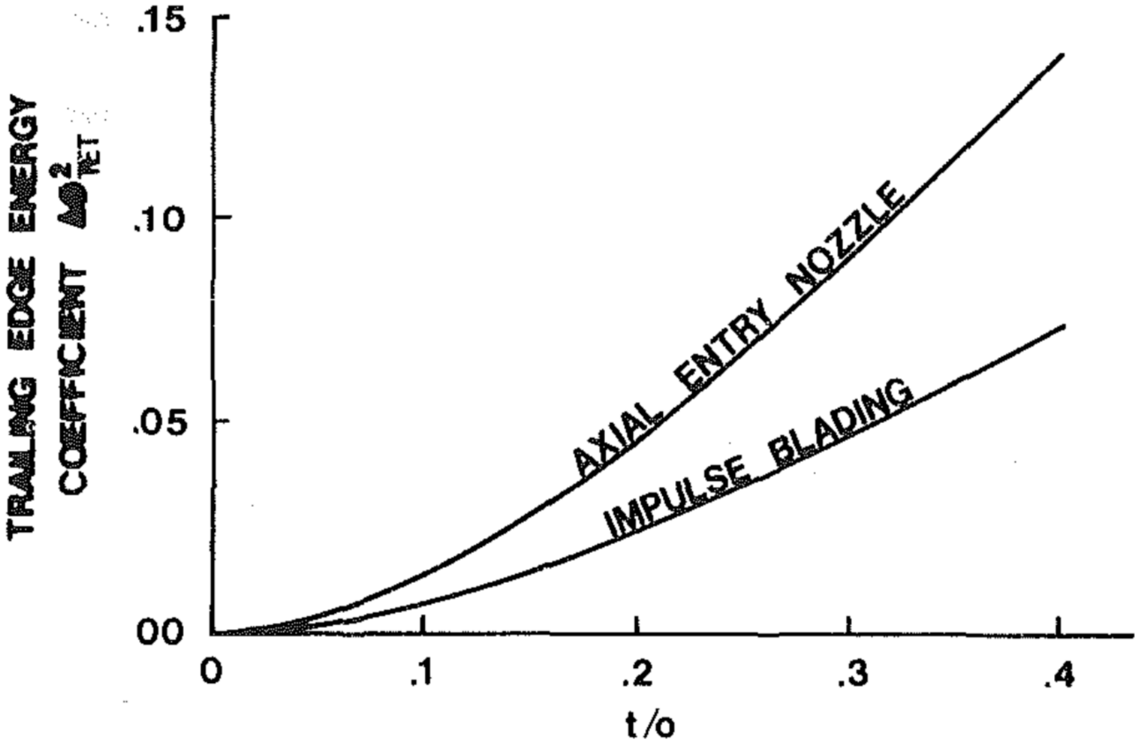

Figure 2.22: Trailing Edge Loss Coefficient (Energy) for NGV and Rotor

In Figure 2.22, the trailing edge loss is plotted in terms of the energy loss coefficient. For any combination of blade angles, interpolation between these curves can be achieved by Equation x. In addition, the energy loss coefficient can be converted into the pressure loss coefficient using Equation x.

$$\Delta\phi_{te}^2 = \Delta\phi_{te(\beta_1=0)}^2 + (\frac{\beta_1}{\alpha_2})^2[\Delta\phi_{te(\alpha_2=0)}^2 - \phi_{te(\beta_1=0)}^2] \tag{2.29}$$

$$Y_{te} = \frac{[1 - \frac{\gamma-1}{2}M_2^2(\frac{1}{1-\Delta\phi_{te}^2} - 1)]^{\frac{-\gamma}{\gamma-1}} - 1}{1 - (1 + \frac{\gamma-1}{2}M_2^2)^{\frac{-\gamma}{\gamma-1}}} \tag{2.30}$$

2.4.4 Denton Loss Model

Previous sections illustrate several performance parameters of turbine blade cascades, which are the flow exit angle, stagnation pressure loss coefficient and energy loss coefficient. However, Denton (1987) holds the view that a more rational measure of loss coefficient should be used for the calculation of the efficiency of turbomachinery, which the entropy creation can be used. It has commonly been assumed that any irreversible flow process creates entropy and reduces the machine isentropic efficiency; thus, entropy is an excellent measure, for it does not depend on the frame of reference of the turbomachinery. However, the value of entropy creation in the turbomachinery cannot be measured directly, which requires to be inferred by measuring other properties involving flow temperatures, pressures and densities. As shown in Equation 2.31 and 2.32, the specific entropy for a perfect gas can be calculated [65, 87].

$$s - s_{ref} = C_p ln(\frac{T}{T_{ref}}) - Rln(\frac{P}{P_{ref}}) \tag{2.31}$$

$$s - s_{ref} = C_v ln(\frac{T}{T_{ref}}) - Rln(\frac{\rho}{\rho_{ref}}) \tag{2.32}$$

From Equation 2.32, assume the stagnation temperature is constant when the adiabatic flow goes through a turbine stator, the loss of stagnation in stator blades and cascade flows can be used to synonymous with the increase of entropy as illustrated in Equation 2.33. It is essential to understand the difference between the total and specific entropy, which in this case, the obtained total rate of entropy creation must be divided by the mass flow rate to figure out the specific entropy.

$$\Delta s = -Rln(\frac{P_{02}}{P_{01}}) \tag{2.33}$$

To understand how the generation of entropy reduces the machine efficiency, one must understand the physics behind the relationship the entropy creation and flow properties. J. Denton (1987) holds the view that the entropy creation could be described as the turbomachinery continually making indestructible 'smoke' due to several different mechanisms and convect them through the machine to its exit. The concentration of 'smoke' from different sources is proportional to the loss of machine efficiency, which the entropy loss coefficient for turbine blades can be calculated by Equation 2.34 [65].

$$\zeta_s = \frac{T_2 \Delta s}{h_{02} - h_2} \tag{2.34}$$

The 'smoke' could be generated by many sources; therefore, there are many complex factors that would influence the efficiency of the turbomachine, which requires the designer to have an excellent physical understanding of how the flow moves through the turbine blade. Most of those factors can be related to the generation of entropy; therefore, the definitions of the machine loss coefficient and the entropy generation must be understood by the designer to obtain a good judgement in designing a turbine blade with high efficiency. The loss in the gas turbine can be divided into three categories, which are the "profile loss", "endwall loss" and "leakage loss". The relationship between entropy and gas turbine efficiency is described as follows.

Considering the expansion process of a gas turbine, the machine isentropic efficiency can be calculated by using the enthalpy-entropy diagram as illustrated in Equation 2.35.

$$\eta_{isen} = \frac{h_1 - h_2}{h_1 - h_2 + T_2(s_2 - s_1)} \tag{2.35}$$

The Equation 2.13 is based on the assumptions of no external heat transfer, and the difference between the static and stagnation conditions are neglected, meaning the static temperature is constant along 2 to 2s as shown in Figure 2.23.

It can be seen in Equation 2.13 that within a fluid dynamic process, the local temperature is generally related to the magnitude of the entropy creation. It has been proven that $\Delta T = \zeta \times 1/2V^2$ is the formula to calculate it; therefore, the flow would create less entropy during the same process at a higher temperature than at a lower temperature. Additionally, the change of enthalpy is proportional to the square of flow speed. The most distinguishing factor that can justify the creation of entropy is irreversibility. According to many textbooks in the field of thermodynamics, the

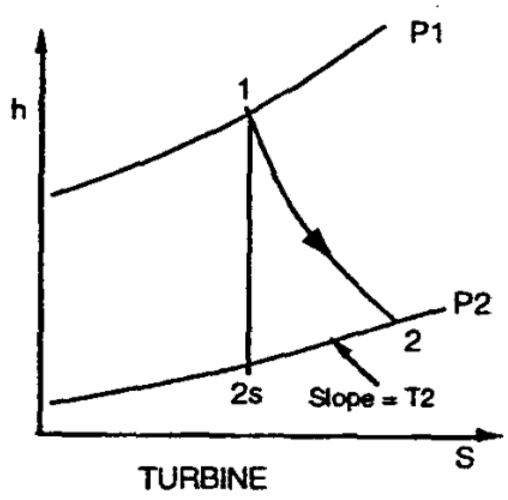

Figure 2.23: Enthalpy vs Entropy Diagram [65]

fluid dynamic processes that lead to the creation of entropy are summarised as follows.

Firstly, entropy creation would occur due to the viscous friction inflow boundary layers or free shear layer (for instance, a leakage jet). Secondly, the heat transfer across different temperatures is irreversible, which could also cause entropy creation. Thirdly, non-equilibrium processes such as shock waves and rapid expansion processes in the turbomachinery would create entropy, causing lower efficiency in the system. Although the definition of entropy creation inside turbomachinery is relatively straightforward, its numerical calculations from different sources are mostly semi-empirical equations as many correlated variables are involved. It is also difficult to quantify the turbine loss coefficients as recent studies have shown that different loss mechanisms (sources of entropy) are dependent on each other. For instance, it is thought that the profile loss is produced by the blade boundary layers that are located away from the end walls. The profile loss is generally assumed to be in two-dimensional flow, in which any boundary layer would involve extra losses arising near the trailing edge [29]. Additionally, the endwall loss is commonly referred to as the 'secondary loss' for it is partly generated by the secondary flows produced by the annulus boundary layers through the turbine blade row, for the tip leakage loss, which is also generated by the flow that goes through the hub clearance of turbine stator and the tips of the turbine rotor. Thus, as the turbine being analysed in this project operates under low Mach number flows, it would be important to measure the turbine efficiency by calculating the stagnation pressure loss coefficient (Y_p) as demonstrated in subsection 2.3.1.3. The following subsection introduces a useful loss model by J. Denton in 1987 that can be used to estimate the stagnation pressure loss coefficient.

2.4.4.1 The Pressure Loss Model by J. Denton

According to the flow physics summarised by J. Denton, entropy can be created when viscous shear occurs in the flow inside a turbo-machine, in which the wakes near the edges of separate regions (trailing edges) would generally have high rates of shearing. Due to the flow being generally unsteady and very complicated between the turbine blades, it would be almost impossible to calculate the local entropy. Thus, the control volume approach can be used to quantify the total entropy, which applies the theory of mass, energy and momentum conservation. With regards to turbomachinery applications, J. Denton (1987) gave an actual example of estimating stagnation pressure loss coefficient (Y_p) based on the calculation of entropy generation from different sources behind the trailing edge as described in Equation 2.36 [65].

$$Y_p = \frac{\Delta P_o}{0.5\rho V_{te}^2} = -\frac{C_{pb}t}{w} + \frac{2\theta}{w} + (\frac{\delta^* + t}{w})^2 \tag{2.36}$$

As shown in Equation 2.36, there exists three main sources of entropy generation that could lead to the increase of stagnation pressure loss coefficient, which is the base pressure loss ($-\frac{C_{pb}t}{w}$), the boundary layer losses ($\frac{2\theta}{w}$) and the mixing losses ($(\frac{\delta^*+t}{w})^2$). Figure 2.24 shows a blade with the nomenclatures involved in Equation 2.36.

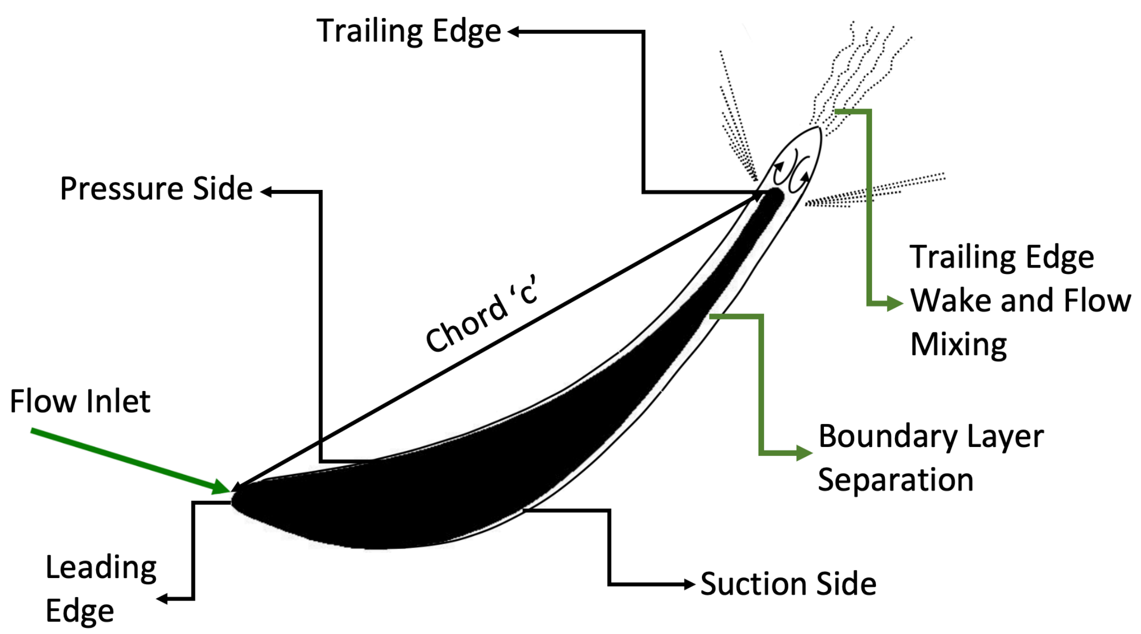

Figure 2.24: Two-dimensional Loss Mechanism Drawing

As shown in Figure 2.24, the boundary layer losses generally increase as the growth of the boundary layer from the leading edge to the trailing edge. Also, the graph shows the mixing losses after the trailing edge and the wakes generated.

2.4.5 Review of Using Different Mean-Line Models for Turbomachinery Loss Predictions

2.4.5.1 Previous Cases Studies

In the previous sections, several empirical loss models used for the mean line performance prediction for gas turbine blades were introduced. Many previous researches have been conducted to validate and improve the existing loss correlations based on experimental and numerical investigations on various types of gas turbine blades. Ennil et al. compared the loss prediction performance of A&M, C&D and K&O models on a small-scale turbine blade against the validated CFD results based on RANS SST $k-\omega$ turbulence model as shown in Figure 2.25 [88].

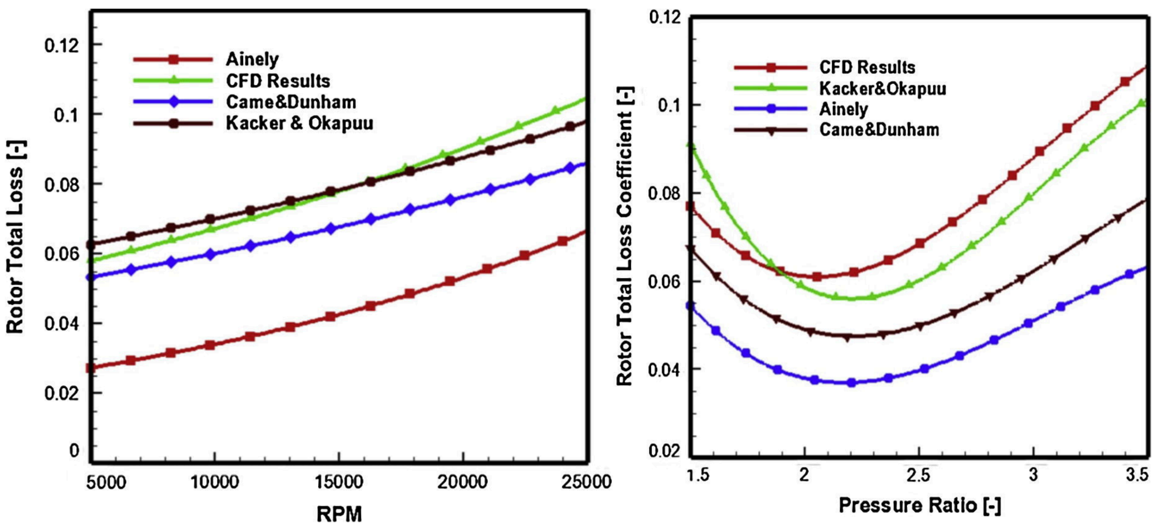

Figure 2.25: Loss Models Comparison By Ennil et al. [88]

According to the comparison of the rotor total loss at different RPMs and their corresponding pressure ratios, it was found by Ennil et al. that for small-scale axial turbine blades, the K&O model has the closest predictions to the CFD results [88].

In 2023, Zhang et al. applied the K&O model and CFD simulations to successfully evaluate the mainstream loss of a large cooled turbine airfoil, including the trailing edge loss, mixing loss and friction loss [89].

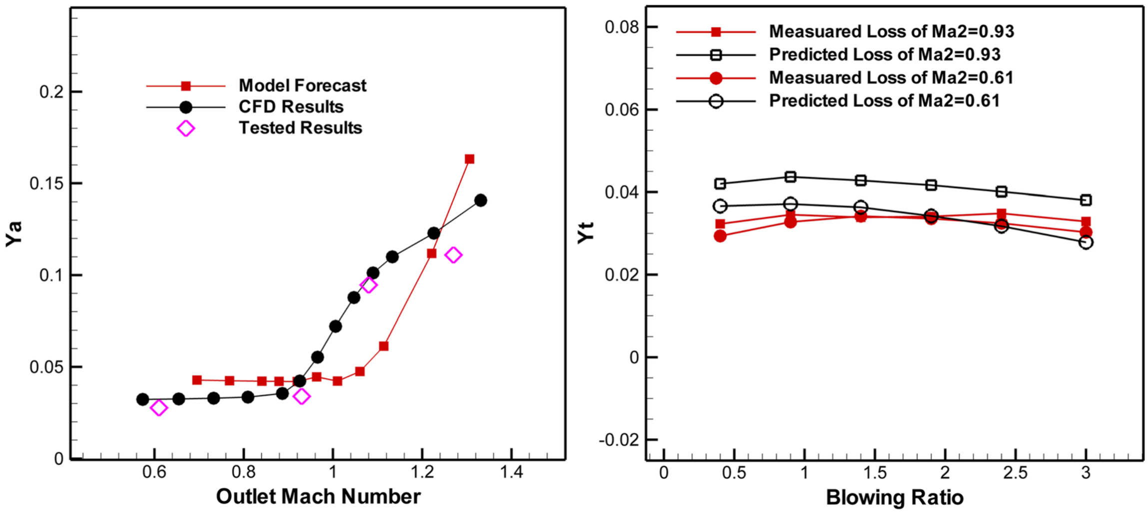

Figure 2.26: Cooled Gas Turbine Blade Loss Predictions Based on K&O Models By Zhang et al. [89]

Although the correct trend of loss increment can be predicted as shown in Figure 2.26, there still exists prominence of efficient loss modelling, which one significant limitation is its inability to predict the transonic blades. To resolve this inadequate prediction performance, Li et al. proposed a modified shock loss model based on linear cascade experimental data. The developed mathematical equations are listed as Equation 2.37 to 2.39 [90].

$$M_{on} = 0.8\frac{o}{s} + 0.63 \tag{2.37}$$

$$M_{off} = M_{on} + 0.55 \tag{2.38}$$

$$Y_{shock} = \begin{cases} 1 & \text{if } Re \leq M_{on} \\ 1 + K_{sh}[1 + cos(\frac{M_2 - M_{on}}{M_{off} - M_{on}} 2\pi - \pi)] & \text{if } M_{on} < M_2 < M_{off} \\ 1 & \text{if } Re \geq M_{off} \end{cases} \tag{2.39}$$

To study the aerodynamic performance of a curved back transonic turbine blade profile, Rajeevalochanam et al. applied the original K&O model and the modified model by Li et al. along with the CFD and experimental data [91].

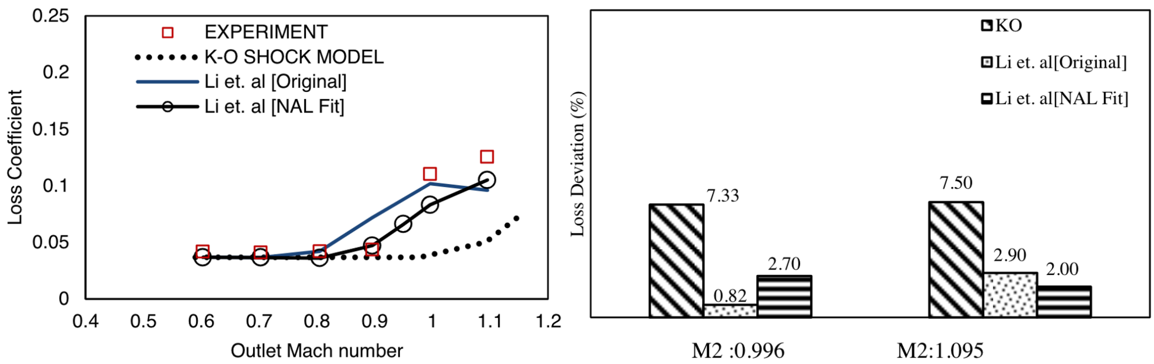

Figure 2.27: Transonic Turbine Blade Loss Prediction Based on K&O Models By Rajeevalochanam et al. [91]

As shown in Figure 2.27, compared to the original, the modified version of the K&O model by Li et al. has much better performance in predicting the loss coefficient for transonic turbine airfoils. However, at the designed Mach numbers of 0.996 and 1.1, the losses were still under predicted by 0.8% and 2.9%. Based on the CFD results by Rajeevalochanam et al., the difference was caused by the stator-rotor interaction, which the impact of the rotor downstream would lead to loss plateau of the stator mean span [91].

2.4.5.2 Advantages and Disadvantages of Mean Line Performance Predictions Models

After the review of recent studies, it was found that the mean line models are extensively utilised in the preliminary design stages of turbomachinery due to their balanced efficiency and reasonable accuracy. Through a detailed review of different case studies, the pros and cons of the mean line performance prediction methods are summarised as follows.

Pros

- Simplicity and Speed:
  The complexity of the blade geometries and the 3D flow within the gas turbine passages are greatly reduced, leading to the simplified calculations of the turbine performance.

- Integrated Design Process:
  The models can be integrated into the design process of the turbomachinery

blades, meaning swift assessment and optimisation for different individual designs can be achieved.

- Good for Overall Performance Predictions:
  At the initial design phase of turbomachinery blades, the mean line modes are valuable tools that focus on the overall performance rather than the intricate details of the flow field.

Cons

- Reduced Accuracy:
  As mentioned before, the simplification of the blade geometries and complicated flow field have led to reduced accuracy compared to experiments and CFD simulations, especially in applications with complex flow behaviours like secondary flows, boundary layer transition, and turbulent mixing. In addition, some assumptions made in the models might not be true in different cases, such as one-dimensional and adiabatic.

- Limited Scope:
  The mean line models normally do not capture the local variations in performance due to the complex flow behaviour near the root and hub regions. Also, unsteady flow fields and the impact of rotor-stator interaction are often not represented in these models.

To sum up, the mean line performance models are useful tools in the field of gas turbine blade study and optimisation. They deliver valuable advantages including high computational efficiency, swift assessment of blade design and good overall performance predictions. These features make mean line models indispensable in preliminary design and optimisation studies. However, it is also crucial to acknowledge the limitations, including the reduced accuracy and limited scope. Thus, for different turbine blade applications such as MGTs, the best mean-line model to use would need to combine the predicted loss with experimental data or validated CFD results.

2.5 Reverse-Engineering of Turbomachinery Parts

To conduct RE of geometries with complex shapes such as turbine blades, it is important to select an appropriate digitising technique, which would either be a contact or non-contact method [93, 94]. The operating steps for both techniques are summarised in Figure 2.28. It can be seen that the RE steps for contact and non-contact measurement are quite similar, which the only significant difference is how the data cloud is acquired. By testing various contact and non-contact equipment, Mahboubkhah et al. (2016) discovered that the reported information by the digitising equipment manufacturers is not always reliable, meaning experimental validations are always required for the RE models [95]. Thus, CFD simulations and experimental data were obtained in this study to investigate the performance of the RE models.

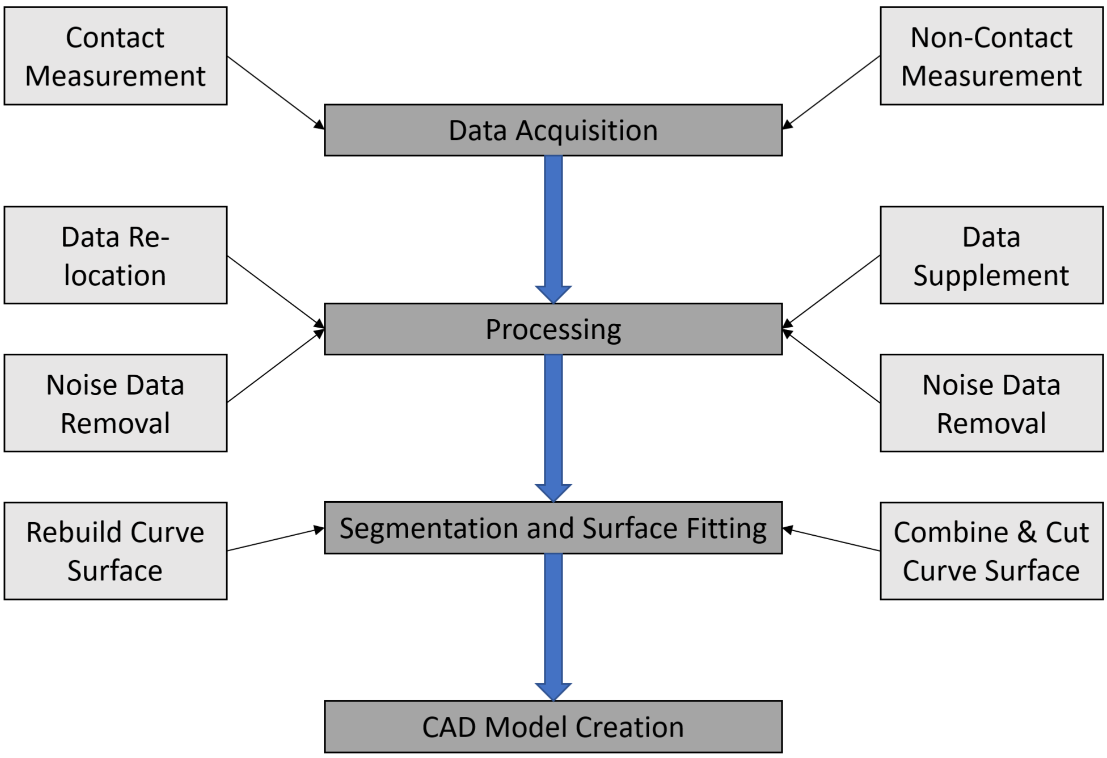

Figure 2.28: Contact & Non-contact RE Flow Chart [94]

2.5.1 Gas Turbine Blade Reverse-Engineering Strategies & Case Studies

After the geometric data acquisition, it is important to select an appropriate RE strategy, which would either be 'what the part actually is' or 'what the part could be'. The strategy of 'what the part could be' has been studied by many in the field of RE. In 2006, Mohaghegh et al. described a new method to reverse-engineer aerofoils from existing turbine blades based on design intent, stressing the importance of 'what the part could be'. It was shown by Mohaghegh et al. that incorporating crucial design points is essential during the RE process as the measuring equipment could cause many uncertainties. By applying design key points, the new method of utilising segmentation and constraints fitting algorithm (SCFA) was tested on an industrial gas turbine blade as shown in Figure 2.29 [96].

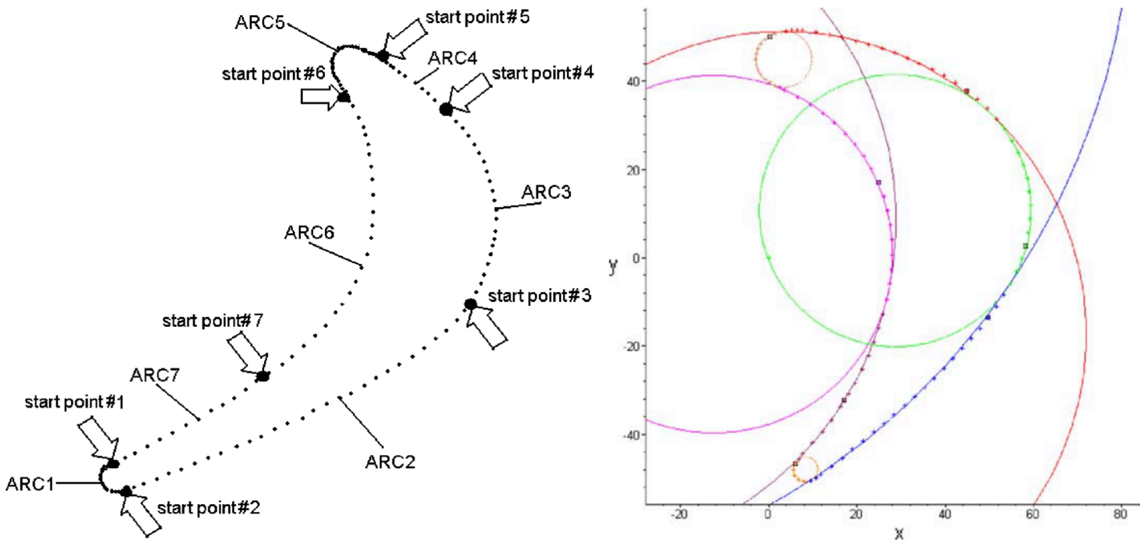

Figure 2.29: Gas Turbine Balde RE Based on Segmentation Andconstrained Fitting Algorithm (SCFA) [96]

As shown in Figure 2.29, the shape of the gas turbine blade was recreated by fitting circles at different design points, such as the leading edge and trailing edge. Based on the SCFA method, the rebuilt profile shows only 0.02mm deviation away from the digitised points average level [96].

In 2007, She and Chang proposed a new RE process of turbine blade disks by utilising a ZEISS RPISMO7 coordinate measuring machine, which proved the possibility of applying modern CAD techniques to re-construct turbine geometries with complex shapes [97]. Li et al. presented a novel parameterisation approach for the RE of turbine blades in 2004, in which the essential features were extracted from the points cloud to re-build the blade geometry based on aerodynamic rules [98].

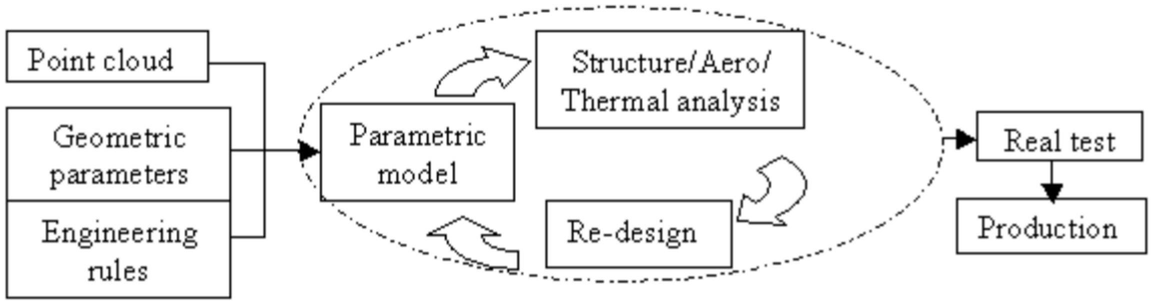

Figure 2.30: Parametric Reverse-Engineering By Li et al. [98]

As displayed in Figure 2.30, it was believed by Li et al. that the engineer should care more about the aerodynamic performance than its geometric shape during the RE of gas turbine blades. The parametric RE strategies could also enable the user to easily redesign the turbine blade shapes by adjusting various parameters [98].

Overall, most existing studies of the RE of turbine blades have only focused on 'what the part could be' as smooth surfaces are often required for turbine blades to reach high aerodynamic efficiency [171]. Also, previous researchers have not treated the RE of MGTs in much detail compared to regular-size gas turbines. Thus, the application of different RE strategies on the MGT was investigated and compared in this research project (Chapter 4).

2.6 Computational Fluid Dynamics on Turbomachinery Review

With the advancement of analytical tools and computational fluid dynamics (CFD) techniques, the integration of these methodologies has become increasingly prevalent in the aerodynamic design of turbine blades. In general, engineers can estimate the required pressure and velocity distributions on the turbine blade profile (surface) theoretically, providing essential input data for CFD tools to generate more accurate solutions. Compared to experimental measurements, CFD tools offer the ability to analyse flow characteristics in locations where it is impractical or hazardous to install measuring instruments [99]. Although CFD tools introduce a novel third approach for designers, they serve to complement and enhance the understanding of results obtained through theoretical and experimental methods, rather than replacing these traditional approaches (as illustrated in Figure 2.31).

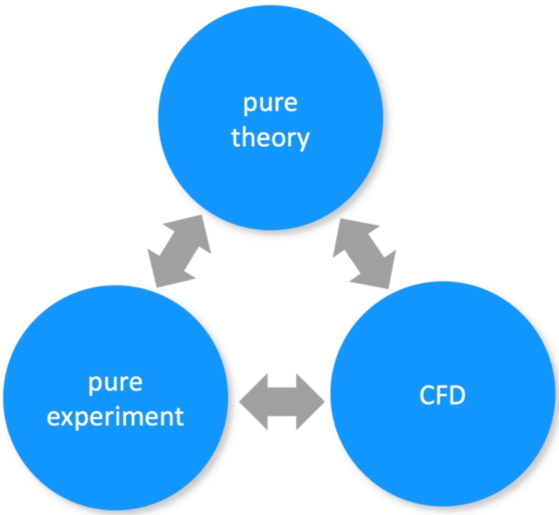

Figure 2.31: Fluid Dynamics: The Three Dimensions [100]

Thus, as CFD tools incorporate increasingly intricate physics and geometries, the verification of approaches and validation of data have gained prominence through the application of theoretical and experimental results. It is essential that related research is conducted after attaining sufficient mesh quality and satisfying iteration convergence criteria [101]. The subsequent subsections present critical tools and models employed in this doctoral project, encompassing mathematical and turbulence models, near-wall treatments, and the meshing process.

2.6.1 Mathematical Models

Computational fluid dynamics (CFD) tools are fundamentally based on the underlying physical laws that govern fluid dynamics. These physical laws can be represented as a series of fundamental governing equations, which include the continuity, momentum, and energy equations (see in Appendix A).

In practical applications, viscous flows exhibit dissipative transport phenomena, including thermal conduction, friction, and mass diffusion, resulting in an increase in entropy within the flow [103]. The decline in efficiency experienced by turbomachinery is primarily attributed to the rise in flow entropy [104]. When the Reynolds number of a flow reaches a specific threshold, the flow transitions into a turbulent state. Turbulent flow is characterised by chaotic motion and the formation of eddies, which are vortical structures that manifest at multiple scales. The large-scale eddies possess the majority of the flow kinetic energy, which subsequently cascades to smaller scales through a process known as direct energy cascade [105, 106]. In 1941, Kolmogorov discovered the existence of the smallest scale of vortical structures, at which point the kinetic energy is converted into thermal energy due to viscous dissipation. This smallest scale of the vortical structure is referred to as the Kolmogorov length scale. The dissipation of energy, denoted by ϵ, can be expressed using Equation 2.40 [107].

$$\epsilon = \frac{Energy\ to\ be\ dissipated}{Time\ to\ dissipate} \tag{2.40}$$

Obtaining reliable CFD results for turbulent flows necessitates the proper selection of an appropriate turbulence model. In principle, the governing equations for any flow can be solved directly without turbulence models through Direct Numerical Simulation (DNS). However, DNS requires resolving an extensive range of temporal and spatial scales in turbulent flow, from large vortical structures to the Kolmogorov length scale. This necessitates substantial mesh resolution and computational resources, which scale approximately with the cube of the Reynolds number as the flow velocity increases [108]. Consequently, the demands for intricate mesh and small time steps limit the applicability of DNS to low Reynolds flows in simple geometries within engineering contexts.

In contemporary research, most studies employ either Large Eddy Simulation (LES) or Reynolds-Averaged Navier-Stokes (RANS) models. Smagorinsky initially proposed the LES model to reduce computational time by modelling small-scale eddies while only computing large-scale motions. In general, LES is less accurate than DNS but considerably more accurate than RANS, as the latter models all eddies [109]. Nevertheless, RANS remains the preferred choice for most engineering applications, as it can provide adequately accurate results without excessive computational resources and time consumption.

2.6.2 A Brief Review of RANS Turbulence Models for Turbomachinery

The fidelity of flow behaviour predictions within gas turbine blade passages is critically dependent on the choice of turbulence model employed in computational simulations. The RANS turbulence models strike a balance between computational practicality and the precision needed for such complex flow environments. All the transport equations for the following included turbulence models are illustrated in the Appendix A.

2.6.2.1 $k - \epsilon$ Turbulence Model

The $k - \epsilon$ turbulence model is a widely utilized model in engineering computations, developed to solve the modelled transport equations for turbulent kinetic energy (k) and the dissipation rate (ϵ). When wall-bounded turbulent flows are involved in CFD simulations, it is employed in conjunction with an appropriate wall function [111].

Pros: One significant advantage of the $k - \epsilon$ model is its standardisation in the industry, especially for simulating mean flow characteristics in turbulent flow conditions. Its simplicity, stemming from the two-equation model structure, facilitates a more computationally efficient approach compared to its more complex counterparts. This aspect is particularly beneficial in industrial applications where computational resources are a concern. In addition, the $k - \epsilon$ model is adaptable, with variations like the Standard, Realizable, and RNG models, each tailored to perform optimally under specific fluid flow conditions. Such adaptability enhances its utility across a broad spectrum of turbulent flow scenarios [112].

Cons: Despite being widely used in many engineering applications, the $k - \epsilon$ model exhibits notable limitations, especially in complex flow dynamics characteristic of gas turbine blade passages. It has been reported to yield inconsistent and diffusive results in scenarios involving swirling and recirculating flows, common in combustor geometries of gas turbines. Such inconsistencies are attributed to its inadequacies in handling complex flows, particularly those with strong pressure gradients, curvature, rotation, or separation. Additionally, the model is known to overpredict turbulent eddy viscosity in regions of high shear, leading to potential inaccuracies in simulating the intricate flow dynamics around turbine blades [113].

2.6.2.2 $k-\omega$ Turbulence Model

The $k-\omega$ turbulence model, designed to resolve the sublayer of the flow boundary layer, solves the transport equations for the turbulent kinetic energy (k) and specific dissipation rate (ω), without considering damping functions. Although not as widely used as the $k-\epsilon$ model, the $k-\omega$ model offers a relatively simple and numerically stable approach, particularly for low-Reynolds number flows and transitional flows [110]. In practice, the Shear Stress Transport (SST) model is often combined with two-equation models, such as the $k-\omega$ turbulence model, to mitigate its sensitivity to free stream effects [114]. Figure 2.32 illustrates a comparison between CFD results based on different turbulence models and experimental data obtained by Driver (1985).

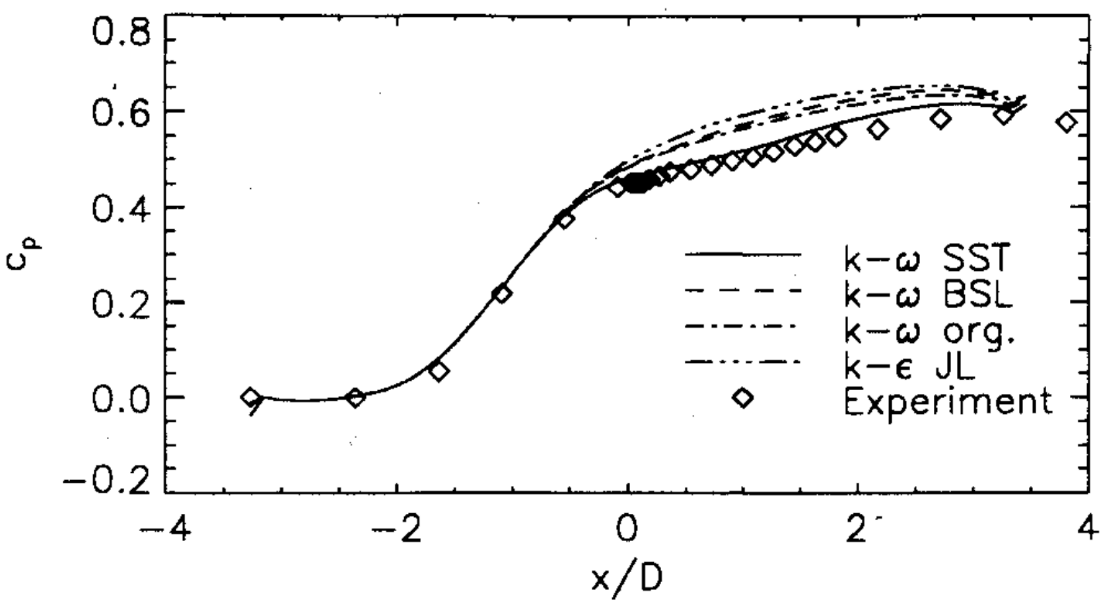

Figure 2.32: Wall Pressure Distribution under Adverse-Pressure Gradient Flow Predictions Comparison [115]

It can be seen from Figure 2.32 that the $k-\omega$ model provides better predictions for flows with separation and adverse pressure gradients than the $k-\epsilon$ model [110]. If the findings by Driver in 1985 are accurate, the most precise results for adverse-pressure gradient flow can be achieved by employing a combination of the $k-\omega$ turbulence model and the SST model (in the inner boundary layer), as this combination produces results closest to the experimental data [114, 115]. Moreover, the SST model, proposed by Menter, combines the advantages of the $k-\epsilon$ and $k-\omega$ models by utilizing a blending function that smoothly transitions between the two models depending on the flow characteristics. This blending allows for accurate prediction of both the inner boundary layer and the free stream, making it particularly suitable for complex flows involving separation and adverse pressure gradients [114]. The summarised advantages and limitations of the $k-\omega$ model are listed as follows.

Overall, the choice of turbulence model depends on the specific flow characteristics and the desired level of accuracy. The $k-\omega$ model, when combined with the SST model, has been shown to offer improved predictive capabilities for adverse-pressure gradient flows, making it a promising candidate for further investigation and application in such situations [114, 115].

2.6.2.3 Transitional SST ($\gamma - \overline{Re_{\theta,t}}$) Turbulence Model (4 Equations)

As previously discussed, turbomachinery operating under relatively low Reynolds number flow may experience flow transition within the turbine blades. A significant portion of the boundary layer could be laminar before transitioning to turbulent flow. Consequently, relying solely on fully-turbulent models may not accurately represent real flow behaviour. In such cases, the four-equation transitional Shear Stress Transport (SST) model ($\gamma - \overline{Re_{\theta,t}}$) has been specifically developed to enhance the ability of Computational Fluid Dynamics (CFD) to predict the flow transition process based on empirical data. Pioneering work on the $\gamma - \overline{Re_{\theta,t}}$ turbulence model based on local correlation was conducted by Langtry and Menter and has been validated across a variety of engineering applications, including turbomachinery, airfoils, and high-speed flows [116, 117].

Figure 2.14 shows a standard test case of the comparison between the experimental data to the $\gamma - \overline{Re_{\theta,t}}$ model and another full turbulence model, which the flow over a flat plate with a Mach number 0.15 is involved in this case [118].

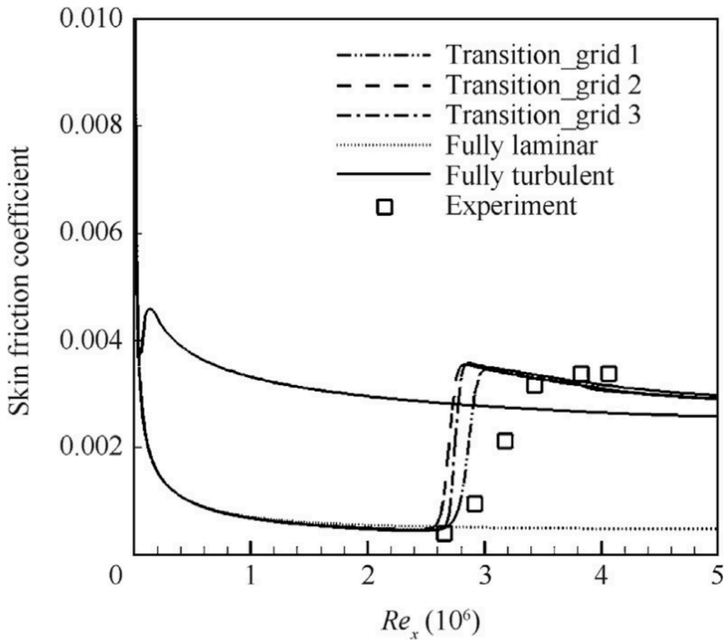

Figure 2.33: Experimental data and CFD predictions of Skin friction coefficient distribution along flat plate [119]

As shown in Figure 2.33, the transitional turbulence model provided much better predictions than the results from fully laminar and full turbulence models when flow transition is involved in the problem. Thus, in general turbomachinery applications with low Reynolds numbers, it is suggested to apply the transitional turbulence model for simulating the flow behaviour within turbine blades more accurately.

2.6.3 Large Eddy Simulation (LES)

Different from the turbulence models discussed in prior subsections, Large Eddy Simulation (LES) operates by resolving large-scale turbulent structures, while employing models for the smaller-scale structures. This approach typically demands greater computational resources compared to the comprehensive modelling of all turbulent structures as performed by conventional turbulence models. However, with the advancement of computational techniques, the LES has been increasingly employed in recent years to investigate the complex flow phenomena within gas turbine blade passages. The subsections in the Appendix A.1.2 demonstrate the governing equations for the LES models and review the recent studies using LES for gas turbine blade performance analysis. For turbomachinery applications, the pros and cons of the LES approach are briefly described as follows.

Pros: Compared to the RANS, the LES models are particularly effective in capturing complex, unsteady turbulent flows, offering a higher level of accuracy in engineering applications with significant flow separation, transition, or vortex shedding. Additionally, by resolving the larger eddies directly, LES provides a more detailed and physically accurate representation of turbulent flows, which is crucial for understanding flow behaviour around turbine blades. Finally, for turbomachinery applications, LES models are valuable in research and design optimisation, providing detailed insights into flow physics [100].

Cons: As mentioned earlier, the primary drawback of the LES approach compared to the RANS models is the much higher computational cost. To accurately predict near-wall turbulence with LES, additional modelling or finer grids are required, which further increases the calculation costs [100, 120].

2.6.4 Near-Wall Functions

It is known that the boundary layer transition is caused by the fluid viscosity, and many experimental results have suggested that the gradients of many flow properties (such as velocity and temperature) are substantially close to the wall boundary. Thus, it is known that to obtain accurate results of those gradients, a sufficient grid resolution is required near the wall, which a suitable wall function will be automatically selected based on the wall meshing quality, which is measured by the value of dimensionless wall-normal distance y^+ as described in Equation 2.41.

$$y^+ = \frac{yu_\tau}{\upsilon} = \frac{y\sqrt{\tau_w/\rho}}{\upsilon} \tag{2.41}$$

It can be seen in Equation 2.41 that the value of y^+ depends on the friction velocity that is based on the value of wall shear stress. The reason for that is that for no-slip boundary conditions, the velocity at the wall is zero, meaning the free stream velocity is not effective near the wall, which the value wall shear stress (or turbulent kinetic energy based on the CFD codes) is required to determine the y^+ value [127]. Thus, it is difficult to determine the value of y^+ without additional information from CFD simulations. It is known that the value of y^+ is determined by the near-wall mesh quality, which is commonly measured by the first layer distance (the distance between the cell centroid and the wall y_p). Therefore, the general approach is to select the desired value of y^+ to estimate the y_p value based on empirical data from simple flow models, which is shown in Equation 2.42.

$$y_p = \frac{y^+\mu}{\rho u_\tau} = \frac{y^+\mu}{\rho\sqrt{\frac{\tau_w}{\rho}}} = \frac{y^+\mu}{\rho\sqrt{\frac{(1/2\rho U^2)c_f}{\rho}}} \tag{2.42}$$

Where the skin friction coefficient (c_f) can be estimated by empirical results from well-documented similar problems such as the flow boundary layer on a flat plate, iterations of Equation 2.42 could be required according to the simulation results of the skin friction coefficient to increase accuracy. It also can be seen in Equation 2.42 that the selection of y^+ value has a direct impact on the near-wall mesh quality, which the wall functions based on the value of y^+ are demonstrated as follows.

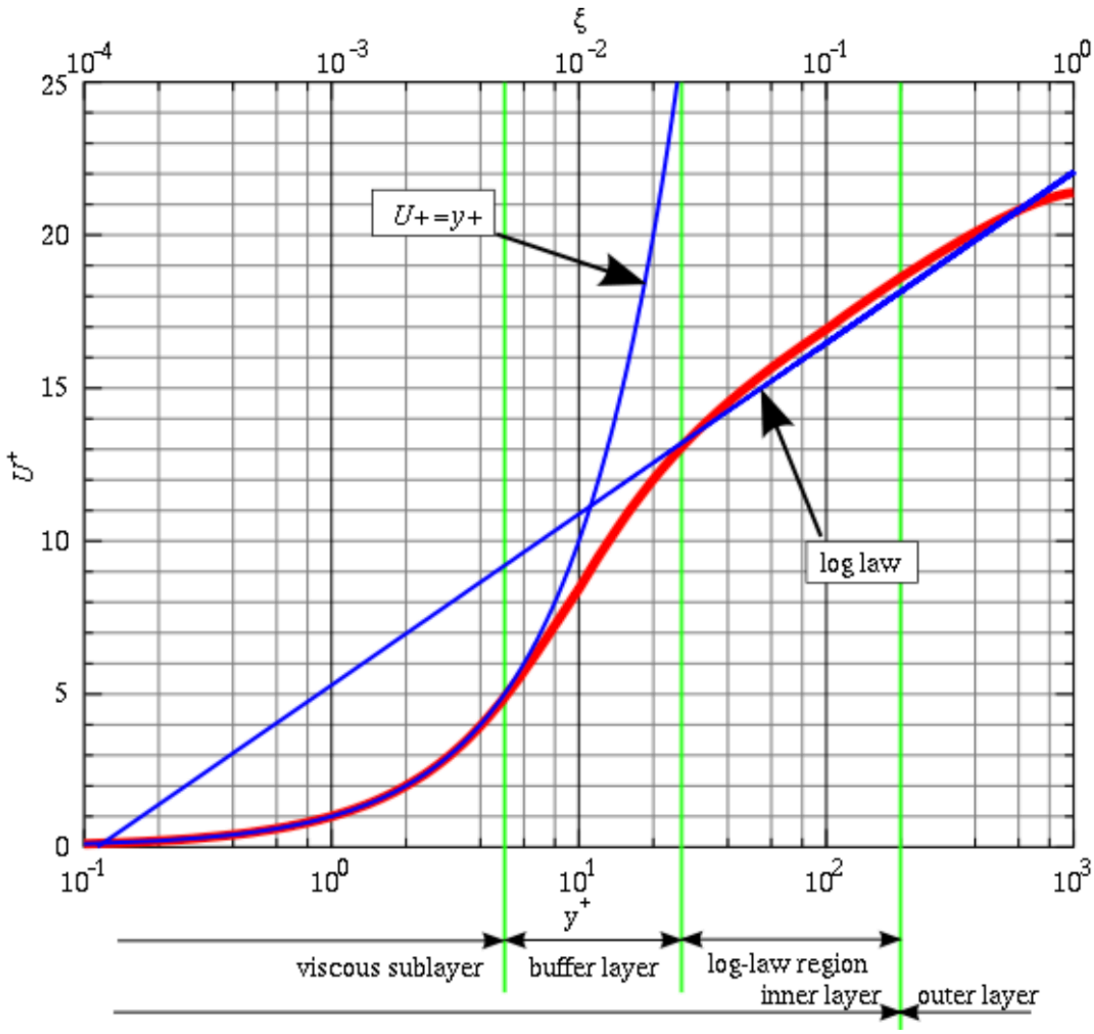

Figure 2.34: The Law of the Wall: Tangential Velocity vs. Normal Distance $y+$ [128]

In modern CFD codes, the pre-defined wall functions are a group of empirical functions designed to model the flow properties variation close to the wall using DNS simulations and experimental measurements, which B.E. Launder first introduced the additional equations (depending on the turbulent model) for the unsolved region near the wall and Spalding in 1972 as the blue lines shown in Figure 2.34 [129]. As shown in Figure 2.34, the red line represents the flow behaviour near the wall that has been observed by using DNS and experimental methods, which can be divided into three regions, including the viscous sublayer ($y+ < 5$), the buffer layer ($5 < y+ < 30$) and the logarithmic area ($y+ > 30$). The empirical equations (blue lines) for those regions are summarised in Equation 2.43 and 2.44, which describe the flow behaviour within the viscous sublayer and the logarithmic area.

$$U^+ = y^+ \tag{2.43}$$

$$U^+ = \frac{1}{\kappa} ln(y^+) + B \tag{2.44}$$

Where for Equation 2.44 the Karman constant κ and B are the empirical coefficients derived to fit the red curve in the logarithmic area. The modelling of the buffer layer region is the most difficult one, as it can be seen from Figure 2.34 that none of the empirical functions fit with the observed data. To obtain an accurate solution in the buffer region, Splading (1961) came up with a single, smooth function through the whole $y+$ range, which is shown in Equation 2.45 [130].

$$y^+ = f(U^+) = U^+ + e^{-\kappa B}[e^{\kappa U^+} - 1 - \kappa U^+ - \frac{(\kappa U^+)^2}{2} - \frac{(\kappa U^+)^3}{6} - \frac{(\kappa U^+)^4}{24}] \tag{2.45}$$

Equation 2.45 is a single smooth curve that is valid for $y^+ < 300$, which has commonly been assumed to have a good agreement with the observed data. However, for the buffer layer region, there still exists lots of uncertainties and errors for the predicted data and the physics behind them. Therefore, many researchers hold the view that the choice of y^+ value should avoid the buffer layer region ($5 < y+ < 30$) to reach the solutions that are independent of the distance of the first node above the wall(y_p). The y^+ value also should not be too large ($y^+ > 30$) for scenarios that involve separation curvature, and adverse or strong pressure gradients, which could lead to a significant loss inaccuracy. Many pieces of evidence in the industry have proven that an accurate solution would typically be achieved when the value of y^+ is reduced below unit (within the viscous sublayer $y^+ < 1$), which the best approach is to run a well-known two-dimensional model to check if the selected wall function can predict the flow behaviour and physics accurately [131].

2.6.5 Mesh Matters

Before the actual solution phase, the required work of the CFD process is called pre-processing, which involves the geometry creation and mesh generation. The geometry acquisition can be achieved by either using CAD software (such as DesignModeler and BladeGen) or importing geometry from an existing object (such as laser-scanning). After the geometry creation, the most crucial step is the discretisation, which is also known as the meshing process. To understand the word 'discretisation', one must know that it comes from 'discrete', which can be defined as the separate, individual things that form a whole object. Generally, for CFD applications, discretisation can be described as the process of using a finite number of discrete points or volumes throughout a domain to solve a closed-form mathematical expression (for instance, an integral or differential equation) that can be viewed as processing an infinite continuum of values in the same domain. In CFD applications, creating a network of points and cells is called the mesh, which is a significant step before the computation process [100]. The mesh quality can have a significant impact on the rate of convergence, solution accuracy and computational resources required in the CFD process. Thus, selecting the most suitable mesh is significant to achieve the most accurate results with the least computational resources. Figure 2.35 shows the standard shapes of computational cells that can be generated by CFD software.

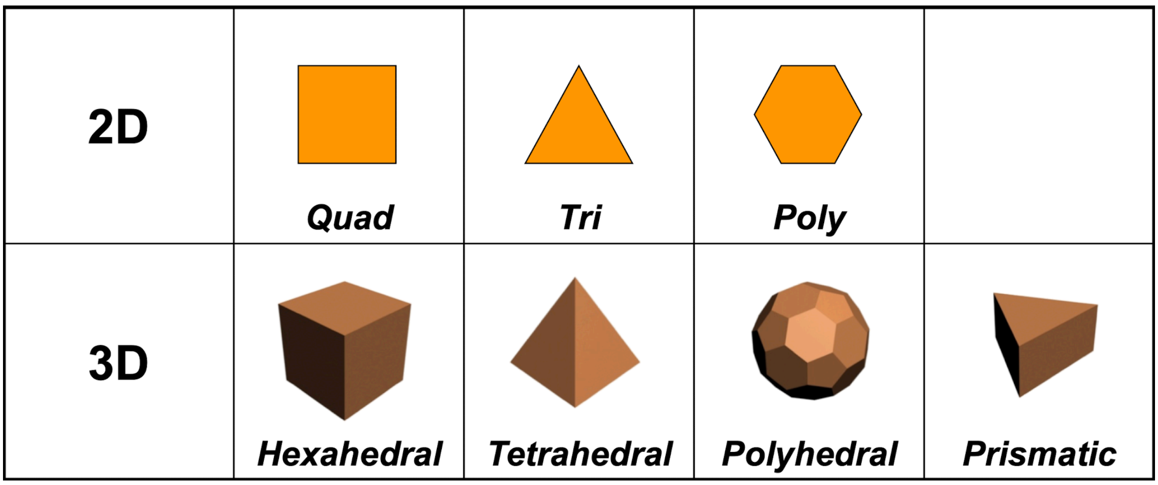

Figure 2.35: Computational Cell Shapes (structured, unstructured and hybrid) [132]

As shown in Figure 2.35, the designer can either choose structured, unstructured or hybrid cell shapes for the meshing process. It is commonly believed that structured meshes can provide efficiency and simplicity, which would consume less computational resources than unstructured mesh with the same amount of cells. However, for complicated geometries, the structured mesh would normally require more cells than unstructured mesh due to the incapability of grading in size as rapidly. Thus, the third option is applying the hybrid structured/unstructured approach by decomposing complex domains into blocks that can be supported by structured meshes. However, the drawback of the hybrid method is that it cannot be automatically generated, which would require the operator to manually adjust the decomposition process [133]. Figure 2.36 is an example of the structured grids that show how the mesh decomposes the flow domain into the control volumes.

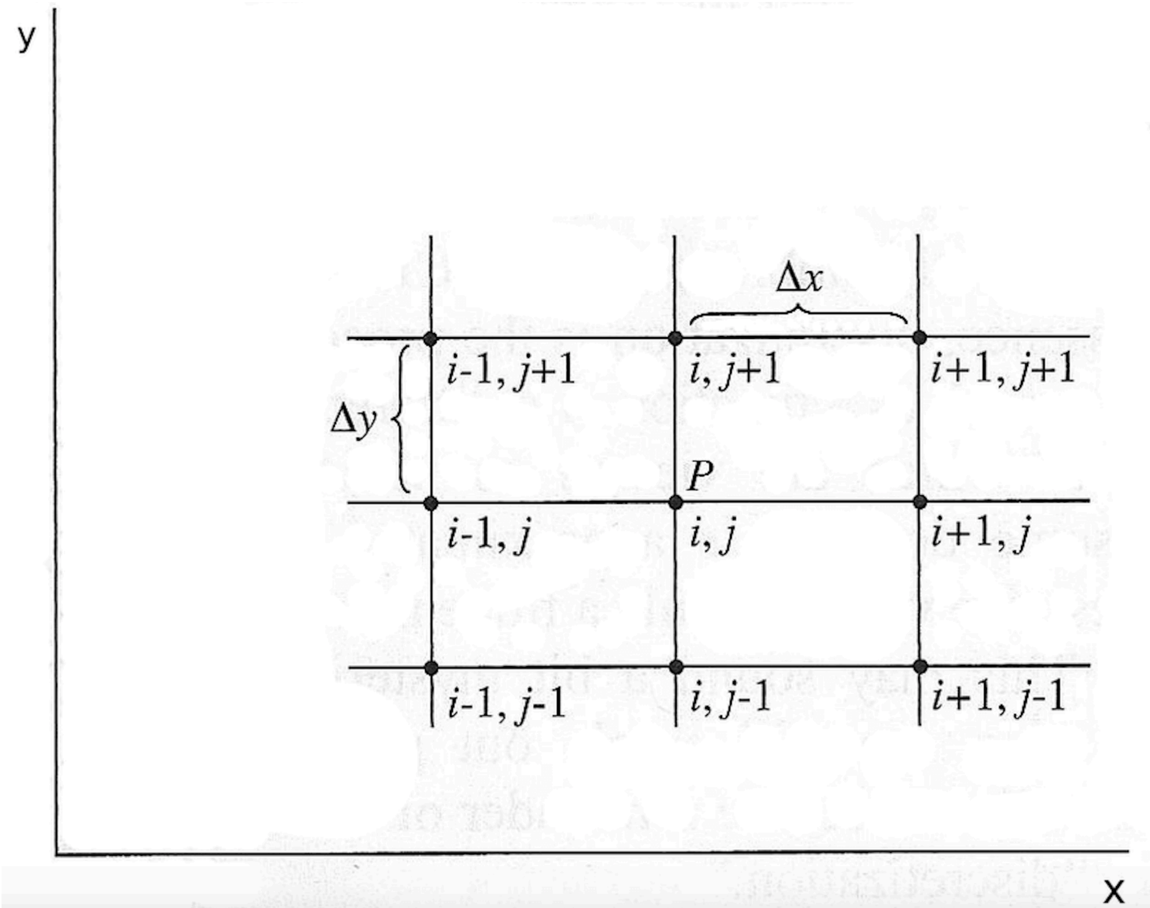

Figure 2.36: Discrete Grid Points [100]

In Figure 2.17, it is commonly assumed that Δx and Δy are constant for structured mesh, which the uniform spacing will be one of the assumptions in this project for simplicity.

2.6.6 Development of CFD Technique for Gas Turbine Blades

Recent studies have highlighted the importance of CFD in understanding the flow behaviours within gas turbine blades, which play a crucial role in determining the overall performance and efficiency of gas turbines. In 2002, Lakehal conducted a comparative study of CFD results for turbine blade near-wall regions with developed channel flow at Re=211, utilising DNS and the two-layer $k-\epsilon$ model. This comparison serves as an example of the application of DNS in tandem with a specific turbulence model [123].

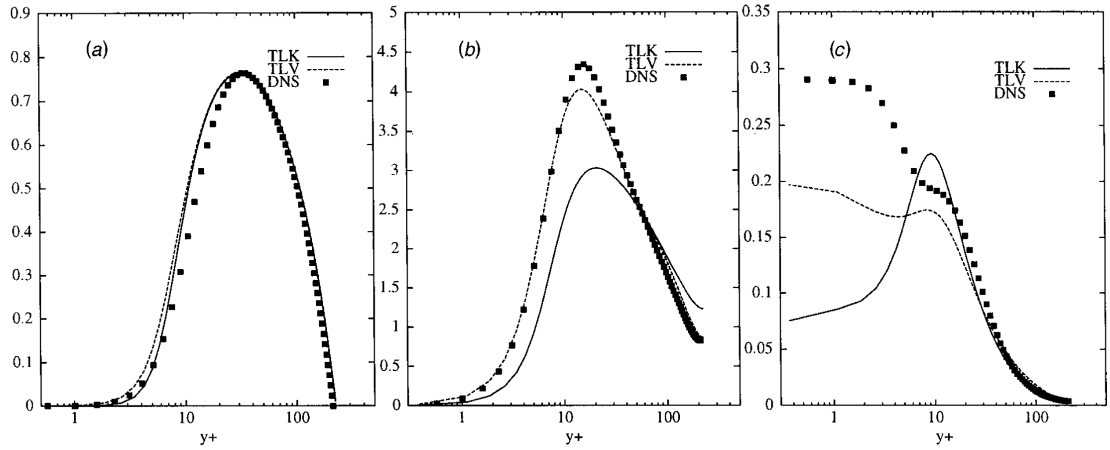

Figure 2.37: Blade Near-wall CFD Results at Re=211 (Left: Shear Stress $\overline{u'v'}^+$; Middle: Turbulent Kinetic Energy k^+; Right: Dissipation Rate ϵ^+ [123]

As shown in Figure 2.37, the excellent data acquired by Lakehal show that CFD results by RANS $k-\epsilon$ model and DNS have almost identical profile when the $y^+ > 30$. However, it also shows that for the near-wall region ($y^+ < 30$), the results by RANS do not give a good agreement with the observed behaviour by experiments and DNS results [123].

Despite the limitations of RANS equations in capturing the full range of flow behaviours near the wall, they have still been widely employed in gas turbine blade studies due to their lower computational cost and time requirements. To carry out RANS simulations, it is important to select an appropriate turbulence model. Karczewski and Blaszczak carried out RANS simulations of a 1.5-stage turbine and compared the performance of three different turbulence models ($k-\epsilon$ Chien, $k-\omega$ Wilcox and SST

Menter), which they found the SST model predicts the closest results compared to the experimental data. However, to the small difference between each turbulence model, Karczewski and Blaszczak stated that the choice of turbulence should be based on the research objective [124].

To compare the performance of RANS and LES, Dave and Frank carried out a numerical study focusing on cross-flow turbines with both confined and unconfined flow conditions ($Re = 4.5 \times 10^4$). Their findings revealed that the RANS model exhibited a higher sensitivity to confinement, which led to an over-prediction of power generation due to the suppression of flow separation as shown in Figure 2.38 [125].

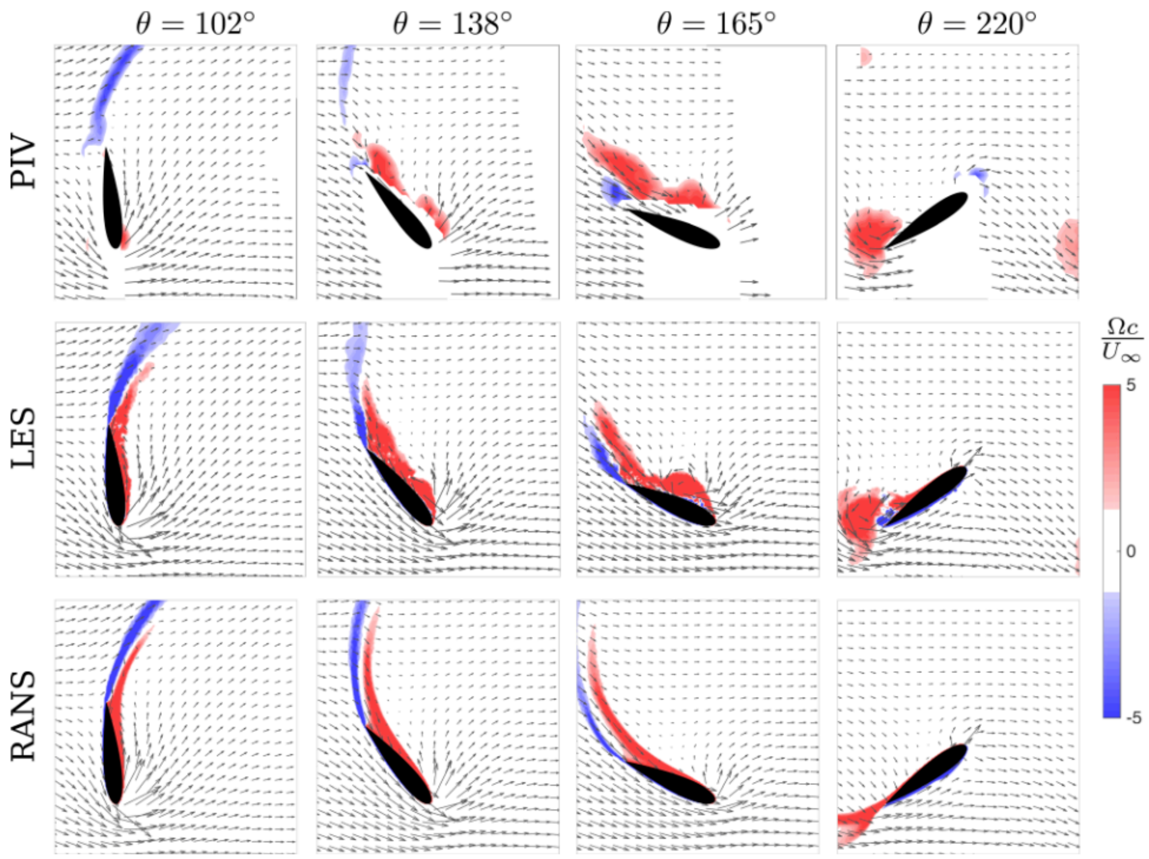

Figure 2.38: Phase-averaged Velocity (Vector) and Vorticity (Contour) From RANS, LES and Experimental Data ($Re = 4.5 \times 10^4$) [125]

The authors posited that the RANS model might not be well-suited for predicting transitional flow, as it is primarily designed for fully turbulent flow and exhibits less sensitivity to variations in the Reynolds number. In contrast, their simulations employing the LES model demonstrated a better agreement with the experimental data

[125].

In another investigation of turbulent flow and heat transfer within high-pressure gas turbine C3X stator vanes, Dong and Amano employed both RANS and LES/DES simulations. Through their comparative analysis, they observed that the aerodynamic load predictions obtained from RANS, LES, and DES models were in close agreement with each other and exhibited a strong correlation with experimental data. Nonetheless, they identified differences in the transition predictions among the models, noting that the LES model demonstrated superior performance in capturing flow behaviour prior to the separation point on the vane suction side. Conversely, the DES and RANS models exhibited better performance in the region beyond the separation point, as well as in most areas on the pressure side of the vane [126].

2.6.7 Impact of Surface Roughness on Gas Turbine Aerodynamic Performance

2.6.7.1 Relevant Studies Based on Commercial CFX Solver

In recent years, a growing body of research has focused on understanding the influence of surface roughness on the aerodynamic performance of gas turbines (GTs). Owing to the considerable differences in Reynolds numbers between GTs and MGTs, the implications of surface roughness may diverge significantly between these two types of turbines. Despite this, there has been a marked lack of investigations that specifically examine the effects of roughness on MGTs, leading to a limited comprehension of the role surface roughness plays in determining aerodynamic performance at this scale. Nevertheless, it is crucial to examine and summarise recent studies addressing the impact of roughness on gas turbine aerodynamic performance, as some findings from these investigations could be relevant for comparison with the research conducted in this project.

To study the roughness effect on a low-speed, single-stage axial turbine, Kang et al. applied CFX-Tascflow with 5 equivalent sand grain roughness, which ranges from transitional rough to fully rough regime. They found that the applied surface roughness on the GT blade does not significantly affect the pressure distribution or deviation angle changes, but would lead to the change of stage work coefficient and overall efficiency. The efficiency drop was found to be attributed to the increased profile loss by thickened boundary layers with the existence of surface roughness [138].

Lutum et al. also carried out numerical studies utilising ANSYS CFX to investigate the impact of surface roughness on heat transfer of an axial GT stator endwall. The surface roughness at different locations was experimentally measured and applied in CFX with steady-state simulations. They discovered lower heat transfer levels for hydraulically smooth cases compared to the measurements. Good agreement was found for the systematic variation of the sand grain roughness model and experimental data. However, the model was unable to resolve the impact of flow acceleration on heat transfer enhancement in conjunction with surface roughness. Thus, it was stated by Lutum et al. that a modified model that can better predict the transitional and fully rough regimes is required to be developed [139].

For the research of roughness effect for MGTs, the only published study was conducted by Gamil et al., in which they applied RANS simulations on a micro axial turbine with sand grain roughness of $3\mu m R_a$, $6\mu m R_a$, $20\mu m R_a$, and $100\mu m R_a$. Figure 2.39 shows the total pressure loss plotted by Gamil et al. for different levels of surface roughness [140].

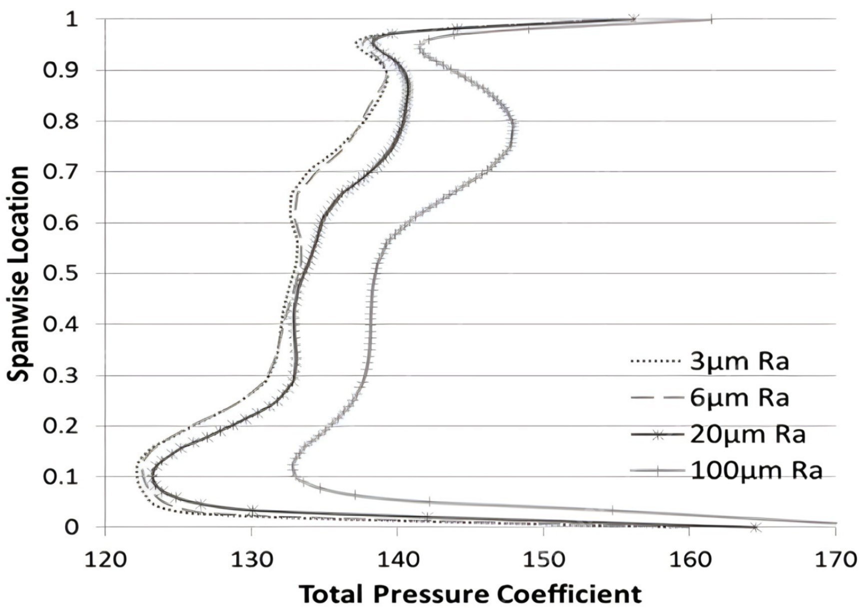

Figure 2.39: TwinGen MGT Rotor Total Pressure Loss With Different Levels of Roughness [140]

It can be seen from Figure 2.39 that the impact of roughness is relatively small when the arithmetic roughness is lower than $20\mu m$. However, as the rotor blade surface becomes rougher, the total pressure loss increases rapidly. Overall, Gamil et al. discovered the stage efficiency loss for $6\mu m R_a$, $20\mu m R_a$, and $100\mu m R_a$ are 0.8%, 4%, and 12%. To minimise the loss, it was recommended to control the surface roughness of the TwinGen MGT blades to be lower than $6\mu m$ [140].

2.6.7.2 CFD Model for Surface Roughness

To correctly resolve the influence of surface roughness near the wall with RANS simulations, several roughness modifications have been developed. To activate the roughness factor in CFX, a downstream shift in the logarithmic velocity profile equation was used as shown in Equation 2.46 [134].

$$u^+ = \frac{1}{\kappa} ln(y^+) + B - \Delta B \tag{2.46}$$

The downstream shift can be described as a dimensionless function of the roughness height, of which the B is an empirical factor of 5.2 according to previous experimental studies [134].

$$\Delta B = \frac{1}{\kappa} ln(1 + 0.3Re_k) \tag{2.47}$$

$$Re_k = \frac{k_s u_\tau}{\nu} \tag{2.48}$$

In Equation 2.48, the k_s represents the function of sand grain roughness, which the three regions of the model would be determined by the roughness Reynolds number (Re_k). There are three regimes of roughness, which are listed as follows.

- Hydraulically Smooth ($0 < Re_k < 5$);
- Transitional Rough ($5 < Re_k < 70$);
- Fully Rough ($70 < Re_k$);

For a hydraulically smooth surface, the viscous sublayer would be fully established near the wall. As the roughness Reynolds number increases to the transitional regime, the viscous sublayer would be disturbed until the viscous effects become negligible when fully rough ($70 < Re_k$) [134].

To represent the shape and spacing of the roughness elements, the roughness constant (C_s) is often used. According to experimental data of rough pipes by Nikuradse in 1950, the value of C_s is generally assumed to be 0.5 for uniform sand grains [137].

In some applications, the CFD codes combine the ΔB in to a modified formulation of near-wall kinematic viscosity (E). The equation 2.46 can be re-organised into Equation 2.49 and 2.50.

$$u^+ = \frac{1}{\kappa}ln(\frac{Ey^+}{e^{\Delta B}}) = \frac{1}{\kappa}ln(E'y^+) \tag{2.49}$$

$$E' = e^{\Delta B} \tag{2.50}$$

According to the manual, the commercial CFD codes solve the wall roughness in the following 5 steps [134].

- Proceed the boundary cell face
- Calculate y^+ and Re_k
- Calculate ΔB or E'
- Calculate ν_w
- Resolve momentum equations of u^+

Despite wide applications of the roughness modification functions, several previous studies have also stated the challenge of using current commercial CFD codes to accurately simulate the impact of surface roughness. Alldieck et al. studied the interaction of transition and turbulence models for rough wall boundary conditions with solver TRACE. It was discovered even if the model has no sensitivity to the applied roughness, and the transition process could be influenced by the rough wall. However, none of the model combinations could precisely predict the experimental results [135]. Blocken et al. researched various commercial codes by utilising ANSYS Fluent and CFX, in which they noted that the CFD results could be highly dependent on the type of roughness modification applied to the wall functions. It was suggested by Blocken et al. that further improvements in the modelling of the rough wall effect on the transition onset are needed [136].

2.6.7.3 Summary

This subsection has reviewed the crucial role that CFD plays in advancing the design and analysis of turbine blades. From the fundamental mathematical models that capture the core physical laws governing fluid dynamics to advanced turbulence models like RANS $k-\epsilon$, $k-\omega$, transitional SST and LES models, CFD provides a robust framework for predicting and understanding the complex flow behaviours within turbomachinery passages. Each model brings its advantages and limitations, offering varying degrees of precision and computational efficiency.

Moreover, the review highlighted the significant impact of surface roughness on turbine performance and its model in CFX. As the roughness level increases, especially beyond certain thresholds, it can lead to marked increases in aerodynamic losses due to changes in flow characteristics such as boundary layer thickness and turbulence intensity. These changes can degrade the aerodynamic efficiency, highlighting the need for careful simulation and optimisation of surface conditions.

Given these insights, the following chapters will involve a detailed comparison of these CFD models against experimental data from Wren100 engine tests and wind tunnel cascade tests. The objective is to identify the most accurate and computationally efficient models for analysing the aerodynamics of the Wren100 MGT blades. This comparison is crucial for selecting models that not only predict accurate flow behaviours but also align with the practical constraints of engineering applications, such as computational resources and time constraints.

Chapter 3

Experimental Methods

3.1 Introduction

In this chapter, the experimental facilities, instrumentations, and techniques applied for data acquisition are presented. The experimental research was conducted on two individual configurations. Firstly, based on the parametric study, the re-designed Wren100 stator was manufactured and tested in the micro jet engine rig. The second, T106 and the scaled Wren100 stator mean section profile cascade were tested in the UoS wind tunnel facility. Profile loss of both two types of turbine blades was estimated based on the measurements of the total pressure loss coefficient at different locations on the flow exit plane.

The data acquisition and logging equipment are also described in the following subsections with the details of each instrumentation. For the micro jet engine tests, the measurement techniques are conventional thrust tester, quick response static pressure transducers and thermocouples. For the wind tunnel tests, a pitot tube was mounted on an electric lifting device near the exit regions of the blades.

3.2 Wren100 Jet Engine Experiments

This section delineates the test facilities and measurement techniques employed for the acquisition of the Wren100 engine test data. The equipment encompasses a micro turbojet engine and a test cell environment with special sensors and the Jet-A1 fuel tank that was meticulously designed for academic research purposes.

3.2.1 Jet Engine Experimental Facilities

The experimental configuration involved the mounting of the Wren-100 jet engine onto a test bed, which was equipped with a force sensor for measuring the generated thrust (Figure 3.1). The instrumentation setup incorporated eight electrical static pressure transducers and eight thermocouples, positioned at various locations of the jet engine. This arrangement enabled the real-time monitoring of inlet pressure and temperature of the engine, as depicted in Figure 3.2.

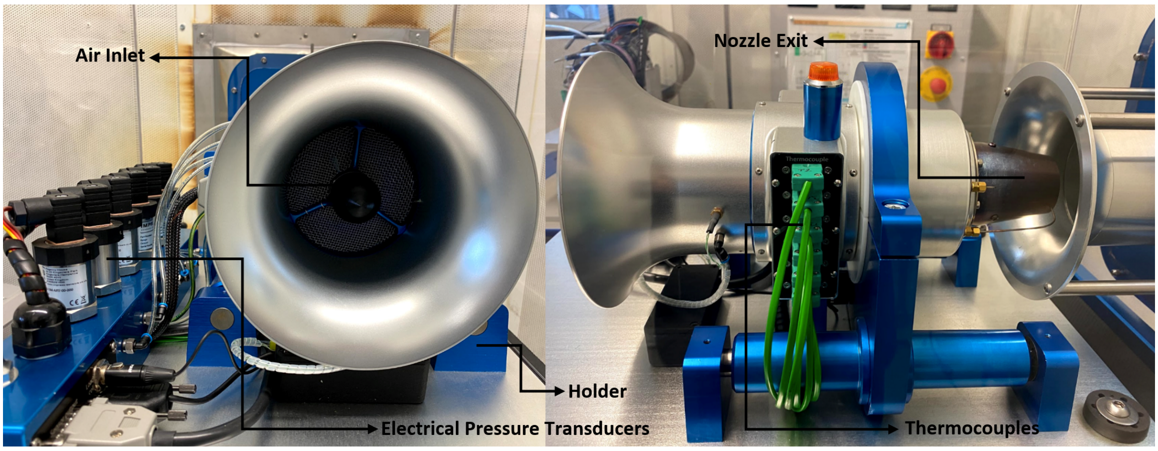

Figure 3.1: Wren100 Experimental Instrumentations

In this PhD project, the research area was narrowed to the single-stage turbine stator and rotor, meaning only P_4, P_5, P_9, T_{04}, T_{05} and T_{09} were recorded for CFD inputs and data validation as shown in Figure 3.3.
The temperature sensors used are Omega thermocouples with different measuring ranges as displayed in Table 3.1, in which the standard limits of error is 1.5 $°C$ or 0.25% FSO (Full-Scale Output) according to the manufacturer specifications [141].

	T_0	T_1	T_2	T_{3a}	T_{3b}	T_4	T_5	T_9
Range ($°C$)	0~50	0~50	0~50	0~135	0~175	0~1200	0~800	0~800

Table 3.1: Wren100 Thermocouples Operating Ranges

For the pressure sensors, the specific models used are the IMP-G series transmitters developed by Impress Sensors & Systems Ltd. The standard accuracy is ± 0.5% FSO. The complete technical details for sensors installed at different monitoring positions are listed in Table 3.2.

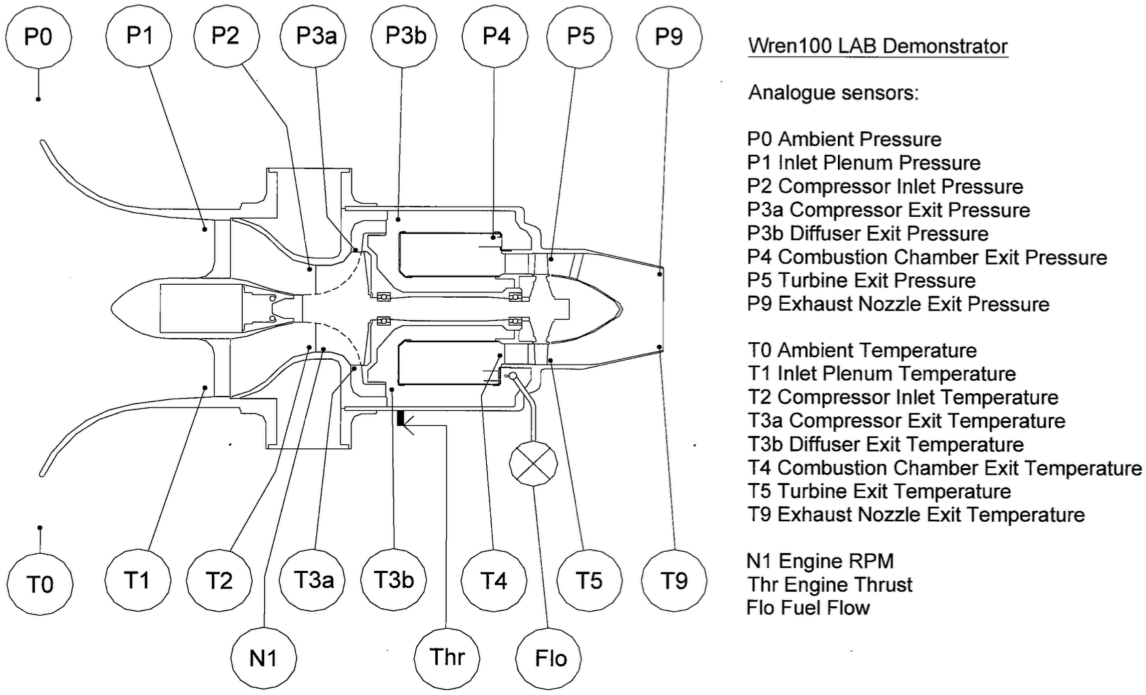

Figure 3.2: Schematic Diagram of Wren100 Sensors Layout

	P_0	P_1	P_2	P_{3a}	P_{3b}	P_4	P_5	P_9
Range (bar)	0.8∼1.1	0∼0.6	0∼1	0∼1.2	0∼2.5	0∼2.5	-1∼1	-1∼1

Table 3.2: Wren100 Pressure Sensors Operating Ranges

Initially, the Wren100 engine was tested with seven fixed speeds from 100kRPM to 160kRPM with a specific control panel. LabView, a computer application designed to visualise hardware configuration and measurement was used to create a log file to store data acquired by the pressure and temperature sensors. The logging rate was set to 1Hz. At the start of a test, the jet engine would pre-heat itself until the RPM reached 50k RPM. Then, the throttle control on the control panel was used to adjust the RPM required for the testing.

3.2.2 Redesigned MGT Components Manufacture & Assemble

3.2.2.1 Equipment Introduction

As part of the experimental research, redesigned components of the Wren100 micro gas turbine were manufactured and installed inside the engine for further performance tests. The redesigned wren100 stator vanes were manufactured by SLM280, a metal

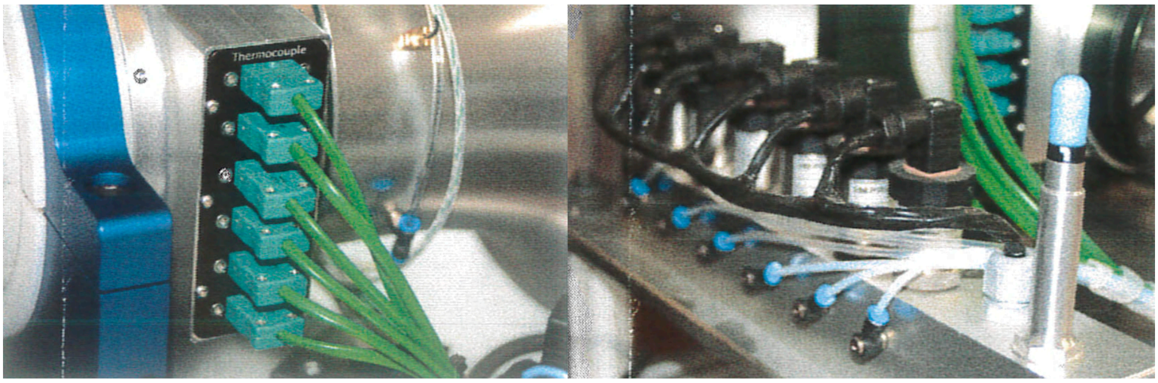

Figure 3.3: Wren100 Temperature (Left) and Pressure (Right) Sensors

3D printer that uses multiple lasers and closed-loop powder handling as shown in Figure 3.4. It is ideal for medium to high-volume metal additive manufacturing part production and prototypes. It has a building envelope of 280 x 280 x 365 mm and can be equipped with up to two 700W fibre lasers to accelerate the printing process of many metal additive powders [144].

Figure 3.4: SLM280 Metal 3D Printer

3.2.2.2 Turbine Blades Manufacturing Procedure

The operating procedure for the SLM280 is summarised as follows. Firstly, the 3D CAD file of the designed turbine blade needs to be converted to STL file format. By using the SLM solution software, the STL file of the blade can be sliced into thin layers to generate necessary support structures. Secondly, the 3D printer bed needs to be cleaned and properly calibrated. At the same time, the appropriate metal powder is required to be filled into the supply container, which in this project is stainless steel. Thirdly, the printing process can be automatically started by using the dedicated software. The printer bed will be lowered to make space for the first layer of powder to be melted. Then, the 3D object can be printed layer by layer in stainless steel. Finally, when the printed blade cools down, the post-processing procedure can then be carried out depending on its quality.

3.3 Wind Tunnel Blade Cascade Experiments

In order to conduct wind tunnel tests to evaluate the performance and aerodynamic characteristics of the turbine blade profile, appropriate experimental facilities, data collection instrumentation, and model preparation were necessary. In this study, two different configurations of the cascade, namely T106 bladed and scaled Wren100 stator vane mean section, were investigated. The experimental tests were performed in a large wind tunnel located in the laboratory for experimental tests at the University of Sheffield.

The experimental facilities utilised in this study are critical components for conducting wind tunnel tests. The large wind tunnel used in this study provided a controlled airflow environment, allowing for precise measurements of the aerodynamic properties of the stator vanes. The wind tunnel also allowed for adjustments to be made to various airspeeds of the air, which enabled the testing of the stator vanes under various operating conditions. The data acquisition equipment is demonstrated together with the instrumentation details. The technique of measurements includes fast-response and conventional static pressure and total pressure measurements with the use of pitot-tubes.

3.3.1 Experimental Facilities

The schematic diagram of the large wind tunnel displayed in Figure 3.5, is of a conventional design with the honeycomb shape inlet and a motor fan with a maximum velocity of 50mph (around 22.35m/s).

The large wind tunnel has a working section of 1.2 x 1.2 x 3m, where the cascades and the data acquisition instrumentations were mounted. The contraction ratio is

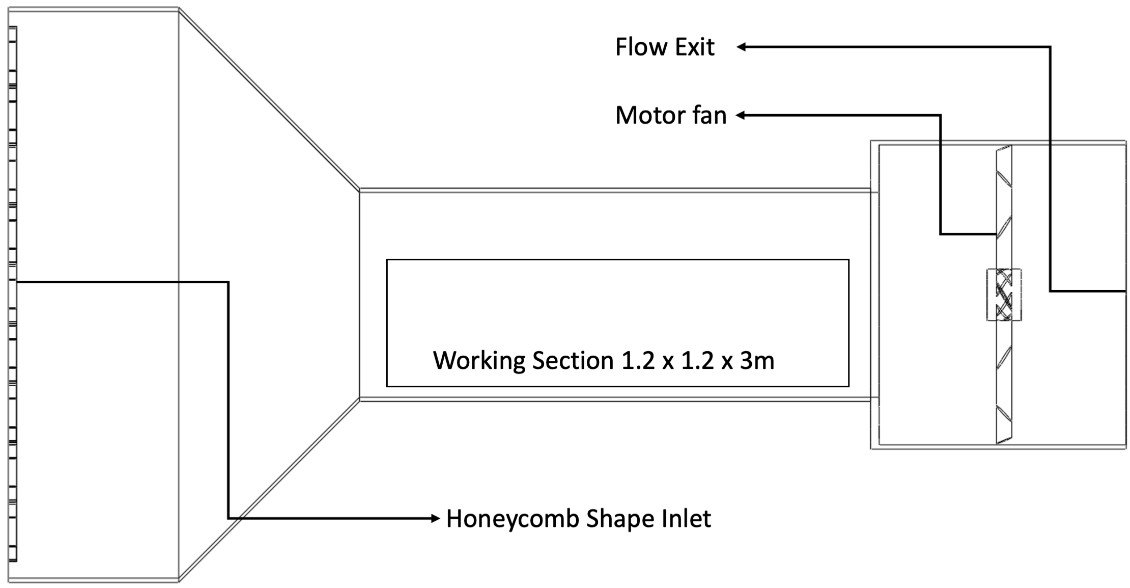

Figure 3.5: Large Wind Tunnel Schematic Diagram

6:1, and the control of flow speed is achieved by the rotational speed of the motor fan.

3.3.2 T106 Low Pressure Turbine & Scaled Wren100 NGV Mean Cascades

The T106 low-pressure turbine and the scaled Wren100 NGV mean cascades, shown in Figure 3.6 and Figure 3.7, consist of three main components, including the flow guiding ducts and the tested blade profiles. Both rigs were mounted individually in the working section of the large wind tunnel. A total pressure sensor was mounted in front of the tested blades. In addition, the total and static pressure exiting the blade passages were measured by the pitot tube located at 10% chord distance downstream of the trailing edge (TE). With the manual locomotion mechanism, the downstream pitot tube was moved circumferentially from low to high pitch distance. To minimise the influence of the cascade wall, the flow around the middle blades (yellow part) was monitored.

In the case of the T106 cascade rig, its positioning on the wind tunnel floor during the tests was necessitated by its substantial weight. Nevertheless, this setup presented challenges with regard to the influence of the floor boundary layer intruding into the cascade, thereby potentially impacting the flow characteristics within the rig.

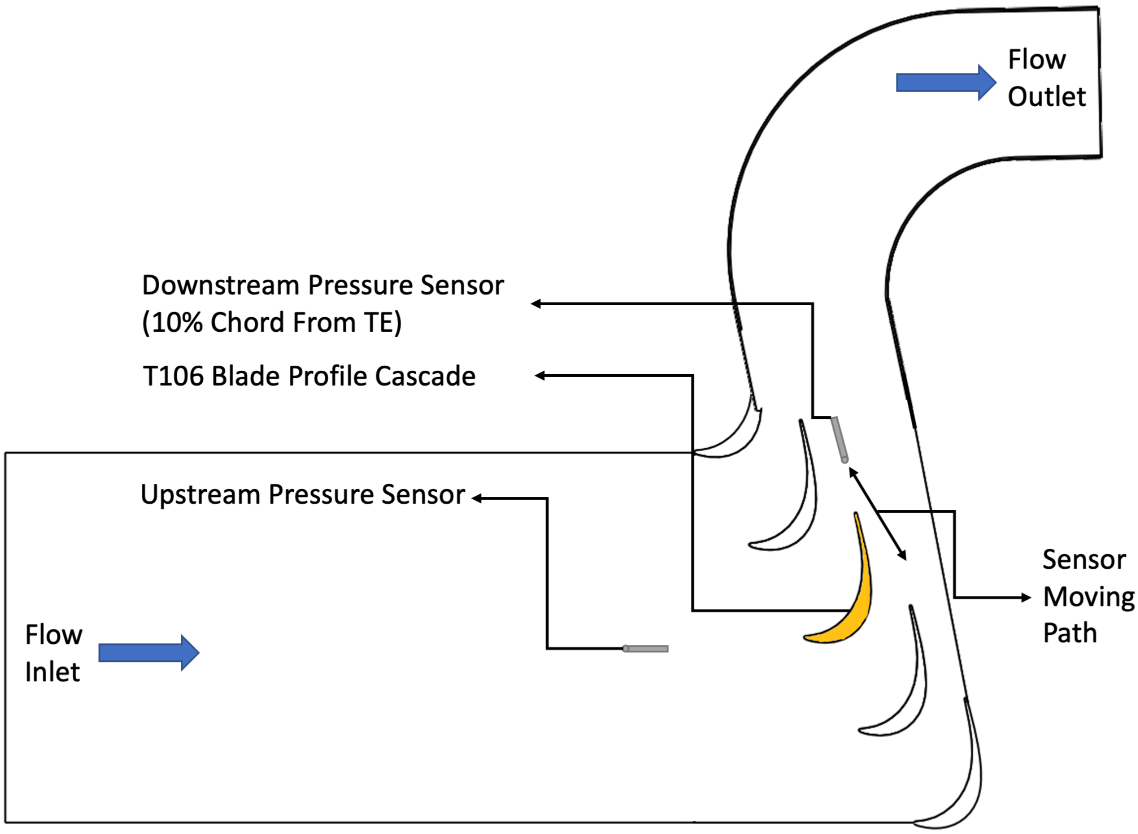

Figure 3.6: T106 Blade Cascade (On Floor) Schematic Diagram

In contrast, the Wren100 NGV mean cascade, with its comparatively lighter weight, was able to employ an elevated setup during wind tunnel testing. This strategic positioning was aimed at mitigating the influence of the floor boundary layer, thereby reducing its potential to distort the flow conditions within the cascade rig.

With the above experimental rigs and instrumentations, multiple tests were carried out with several variables averaged and recorded under different wind speeds (Reynolds Numbers) as listed in Table 3.3.

Motor Fan Rotational Speed	Inlet Total Pressure	Outlet Pressure	Outlet Total Pressure
RPM	P_{01}	P_2	P_{02}

Table 3.3: Wind Tunnel Cascade Monitored Variables

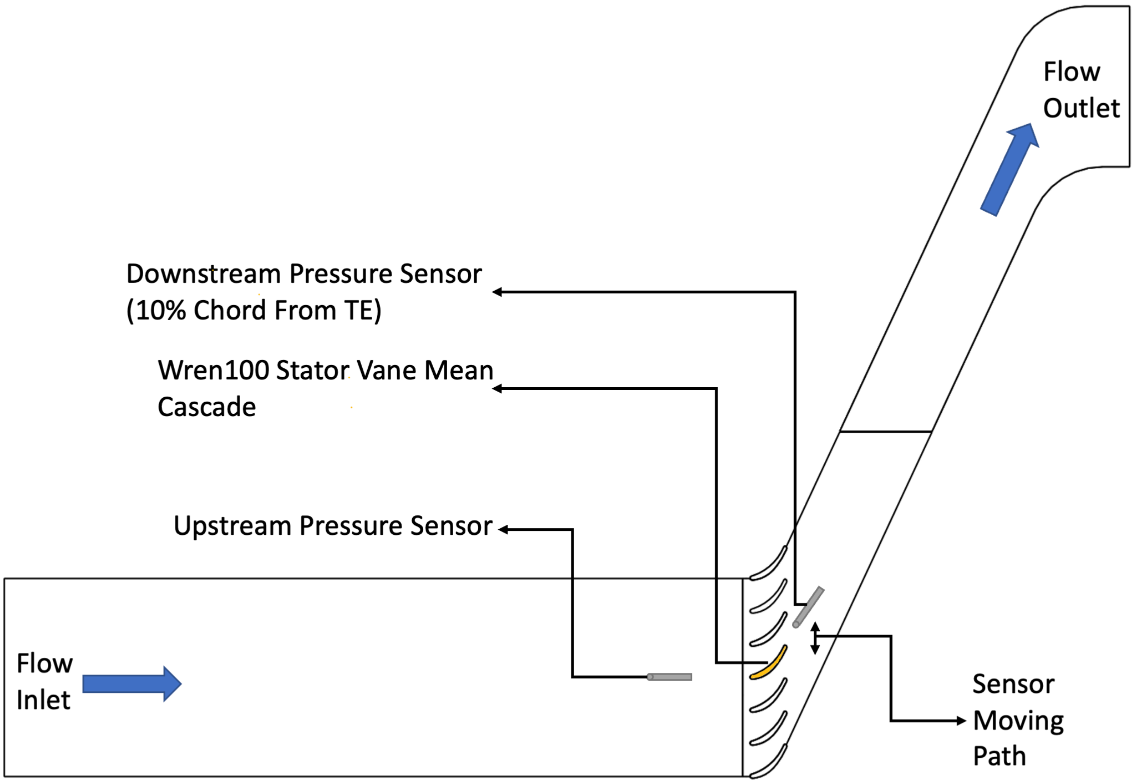

Figure 3.7: Wren100 NGV Mean Cascade (Lifted) Schematic Diagram

3.3.3 Pressure Measurements

The pressure data acquisition was carried out with the FCO510 micro-manometer and static/total pressure pitot tubes. As shown in Figure 3.8, the FCO510 micro-manometer is an accurate measuring instrument for ultra-low-range differential pressures based on its microprocessor. The time-averaged variables it can display include static/total pressure, air velocity, volume flow and temperature [145].

As presented in Table 3.3, after the time-averaged values of the pressure at the inlet and outlet of the T106 and Wren100 stator mean profiles were measured. Several physical quantities could then be calculated to analyse the aerodynamic performance of the blade profiles. The exit velocity can be calculated by Equation 3.1.

$$c_2 = \sqrt{\frac{2(P_{02} - P_2)}{\rho}} \tag{3.1}$$

Then, with the exit velocities acquired, the profile loss for two blades was then estimated by calculating the stagnation pressure loss coefficient as shown in Equation.

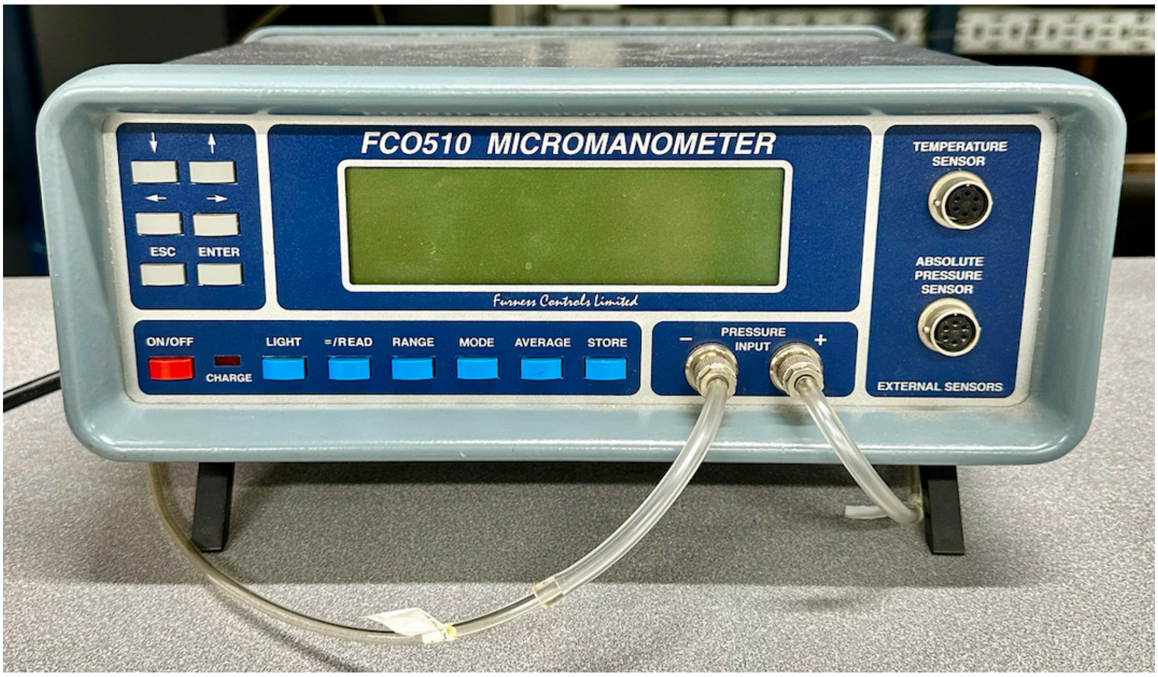

Figure 3.8: FCO510 Micro-Manometer

$$Y_p = \frac{P_{01} - P_{02}}{P_{01} - P_2} = \frac{P_{01} - P_{02}}{0.5\rho c_2^2} \tag{3.2}$$

To acquire the single value of Y_p for multiple spanwise positions, the area average data can be calculated by using the trapezoidal rule for numerical integration, which is a formula for a set of data points (x_i, Y_{pi}).

$$\overline{Y_p} = (\frac{1}{b-a}) \sum [0.5(Y_{pi} + Y_{p(i+1)})(x_{i+1} - x_i)] \tag{3.3}$$

Where a and b are the starting and ending points of the spanwise distance range, x_i is the spanwise distance for the i^{th} data point.

3.4 Surface Roughness Measurement

3.4.1 Equipment Introduction

To assess the quality of reverse-engineered micro gas turbine blades and evaluate the impact of surface roughness on the aerodynamic performance of the micro engine and cascade experiments, detailed roughness data were acquired using the InfiniteFocusSL optical microscope, professional roughness tester produced by Bruker Alicona as shown in Figure 3.9 [146].

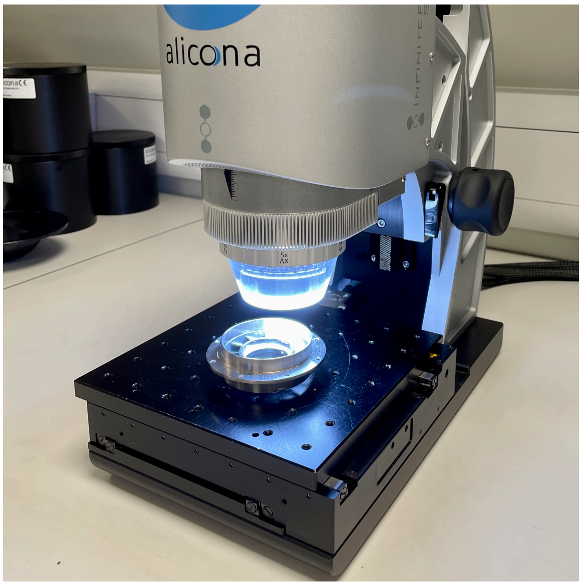

Figure 3.9: Alicona InfiniteFocusSL Roughness Tester

The InfiniteFocusSL is a high-resolution optical microscope that employs focus variation technology to obtain accurate and non-contact surface roughness measurements. This instrument provides a vertical resolution of up to 10 nm and a lateral resolution of up to 1.4 μm, allowing for the precise characterisation of the blade surface topography [146].

3.4.2 Surface Roughness Measurements

Before taking the roughness measurements, the blade sample needs to be carefully prepared, which any dust or debris on the blade surfaces was removed using compressed air. The blade sample can then be mounted on the test bed, with the instrument adjusted properly to ensure optimal focus on the measured surface. In this study, several parameters are used to describe the texture of the blade surface, and the most important one is the arithmetic mean roughness (R_a).

Figure 3.10 displays the schematic diagram of the arithmetic mean roughness of the measured surface, which can be directly acquired from the Alicona tester as described in Equation 3.4.

$$R_a = \frac{1}{n}\sum_{i=1}^{n}|y_i| \tag{3.4}$$

However, to activate roughness in CFD simulations, the arithmetic mean roughness

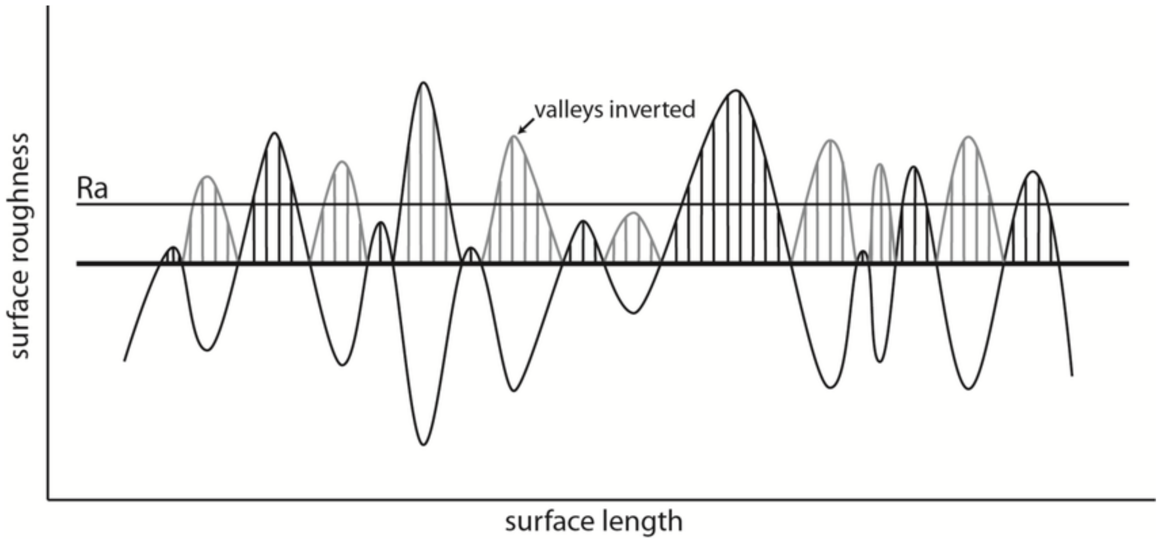

Figure 3.10: Schematic Diagram of the Arithmetic Mean Roughness [147]

is not enough, as the sand grain roughness is required for the numerical setup. In definition, sand grain roughness, also known as equivalent sand grain roughness, is a measure of surface roughness that characterises the surface texture in terms of the size of sand particles that would produce an equivalent level of flow resistance. Based on their experimental research, Adams et al. stated that the direct use of arithmetic mean roughness in turbomachinery to study its impact could lead to huge errors. Figure 3.11 shows the schematic diagram of surface roughness side view represented by a row of balls of diameter of ε, which is known as the sand grain roughness [148].

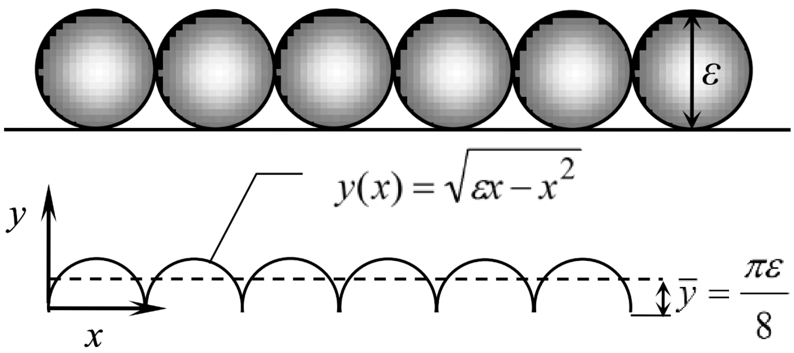

Figure 3.11: Sideview of Surface Roughness Represented By A Row of Spheres [148]

Adams et al. also proposed a conversion algorithm based on experimental data, which are listed in Equation 3.5, 3.6, 3.7 and 3.8 [148].

$$R_a = \frac{1}{\varepsilon} \int_{x=0}^{\varepsilon} |y - \overline{y}| \, dx \tag{3.5}$$

$$y(x) = \sqrt{\varepsilon x - x^2} \tag{3.6}$$

$$\overline{y} = \frac{\pi\varepsilon}{8} \tag{3.7}$$

$$R_a = \frac{\varepsilon}{2}[\frac{\pi}{2} - cos^{-1}(1 - \frac{\pi^2}{16})^{1/2} - \frac{\pi}{4}(1 - \frac{\pi^2}{16})^{1/2}] \tag{3.8}$$

According to the analytical models and experimental data, the estimated equivalent sand grain sphere (ε) can be calculated by Equation 3.9.

$$\varepsilon = k_s = 5.863R_a \tag{3.9}$$

3.4.3 Error Analysis for Experimental Setups

3.4.3.1 Wren100 Engine Test Error Estimation Based on an Iterative CFD Method

In this subsection, the limitations and systematic errors for the engine test results were investigated to confirm the engine performance, and the potential sources of errors are illustrated as follows. Firstly, many previously published studies have shown the existence of total temperature non-uniformity in the regions between the combustion chamber and the stator inlet, which are normally described as "hot" and "cold" spots [177]. Several studies have been conducted for more accurate data acquisition of non-uniformity total temperature between the combustor and turbine inlet. Martin et al. utilised large-eddy simulation on the interface between the stator inlet and the combustion chamber. SPOD (spectral proper orthogonal decomposition) method was applied to acquire partial reconstructions with different frequencies, which could then replicate realistic inlet boundary conditions for isolated turbine simulations [177]. In this experimental study, due to the total inlet temperature being measured at a single point before the stator as displayed in Figure 3.2, it is uncertain whether the value can represent the real operation condition, which can only be used as an initial boundary condition for the CFD iteration.

Secondly, the acquisition of static pressure measurements in the outlet regions of the Wren100 MGT is also subject to several sources of error. One such factor pertains to the placement of the static pitot tube within the fluid domain, which can introduce disturbances in the flow and lead to zero-point errors in the measured static pressures. Additionally, the placement of the static pitot tube at a distance from the

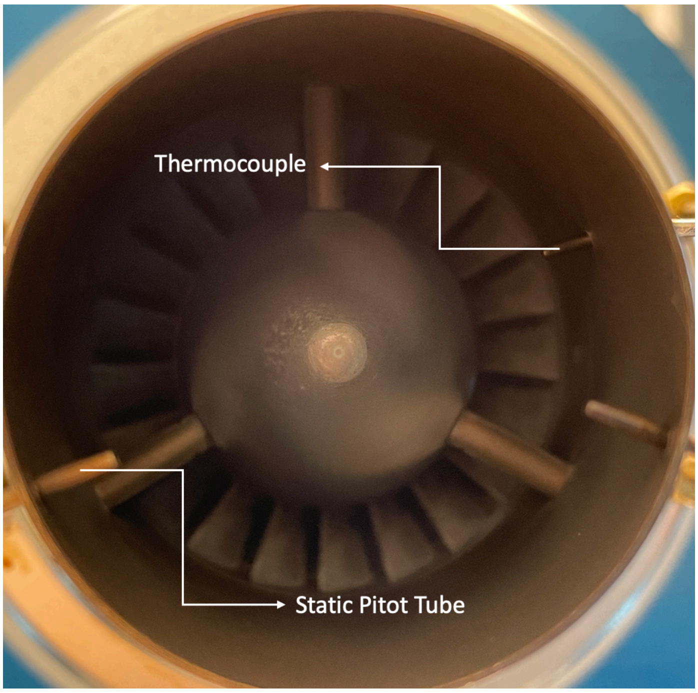

Figure 3.12: Source of Error in Static Pressure Measurements

nozzle wall can result in significant discrepancies between the measured and actual static pressure values. Despite the limited utility of outlet static pressure data, it can still provide valuable insights into the pressure field within the turbine nozzle when used in conjunction with other relevant data sources.

Overall, based on the current uncertainties, the only reliable information from the experimental tests is the mass flow rate and thrust. Due to the lack of information at the nozzle, the outlet total pressure used for iterations was acquired from the experimental research conducted by Golchin et al. on the same MGT as shown in Table 3.4 [142].

To evaluate the performance of the Wren100 turbine, CFD iterations were performed based on acquired data, including two different reverse-engineered geometries and reliable boundary conditions obtained from externally published sources. The iteration process involved first conducting an initial CFD simulation using experimental data to generate the nozzle exit velocities (C_2). Subsequently, since the nozzle was known to be un-chocked, the static pressure could be estimated using Equation 3.10 based on the known exit total pressure and other relevant parameters. This approach allowed for the determination of accurate boundary conditions and the subsequent

Engine Shaft Speed (RPM)	Total Pressure After Turbine (bar)
160,000	1.34081
150,000	1.23453
140,000	1.15216
130,000	1.09769
120,000	1.04720
110,000	0.99804
100,000	0.96749

Table 3.4: Wren100 Engine Test Datum by Golchin et al. [142]

assessment of the turbine performance.

$$P_2 = P_{02} - \frac{1}{2}\rho C_2^2 \tag{3.10}$$

The predicted P_2 can then be used as the updated information for the next CFD iteration. With the necessary geometric data, the updated inlet total temperature can also be estimated based on the stage loading coefficient as shown in Equation 3.11, in which the β_2 and β_3 were also acquired from the reverse-engineered models (Table 4.3).

$$\psi = \frac{C_p \Delta T_0}{\frac{1}{2}U^2} = \frac{2C_x}{U}(tan\beta_2 + tan\beta_3) \tag{3.11}$$

Finally, the new boundary conditions can be put into the CFD solver for the updated iteration of P_2 until the values of thrust and mass flow rate converge to a constant value.

3.4.3.2 Error Sources in Metal Additive Manufacturing Using SLM280

The precision of metal additive manufacturing using SLM280 can be influenced by several factors, leading to potential errors in the final products. Research by Andreacola et al. highlights that inconsistencies in powder material characteristics, such as size distribution and chemistry, directly impact the density and mechanical properties of the printed parts [149]. This variability can cause deviations in dimensional accuracy and surface quality. In addition, the calibration of laser parameters is critical; misalignments or incorrect settings can lead to defects like porosity or warpage [150]. Thermal management issues, such as uneven cooling and residual stresses, are also prevalent challenges that affect the geometric fidelity and structural integrity of the components [151, 152, 153].

3.4.3.3 Error Sources in Wind Tunnel Cascade

FCO510 & Pitot-Tube: When employing the FCO510 micro-manometer and pitot tubes for wind tunnel cascade testing, several sources of error must be considered. The precision of dynamic pressure measurements can be compromised by the alignment and geometric accuracy of the pitot tubes, as well as by environmental factors such as temperature fluctuations and vibrations. Calibration drift in the micro-manometer can introduce additional potential inaccuracies, influencing the reliability of the pressure readings. Installation errors, such as the placement of the pitot tube relative to flow disturbances (after trailing edge), can significantly affect the accuracy of the measurements and wake capture.

Rig Vibration: Wind tunnel tests for aerodynamic studies, particularly in cascade rigs, can be significantly affected by vibrations. These vibrations, often induced by the airflow itself, can distort the flow field measurements and lead to erroneous data. Eid et al. discuss the design considerations necessary to minimise vibrations in wind tunnel setups, emphasising the importance of structural rigidity and proper damping mechanisms to ensure accurate data collection [154]. Further studies by Zhang et al. underline the necessity of advanced vibration analysis and control strategies to mitigate the impact of structural resonances on experimental results [155].

Floor Boundary Layer Effects: The influence of the floor boundary layer is another critical factor in wind tunnel tests, especially in setups where the rig is close to the floor. The boundary layer that develops on the tunnel floor can interact with the test section flow, altering the velocity profiles and turbulence characteristics of the airstream. Catarelli et al. highlight that modifications to the tunnel floor, such as the introduction of boundary layer suction or tailored surface roughness, can significantly reduce these interactions, thereby improving the flow quality around the test models [156].

3.4.4 Summary

To sum up, this chapter outlines the experimental instruments and methods employed in this PhD research. The Wren100 jet engine tests were conducted to establish initial boundary conditions for CFD simulations, including temperature and pressure measurements. Surface roughness evaluations were performed at the UoS tribology lab to ascertain the roughness metrics for both original and rebuilt MGT components. Wind tunnel cascade experiments were utilised to validate CFD models for MGTs under both smooth and rough blade conditions. Following the proposal of redesigns for the MGT blades, the modified components were fabricated using the SLM280 metal 3D printer. Collectively, this chapter delivers a detailed overview and error analysis of the experimental procedures undertaken in this study.

Chapter 4

Development of Micro Gas Turbine Reverse-Engineering Strategies

4.1 Introduction

Various research studies have been conducted to improve the design of MGTs, which sometimes would require the engineer to reverse-engineer the original 3D CAD files. Conventional techniques start with the function required of the product and move through a design process to the end product, whereas the reverse engineering (RE) process starts with the existing product and through various techniques re-construction the geometry of the product [92]. Many techniques exist to obtain the geometry of the product, including contact and non-contact approaches, but they all have the same aim, i.e. to capture the most accurate representation of the geometry. However, it is important to select the most appropriate RE method to balance the most appropriate geometry accuracy versus the time taken (and so cost) involved.

In the following sections, the development and comparison of different RE strategies are presented. The selections of the RE models for further analysis and redesign are demonstrated in the next chapter based on the CFD and experimental results.

4.2 Non-contact Measurement Process of the Micro Turbine Blade - General Workflow

In this section, the basic geometric characteristics of the Wren series turbine parts and the process of using the Alicona laser scanning device (described in Subsection 3.4.1) to capture its three-dimensional geometries are illustrated. The Wren series turbines were initially designed by Wren Power Systems Ltd. for a model jet engine.

4.2.1 Direct Scan

In order to formulate a suitable reverse-engineering approach, the stator vane of the Wren44 turbine was initially subjected to scanning and subsequent reconstruction. The Wren44 turbine is characterised by a nominal maximum thrust of $44N$ and comprises an axial turbine that encompasses 17 stator vanes with blade heights approximately measuring $10mm$, as depicted in Figure 4.1. Owing to the miniature size and intricately twisted profiles of the Wren44 turbine components at different blade heights, direct laser scanning proved to be an arduous task in acquiring the requisite 3D geometry.

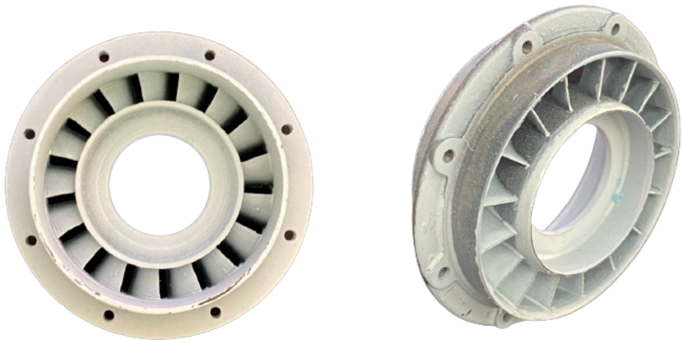

Figure 4.1: Wren44 Stator Vanes

The acquired 3D geometry in Figure 4.2 exhibits noticeable deficiencies in capturing the details of the trailing edge, which can be attributed to the high surface reflectance and obstruction of light by the vanes shroud. Nevertheless, a rough 3D CAD representation of the Wren44 stator vane was achieved by amalgamating multiple laser-scanned data from disparate perspectives through the process of RE.

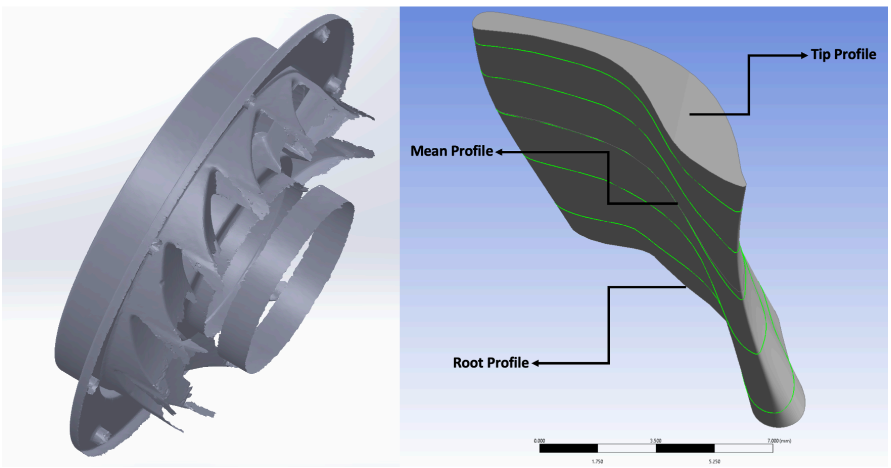

Figure 4.2: Wren44 Stator Direct Laser Scan

As shown in Figure 4.2, the reverse-engineered Wren44 stator vane has very unusual blade shapes at the root, mean and tip sections. All the essential blade characteristics of the re-generated Wren44 stator vane were summarised in Table 4.1.

Characteristics	Unit	Root	Mean	Tip
Chord	mm	23.41	23.87	26.32
Blade Stagger	$^\circ$	14.98	23.91	23.3
Pitch	mm	14.81	14.81	14.81
SS Length	mm	26.3	26.5	29.22
PS Length	mm	25.2	24.6	27.56
Inlet Flow Angle	$^\circ$	0	0	0
Exit Flow Angle	$^\circ$	48.67	58.93	54.36

Table 4.1: Wren-44 NGV Blade Characteristics

4.2.2 Silicone Mould and Epoxy Resin Tooling

The reverse-engineering outcomes obtained through the direct scanning method explicated in the preceding section reveal that the generation of a viable blade model was unfeasible, primarily attributed to the intricate blade geometry and the high reflectance of the metal blade surface. To enhance the quality of laser-scanning, the author developed a novel technique utilising silicone mould and epoxy resin tooling for the reverse-engineering process of the Wren100 turbine stator and rotor. This study involves a turbine of comparable dimensions to that of the Wren44 model, comprising a stator with 13 vanes and a rotor with 21 blades, as depicted in Figure 4.3. The twisted profiles of each vane and blade, which vary from the root to the tip, render the conventional non-contact reverse-engineering method ineffective due to the intricate nature of the structures.

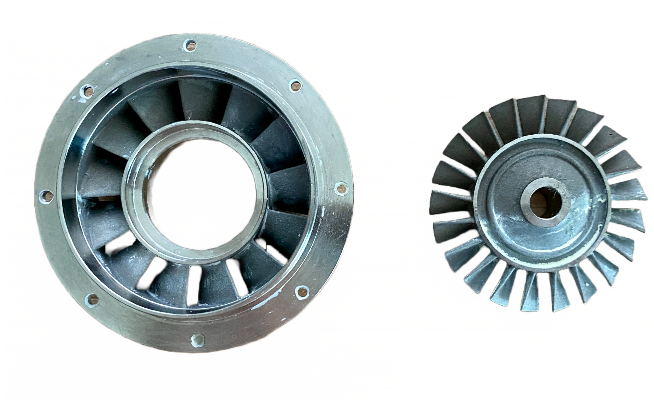

Figure 4.3: Wren100 Stator and Rotor

Hence, to recreate the turbine parts, the first step is using liquid Silicone to make the mould for the Wren100 stator and rotor blades. As shown in Figure 4.4, the liquid silicone rubber used in this project is the Limino two-part platinum-cured elastomer, which was poured on the Wren100 stator and rotor blades in two separate containers with a mixing ratio of 1:1 for solidification [172].

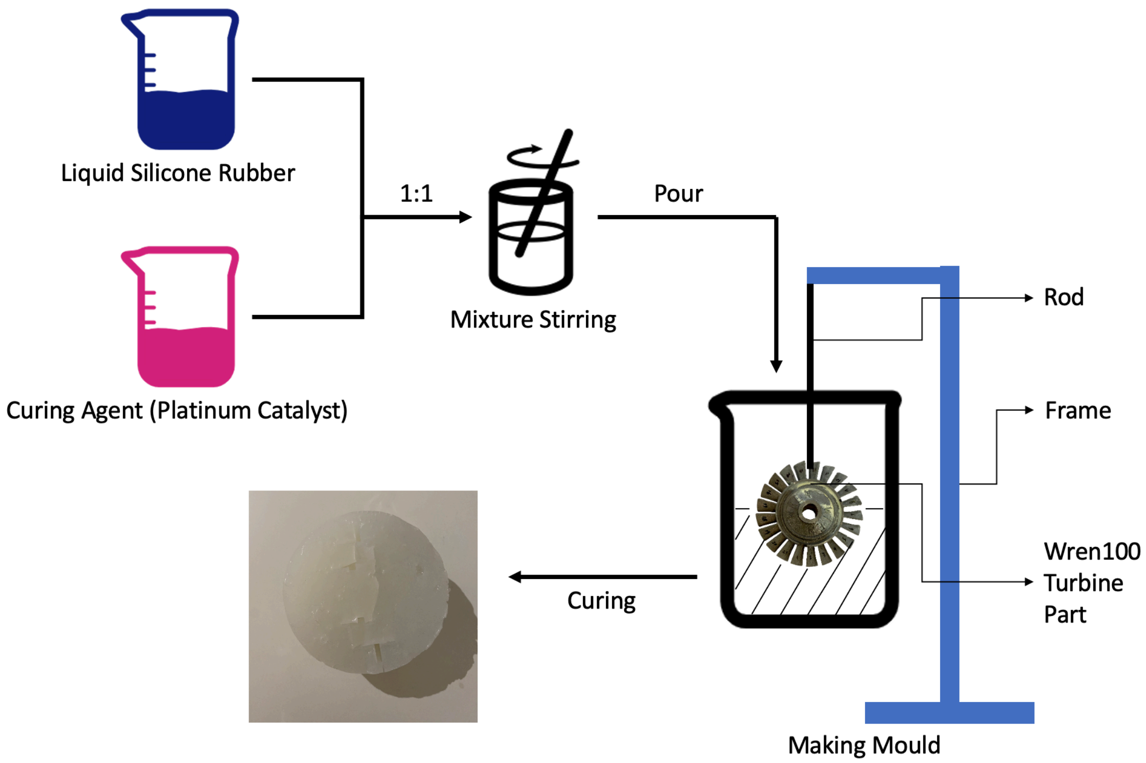

Figure 4.4: Schematic Diagram of Making Silicon Mould for MGT Blades

After the liquid silicone rubber was solidified, the turbine stator and rotor were taken out from their containers, which left cavities that could be used to build models. With the silicone rubber moulds, liquid EP resin was injected into the mould to rebuild the Wren100 stator and rotor blades. The injection process of the liquid EP resin was similar to the liquid silicone rubber, in which the liquid EP resin includes the resin and hardener with a mixing ratio of 1:1 [173]. To increase the surface reflectance of the blade models, white paint was blended in the liquid EP resin. When solidified, the EP resin models of the Wren100 stator and rotor blades were taken out of the silicone rubber mould for further geometrical acquisition. Figure 4.5 shows all the models created by EP resin, in which each vane and blade was cut out for better scan quality.

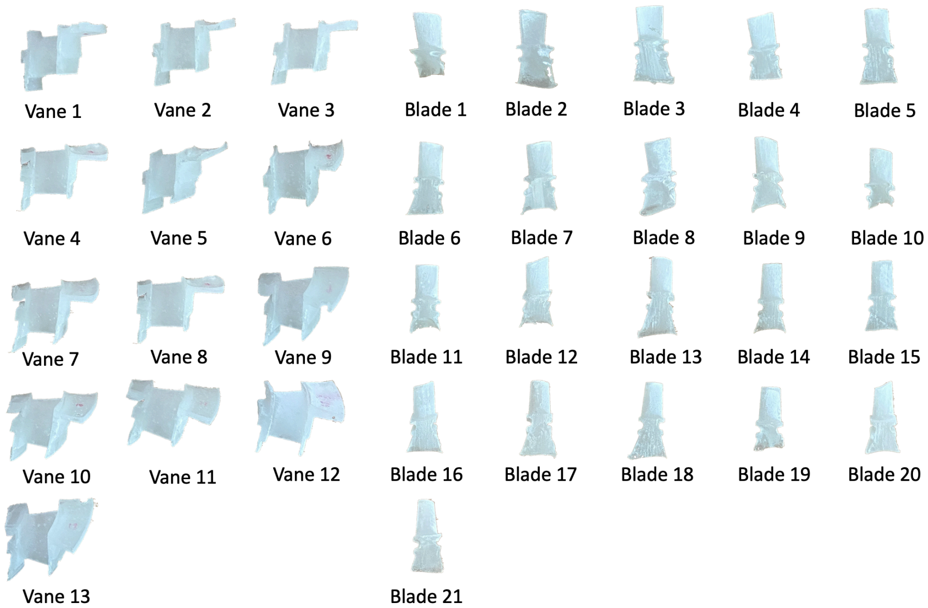

Figure 4.5: Models of Wren100 Parts Based on EP Resin

To verify the quality of the models rebuilt by EP resin, samples of the surface roughness from the original and RE blades were measured and compared by InfiniteFocusSL as displayed in Figure 4.6.

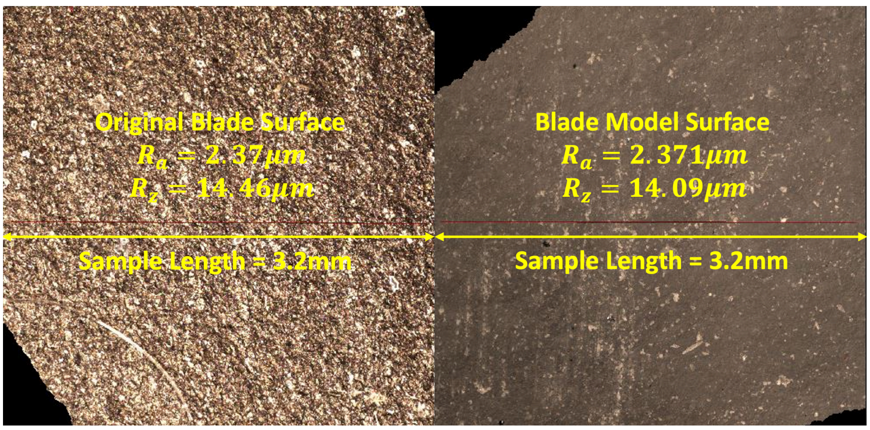

Figure 4.6: Samples of Measured Roughness (Left: Metal Blade; Right: Resin Model)

Figure 4.6 shows one sample of roughness comparison between the original blade and the EP resin model, in which the average blade surface roughness height between the original metal blade and EP resin model is almost the same. More measurements were carried out for all 13 stator vanes and 21 rotor blades; the average roughness for the original turbine parts and EP resin models are summarised in Table 4.2. The complete roughness test data are also recorded in Appendix B.1.

Samples	Ave. R_a (μm)	Ave. R_z (μm)
Stator (Original)	2.472	14.722
Stator (EP Resin)	2.005	11.932
Rotor (Original)	2.606	15.195
Rotor (EP Resin)	2.433	15.174

Table 4.2: Wren100 Arithmetic Roughness (Original vs. Rebuild)

After the Wren100 stator and rotor blades were rebuilt with EP resin, laser scanning was used to obtain their geometries. The EinScan Pro 2X Laser Scanner was used to obtain the geometry of the turbine blade, and the operating principles can be summarised as follows [174]. As the device that is used to analyse real-world objects to collect data on its surface geometry, and possibly its colour appearance, a 3D laser scanner uses 'cameras' to capture distance information of different sides of the object. During the scanning process, millions of digital points are generated by the laser scanning software, which is then merged to re-create the geometry. Normally, multiple (in some cases hundreds of) scans would be necessary to obtain the surface details of all sides of the object. The software would create a universal reference system to bring each group of scanned points together to generate the whole model, a process that is generally referred to as registration or alignment [175, 176]. After alignments of multiple scanned data, the three-dimensional description of the turbine parts can then be exported to the STL file, which can be imported into ANSYS SpaceClaim for further RE process. For the RE of the Wren100 turbine, the point clouds of 13 stator vanes and 21 rotor blades were acquired, and each model consists of millions of coordinates. Therefore, to generate 3D solid geometries, the profiles at different radial heights were captured from each stator vane and rotor blade.

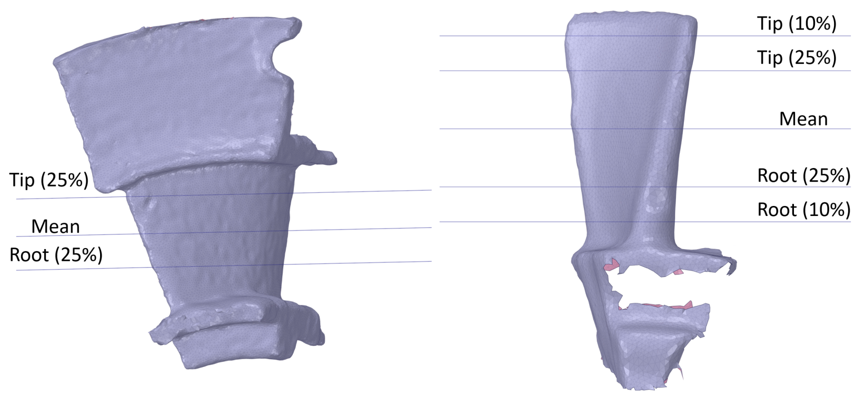

Figure 4.7: Stator & Rotor Profiles Acquisition

As shown in Figure 4.7, three sections of profiles were captured by different planes located at 25% span from the root (Root (25%)), mean and 25% span from the tip (Tip (25%)) for the stator vane. The reason for not capturing the profiles directly from the root and tip sections is the vane profiles at the root and tip sections are blocked by the circular shroud of the stator, meaning the scanned data could be incomplete near the root and tip sections due to the existence of dark corners. As the rotor disk has no shroud, better laser-scanned quality due to no light blockage allowed blade profiles to be captured closer to the root and tip (10% span) compared to the stator vanes (25% span). Then, with the scanned data for the Wren100 stator and rotor blades plotted in the Cartesian system, average profile coordinates were calculated at different radial blade heights. As the turbine blade profile change at different radial heights is normally required to be smooth, linear interpolation was applied to acquire the 2D profiles at the root and tip sections to give a great perspective to understand the original design intent. Finally, to acquire the three-dimensional geometries of the stator and rotor, the last essential step is to select an appropriate reverse-engineering strategy, the details of which are demonstrated in the following subsections.

4.3 Reverse-Engineering (RE) Strategies

Due to the complexity of gas turbine blades, the RE process would require the engineer to select a suitable strategy. The design of a turbine blade normally requires the engineer to handle hundreds of parameters, including chord, stagger, pitch, etc. Thus, the important question in the field of RE is whether to consider all of those parameters or just use some essential characteristics to re-create the model. The RE strategies can often be divided into "what the part really is" (discrete) and "what the part could be" (parametric). In this research, the 3D blade geometries were re-constructed and compared based on discrete and parametric strategies. For the discrete strategy, all the original design parameters were considered for the RE model by applying spline to the average scanned profile coordinates. The parametric strategy used ANSYS BladeGen, which can be used to rebuild the 3D geometry by choosing seven specific parameters of the blade (LE & TE diameters, LE Beta angle, exit angle, blade stagger, LE & TE wedge angle).

4.3.1 Discrete Startegy

The first RE strategy is directly generating splines from the averaged data points to create different layers of profiles, in which the two-dimensional shape information was applied to re-create the three-dimensional reconstruction of one stator vane and one rotor blade in unprecedented detail, as shown in Figure 4.8.

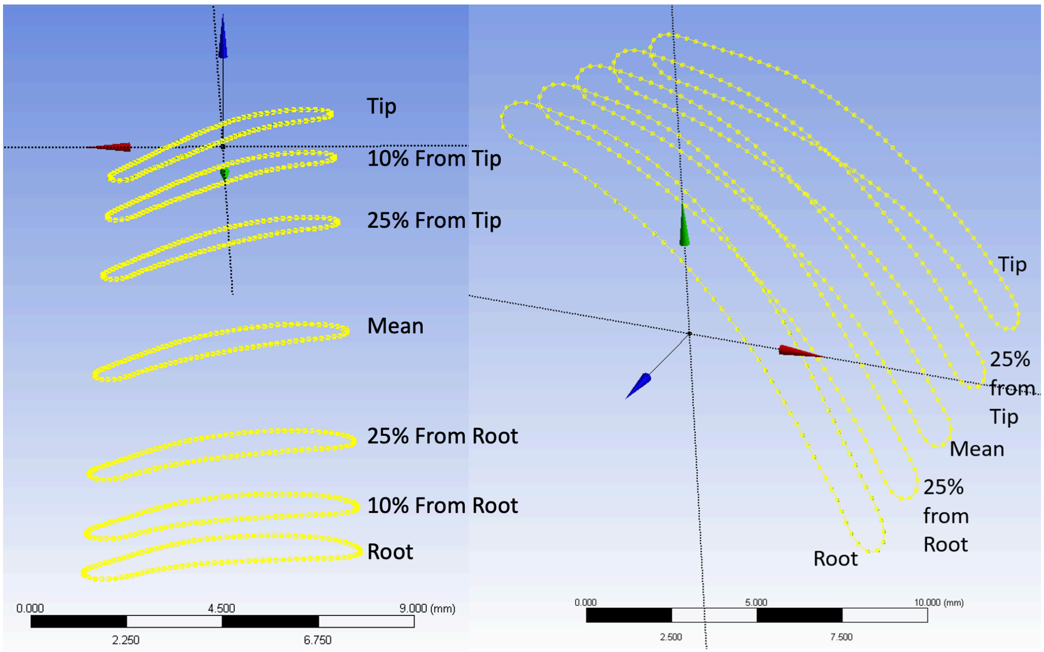

Figure 4.8: Reverse Engineered Wren100 Rotor & Stator (Discrete)

With the profiles at different blade heights, the stator vane and rotor blades were then automatically generated by commercial CAD software such as Solidworks. For the discrete strategy, no blade characteristic was acquired for the models were generated directly from the averaged data coordinates, which potentially adds difficulties to further design modifications.

4.3.2 Parametric Startegy

The second RE strategy used is re-constructing the three-dimensional geometries of the Wren100 turbine based on blade parameters, which can be acquired by finding the base circles for the LE and TE. To locate the base circles, iterations were used by firstly drawing circles based on points 1, 4 and 7 of points of the PS and SS groups. The new circle then shifted one point forward, which fitted accordingly to points 2, 5 and 8. The process was repeated until the circle covered most of the points on one side of the aerofoil. Finally, the smallest circles that are tangent to the PS and SS circles are the base circles. All the iterations were conducted manually without specialised software or scripts.

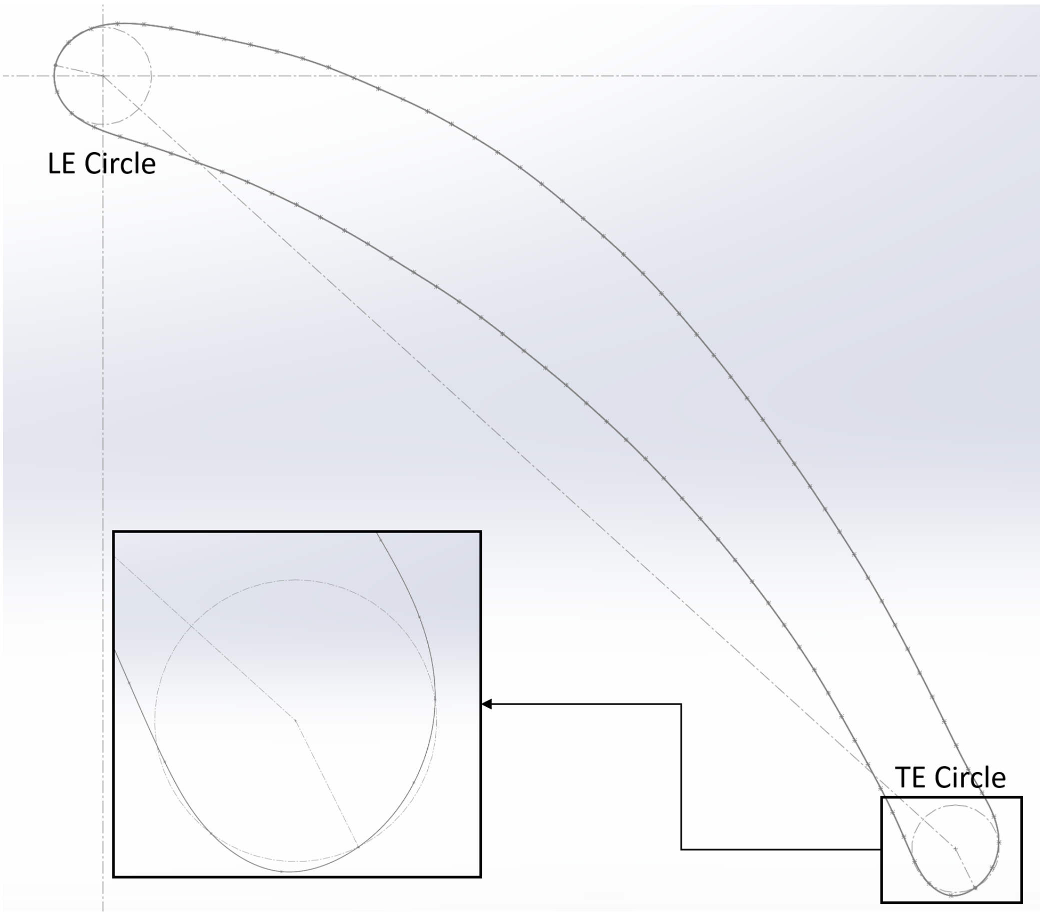

Figure 4.9: Turbine Characteristics Acquisition With LE & TE Base Circles (Sample: Wren100 Stator Vane Mean Span)

During the iterative process, the base circles might not cover all the points due to the rough surface of the laser-scanned model, as shown in Figure 4.9. As the goal was to re-create what the part could be, the blade characteristics acquired from the base circles are still acceptable for further reverse engineering. The Wren100 stator and rotor blade characteristics (Root, Mean and Tip Section of Stator & Rotor) are listed in Table 4.3.

Section	d_{LE}	d_{TE}	β_2/β_3	ξ	θ_{LE}	β_{LE}	θ_{TE}
$Stator_{Root}$	1.4	1.0	59.5	34.5	2.0	15.0	0.0
$Stator_{Mean}$	1.3	1.0	65.0	43.5	9.0	6.0	1.5
$Stator_{Tip}$	1.3	1.2	66.0	49.0	10.50	0.0	2.0
$Rotor_{Root}$	5.6	1.2	45.0	15.0	27.0	27.0	4.5
$Rotor_{Mean}$	1.1	0.9	55.0	37.2	21.0	9.0	3.8
$Rotor_{Tip}$	0.9	0.6	62.0	50.4	15.0	3.0	3.3

Table 4.3: Wren100 Stator & Rotor Blade Characteristics

With the acquired blade characteristics, the three-dimensional geometries of the Wren100 stator and rotor were re-created by using ANSYS BladeGen. Figure 4.10 shows the sample of the Wren100 rotor mean section generated by BladeGen, in which the values of the LE and TE wedge angles were taken from the RE models. However, the LE beta angles were all assumed to be zero for model simplification as they cannot be measured accurately based on the RE models.

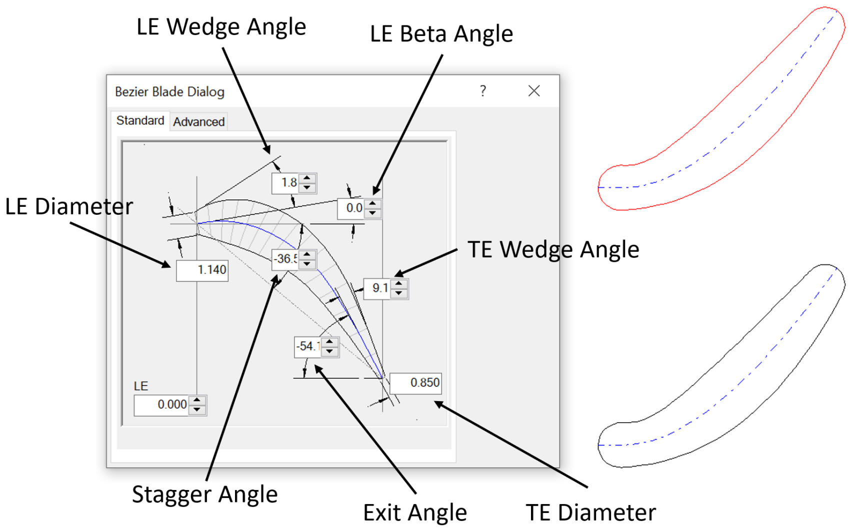

Figure 4.10: Sample of Wren100 Rotor Mean Section Profile (BladeGen)

4.4 Summary

This chapter develops processes for using high-precision laser-scanning equipment for micro gas turbine reverse-engineering (RE) for future CFD model validation via experimental testing and high-fidelity computational simulation. As the Wren100 turbine parts were not received at the beginning of this project due to the impact of COVID-19, a reverse engineering approach was tested based on the Wren44 nozzle guide vanes by direct laser scan. It was found direct scan could not capture all the geometric details. Due to the small blade sizes (blade heights less than 10mm) and high surface reflectance, the laser-scanning equipment could not directly capture enough surface details of the metal Wren100 turbine blades. To solve that problem, a novel method of RE using the silicone mould and resin tooling was developed for better scanning and rebuilding quality. Laser-scanning was used to acquire point clouds of resin turbine parts covered in white paint to reduce surface reflectance. This then allowed the three-dimensional geometry of the stator and rotor to be re-created based on two reverse engineering strategies. These are "what the blade really is" (Point Cloud/Discrete) and "what the blade could be" (Parametric). The latter is based on a reduced number of design parameters obtained from the Point Cloud data, with turbine design software being used to generate the rest of the blade shape. This is termed a Reduced Design Parameter Model, or RDPM.

In Chapter 5, two different RE strategies are compared based on computational simulations and experimental data. The more appropriate RE models of the MGT were also selected for further engine performance analysis and redesign.

Chapter 5

Computational Methods

5.1 Introduction

In this chapter, the process of establishing the appropriate computational model that can be used to accurately predict the flow behaviour inside a micro gas turbine is described. As the parametric study will be carried out based on the computational model, the simulated aerodynamic loss, turbine thrust and mass flow rate at different rotational speeds (RPM) were of particular interest. In addition, to investigate the impact of turbine blade surface roughness, a proper selection of wall functions was also an essential objective.

To achieve the above goals, the approach was to carry out CFD simulations with increasing complexity from two-dimensional to three-dimensional. According to Menter (1994), for CFD simulations by two-equation turbulence models, slight changes (5-10%) in the modelling constants could lead to entirely different results. Thus, testing the model against different types of flows through experimental or DNS data is the only way to establish the validity of CFD results as the modelling of turbulence introduces significant uncertainty. The verification and validation process is generally semi-empirical as it is unclear whether the changes in flow could lead to improvements or deterioration of simulation results, which caused the slow progress in the modelling of turbulence [114]. Therefore, an extensive range of simulation data at different scales of turbomachinery (T106 blade, Wren44 stator vane and Wren100 turbine) were acquired, and the CFD validation process was achieved by comparing the selected RANS and LES models with existing experimental data and the online published Database. As result, the setups for both models are documented as the following items and Table 5.1 to ensure reproducibility and validity of the simulations.

	RANS Setup	LES Setup
Turbulent Model	4-equations $\gamma - \theta$ Model	WALE (Wall-Adapting Local Eddy-Viscosity) Model
Time Integration	Steady-State	Transient Number of Timesteps per Period (Timestep = 3.96823e-07s)
Numerical Order	High Resolution Scheme	Second-Order Backward Euler High Resolution Scheme
Convergence Criteria	RMS $1e-6$	RMS $1e-6$ with Max. Coeff. Loops of 10
Computational Time	$\sim$ 24 hrs	$\sim$ 120 hrs

Table 5.1: CFD Setup Parameters for RANS and LES Models (Wren100 Stator-Rotor)

Wren100 Stator-Rotor Setups (RANS and LES)

- Computational Domain Boundaries: extended around 3 blade heights upstream and downstream from the blade mid-section (31.13mm). The spanwise width was set to original blade height (10.25mm).
- Distance Between Stator and Rotor: 3mm.
- Boundary Conditions: Depend on RPM (Total Pressure & Temperature Inlet; Pressure Outlet)
- Near-Wall Treatment: $y^+ < 1$
- Inlet Turbulence Intensity = 5%

Details for those setups are demonstrated in the following subsections. Cascade tests inside a wind tunnel for the scaled mean section of the Wren100 stator vane were also carried out as a part of the experimental validation. Overall, suitable computational models were developed in this research project and will be carried forward in the analysis of and improvement of the main gas path aerodynamic efficiency of the Wren100 engine in Chapter 6.

5.2 CFD Verification and Validation Overview

The purpose of the following subsections is to find a reliable and accurate computational approach for the MGT stator and rotor system. To determine the accuracy of computational model implementation, verification of the simulation process was conducted by the quantification of round-off error, iterative convergence error and mesh independence study (discretisation error). Validated CFD models have been generated to be used in later chapters to give better insight into MGT flow passage, in which the simulation results showed good matches to the jet engine tests, wind tunnel cascade data and high-fidelity LES results.

The summary of the CFD models and the development process are presented in the following sections to provide foundations for future chapters.

5.2.1 Spatial Discretisation

As illustrated in Subsection 2.6, to capture the simulated flow behaviour with sufficient accuracy, fine mesh would be required within the limits of the available computational resources. In particular, for cases like turbine blades with bounded regions, it is suggested to add mesh refinement near the wall area where there could exist steep flow gradients. In this section, the dimensions of the mesh and the boundary conditions are outlined for the following objects.

- 2D T106 Turbine Blade
- 3D Wren44 MGT Stator
- 3D Wren100 MGT Stator & Rotor System

In this research project, all the CFD simulations were carried out based on the mesh generated by ANSYS workbench mesh or TurboGrid, which both are commercial software that can produce structured and unstructured meshes. To ensure that the meshes created meet the requirements of various turbulence models, guidelines on the first cell heights of wall adjacent cells and cell types are described as follows.

Firstly, to better resolve the flow characteristics, one possible approach is to separate the fluid domain into different areas that can be managed individually. Figure 5.1 shows the mesh blocks generated by TurboGrid, in which finer mesh can be seen near the leading edge and trailing edge where the velocity gradients would be steeper. More advanced blocking procedures can also be done manually by other more specific software such as ICEM.

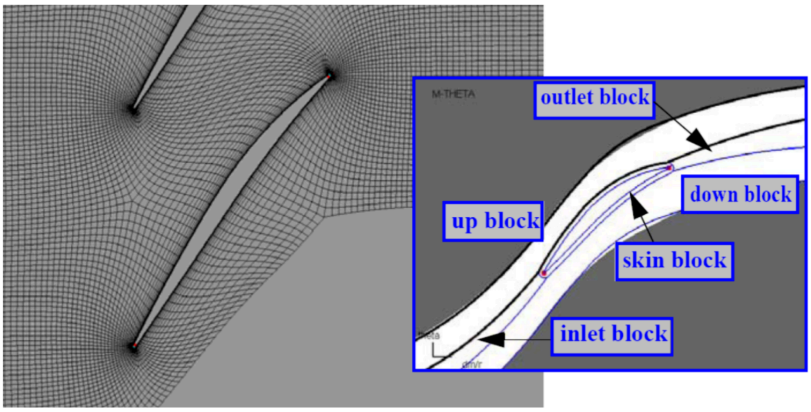

Figure 5.1: Default TurboGrid Mesh Blocking

Secondly, a finer mesh is required near the wall for turbulence models to resolve boundary layers. For the $k - \epsilon$ and $k - \omega$ turbulence models, it is mandatory for y^+ to be smaller than 5.

Finally, for mesh types, structured cells often require less computational memory and are fast to generate compared to unstructured mesh [157, 158]. By reducing the size of grid points in a given region, both meshing methods can generate high-density cells, meaning a higher order of the Taylor series expansion of the differential equations can potentially be achieved. However, the structured mesh is normally difficult to setup for complex objects compared to unstructured mesh. Table 5.2 shows the summary of guidelines for 2D and 3D meshes created for the CFD study in this project.

	Quadrilateral Mesh	Tetrahedral Mesh
Skewness	Max. of 0.8	Max. of 0.8 & Max. average of 0.3
Aspect Ratio	Max. of 50 outside boundary layer	Max. of 7 at the interface between unstructured and structured mesh

Table 5.2: Mesh Criteria Applied for High Quality Grids [159, 160]

As shown in Table 5.2, the skewness and aspect ratio are normally used to specify the mesh quality, which describes how the cell is distorted from the ideal shape. The skewness represents how the cell deviates from a line or plan (2D or 3D), which should not exceed 0.8. The aspect ratio represents the level of stretch of the mesh cell, which the maximum value for different types of mesh is also suggested in Table 5.2 [159, 160].

5.2.2 2D T106 Turbine Blade Mesh

To achieve high accuracy and good control of the mesh spacing, it is recommended to use structured mesh for the 2D T106 blade case. Not many studies have been conducted to compare different mesh types and their characteristics. Yang et al. applied the O-mesh and C-mesh to study the subsonic flow over un-stalled pitching aerofoils, in which the force coefficient results were almost identical [161]. Thus, to ensure high-quality data is generated, the most significant factor is the number of elements and the areas where there are the highest gradients in the flow.

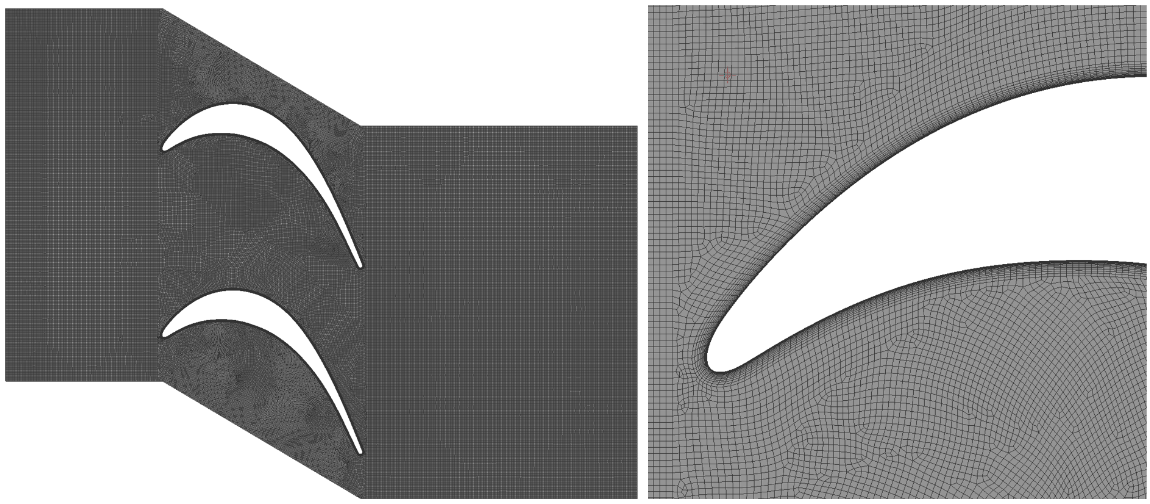

Figure 5.2: T106 Mesh Generation

It can be seen in Figure 5.2 that structured mesh can be automatically generated. To achieve a good mesh refinement at the boundary wall, inflation layers were added to ensure the $y+$ met the requirements of the specific wall functions.

5.2.3 3D Wren44 & Wren100 MGT Mesh

Many previous studies have been carried out with the use of various mesh types to simulate gas turbine blades in the literature. In this study, structured cells were automatically generated by TurboGrid for the Wren44 stator flow passages as shown in Figure 5.3.

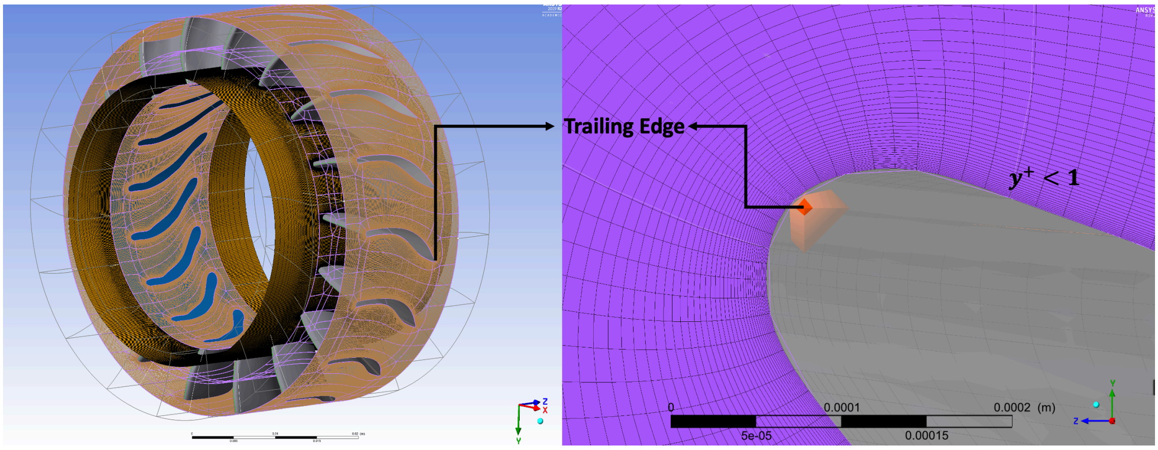

Figure 5.3: Wren44 Mesh Generated by ANSYS TurboGrid ($Re \approx 23,089$, $y^+ < 1$)

Similar to the Wren44 stator vanes, structured meshes were also generated for the Wren100 stator and rotor parts. For the computational domain of the rotor blades, the tip clearance was also included as displayed in Figure 5.4.

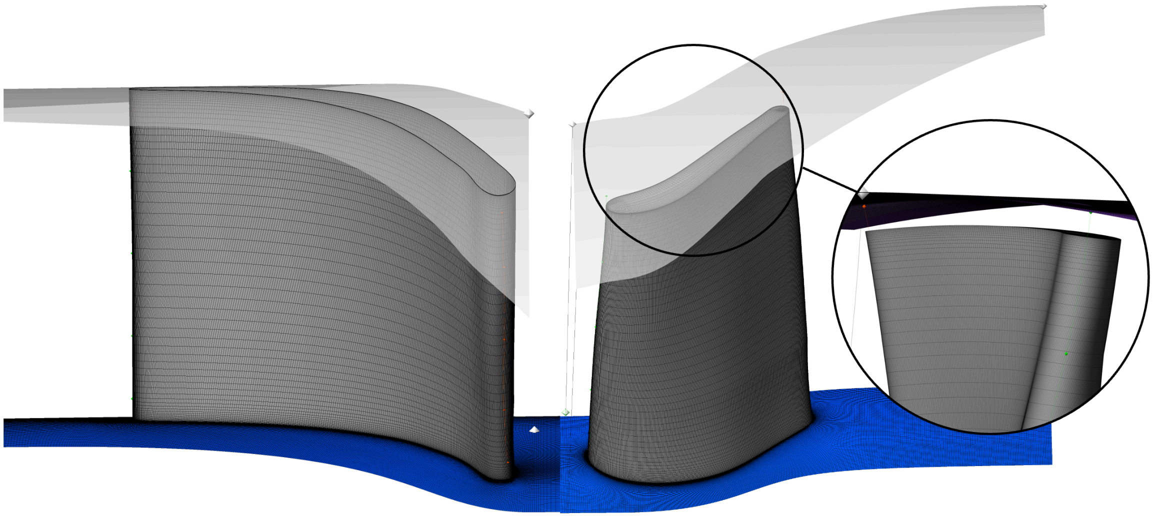

Figure 5.4: Wren100 Mesh Generated by ANSYS TurboGrid ($Re \approx 50,000$, $y^+ < 1$)

As shown in Figure 5.4, constant tip clearance was assumed based on the reverse-engineered blade data.

5.3 2D Blade Simulation Verification and Validation

The purpose of this subsection is to find a reliable and accurate computational approach for a two-dimensional blade profile. To determine the accuracy of computational model implementation, the quality of the CFD model was checked by conducting the quantification of round-off error, iterative convergence error and mesh independence study (discretisation error). To measure the uncertainty of input variables and physical model, the appropriate validation process was conducted based on the T106 cascade, which is the existing data from a European research project for low-pressure turbine profile conducted by Steiger et al [165].

5.3.1 Initial CFD Inputs & Mesh Sensitivity Study

According to the experimental data acquired by Steiger, during the research of low-pressure turbine blade cascades, the two-dimensional schematic diagram of the T106 cascade is shown as Figure 5.5, which the inlet velocity and inflow angle ($tan(\alpha_1)$) were set to be 7.679m/s and 0.773. The default turbulence intensity was set to be 5%.

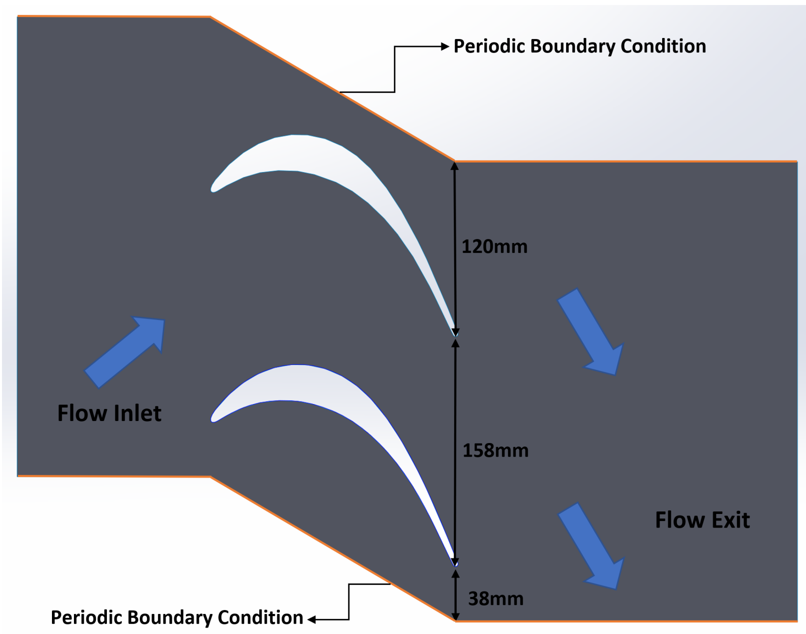

Figure 5.5: T106 Blade Two-Dimensional Cascade Geometry

As the Reynolds Number of the 2D inlet flow was relatively low ($Re = 21,4000$), the boundary layer thickness can be estimated by Blasius approximation shown in Equation 5.1. However, it is essential to note the limitations of this estimation due to the fact it is based on a flat plate calculation.

$$\delta_{bl} \approx \frac{4.91x}{\sqrt{Re_x}} = 2.10mm \tag{5.1}$$

For the wall treatment of the CFD model, an initial guess of the first cell height (y_p) was conducted to make sure the value of y^+ be lower than unit as described in Equation 5.2, 5.3 and 5.4 [103].

$$y_p = \frac{y^+\mu}{\rho u_\tau} = \frac{\mu}{\rho u_\tau} \tag{5.2}$$

$$u_\tau = \sqrt{\frac{\tau_w}{\rho}} = \sqrt{\frac{(1/2\rho U^2)c_f}{\rho}} \tag{5.3}$$

$$c_f = [2log_{10}(Re) - 6.5]^{-2.3} = \frac{\tau_w}{1/2\rho U^2} \tag{5.4}$$

Where the c_f is the skin friction coefficient, which the initial guess of its value was based on empirical results of flow going over a flat plate for the further CFD verification and validation[162, 103].

For the validation data, based on the experimental cascade results (as shown in Figure 5.6) and the loss model summarised by Denton, the average experimental results of stagnation pressure loss coefficient can be calculated by Equation 5.5.

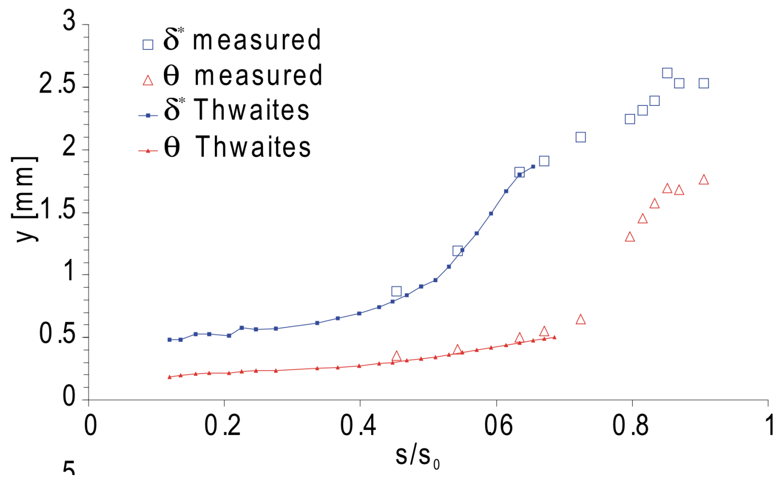

Figure 5.6: Experimental Value of Steady Integral Parameters of T106 Cascade (Re=214,000) [165]

$$Y_p = -\frac{C_{pb}t}{w} + \frac{2\theta}{w} + (\frac{\delta^* + t}{w})^2 = -0.0222152C_{pb} + 0.02428 \tag{5.5}$$

Where the base pressure (C_{pb}) is an empirical value, which, according to Denton (1987), generally ranges from -0.2 to -0.1 [65]. Therefore, the experimental values of the stagnation pressure loss coefficient based on the loss model range from 2.65% to 2.87%.

To acquire high-fidelity numerical results, the process of CFD simulations could be treated as defining boundary conditions and mesh, which the more refined mesh would often lead to solutions with higher accuracy. The objective of the mesh sensitivity study is to find the convergent results with the fewest number of elements possible. Figure 5.7 shows a method to study the convergency for the mesh independence results, in which the resultant goal values (C_p and Y_p) were plotted against the cell count and number of inflation layers.

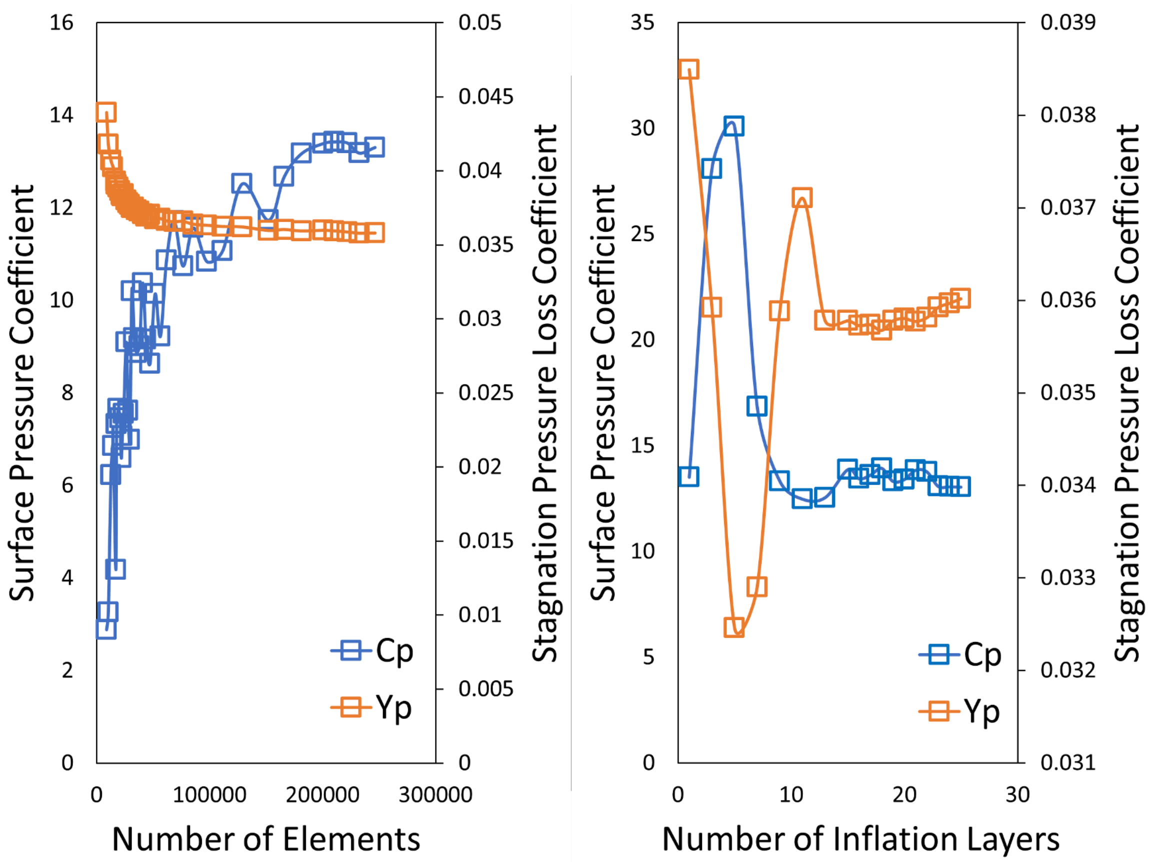

Figure 5.7: Quantification of Discretisation by Studying Impact of Systematic Refinement of Meshes for 2D T106 LP Turbine Blade

5.3.2 CFD Models Study of 2D T106 Blade

After confirming the two-dimensional geometry and initial boundary conditions, several computational fluid dynamics (CFD) simulations were performed at varying levels of machine accuracy, including both single and double precision. Among these, double precision was chosen for further simulations. An overview of the inputs for the CFD verification and validation of the T106 blade is listed as Table 5.3.

Re	Mesh	TU Model	Discretisation Scheme	Y_p (%)
214,000	Structured	$k-\epsilon$, RNG	Second Order	5.14%
214,000	Structured	$k-w$, SST, Low-Re Correlations	Second Order	3.4%
214,000	Structured	$k-w$, SST	Second Order	3.18%
214,000	Structured	$k-w$, Standard, Low-Re Correlations	Second Order	3.24%
214,000	Structured	$k-w$, Standard	Second Order	3.21%
214,000	Structured	4-eq. Transitional SST	Second Order	2.73%

Table 5.3: CFD Inputs and Y_p Output for 2D T106 Blade Simulations

For the CFD information shown in Table 5.3, the residual convergence criteria of all the simulations reached 10^{-12}, and the effect of systematic variation of truncation error, such as the discretisation scheme (first and second-order) was investigated in different groups of simulations. In the 2D T106 simulations, achieving a residual convergence criterion of 10^{-12} significantly surpasses the commonly accepted standard of 10^{-6}, as discussed in the literature review (Chapter 2.6). This exceptional level of precision not only emphasises the accuracy and reliability of the results but also highlights the meticulous approach adopted in the CFD analysis, offering a higher degree of confidence for the verification process. The flow Reynolds number applied in the CFD simulations was 214,000, and the flow inlet incidence was set to zero according to the experimental measurements of cascade tests by Steiger [165]. It is known that the Denton modelled Y_p ranges from 2.65% to 2.87% from the earlier calculations. Thus, the average stagnation pressure loss coefficient is predicted based on the 4-eq. transitional SST model is within the experimental results.

To further analyse the performance of the 4-eq. transitional SST model for 2D low Reynolds number blade applications, the simulation data was compared against the experimental wind tunnel cascade results for the wake capture downstream the T106 trailing edge.

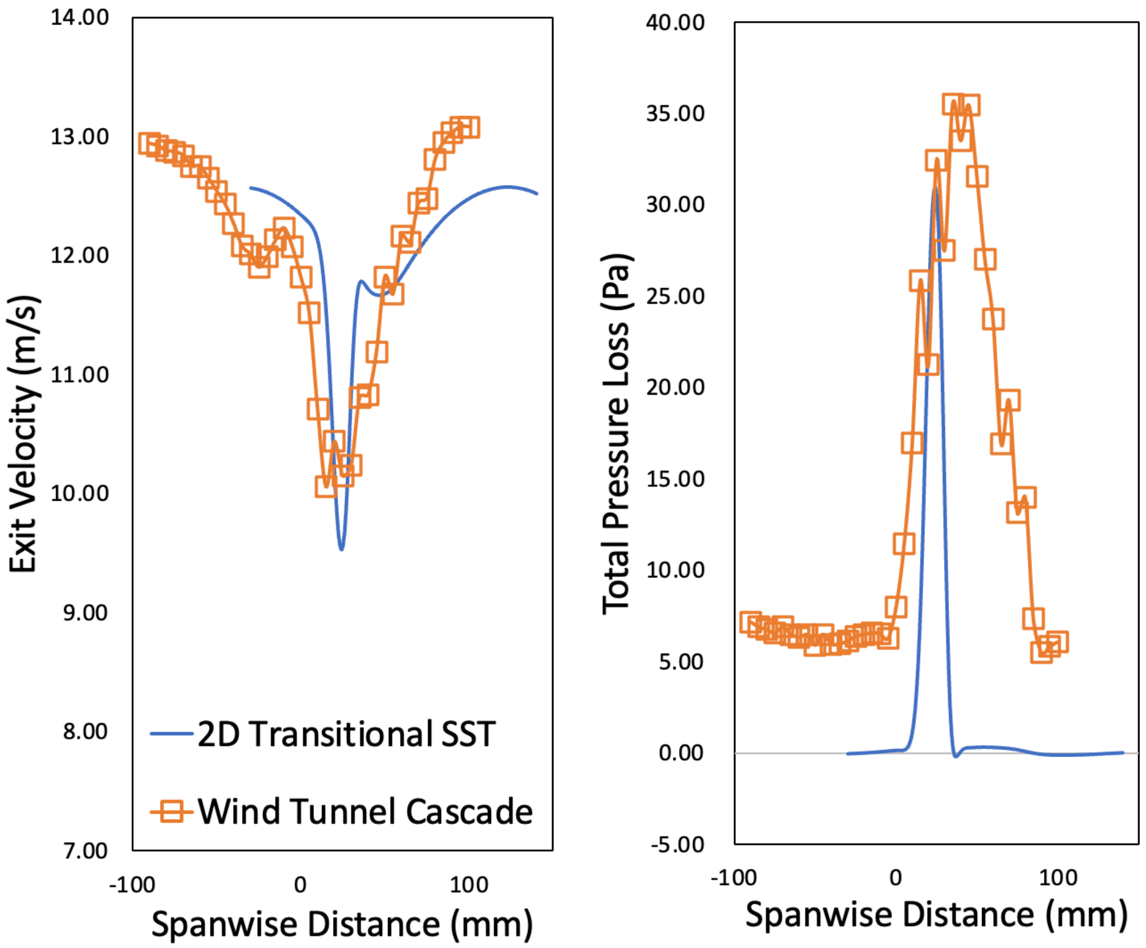

Figure 5.8: 2D Transitional SST Model Vs. Wind Tunnel Cascade (T106, Re=214,000)

As shown in Figure 5.8, the Transitional SST model could capture the location and depth of the T106 blade trailing edge wake with reasonable accuracy. It was observed that the wake predicted by the transitional SST model was slightly wider compared to the experimental data. Furthermore, at the centre of the wake, the peak total pressure loss predicted by the transitional SST model was found to be somewhat higher than the cascade data. This discrepancy between the computational and experimental results could be attributed to the following two main factors.

1. Two-Dimensional Simulation vs Three-Dimensional Experiment: The CFD simulations were conducted based on a 2D model, while the actual T106 cascade is a 3D rig. Therefore, the 2D simulations might not fully capture the three-dimensional phenomena like secondary flows or end-wall effects that can influence the trailing edge wake behaviour. These phenomena are important in turbomachinery cascades, as they can contribute to the widening of the wake and increase in total pressure loss.

2. Wind Tunnel Floor Effects: The positioning of the T106 cascade rig on the floor of the wind tunnel, rather than being elevated, might have contributed to additional flow disturbances. The floor boundary layer could potentially enter the cascade rig and generate additional losses, thereby influencing the wake behaviour. This could explain the higher total pressure loss observed in the computational results compared to the experimental data.

Recommendations: Overall, the 4-eq. transitional SST ($\gamma - \overline{Re_{\theta,t}}$) turbulence model was recommended for 2D blade simulations under low Reynolds numbers as it offers a reasonable degree of accuracy, capturing key aspects of the flow physics with a less complex and computationally intensive setup compared to full 3D simulations or higher-fidelity turbulence models.

5.4 3D MGT Verification and Validation

In this section, the initial verification process is described based on the Wren-44 NGV blade to determine an accurate CFD approach to simulating the operation of micro gas turbines. Due to the geometries of Wren-100 NGV and rotor blades provided by Turbine Solutions Ltd. being unavailable and the impact of the COVID-19 pandemic, the verification process was conducted based on the reverse-engineered Wren-44 NGV blade at the beginning of this research project. The reason for selecting the Wren-44 engine is the Wren-44 engine is produced by the same company (Turbine Solutions Ltd.) as the Wren-100 engine, which has a similar size and geometrical design. Based on the Wren44 stator CFD verification data, the proper verification and validation process for the Wren100 stator-rotor system is also presented in this section.

For the selection of turbulence models, the Large-Eddy Simulation (LES) and the 4-eq. Transitional SST models were chosen as the primary models for the MGT research. As described in the previous chapter, the LES model is a proven method in predicting wall-bounded flows with higher fidelity compared to RANS turbulence models, for it directly resolves large-scale turbulent structure [163]. However, due to the high computational cost of the LES, the 4-eq. Transitional SST model was another suitable candidate for the MGTs aerodynamic study of the relatively low Reynolds number involved in these systems.

In summary, the following subsections provide detailed verification and validation for the CFD models of the Wren100 stator and rotor. A comprehensive examination of the performance of different turbulence models, including the RNG $k-\epsilon$, $k-\omega$, SST and 4-eq. Transitional SST were compared against the high-fidelity LES simulations and experimental data. Furthermore, as two versions of the Wren100 MGT parts were created (discrete and parametric), the recommendations for further development of MGT blade reverse-engineering are also presented based on the comparison between the numerical predictions and experimental results.

5.4.1 High Fidelity LES WALE Simulations

5.4.1.1 Solver Setup & Boundary Conditions

To carry out time-resolved LES simulations for the micro gas turbine system, transient calculations were required to obtain the necessary information for the CFX solver.

Equation 5.6 shows the single sector passage time as the rotor operating at a specific rotational speed (RPM).

$$t_{passage} = \frac{1}{\frac{RPM}{60}} \cdot \frac{1}{N_{rotor}} \tag{5.6}$$

Where the $t_{passage}$ is the time for one sector passage and the N_{rotor} is the number of rotor blades. With the above information, the value of the time step can then be calculated by equation 5.7.

$$t_{step} = \frac{t_{passage}}{N_{TimeStep}} \tag{5.7}$$

Where $N_{TimeStep}$ is the CFX input for the number of time steps, which in this case ranges from 50 to 100. Consider the computational cost; take the 120,000RPM case as an example, the LES configurations are 5 sectors of passage time that were calculated with 60 time steps for each t_{step} due to time limitations for each round of simulation (around 120hrs). The detailed LES transient configurations are listed in Table 5.4.

RPM	$N_{TimeStep}$	$t_{passage}(s)$	$t_{step}(s)$	$t_{total}(s)$
160,000	60	1.79×10^{-5}	2.98×10^{-7}	8.93×10^{-5}
150,000	60	1.90×10^{-5}	3.17×10^{-7}	9.52×10^{-5}
140,000	60	2.04×10^{-5}	3.40×10^{-7}	1.02×10^{-4}
130,000	60	2.20×10^{-5}	3.66×10^{-7}	1.10×10^{-4}
120,000	60	2.38×10^{-5}	3.97×10^{-7}	1.19×10^{-4}
110,000	60	2.60×10^{-5}	4.33×10^{-7}	1.30×10^{-4}
100,000	60	2.86×10^{-5}	4.76×10^{-7}	1.43×10^{-4}

Table 5.4: ANSYS CFX LES Configurations

5.4.1.2 Parallel Implementation

Due to the complex geometries of the reverse-engineered micro gas turbine geometries and the need to resolve small scales, a large number of grid elements are usually required (typically above 10 million). In this study, 60 time steps coupled with 5 periods per run were applied for each run of the LES simulations, meaning it was unfeasible with a single-core processor machine, in which large-scale parallel facilities that could achieve a reasonable turnaround time were required for the calculations. Thus, a high-performance computer with 32 cores, 64 logical processors and 128GB of memory was utilised to perform the simulations.

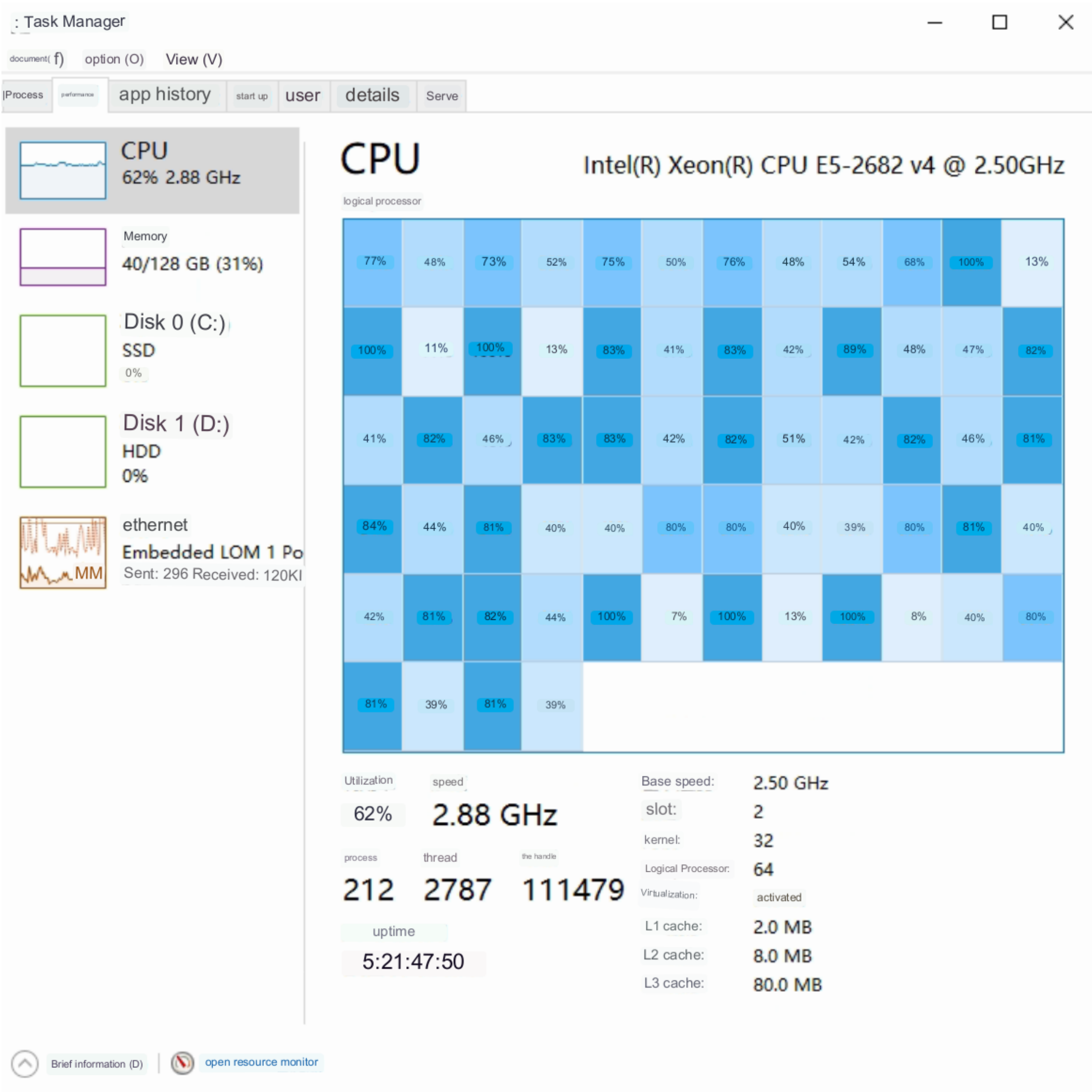

Figure 5.9: High-Performance PC For High Fidelity LES Simulations

As described before, the mesh for the MGTs are structured multi-block CFD codes automatically generated by ANSYS TurboGrid, which are relatively straightforward to implement in parallel solver by the high-performance PC shown in Figure 5.9 using domain decomposition.

5.4.1.3 Phase-Averaged Analysis using LES Simulations

The evaluation of gas turbine performance often requires an analysis of the complex and transient behaviours exhibited by the flow inside the blade passages. However, extracting meaningful insights from these simulations and aerodynamic performance comparisons can be challenging due to their inherently transient nature. A common approach to dealing with this issue is to apply phase-averaging techniques. The phase-averaged method aims to identify and quantify the repeatable and coherent features within the turbine blade passages, filtering out the more random, instantaneous fluctuations. For the MGT simulations applied in this research project, one phase corresponds to the single passage time ($t_{passage}$) of the rotor blade. The instantaneous flow variables at a given location in the MGT are recorded at regular time intervals within a phase and then averaged to obtain the phase-average results [164].

The phase-averaged value $\overline{Q}$ of a quantity Q at phase ϕ can be calculated using Equation 5.8.

$$\overline{Q}(\phi) = \frac{1}{N}\sum_{i=1}^{N} Q(\phi_i) \tag{5.8}$$

Where N is the number of timesteps within the phase, and ϕ_i is the phase at timestep i. In the case of ANSYS CFX simulations, these phase values were manually obtained at different timesteps (e.g., $\phi = 0.1, 0.2, ..., 1.0$), and the phase-averaged quantities calculated as described in Equation 5.8.

This approach has been used extensively in the literature to analyse the transient behaviours in other turbo-machineries. It offers a way to isolate the mean and coherent part of the flow, facilitating the identification and study of the underlying physical mechanisms. However, it is important to note that the quality of the phase-average results is directly dependent on the temporal resolution of the LES simulation. Higher temporal resolutions, such as smaller timesteps, would usually lead to more accurate phase-average results, but at the cost of increased computational resources [164].

5.4.2 Wren44 NGV CFD Verification (RANS)

For the Wren44 stator CFD verification, due to the inability to acquire traditional boundary conditions, theoretical calculations were initially conducted with the reverse-engineered geometry to generate necessary inputs for the CFD simulation. To better simulate the flow transition process on the turbine blade surface, the four-equations transitional SST model was selected for the simulations. To analyse the numerical uncertainties and errors, simulations based on a different solver (ANSYS CFX) and different turbulence models (the $k-\omega$ SST turbulence model) were conducted for the data comparison of the results.

5.4.2.1 Initial CFD Inputs & Mesh Sensitivity Study

Figure 5.10 shows the direct laser-scanned geometry of the Wren-44 engine NGV, which is part of a micro axial gas turbine that contains 17 vanes. The fluid domain and mesh are shown in Figure 5.3 and 5.11, with the inlet and out boundary conditions set one chord length before the leading edge and after the trailing edge.

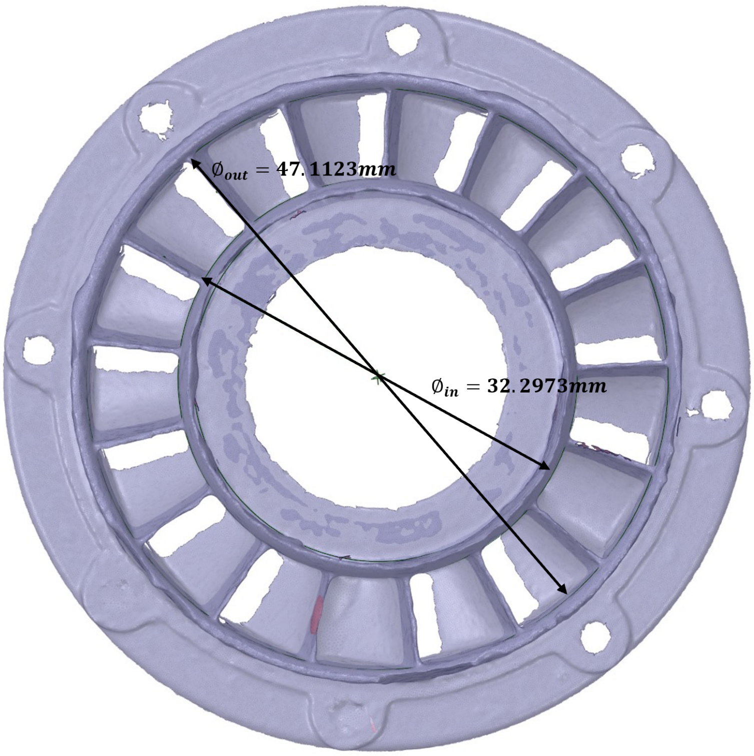

Figure 5.10: Reverse-Engineered Wren-44 NGV (Direct Scanned Geometry)

The CFD verification process was carried out with several initial inputs based on real engine performance data, which included the fuel & air mass flow inlet, inlet temperature, outlet temperature and outlet static pressure. As the values of those variables were unknown before the first CFD simulation, initial boundary conditions were assumed based on the published experimental study carried out by Gronman et al. as listed in Table 5.5 [166].

$q_{m,fuel}$ (kg/s)	$q_{m,air}$ (kg/s)	T_{inlet} (k)	T_{outlet} (k)	P_{outlet} (bar)
0.0012	0.0998	867.95	783.65	1.075

Table 5.5: Wren44 Stator Initial Boundary Conditions

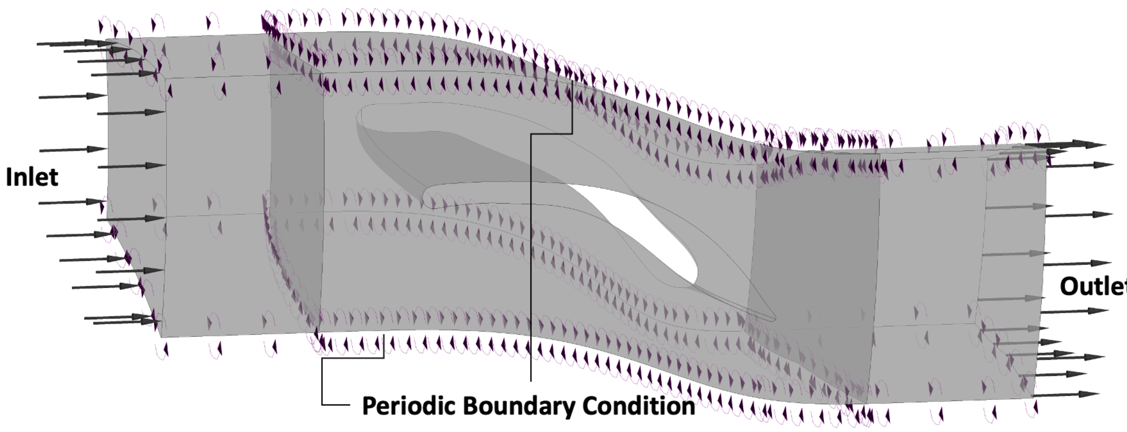

Figure 5.11: Wren44 NGV CFD Fluid Domain

Then, based on the testing data, the required variables for initial inputs of the first CFD simulation are calculated as Equation 5.9, 5.10 and 5.11.

$$A = \frac{\pi}{4}(D_o^2 - D_i^2) = 9.9398 \times 10^{-4} m^2 \tag{5.9}$$

$$v_\infty = \frac{q_{m,fuel} + q_{m,air}}{\rho_{exit} A} = \frac{0.101 kg/s}{0.4781 kg/m^3 \times 9.938 \times 10^{-4} m^2} = 212.571 m/s \tag{5.10}$$

$$Re_x = \frac{v_\infty L_{chord}}{\nu} = \frac{212.571 \times 8.6324 \times 10^{-3}}{7.9475 \times 10^{-5}} \approx 23089 \tag{5.11}$$

With the value of y^+ near the wall assumed to be one and the calculated Reynolds number, the meshing process can be completed by using the ANSYS TurboGrid, which can then be exported to different solvers for further verification and validation.

With the defined boundary conditions, a mesh sensitivity study was conducted for the 3D Wren44 stator vane as plotted in Figure 5.12. The minimum number of elements required for ANSYS CFX and Fluent to achieve the grid independence solution is approximately 2,500,000. It can be found that the change of the stagnation pressure loss coefficient for CFX at a relatively low cell count is much more rapid compared to Fluent. Additionally, CFX predicts slightly higher values of stagnation pressure loss coefficient. A detailed comparison between the two different solvers will be illustrated in the following subsection.

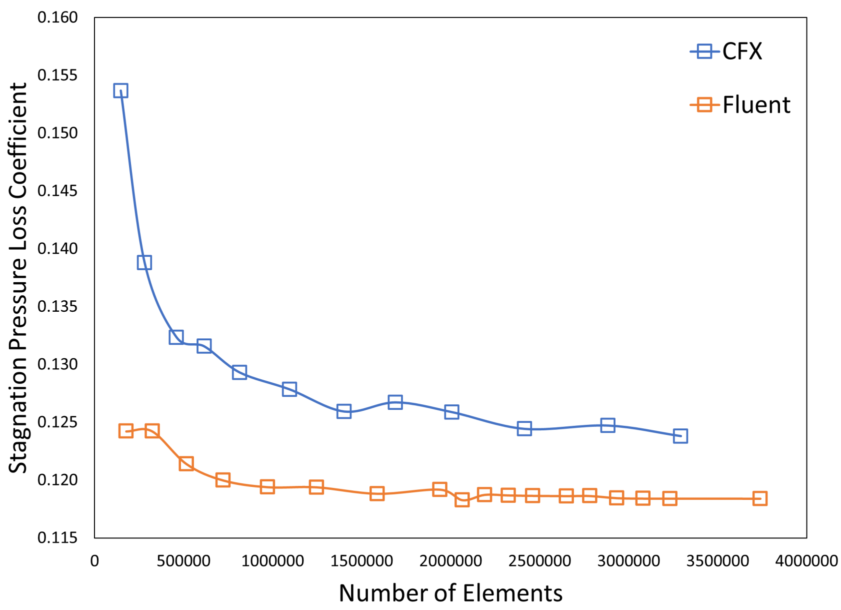

Figure 5.12: Quantification of Discretisation by Studying Impact of Systematic Refinement of Meshes for Wren44 Stator Vane

5.4.2.2 CFD Solver and Turbulence Model Study

In this section, the stagnation pressure loss coefficient, Y_p, as well as blade surface pressure are compared for different solvers and turbulence models. An overview of the inputs for the CFD codes verification of Wren-44 NGV blades with two different solvers is listed as Table 5.6.

Re	**Solver**	**TU Model**	**Residual Convergence Criteria**	Y_p (%)	Required Iterations
23,089	ANSYS CFX	Transitional SST (4 eq.)	10^{-6}	12.28%	150-200
23,089	ANSYS Fluent	Transitional SST (4 eq.)	10^{-4}	11.84%	300-400

Table 5.6: Initial CFD Solutions For Two Solvers

It can be seen from Table 5.6 that the CFX could reach lower residual convergence criteria much quicker with the same mesh compared to Fluent. The reason for that would be those two solvers are based on different discretisation schemes. For the Fluent, the number of control volumes and the number of cell centroids (elements) are considered as the same value. For the CFX, the number of control volumes considered in the calculations is more significant as each element is divided into sub-volumes that are assembled with nodes (cell vertex). The flux through each elemental face is calculated based on all the nodal values instead of just cell centroids [169]. Thorat and Mangate conducted a numerical analysis to evaluate the performance of ANSYS CFX and Fluent in predicting the flow characteristics within turbine compressor blades. Their investigation revealed that Fluent exhibited higher sensitivity to mesh refinement and yielded marginally superior accuracy when utilising a larger number of computational cells during the simulation. However, ANSYS CFX was found to have almost the same accuracy compared to the Fluent as long as the number of elements is below a certain threshold (mesh independence) [170]. Thus, due to the high complexity of the micro turbine blades, ANSYS CFX will be used as the default solver for lower requirements of computational power.

Compared to normal full-size gas turbines, micro gas turbines generally operate under relatively low Reynolds numbers; thus, flow transition was presumed to occur inside the passage of the NGV blades. Several pieces of research can be used to prove the above assumption. Verstraete et al. studied and improved KJ-66 MGT, which flow separation and transition due to low Reynolds number were disclosed by their analysis to be the cause of low efficiency [167, 168]. In addition, as experimental validation is not available for the Wren-44 engine, many factors that could affect the flow behaviour are unknown in this problem. Thus, to select the most appropriate turbulence model, four different turbulence models were applied to compare the performance of predicting the flow within the Wren44 stator vanes. The turbulence models comprised of the $k-\omega$ SST, RNG $k-\epsilon$, SST and four-equations transitional SST model. In addition, large-eddy simulations employing the WALE turbulence model were also conducted for data comparison.

To investigate the abilities of different turbulence models in predicting wakes and flow mixing, by monitoring a line that is located 10% chord distance after the trailing edge, the total pressure distributions are plotted as Figure 5.13.
In Figure 5.13, wake profiles can be observed as the flow leaves the trailing edge, and different turbulence models have similar predictions of wake locations. It can be observed that the transitional turbulence model predicts noticeably lower total pressure loss. The values of total pressure outside the TE wake predicted by $k-\omega$, SST and

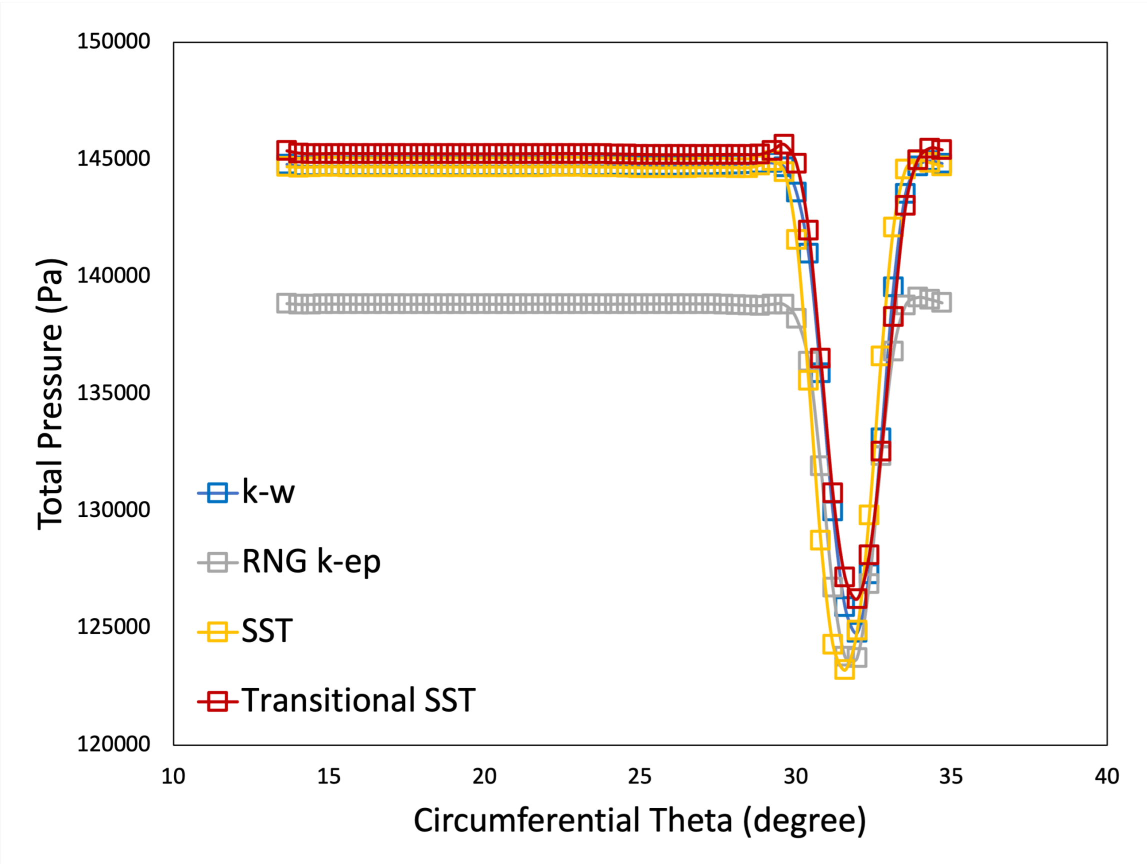

Figure 5.13: Monitored Total Pressure on a Line 10% Chord After Wren-44 NGV TE (Number of Elements $\approx 3,000,000$; $Re = 23089$)

transitional SST model are almost the same. However, with the same boundary conditions, the RNG $k - \epsilon$ predicts much lower values of total pressure after the Wren44 stator trailing edge.

To better visualise the flow separation on the blade suction side, the predicted values of static pressure over the NGV blade surface for different turbulence models are plotted as shown in Figure 5.14.

With regards to different solvers and turbulence models, it can be seen from Figure 5.14 that the results generated with $k - \omega$, SST, 4eq. Transitional SST and LES by ANSYS CFX give quite similar results. Similar to Figure 5.13, the surface pressure predicted by the RNG $k - \epsilon$ failed to match with the LES data. What can be clearly seen in Figure 5.14 is the LES and the transitional models show a sudden decrement of surface pressure on the vane suction side near the trailing edge. This could be

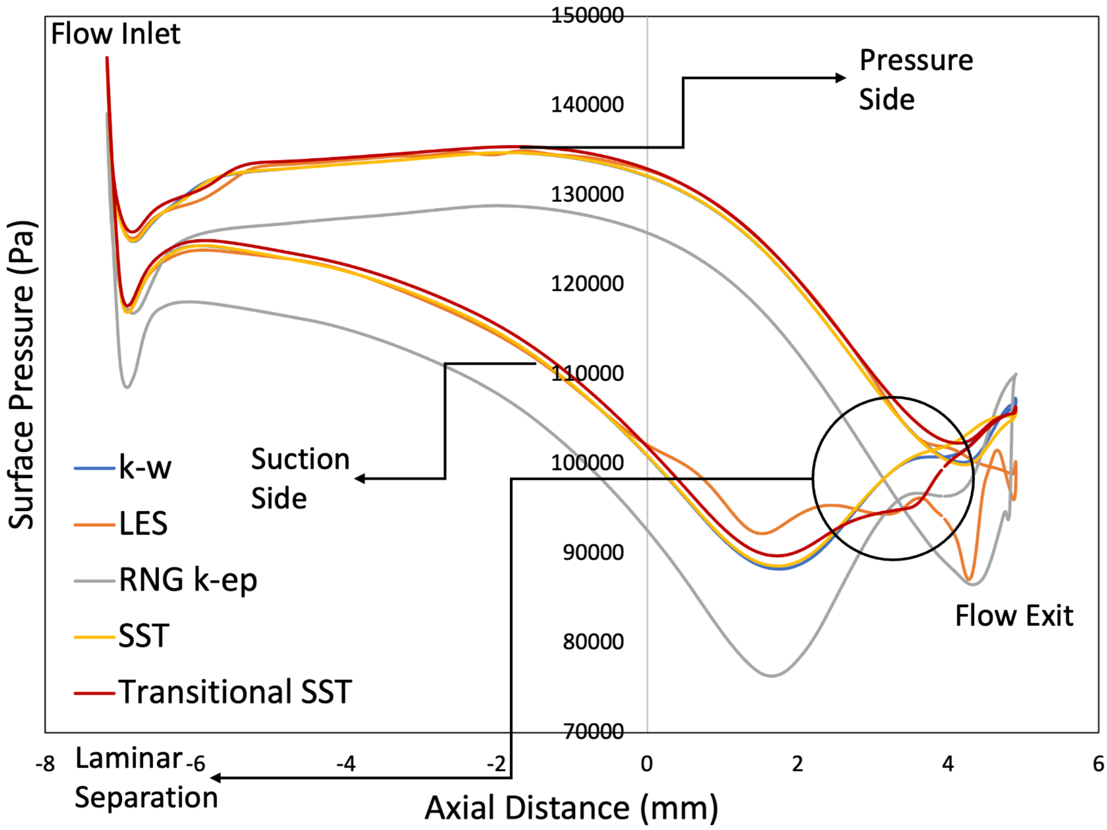

Figure 5.14: Wren44 Stator Surface Pressure Distribution Predicted by Different Turbulence Models (Number of Elements $\approx 3,000,000$; $Re \approx 23089$)

attributed to several potential reasons, including laminar separation, vortex shedding and flow transitioning behaviour. Nonetheless, it was found this flow phenomena could not be captured by the applied fully turbulence models.

To sum up, based on the verification for the Wren44 stator, the four-equation transitional SST turbulence model was suggested for further simulations of the Wren100 stator-rotor system as it was considered by the author to be able to predict the flow transition and laminar separation behaviours much more accurately than other fully turbulence models. Although it could not predict the flow behaviour inside the MGT blade passage with as much detail as the transient LES model, the transitional model could predict the closest overall blade performance with much lower requirements for computational power. As an initial recommendation for MGT blades, further model checking and validations are also described in the following sections based on the Wren100 models and wind tunnel data.

5.4.3 Wren100 CFD Verification and Validation

5.4.3.1 Initial CFD Inputs & Mesh Sensitivity Study

As described in the previous chapter, two reverse-engineered 3D CAD models of the Wren100 stator and rotor were generated based on different strategies, which are the discrete and parametric models. Based on the verified CFD model from the Wren44 NGV case, it was suggested that the 4-eq. transitional turbulence model should also be used for the Wren100 blades for the similar Reynolds number of two turbines. To ensure the accuracy of the CFD model for the Wren100 turbine, proper validation data were acquired from the direct engine tests at 120,000RPM and wind tunnel cascade experiments. The most optimal CFD model that could represent the real MGT aerodynamic performance was selected for further research on the impact of different blade characteristics.

Figure 5.15 displays the fluid domain for the single-stage Wren100 MGT system, which consists of 13 vanes and 21 blades as listed in Table 5.7. To make sure the pitch ratio is close to one, multiple domains of stator and rotor were modelled with periodic boundary conditions. The ratio between the sector angles of the stator and rotor (P_S/P_R) was set to be around 0.97. Similar to the Wren44, the inlet boundary is located one vane chord length upstream stator leading edge, while the outlet boundary is positioned one blade chord length downstream rotor trailing edge.

	Stator	Rotor
Total No. of Blades	13	21
Sector Angle (deg)	83.08	85.71

Table 5.7: Wren100 Single Stage Stator-Rotor System

As shown in Figure 5.15, the mix-plane method is used to handle the interaction between the stator and rotor with RANS steady-state simulations. This approach places a virtual interface between these sections, where flow variables are averaged, simplifying the simulation by reducing computational demands and improving stability without tracking the exact angular position of each blade.

In accordance with the experimental data for jet engines presented in Table 5.8, a meticulous study of mesh sensitivity was conducted for the Wren100 Stator-Rotor system, utilising the transitional turbulence model. This decision was based on the fact that the Wren100 and Wren44 possess similar geometry and Reynolds numbers.

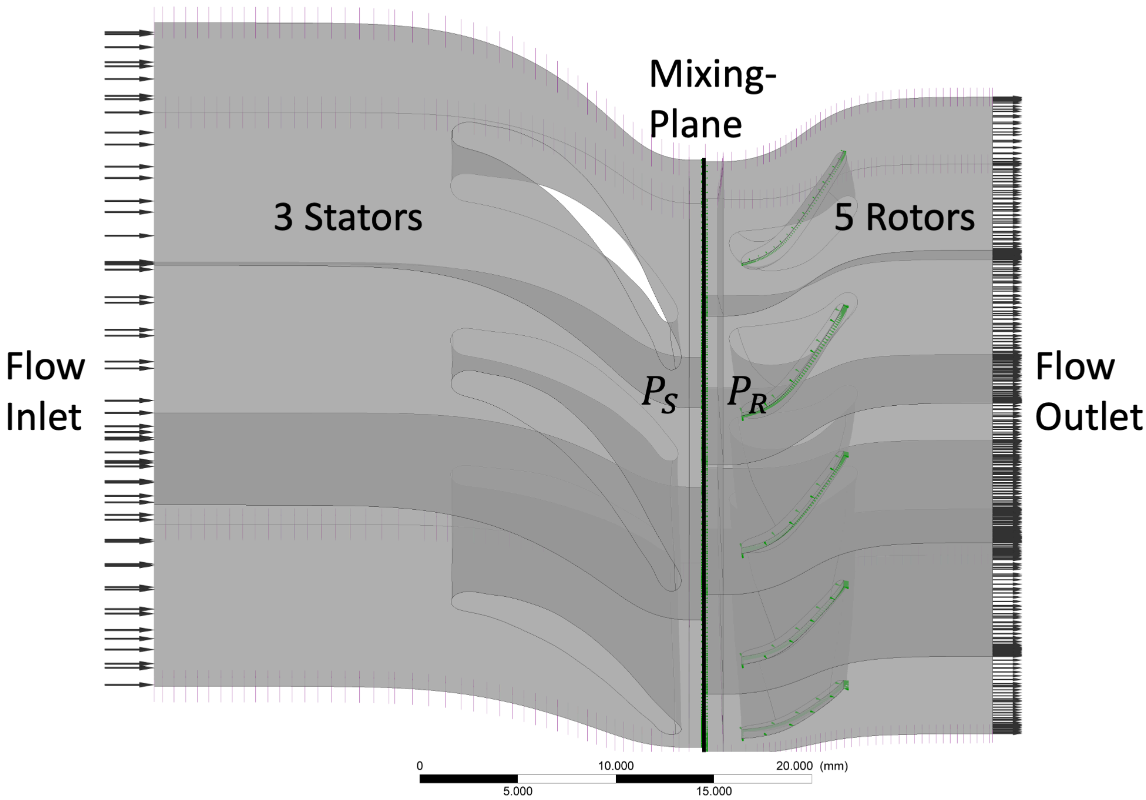

Figure 5.15: Wren100 Stator-Rotor Fluid Domain With Periodic Boundary Conditions

The initial inputs were based on real engine performance data at 120,000RPM as listed in Table 5.8, which the detailed experimental procedure is demonstrated in the next chapter.

T_{01} (K)	P_{01} (bar)	P_2 (bar)	RPM
807.3	1.4772	0.8005	120,000

Table 5.8: Wren100 Initial CFD Inputs Based on Direct Engine Tests at 120,000RPM

With the initial CFD inputs, a mesh sensitivity study was carried out based on the grids generated by ANSYS TurboGrid described in Section 5.2.3, which the value of y^+ was automatically controlled below one. In this case, the variables monitored are the stagnation pressure loss coefficient for the stator and the isentropic efficiency for the rotor.

As shown in Figure 5.16, for the Wren100 MGT single-stage stator-rotor system, the number of elements for ANSYS CFX to achieve mesh independence requires at least

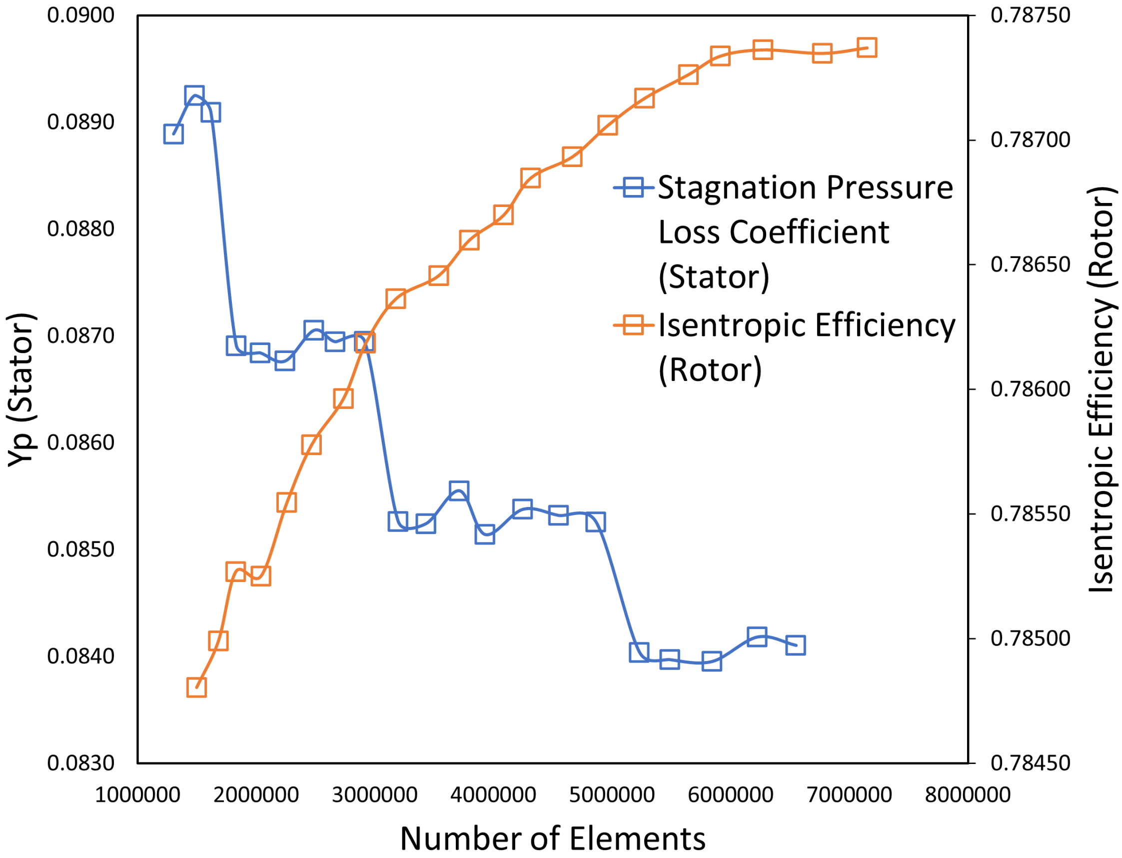

Figure 5.16: Quantification of Discretisation by Studying Impact of Systematic Refinement of Meshes for Wren100 Stator & Rotor System ($y^+ < 1$)

5,300,000 for the stator vane and 6,000,000 for the rotor blade. Thus, a total number of 11,300,000 mesh elements will be used for further CFD simulations.

5.4.3.2 Performance of Different Turbulence Models For Flow Prediction Within A Single Stage MGT

Similar to the Wren44 stator verification process, the performance of different turbulence models in predicting 3D flows inside the Wren100 turbine was also studied. By placing a line 10% chord after the Wren100 stator middle span trailing edge, the values of the exit velocity and total pressure are plotted in Figure 5.17.

It can be seen in Figure 5.17 that the different turbulence models based on RANS simulations predict similar results. However, compared to the phase-averaged LES results, the exit velocities predicted by all the RANS simulations are approximately 19.93% higher despite similar spanwise trends. The general trend of the blade performance is the trailing edge mix-out loss would be larger. In addition, the not flat

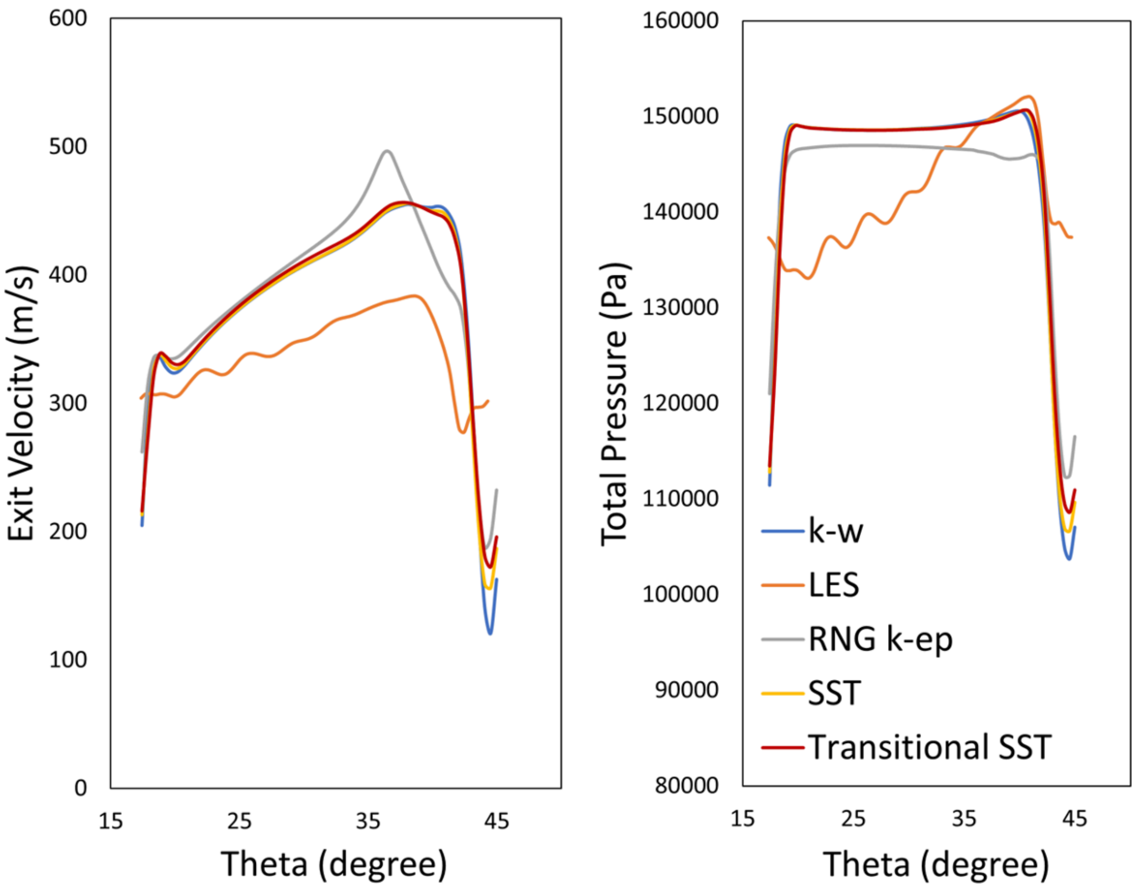

Figure 5.17: Monitored Variables on a Line 10% Chord After Wren100 NGV Mid Span TE (Steady-State vs. Phase-Averaged Transient LES) (Number of Elements $\approx 12,000,000$)

total pressure plot after the mean span trailing edge predicted by the LES model shows that the high unsteadiness between the blades, which the other three turbulence models predicted higher recovery rates outside the vane trailing edge wakes.

The poor rendition of the flow prediction by different turbulence models is also presented in Figure 5.18. It can be seen that although the angle maximum near the main passage regions is well predicted for the $k-\omega$, SST and transitional SST model, the flow behaviours near the trailing edge wake were calculated quite differently compared to the LES model. The instantaneous snapshot from an LES simulation shows the flow field at one specific moment in time, capturing a large range of unsteady, turbulent structures downstream of the MGT stator vane that are not resolved in RANS simulations.

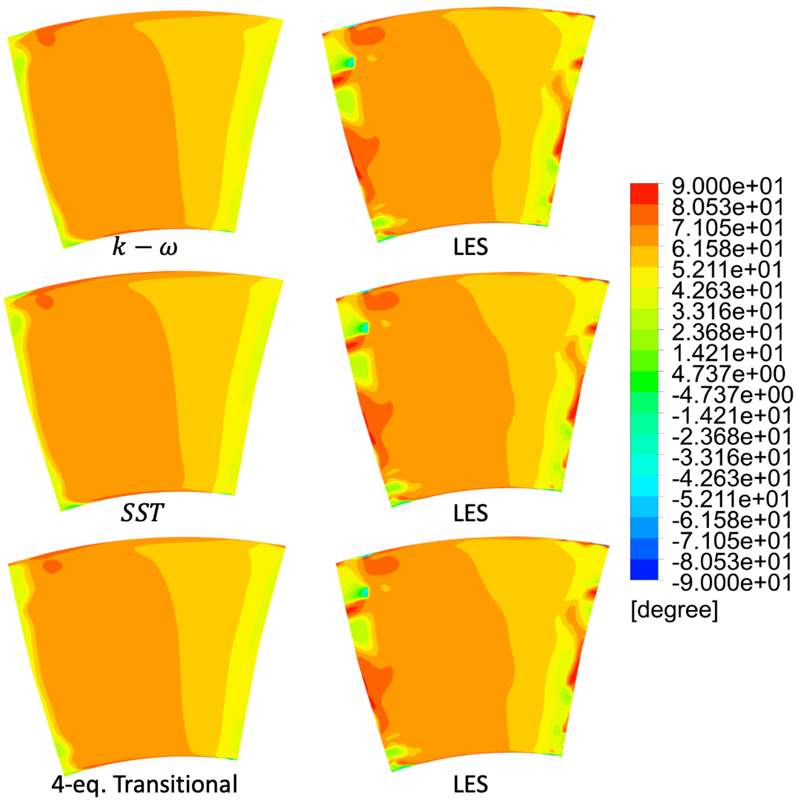

Figure 5.18: Exit Angles Plot 10% After The Stator Trailing Edge (Steady-State vs. Transient LES Instantaneous (t=0.00004762s))

The overall stagnation pressure loss coefficients calculated by different turbulence models are presented in Table 5.9, which indicates that the RNG $k - \epsilon$ should be discarded for it predicts a completely different value of Y_p compared to the LES model.

TU Model	$k - \omega$	RNG $k - \epsilon$	SST	4eq. Transitional SST	LES
Y_p **(Stator)**	3.37%	12.49%	3.74%	3.91%	3.34%

Table 5.9: Mass-Averaged of Y_p For Different Turbulence Models (Wren100 Stator)

To further compare different turbulence models and come up with the final decision, the values of surface pressure predicted are also plotted in Figure 5.19.
The observation of pressure distribution along the stator vane pressure side reveals a noteworthy consistency between the LES data and predictions made by the entire suite of turbulence models, as depicted in Figure 5.19. Nevertheless, a discrepancy emerges in the context of flow transition behaviour on the suction side, wherein the

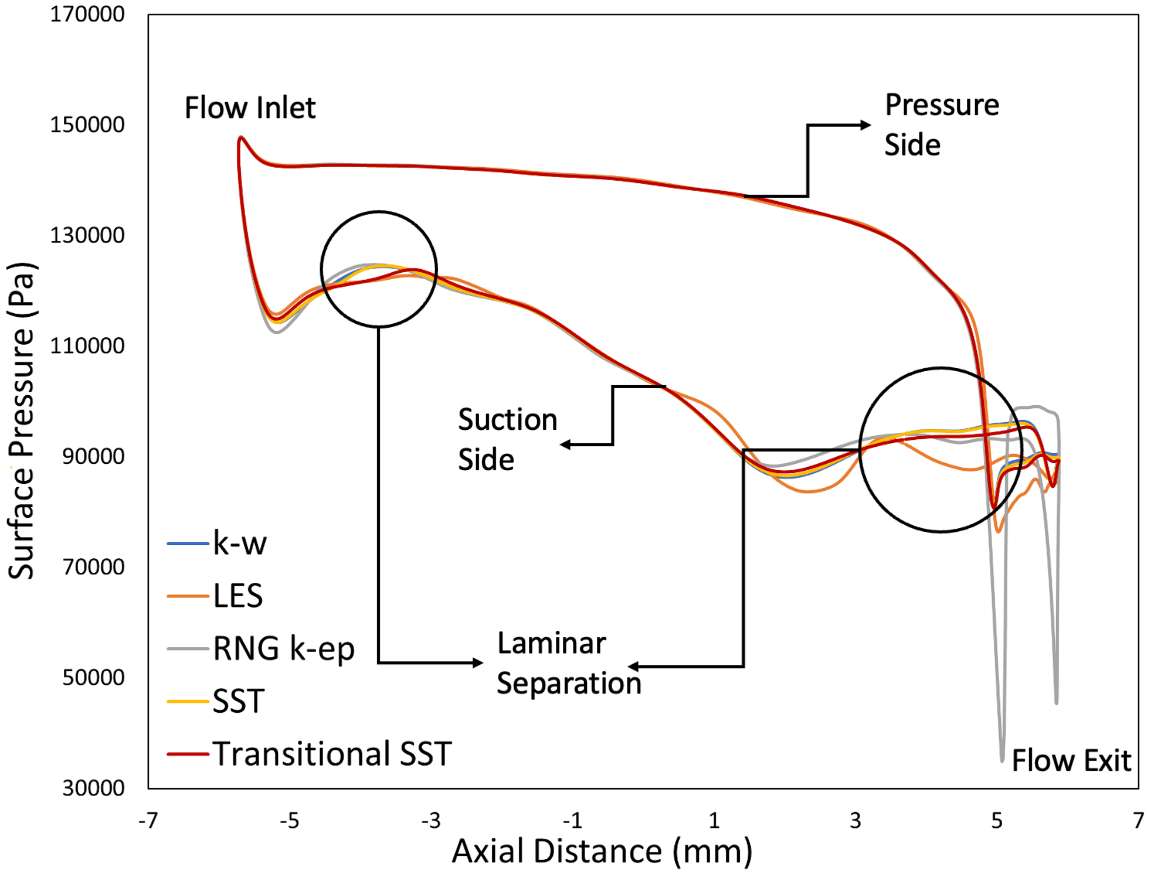

Figure 5.19: Wren100 Stator Surface Pressure Distribution Predicted by Different Turbulence Models and LES (Number of Elements $\approx 12,000,000$)

fully turbulent models, encompassing the $k-\omega$, RNG $k-\epsilon$, and SST models, demonstrate suboptimal prediction accuracy compared to the 4-eq. Transitional SST model.

Upon a comprehensive evaluation of the employed RANS turbulence models, it was discerned that the 4-eq. Transitional SST model exhibited the best balance of accuracy (with the data available). This remained true despite the limited ability of the models to compute the intricate flow dynamics occurring within the wakes trailing the edges. Nevertheless, the model proved sufficient for providing accurate predictions of the overall aerodynamic performance of the MGT blades.

Despite these findings, it is crucial to acknowledge the inherent uncertainties within the LES WALE model. To further substantiate the veracity of these models and to ensure the robustness of the findings, additional validations were conducted. These validations are premised upon wind tunnel cascade tests, the detailed methodology and results of which are elaborated upon in the following subsection.

5.4.3.3 Transitional SST Model Validation Based on Wren100 Stator Mid Span Wind Tunnel Cascade Experiments

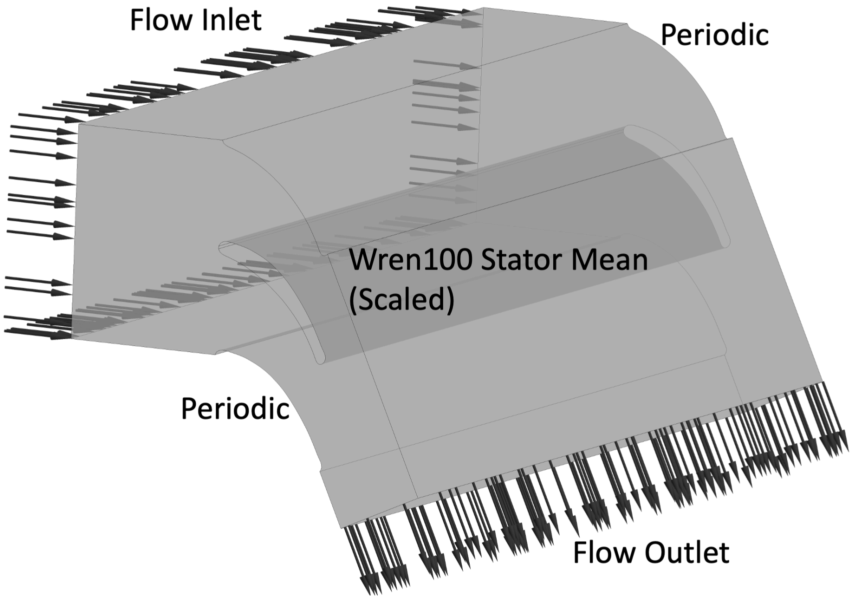

Figure 5.20: Scaled Wren100 Stator Mean Cascade Fluid Domain

To further evaluate the accuracy and reliability of the 4-eq. Transitional SST model, it was compared to experimental data obtained from a wind tunnel cascade. The wind tunnel cascade was simulated using the same turbulence model and matched Reynolds numbers, which the fluid domain of the cascade is displayed in Figure 5.20. Compared to the original MGT stator vane, the cascade only tests the mean profile, which makes the geometry much less complicated for the turbulence model to predict. A comparison of the results was conducted for Reynolds numbers of around 39,576 and 43,973. The data provided include the exit velocity and total pressure loss for different spanwise locations 10% downstream of the blade profile.

The experimental CFD results, including the exit flow velocity and any relevant flow visualisation data, are presented and discussed in the following. These findings provide valuable insights into the aerodynamic behaviour of the Wren100 stator vane and serve as a basis for comparison with the loss predictions obtained from the mean line performance analysis. By validating the reverse-engineered model through experimental testing, a more robust understanding of the Wren100 micro gas turbine performance can be achieved, informing future design optimisations and performance improvements. Figure 5.21 and 5.22 show the graphical representations of the comparison, where the CFD results are plotted against the cascade results under two different Reynolds numbers. The plots demonstrate a strong correlation between the two datasets, further validating the CFD model.

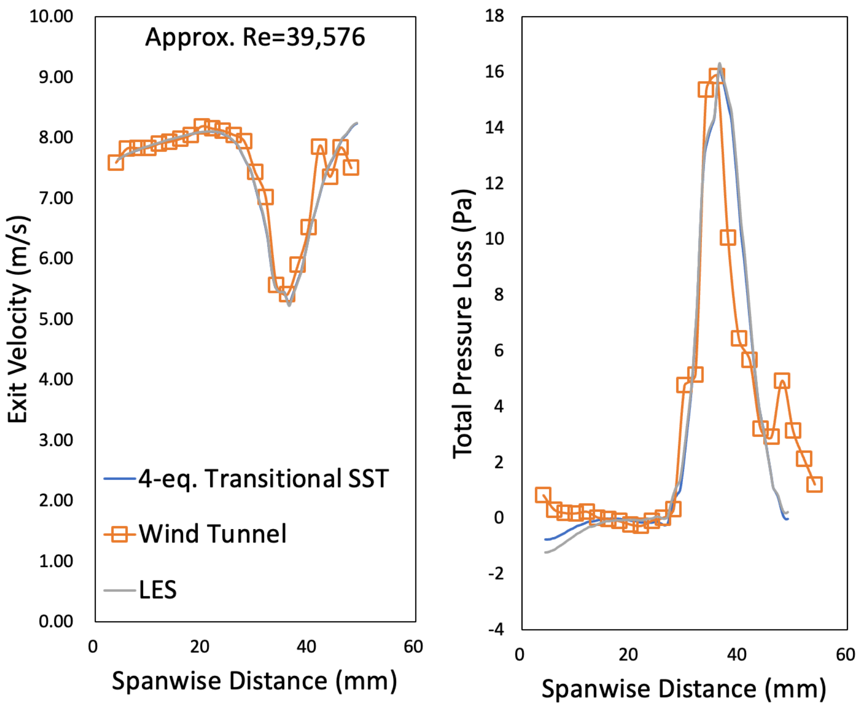

Figure 5.21: Wren100 Stator Mean Profile Exit Velocity and Total Pressure Loss (CFD Vs. Wind Tunnel Cascade) (Re= 39,576)

Upon examination of Figures 5.21 and 5.22, the projected flow patterns 10% chord downstream the trailing edge, as postulated by the 4-equation Transitional SST and the LES WALE models, exhibit notable concordance. A comparison of both CFD models with wind tunnel cascade data reveals a consistent trend. This remarkable agreement between the LES and the 4-equation Transitional SST model contrasts with the performance comparison outlined in previous sections and can be attributed to several potential factors. Firstly, compared to the original blade shape, the geometry of the wind tunnel cascade is much simpler, which can be treated as a two-dimensional problem. This reduced complexity may contribute to the closer alignment between the transitional SST model and the LES WALE model. Secondly, the monitored line is at a 10% chord distance away from the wall region. The 4-equation Transitional SST model is well-known for its ability to accurately capture flow behaviour outside

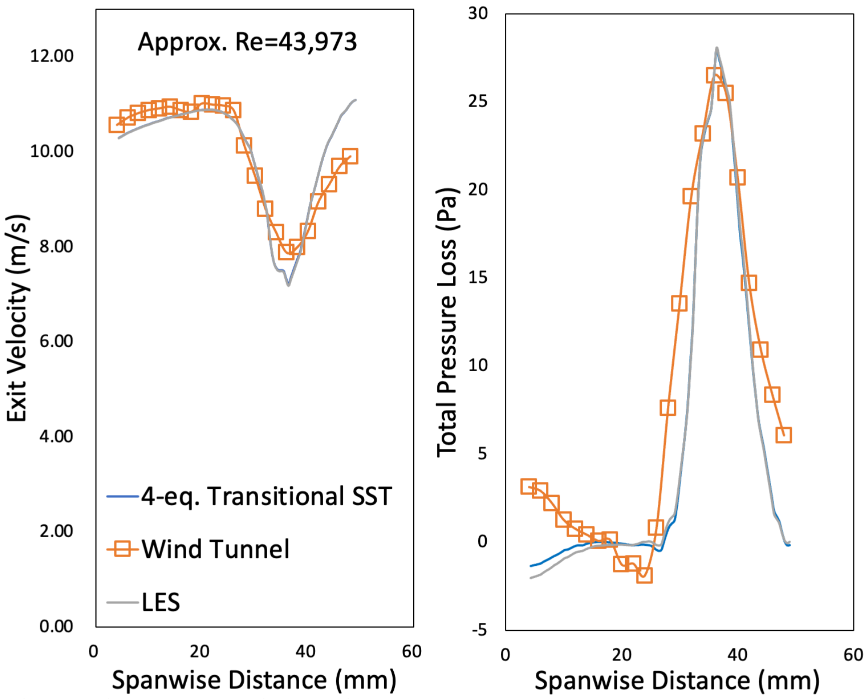

Figure 5.22: Wren100 Stator Mean Profile Exit Velocity and Total Pressure Loss (CFD Vs. Wind Tunnel Cascade) (Re= 43,973)

the near-wall regions. This characteristic may explain the good performance exhibited by the 4-equation Transitional SST model in resolving the overall turbine stage flow behaviour.

To sum up, the 4-eq. Transitional SST model demonstrates adequate accuracy and reliability when compared to experimental data from the wind tunnel cascade. The consistency in trends across different Reynolds numbers, despite minor discrepancies in exit velocity values, confirms that the Transitional SST model is a valid tool for predicting the flow behaviour in such systems. Future studies may seek to optimise the CFD model to further improve its accuracy and applicability to a broader range of flow conditions.

5.4.4 RE Geometries Validation: Discrete Vs. Parametric

5.4.4.1 Normal Engine Operating Conditions

To begin the validation for the CFD models with different reverse-engineered geometrical structures, the time-averaged experimental data and the phase-averaged CFD predictions of the Wren100 engine thrust from 100,000RPM to 150,000 RPM were plotted together as shown in Figure 5.23. For the engine experimental measurements, the accuracy of the thrust sensor and the rotational speeds are approximately $\pm 4.45N$ and $\pm$ 100RPM according to specifications from the manufacturers.

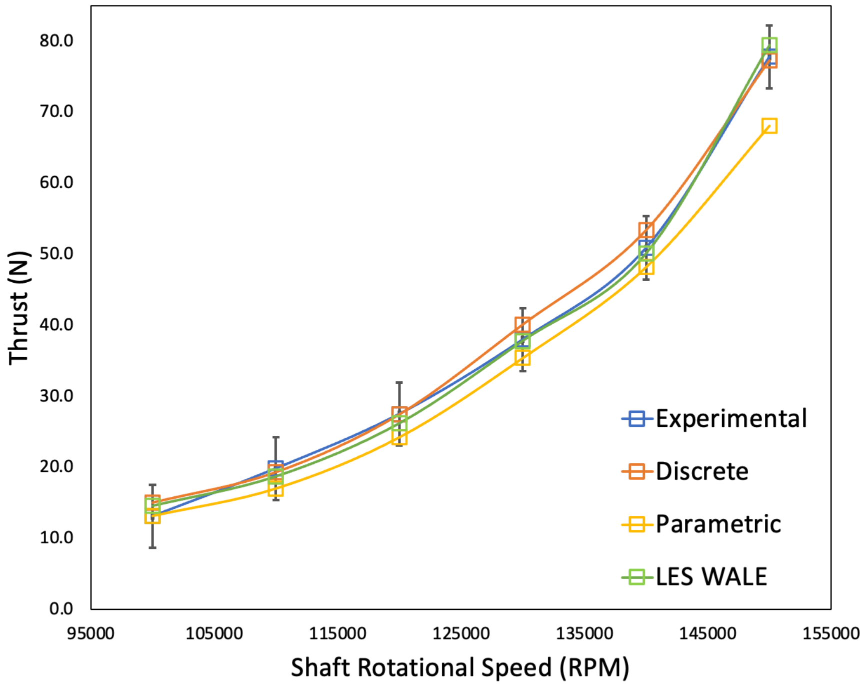

Figure 5.23: Wren100 Turbine Thrust at Different RPMs (Experimental vs. 4-eq. Transitional SST)

It can be seen from Figure 5.23 that both RE models could predict the thrust generated by the Wren100 engine with adequate accuracy when the rotational speeds are below 140,000RPM (within the experimental error span). From 100,000RPM to 150,000RPM, the discrete model predicted very close results compared to the experimental data. However, for the parametric model, as the RPM increases to 150,000RPM, the rise of thrust predicted is not as rapid as the real performance of the MGT. This could be caused by the differences in the 3D reverse-engineered models. Despite the differences, the parametric model can still predict the correct trend of the engine thrust with adequate accuracy.

5.4.4.2 Interpolation Results for Peak RPMs

Owing to the absence of boundary condition data pertinent to the peak operating speed of 160,000 RPM, a methodology leveraging linear interpolation was employed. This interpolation was based on available data corresponding to lower rotational speeds as well as externally sourced data published by Golchin et al. [142]. The Python script utilised to implement this interpolation is comprehensively outlined within Appendix B.2.

Subsequent to the interpolation process, iterative CFD analyses were performed, using the 4-eq. Transitional SST model. This allowed the estimation of boundary conditions corresponding to the MGT operating at the peak RPM of 160,000. Upon obtaining these estimates, the LES WALE model was employed to ascertain the computational performance of the Wren100 stator-rotor system operating at this 160,000 RPM speed. The resulting performance metrics are encapsulated in Table 5.10.

Model	P_2 (bar)	P_{02} (bar)	$\dot{m}$ (kg/s)	F (N)	RPM
CFD	0.587	1.459	0.180	132.8	160,000
Interpolated	0.660	1.328	0.181	103.4	160,000

Table 5.10: Wren100 Turbine Peak Performance (Discrete)

From the data compiled in Table 5.10, a substantial discrepancy can be noted between the thrust predicted by the current CFD model at peak RPM and the actual engine performance under corresponding operating conditions. A probable explanation for this discrepancy is the non-availability of precise boundary conditions derived from experimental engine tests. The boundary conditions applied in this study were extrapolated via an iterative methodology, relying on the 4-eq. Transitional SST model. As the rotational speed escalates, the suitability of persistently utilising transitional turbulence models may diminish, given that significant portions of the flow within the MGT passages might already transition to fully turbulent. This suggests that at 160,000 RPM, the Reynolds number reaches a critical value, prompting a shift to a fully turbulent flow. However, to substantiate this hypothesis, additional investigations with proper boundary conditions should be initiated in the future when the Wren100 engine is available for experimental tests.

5.4.4.3 RE Models Performance at Normal Operating Conditions

To better visualise the difference between the discrete and the parametric reverse-engineered models at normal operating conditions, the velocity and pressure distribution within the Wren100 mean blade passages when operating at 120,000RPM are plotted as shown in Figure 5.24.

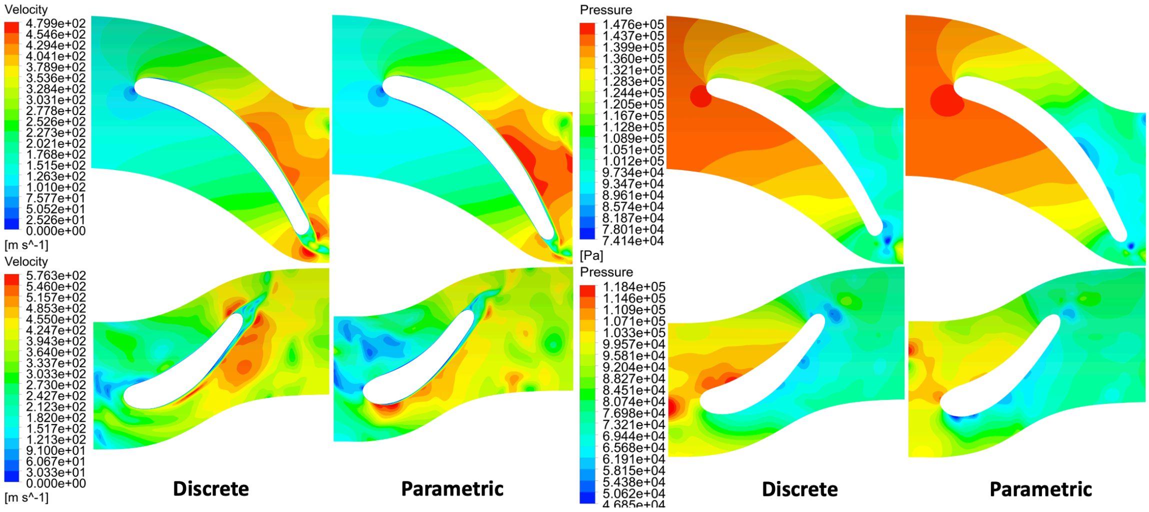

Figure 5.24: Discrete vs. Parametric: Comparison of Velocity & Pressure Contour Plots (120,000RPM, t=0.00004726s)

Upon examination of Figure 5.24, it can be observed that the two RE models of the MGT stator exhibit parallel trends in their velocity and pressure distributions. However, the flow fields surrounding the discrete and parametric rotor blades demonstrate remarkedly different characteristics, especially in the proximity of the blade surface. A potential explanation for this divergence may be conceptualised as follows. The generation of the discrete models was carried out by taking into account digital points dispersed around varying blade sectional surfaces, thus including certain aspects of surface roughness or unevenness in the resultant model. Conversely, the parametric models were created using a handful of parametric variables, leading to the creation of a notably smoother surface, a consequence attributable to the inherent nature of the BladeGen algorithm. The aforementioned minor disparity on the blade surface, compounded by the smaller chord length and the transient nature of the aerodynamics of the rotor blades, culminates in a distinct difference in the flow fields within the rotor blade passages between the discrete and parametric models.

In summary, when the MGT is functioning at comparatively high rotational speeds, the thrust estimations deduced from the discrete models exhibit greater proximity to the experimental data than their parametric model counterparts. The divergence between the two rotor RE models can be attributed to the parametric models consideration of a mere seven-blade characteristics (refer to Table 4.3). This limited scope may preclude a comprehensive representation of actual turbine blades, as it is possible that additional blade parameters have been unavailable in the BladeGen software.

Consequently, it is reasonable to anticipate that the discrete models would more accurately depict the actual MGT components, owing to their consideration of the entire MGT blade characteristics. However, even with a consideration of only seven-blade characteristics, the turbine performance predicted by the parametric models remains within the error span of the sensor at rotational speeds lower than 140kRPM. This is notable in its demonstration of the resilience of these models in spite of limited data inputs. Moreover, the parametric model mirrors the thrust trend predicted by the discrete model and possesses the added advantage of ease of modification. Hence, parametric models hold their own as effective approximations of actual MGT components and serve as valuable tools for subsequent blade optimisation. These findings underscore the potential of parametric models in accurately predicting turbine performance while offering a more streamlined approach for further refinements

5.5 Summary

In the present chapter, an extensive array of low Reynolds number gas turbine blade geometries, encompassing the T106 blade, the Wren44 stator, and the Wren100 stator-rotor system, have been scrutinised. The objective of this critical review was to adopt appropriate simulation parameters and establish a robust foundation for conducting detailed verification and validation studies. This rigorous approach is designed to engender high-fidelity Micro Gas Turbine (MGT) simulations, which are proficient in accurately simulating the operation process of a single-stage MGT. This work represents a vital step in advancing the current understanding and simulation capabilities within this pivotal area of energy engineering.

An incremental, bottom-up approach has been judiciously employed in this study, whereby the complexity of the simulations was systematically enhanced, starting from static two-dimensional T106 aerofoil simulations and culminating in the transient simulation of a rotating single-stage Micro Gas Turbine (MGT). Different turbulent models, along with experimental jet engine tests and wind tunnel cascade tests were compared based on RANS and high-fidelity LES simulations. Subsequently, a concise synthesis of the outcomes derived from these multifaceted studies is presented.

5.5.1 Final Remarks of CFD Models

In conclusion, the performance of different turbulence models in predicting the flow behaviours within the Wren44 and Wren100 turbine blades was investigated as part of the 3D CFD verification process, by simulating the initial engine data. The RNG $k-\epsilon$ turbulence model was deemed unsuitable due to its production of unphysical results. Conversely, the $k-\omega$, SST, and transitional SST models exhibited good performance in calculating the overall performance of the MGT blades, including the stagnation pressure loss coefficient and pressure distribution on the stator vane pressure side. However, due to the relatively low Reynolds numbers, the fully turbulence models were unable to predict the flow transition behaviour on the stator vane suction side as well as the LES and transitional SST model.

Thus, taking into account computational cost, the LES WALE and the RANS 4-eq. transitional turbulence models were ultimately selected for further simulations in the analysis and redesign of the Wren100 blades at normal operating conditions below 150,000RPM. The LES WALE was initially employed to evaluate the aerodynamic performance, potential sources of loss, and the impact of surface roughness on the original MGT stator vanes and rotor blades. During the redesign phase, the 4-eq. Transitional SST model was utilised to rapidly visualise the performance changes due to the requirements for swift adjustments of different blade characteristics. Upon finalising the redesign recommendations, the LES WALE model was also applied to provide a detailed visualisation of how the parameter changes affected the flow field within the MGT blade passages.

5.5.2 Reverse-Engineering Strategies Selection

In this chapter, the validation of two reverse-engineering (RE) MGT models based on discrete and parametric strategies was demonstrated. It was found both the discrete and parametric models could accurately represent the MGT performance at normal operating speeds from 100,000RPM to 140,000rpm, despite a limited set of blade parameters input requirements for the parametric model. At near peak operating speeds, the discrete model could predict closer engine performance compared to the experimental tests.

According to the results, the study concludes that the engineer should focus on 'what the part should be' (parametric) for MGT redesign. The reasons are listed as follows.

Parametric Model Advantages

- Limited blade parameters required;

- Rapid blade parameter adjustments can be achieved.

However, if the engineer aims to obtain the most accurate MGT performance predictions, focusing on 'what the part really is' would be a better solution, as all the blade characteristics the RE equipment could capture would be included in the digital 3D models. This approach necessarily requires the use of mould and resin tooling techniques, which also adds time and cost to the MGT RE process.

Discrete Model Advantages

- Higher accuracy can be achieved for detailed performance analysis.

Overall, both RE models in this study show the poor aerodynamic performance of the Wren100 MGT. Therefore, in the following chapters, the investigation of how the different low Reynolds numbers affect the Wren100 MGT blade aerodynamic losses will be conducted. At the same time, According to the Wren100 turbine base performance acquired from this research, further investigation of the impact of surface roughness and Wren100 MGT blade profile redesign with the latest CFD tools will also be discussed to improve the aerodynamic performance.

Chapter 6

Aerodynamic Performance Evaluation of the Wren100 Stator and Rotor

6.1 Introduction

This chapter focuses on the aerodynamic performance evaluation and redesign of the Wren100 stator and rotor, a single-stage micro gas turbine. Based on current knowledge, achieving optimal performance in such a small-scale turbine is a challenging task, as it is highly sensitive to design changes and operational parameters. This study aims to provide a comprehensive understanding of the aerodynamic behaviour of the Wren100 turbine stator and rotor and offer insights into potential improvements in terms of thrust and efficiency.

Firstly, mean line performance prediction techniques were utilised to roughly estimate the various types of losses present in the turbine, including profile loss, secondary loss, and trailing edge loss. These predictions allowed for a better understanding of the overall performance of the Wren100 micro gas turbine and served as the foundation for further analysis. Cascade tests were conducted on a scaled mean section of the Wren100 stator vane to acquire the profile loss coefficient. This experimental approach provided valuable data on the aerodynamic performance of the original stator vane design and its impact on the overall efficiency of the turbine.

Next, the CFD simulation data of the aerodynamic performance of the Wren100 stator and rotor are presented and discussed. Based on the numerical data, the impact of surface roughness and potential performance bottlenecks of the micro gas turbine blades are analysed for further redesign.

Building upon the findings from the mean line performance predictions and cascade tests, a parametric study was carried out to investigate the effects of design changes on the aerodynamic performance of the Wren100 turbine stator and rotor. Several key parameters, including blade angles, chord length, and blade profile, were systematically varied to determine their influence on the turbine's thrust and efficiency.

The results of this study contribute to the growing body of knowledge on the aerodynamic performance of micro gas turbines and offer practical guidance for the design and optimisation of the Wren100 micro stator and rotor. By identifying potential areas for improvement and exploring the effects of various design changes, this research aims to enhance the performance of the Wren100 micro gas turbine and facilitate its wider adoption in a range of applications.

6.2 Comprehensive Analysis of the Wren100 Stator Vane Aerodynamic Performance

6.2.1 One Dimensional Mean Line Performance Prediction

The reverse-engineering process of the Wren100 micro gas turbine stator and rotor geometries provided a foundation for assessing the aerodynamic performance of the turbine. One of the essential steps in evaluating the aerodynamic performance of the turbine is to predict the losses associated with various sources, such as profile loss, secondary loss, and trailing edge loss. An effective way to estimate these losses is to utilise mean line performance prediction techniques based on established loss models. In this study, three useful loss models, including A&M (Ainley and Mathieson), D&C (Dunham and Came), and K&O (Kacker and Okapuu), were employed to predict the losses in the Wren100 micro gas turbine. These models were selected because of their ability to accurately estimate the different types of losses in the turbine, providing valuable insights into the overall performance of the Wren100 stator and rotor. The mean line performance prediction calculations required specific turbine blade parameters, which were obtained from the reverse-engineered geometries of the Wren100 stator and rotor. These parameters include blade chord length, pitch-to-chord ratio, stagger angle, and other essential blade geometry details. Table 6.1 and 6.2 present the required turbine blade parameters used in the mean line performance prediction calculations. By employing the A&M, D&C, and K&O loss models and utilising the turbine blade parameters derived from the reverse-engineered geometries, a comprehensive understanding of the Wren100 micro gas turbine's aerodynamic performance was obtained. This understanding served as a basis for further analysis and optimisation efforts to improve the turbine's thrust and efficiency.

6.2.1.1 Required Geometrical Dimensions

Parameter	**Number**	**Unit**
Inner Annulus Diameter (I.O.)	17.45	mm
Outer Annulus Diameter (O.O.)	27.70	mm
Reference Diameter	20.50	mm
Annulus Diameter	82.52	mm^2

Table 6.1: Wren100 Annulus Dimensions

Parameter	**Number**	**Unit**
Inlet Blade Angle (β_1)	0	$^\circ$
Blade Chord (c)	15.73	mm
Blade Pitch (s)	10.91	mm
Pitch/Chord (s/c)	0.69	
Blade Opening (o)	4.59	mm
Value of e	9.84	mm
s/e	1.11	
t/c	0.064	
o/s	0.421	
$cos^{-1}(o/s)$	65.12	$^\circ$
Tip Clearance (k)	0	mm
Annulus Height (h)	10.25	mm
Throat Area (A_t)	46.38	mm^2

Table 6.2: Details of Wren100 Nozzle Guide Vane (NGV)

6.2.1.2 Loss Calculations

The mean line performance analysis of the Wren100 micro gas turbine nozzle guide vane (NGV) using the A&M (Ainley and Mathieson), D&C (Dunham and Came), and K&O (Kacker and Okapuu) loss models are displayed in Table 6.3. The analysis considers different Reynolds numbers to investigate the effect of varying flow conditions on the profile loss, secondary loss, and total loss. The discrepancies between the loss predictions of different models are discussed, highlighting the importance of considering multiple models when assessing the overall performance of the Wren100 micro gas turbine. Additionally, the profile loss results obtained from the cascade tests are compared to the predictions from the mean line models. The results provide crucial insights into the overall performance of the Wren100 micro gas turbine and help identify areas for potential improvement.

Loss Model	**Profile Loss Y_p**	**Secondary Loss Y_s**	**Total Loss Y_t**	**Reynolds Number**
A&M	0.030	0.030	0.087	49,885
A&M	0.030	0.032	0.089	43,973
A&M	0.030	0.032	0.090	39,576
D&C	0.190	0.224	0.734	49,885
D&C	0.275	0.224	0.885	43,973
D&C	0.352	0.224	1.022	39,576
K&O	0.108	0.247	0.411	49,885
K&O	0.157	0.247	0.498	43,973
K&O	0.202	0.249	0.583	39,576
Cascade	0.073	-	-	43,973
Cascade	0.171	-	-	39,576

Table 6.3: Wren100 NGV Mean Line Predicted Loss

As evident from Table 6.3, the A&M loss model predicts relatively consistent loss values across different Reynolds numbers, with a slight increase in secondary and total loss as the Reynolds number decreases. The D&C loss model, on the other hand, predicts a more significant increase in profile loss and total loss with decreasing Reynolds number. Notably, the D&C model estimates a total loss greater than one at the lowest Reynolds number, which is unrealistic and suggests potential limitations in the applicability of the loss model to this specific case. The K&O loss model predicts an increase in profile and total loss with decreasing Reynolds number, similar to the D&C model, but with more moderate values. The secondary loss predictions of the K&O model remain relatively constant across the different Reynolds numbers. Comparing the profile loss results from the mean line models with the cascade test data, it is evident that the K&O model predictions are closer to the experimental results, particularly for the lower Reynolds number cases. This suggests that the K&O model may be more accurate in capturing the effects of the Reynolds number on the profile loss of the Wren100 NGV.

To sum up, given the diverse assumptions and methodologies of the different loss models, it is essential to consider the results of all three models when assessing the mean line performance at various flow conditions of the Wren100 NGV. By doing so, a more comprehensive understanding of the losses and the overall performance of the Wren100 micro gas turbine can be achieved, allowing for more effective optimisation strategies to be developed. Furthermore, the unrealistic total loss prediction by the D&C model emphasises the importance of critically evaluating the applicability and limitations of each model in the context of the specific problem being studied.

6.2.2 Mean Profile Cascade Data Analysis

In this section, the profile loss data and the location of the trailing edge wakes from the wind tunnel cascade tests are presented and discussed.

6.2.2.1 Trailing Edge Wakes

From the previous data, it is evident that the exit dynamic pressure and profile loss vary across the different pitches, which indicates the presence of wakes with a non-uniform distribution. For each Reynolds number, there exists a spanwise position with the lowest dynamic pressure and highest total pressure loss in the middle of the trailing edge wake region. Several essential variables measured in the wakes for two different Reynolds numbers are listed in Table 6.4.

Reynolds Number	**Spanwise Position (mm)**	**Min. Exit Dynamic Pressure (Pa)**
43,973	42	47.54
39,576	36	17.22

Table 6.4: Variables Measured Within the Trailing Edge Wakes

It can be seen that the peak total pressure loss drops and shifts downwards spanwisely as the Reynolds number increases. For each spanwise position, the profile loss also tends to be lower at higher Reynolds numbers. This is expected since higher Reynolds numbers correspond to thinner boundary layers, leading to reduced viscous losses and better overall aerodynamic performance. Based on the cascade data, wake thickness and velocity deficit can then be calculated for different Reynolds numbers. The wake thickness is the distance over which the velocity deficit is non-zero, which can be calculated by the half-width method developed by Schlichting as shown in Equation 6.1 and 6.2 [103].

$$\Delta v = v_{\infty} - v \tag{6.1}$$

$$\delta_{wake} = \frac{x_2 - x_1}{2} \tag{6.2}$$

Table 6.5 shows the calculated wake thickness 10% chord after the trailing edge for different Reynolds numbers based on the half-width method.

Reynolds Number	**Max.** Δv (m/s)	**Wake Thickness** $(\delta,\ mm)$
43,973	2.92	26
39,576	2.59	20

Table 6.5: Wren100 Stator Mean Wake thickness 10% Chord After TE

From Table 6.5, it can be observed that the wake thickness increases with the Reynolds number. This can be attributed to the fact that a higher Reynolds number corresponds to more transitional flows, in which the separation on the suction side could be delayed which leads to a more energetic wake immediately after the trailing edge. In addition, more turbulent flow normally spreads and mixes more rapidly with the surrounding flow, leading to a thicker wake downstream. What stands out is the wake thickness is not symmetrical around the maximum velocity deficit point for different Reynolds numbers. This could suggest that the flow separation might not be occurring symmetrically on both sides of the trailing edge. The area-averaged values of the profile loss for the MGT stator mean section are displayed in Table 6.6.

Reynolds Number	**Area Averaged** Y_p
43,973	0.073
39,576	0.171

Table 6.6: Wren100 Stator Mean Area Averaged Y_p

Overall, understanding the profile loss behaviour can inform the development of active or passive flow control techniques that can further enhance the aerodynamic performance of the Wren100 stator vanes. These techniques may include vortex generators, surface roughness modifications, or boundary layer suction. The experimental study of the mean line performance of the MGT stator provided a baseline for further aerodynamic redesign.

6.2.3 CFD Simulation Data Analysis

The following subsection presents the results and discussion of the CFD analysis conducted on the aerodynamic design of the Wren100 micro gas turbine stator. The focus of this analysis is on the performance of the stator under various operating conditions, specifically at 120,000RPM. The reason for the specific rotational speed is as follows. First, higher operating speed was not available during the first three years of the PhD project due to technical reasons and the impact of COVID-19. Thus, the CFD analysis mainly focused on the operational speeds of 100,000RPM, 110,000RPM, and 120,000RPM during the main period of the project. The data from 130,000 RPM to 160,000RPM were acquired at the final phase of the project and were only used as additional validation data for the models developed. Secondly, the Reynolds number of the stator at those rotational speeds closely matches the wind tunnel data. As the wind tunnel provides the highest wind speed obtainable for validating the CFD results, analysing the stator at this rotational speed ensures a more accurate representation of its aerodynamic performance under real-world conditions.

6.2.3.1 Profile Loss

The CFD analysis provided detailed insight into the flow field characteristics within the stator passages. In this case, different spanwise locations (10% root, mean and 10% tip) are analysed to study the impact of blade geometry and operating conditions on the flow field. The objective of this analysis was to identify regions with high profile loss and understand the flow behaviour in these areas, which could potentially impact the aerodynamic performance of the stator vane. Figure 6.1 displays the velocity contour of the stator vanes at different spanwise positions as the rotor operates at 120,000RPM.

As shown in Figure 6.1, the analysis reveals that the flow accelerates as it passes through the stator passage, with the highest velocities observed at the suction side near the trailing edges of the stator vanes, especially for the near-root section. This indicates significantly different flow behaviour of the near-root profile near the trailing edge compared to the other two profiles. It may be attributed to the different blade curvature and twist distribution along the span, which governs the pressure gradients

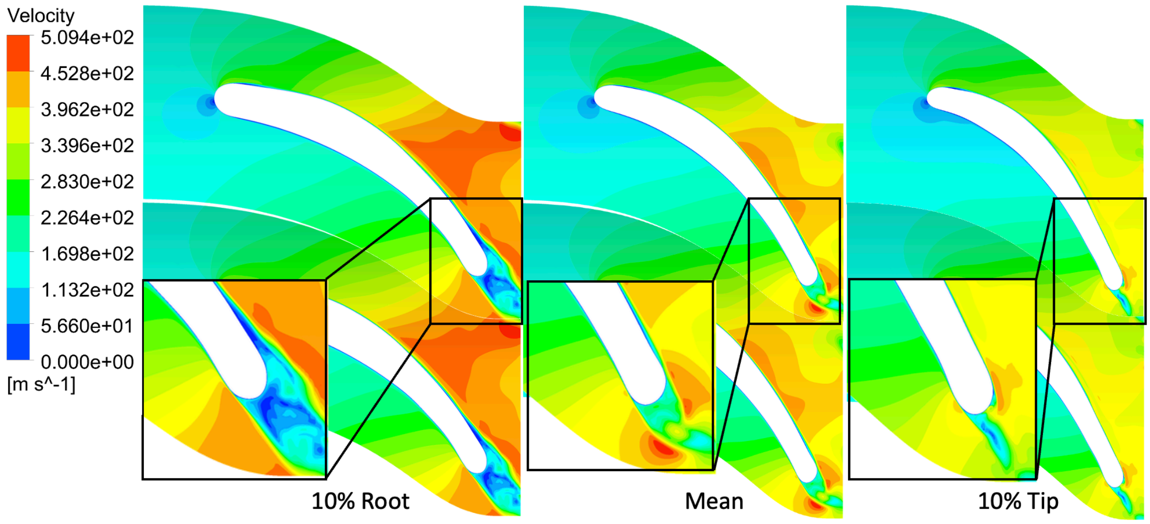

Figure 6.1: Wren100 Stator Instantaneous Velocity Contour at Near-Root, Mean and Near-Tip (Rotor=120,000RPM, t=0.00004762s)

and boundary layer development. The resulting pressure gradient could contribute to increased profile losses, particularly if it leads to flow separation or adverse pressure gradients.

For the near-tip section, flow separation near on the suction side near the trailing edge can also be identified by the relatively low flow speed, followed by a separation bubble located a small distance above the blade surface. The presence of flow separation in this region highlights the complexity of the flow field in the tip region and may have implications for aerodynamic performance and loss mechanisms. In addition, the presence of a separation bubble indicates that the flow has detached from the vane surface, resulting in a localised region of recirculation. This flow behaviour can lead to increased profile losses due to the increased turbulence and energy dissipation within the separated region. To better visualise the flow separation behaviour, the pressure contours were also plotted in Figure 6.2.

It can be seen in Figure 6.2 that the pressure above the stator vane suction side near the trailing edge is notably lower than other regions of the fluid domain, which could indicate reduced aerodynamic efficiency due to the large flow separation. Figure 6.1 and 6.2 also shows the development of a boundary layer on the suction side after the leading edge, which is similar across different vane heights from root to tip. As the formation of the boundary layer is expected, its growth and potential influence on the vane aerodynamic performance will be further analysed. Figure 6.3 displays the

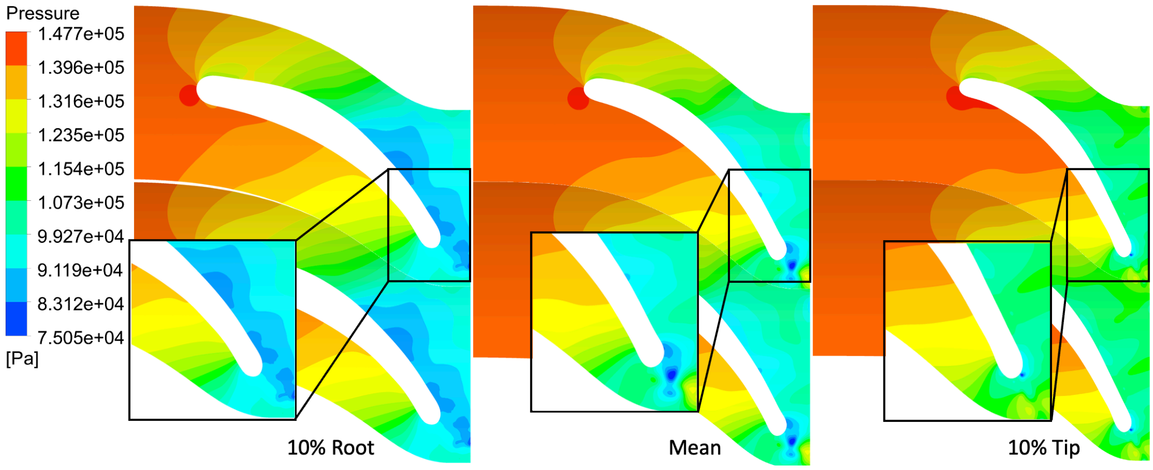

Figure 6.2: Wren100 Stator Instantaneous Pressure Contour at Near-Root, Mean and Near-Tip (Rotor=120,000RPM, t=0.00004762s)

instantaneous skin friction coefficient at the near-root, mid and near-tip regions of the Wren100 stator surface at different directions.

From Figure 6.3 and 6.4, it was found that the flow around the MGT stator vane is evidently complex and three-dimensional. In the Cf_z plot, which aligns with the main flow inlet direction, the positive values of the skin friction coefficient suggest the regions where the flow is well attached to the vane surface. This is the desired behaviour for an efficient stator vane. However, the negative values near the leading edge indicate flow separation, which could be problematic because it creates a wake of turbulent, low-energy flow behind the vane, which increases profile losses. Moreover, when the flow separates and then reattaches, it can cause a separation bubble, which is often associated with a transition from laminar to turbulent flow. While turbulent flow has a fuller velocity profile and can resist separation better than laminar flow, the transition and the turbulence itself generate additional shear stresses and energy dissipation, contributing to profile losses.

6.2.3.2 Secondary Loss

A comprehensive analysis of the secondary loss of the Wren100 stator vane was conducted. The section aimed to identify the secondary flow structures and their impact on the overall performance of the Wren100 stator. As displayed in Figure 6.5, static pressure contours at the hub and tip sections of the Wren100 stator vane were plotted to visualise the endwall effect, which gives insight into the secondary flow patterns

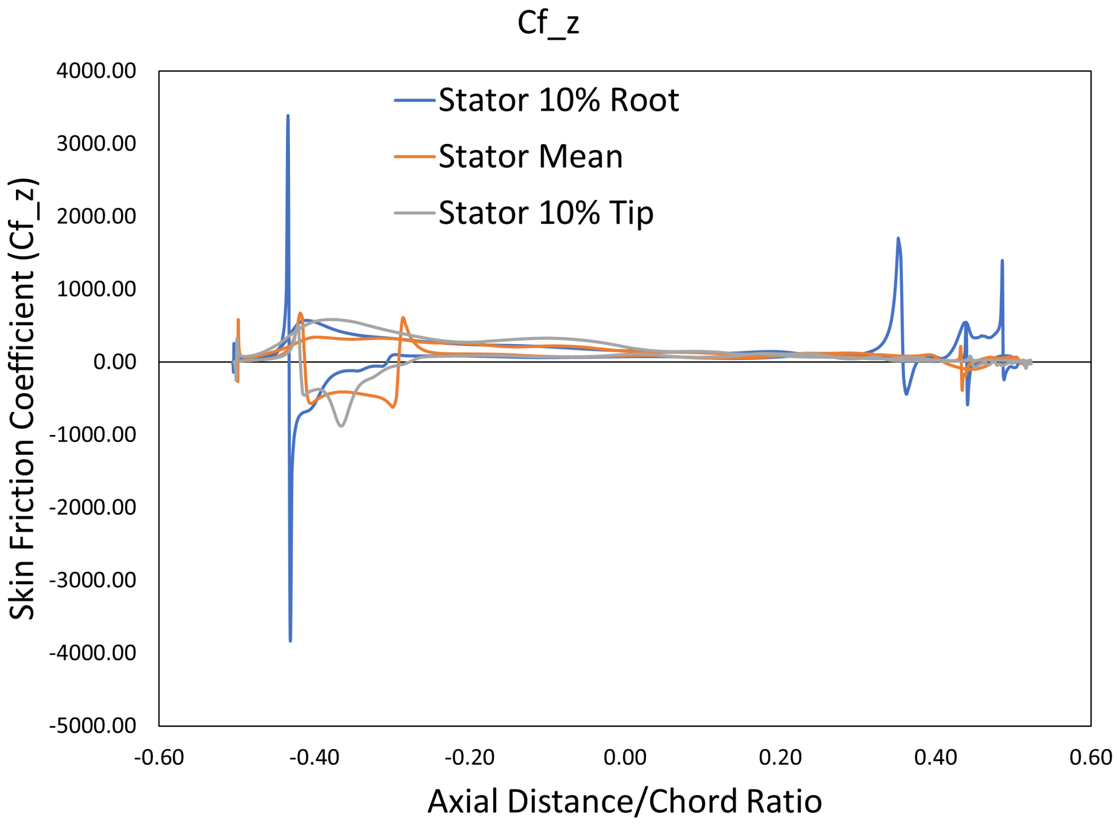

Figure 6.3: Instantaneous Skin Friction Coefficient of the Wren100 Stator Vane at Main Flow (Cf_z) Direction (Rotor=120,000RPM)

and the associated loss in these regions.

On the hub endwall, a high-pressure zone that extends somewhat evenly along the leading edge of the vanes can be visualised, which is a good sign that the flow has been effectively turned by the stator. However, a high gradient of pressure can be seen towards the trailing edge, possibly indicative of flow separation or the development of a secondary flow pattern such as a hub corner vortex. On the tip or shroud endwall, the pressure distribution has higher complexity due to the existence of the tip clearance. The tip leakage flow can be identified by a region of lower pressure on the pressure side of the vane tip, leading to a jet of high-velocity fluid that spills over into the lower pressure region on the suction side. The interaction between the tip leakage flow and the main passage flow forms the tip leakage vortices, which is a significant source of secondary loss. Furthermore, the instantaneous pressure contours show an uneven distribution trend along the spans of the vane, which might be

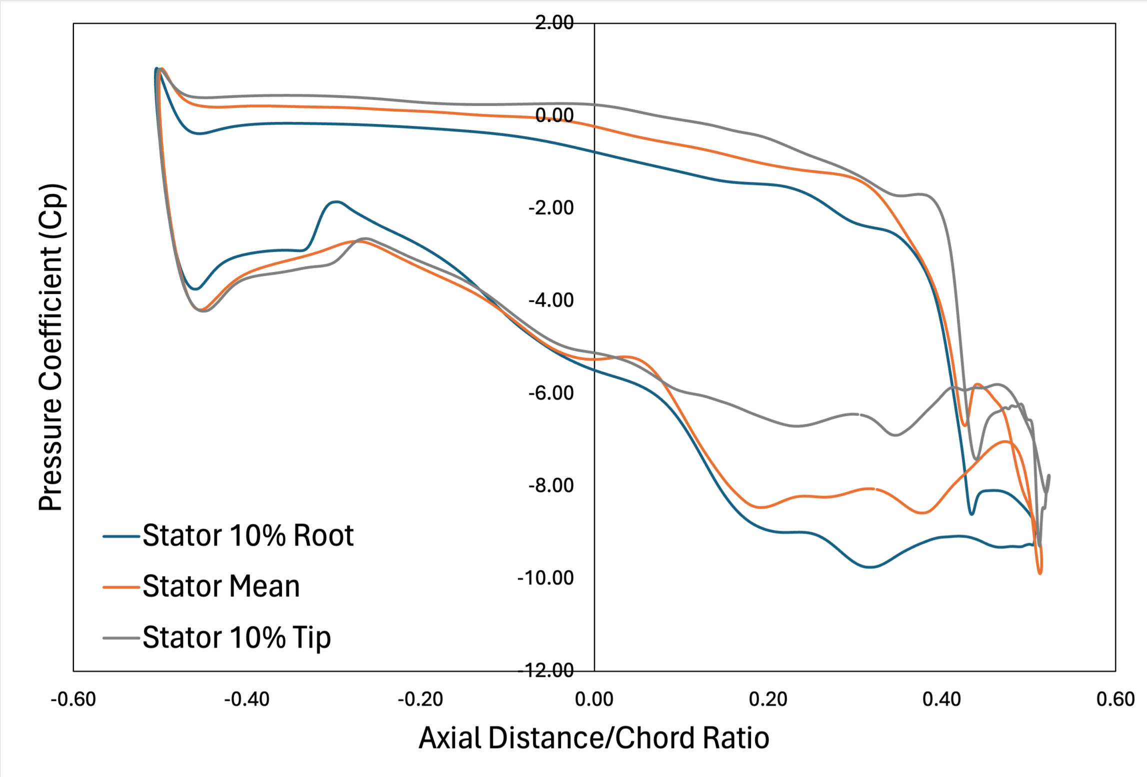

Figure 6.4: Instantaneous Pressure Coefficient (C_p) of the Wren100 Stator Vane (Rotor=120,000RPM)

caused by the 3D nature of the flow within the passage. This uneven distribution can result in non-uniform loading of the vanes and contribute to secondary losses due to additional vortices forming in the flow path.

Figure 6.6 shows the two-dimensional vorticity after the stator vanes when the rotor is rotating at 120,000RPM, which is a measure of local rotation and can be calculated using Equation 6.3.

$$\omega = \frac{\partial v}{\partial x} - \frac{\partial u}{\partial y} \tag{6.3}$$

It can be seen from Figure 6.6 that 13 distinct lines or curves of relatively high vorticity regions extend from root to near-tip regions. The root vane passages regions exhibited the highest level of vorticity, while a gradual decrease in vorticity towards the tip for different phases. This specific flow behaviour suggests the structures of the secondary flows, including horseshoe and passage vortices, are more pronounced near the root region. Additionally, the concentration of vorticity in certain areas, particularly near the trailing edge of the vanes, could indicate trailing vortices. These

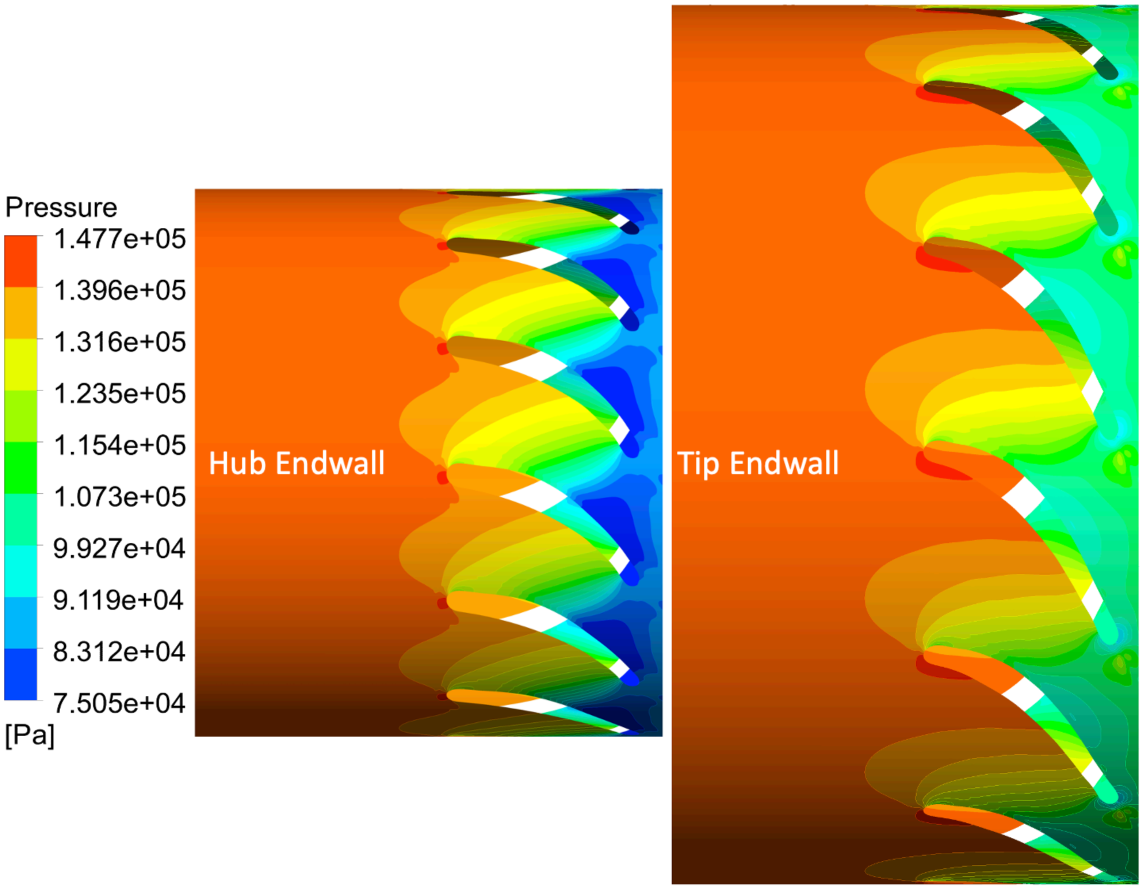

Figure 6.5: Wren100 Stator Endwall Instantaneous Pressure Contouring (Rotor=120,000RPM, t=0.00004762s)

vortices are also significant sources of secondary losses as they represent regions where the flow has a higher degree of disorder and energy dissipation.

To further visualise the impact of blade geometries on the loss caused by the secondary flow, entropy contour plots on the stator vane surface at different phases are displayed in Figure 6.7.

It can be visualised that the entropy generation on the blade suction side remains almost identical for different time phases. The highest entropy generation was observed near the root section close to the trailing edge, which corresponds to high-loss areas where the flow experiences significant mixing and dissipation. This finding aligns with the 2D vorticity contour results, further emphasising the significance of secondary losses in the root region.

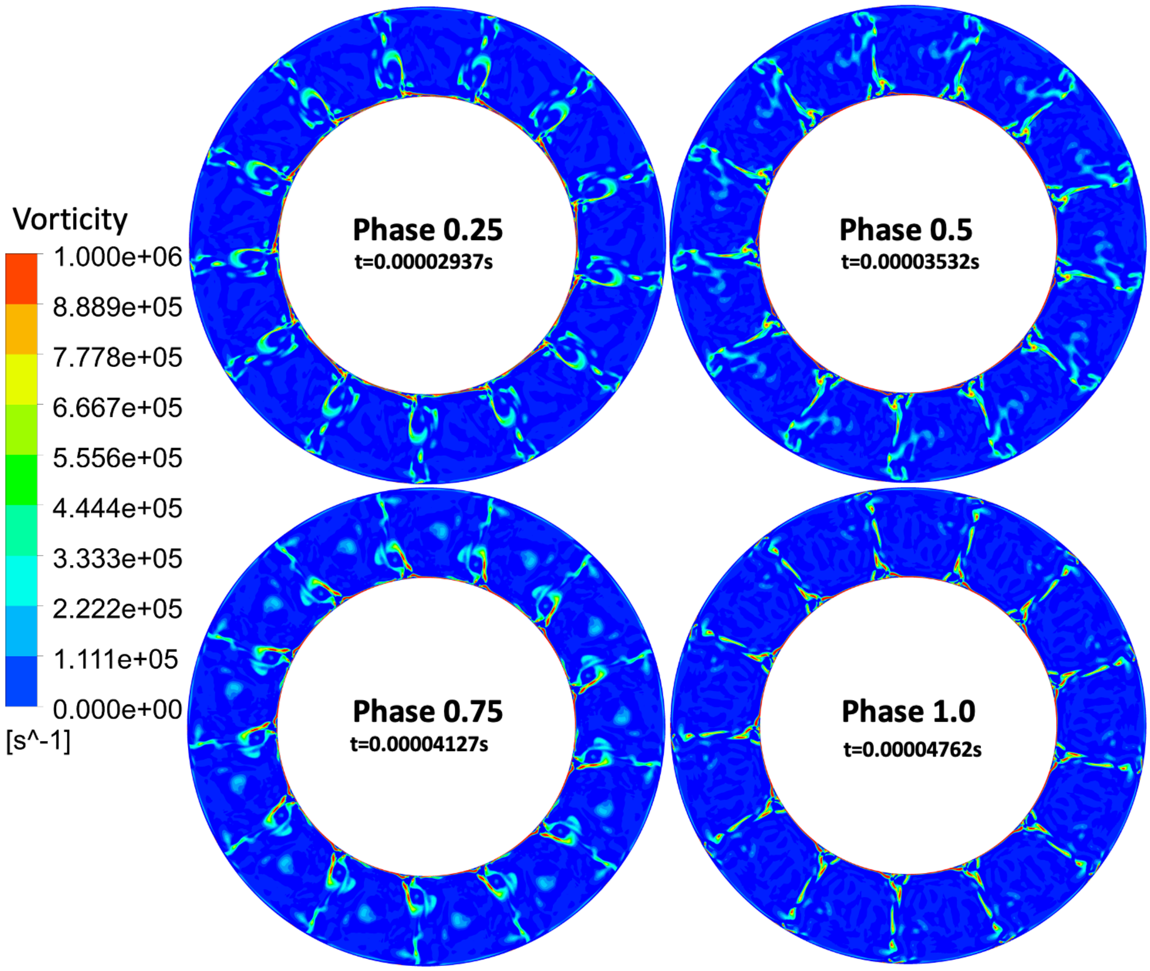

Figure 6.6: Wren100 Stator Exit 2D Vorticity (120,000RPM)

To sum up, the 2D vorticity and entropy plots collectively point towards areas where the flow is more disordered and where energy dissipation is occurring. These regions are typically associated with secondary flow losses in turbomachines. For instance, the wakes of the stator vanes, indicated by high vorticity and entropy, are potential regions where the flow has lost a significant amount of kinetic energy due to viscous forces and turbulence.

6.2.3.3 Trailing Edge Loss

As mentioned in Section 2.4.4, Denton stated that the entropy generation associated with the trailing edge wakes is one of the significant contributors to the turbine blade aerodynamic loss, which can be quantified using Equation 6.4, where s and s_0 are the local and reference entropies [65].

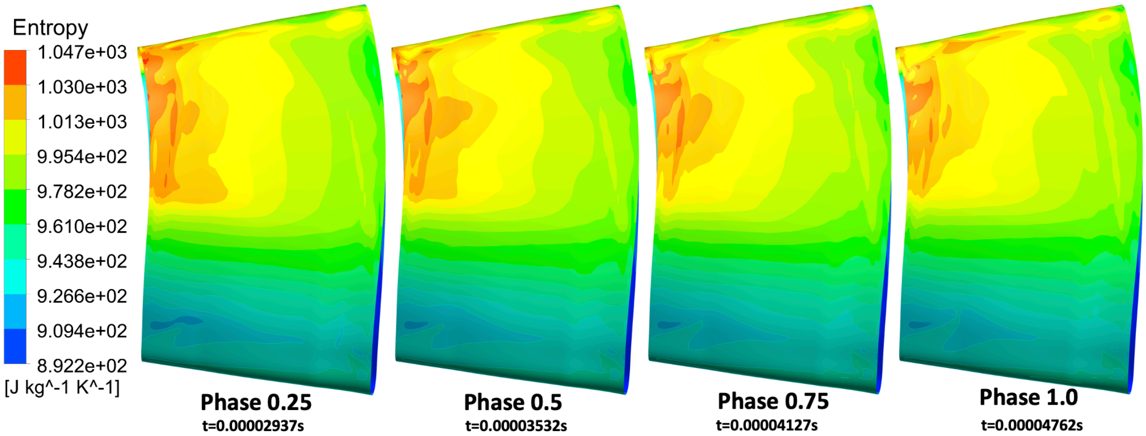

Figure 6.7: Wren100 Stator Suction Side Entropy Contour Plots

$$s_{gen} = \frac{T_2(s - s_2)}{c_p} \tag{6.4}$$

To visualise the trailing edge loss for each sectional profile, instantaneous entropy plots were generated based on the calculated data, providing a snapshot of the thermodynamic loss at the monitored regions. Similar to Figure 6.1 and 6.2, the high entropy regions mostly come from the trailing edge wakes and the flow separation on the suction side, which could indicate increased energy dissipation and aerodynamic loss. Potential redesigns can be made for the blade geometry at those regions to minimise those losses.

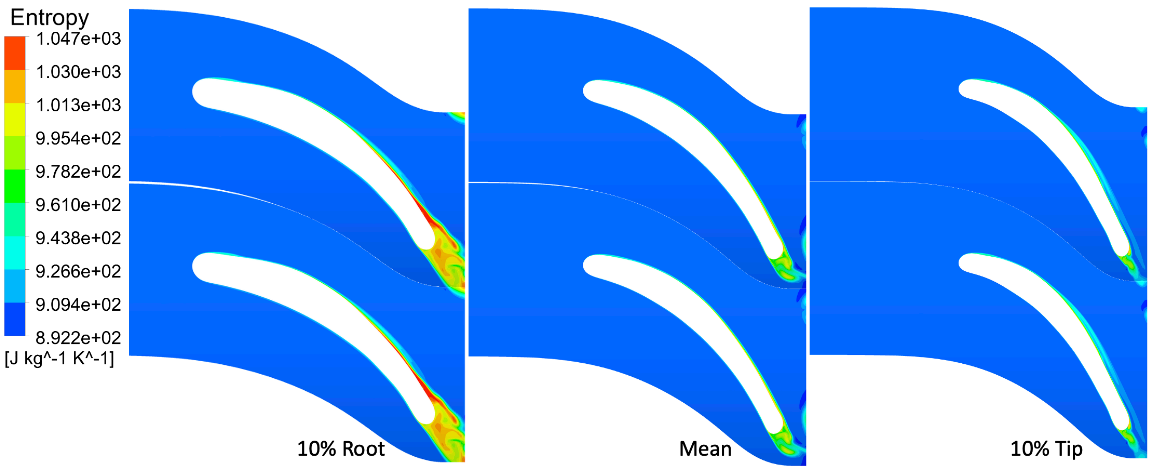

Figure 6.8: Wren100 Stator Instantaneous Entropy Contour (Rotor=120,000RPM, t=0.00004762s)

The observed pattern across different vane heights indicates that the trailing edge loss is not uniform across various spans. The high entropy shown in the near-root span suggests higher loss due to the complex interaction between the hub wall boundary layer and passage flow.

Furthermore, the entropy contour at the stator exit plane was analysed to investigate the sources of entropy generation and their distribution across the blade span. The analysis revealed that there are 13 major entropy generation lines (or curves), corresponding to the 13 stator vanes, extending from the hub to the tip (Figure 6.9).

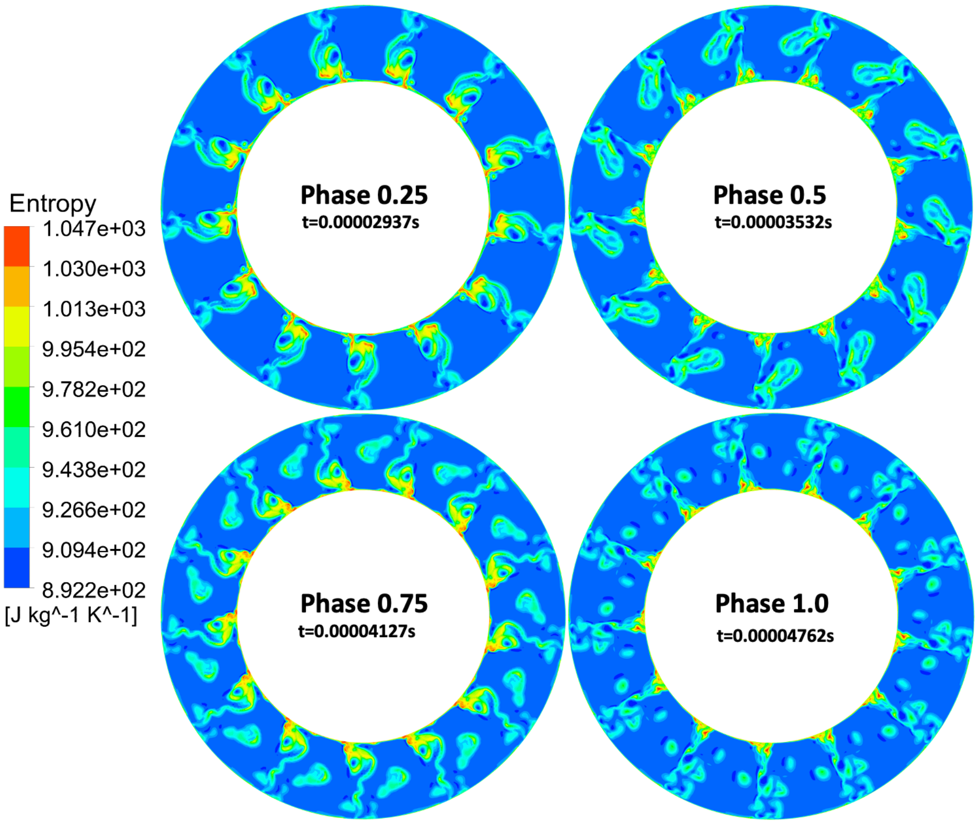

Figure 6.9: Wren100 Stator Exit Entropy Contour (Rotor=120,000RPM)

From the above contour plots, a marked surge in entropy production is witnessed proximate to the root region, while the mid and tip span regions exhibit similar entropy levels. Over the course of various phases, there emerges a spatial periodic redistribution of the high entropy regions, likely induced by the trailing edge wake, or the reflection of the rotor-stator interaction, where the influence of rotor blades causes a periodic disruption to the flow, resulting in the observed temporal and spatial entropy variations. In addition, the spanwise migration of high entropy creation could suggest that the trailing edge loss is not uniform across the blade span. This non-uniformity can lead to additional losses due to secondary flows and spanwise mixing.

Further evaluation of the total pressure loss 10% chord after the trailing edge also proved the poor design of the root profile as shown in Figure 6.10, which shows the locations and thickness of the TE wakes by plotting the phase-averaged total pressure after the trailing edge. Ideally, a stator should turn the flow with minimal total pressure loss, which is not fully achieved here, especially at the stator mid and tip regions.

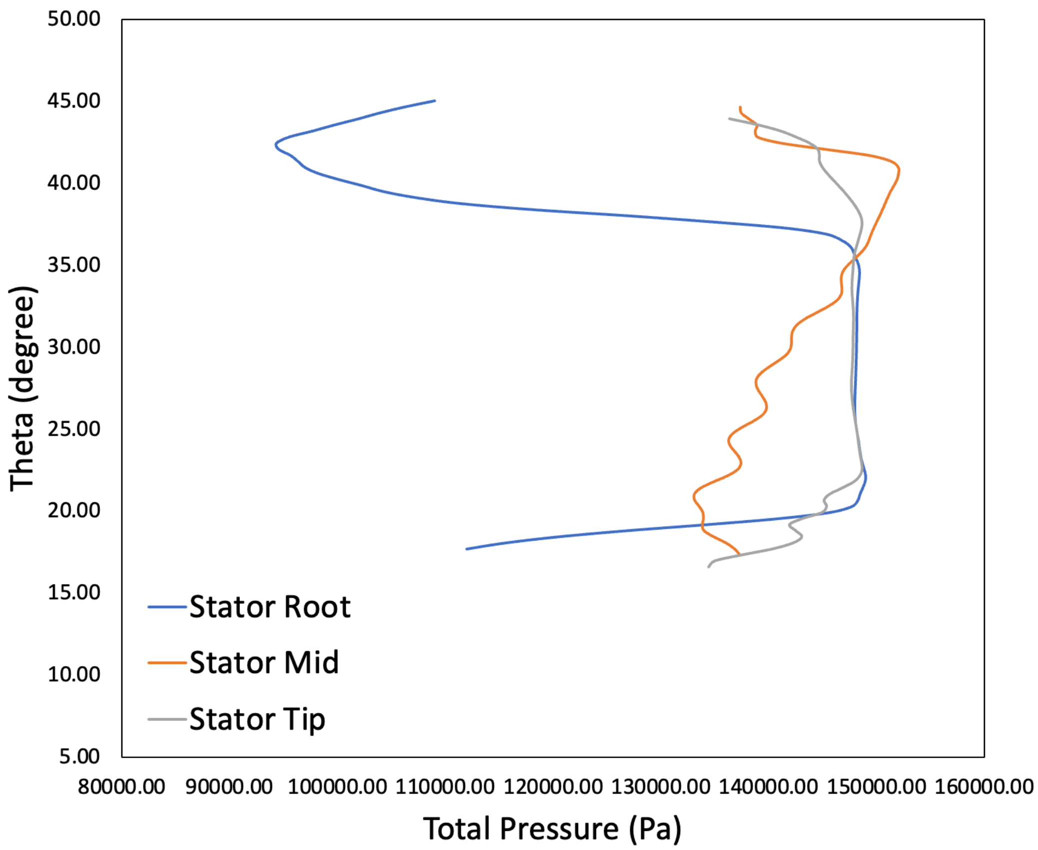

Figure 6.10: Phase-Averaged Total Pressure 10% Chord After Stator TE (10% Root, Mid, 10% Tip)

As shown in Figure 6.10, the peak total pressure loss can be located near the root section, in line with the previously noted high entropy generation in the same region. For the mid-span, much lower total pressure outside the wake regions can be spotted, and the lowest point is approximately 10% lower compared to the root and tip spans. The more gradual transition from low to high total pressure for the mid-span suggests the presence of a slower velocity recovery process in the wake region at mid-span. Based on the high entropy region migration behaviour noted before, this phenomenon could be caused by secondary flows and the different loading distribution across the blade span and the stator-rotor interaction, which further investigations between the transient plane between the rotor and stator are also described in the following section.

In conclusion, the combination of the entropy and total pressure plots suggests that the trailing edge design and the flow conditions at the stator exit are critical for the stator performance. High entropy regions correspond with lower total pressure recovery, pointing towards energy loss in the wake of the stator vanes. The unsteadiness indicated by the entropy plots is also reflected in the total pressure variations, highlighting the dynamic nature of the losses involved.

6.3 Comprehensive Analysis of the Wren100 Rotor Aerodynamic Performance

This section provides a comprehensive analysis of the Wren100 rotor aerodynamics, focusing on several essential factors that influence the efficiency and thrust when operating at different conditions, including different Reynolds numbers (RPMs) and phases (time steps). Unlike the stator, the rotational nature and the existence of the shroud clearance of the rotor blades make the analysis of the tip region much more difficult. The rotor blade profile variation from root to tip region is also much greater compared to the stator profiles, meaning more analysis of different blade heights was needed for the more complex flow field.

6.3.1 CFD Analysis of Flow Field Around Wren100 Rotor Blade

6.3.1.1 Profile Loss

The CFD analysis for the Wren100 rotor was initially compared at two different rotor speeds: 120,000 RPM and 110,000 RPM when the blades are at the same phase. At first, the flow field behaviour of the rotor mean profile was investigated by examining the velocity and pressure contour plots as shown in Figure 6.11 and 6.12.

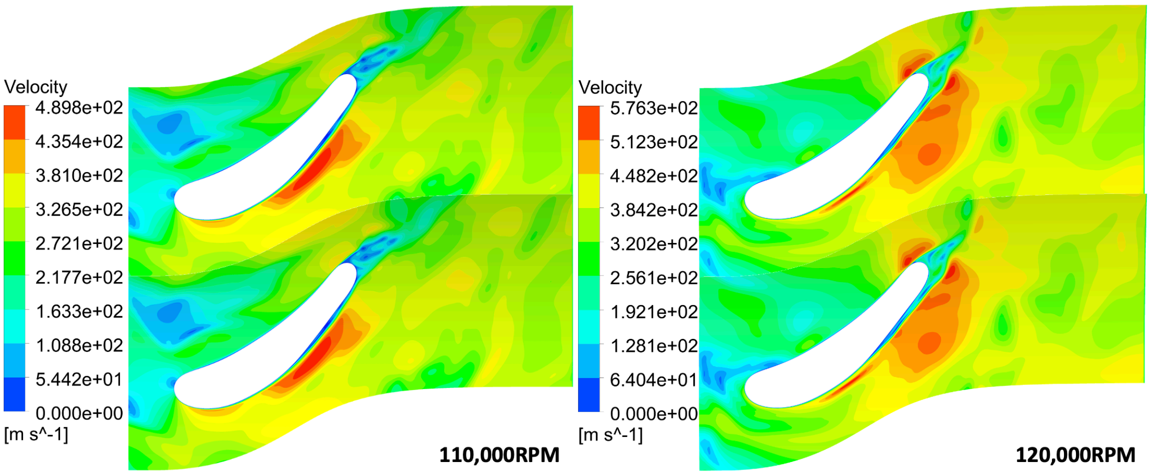

Figure 6.11: Wren100 Rotor Mean Profile Instantaneous Velocity Contour For Different RPMs (Phase 1.0)

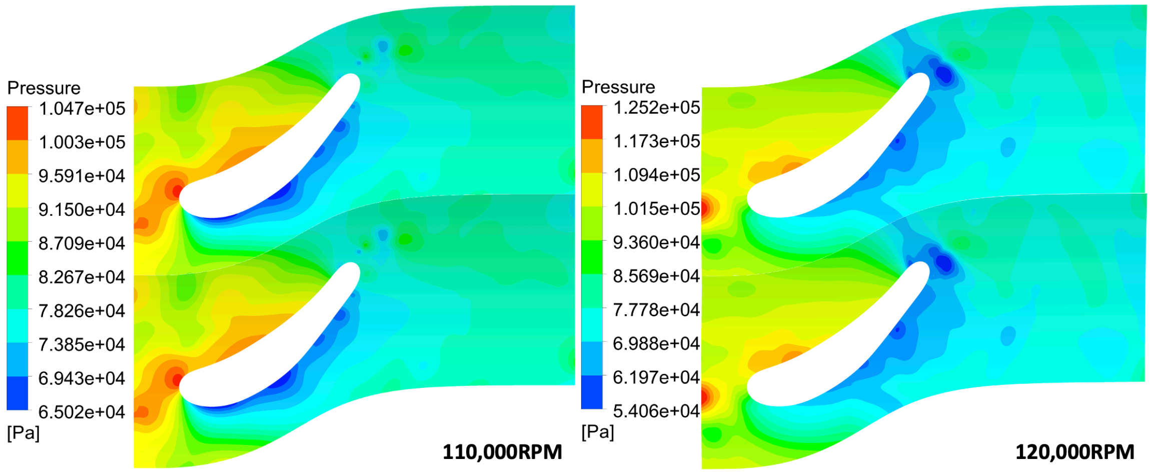

Figure 6.12: Wren100 Rotor Mean Profile Instantaneous Pressure Contour For Different RPMs (Phase 1.0)

From Figure 6.11 and 6.12, it can be visualised an increased presence of flow separation on the suction side of the rotor blade at 120,000RPM compared to 110,000RPM. It could be attributed that as the Reynolds number increases, more portion of the flow transitions from laminar to turbulent, resulting in a thicker boundary layer. In addition, higher RPMs often mean increased energy extraction to accelerate the flow towards the trailing edge to generate thrust. As shown in Figure 6.11, the high-velocity region is closer to the trailing edge for higher RPM at the same phase, which could also indicate higher efficiency. This can be proved by calculating the isentropic efficiency, in which the 120,000RPM is approximately 0.3% higher than 120,000RPM. To study how the flow propagates on the blade suction side, the velocity contour plots for one passage time were divided into several phases as demonstrated in Figure 6.13.

To further investigate the flow field at 120,000RPM, as shown in Figure 6.13, the movement of the high-velocity flow from the leading edge to the trailing edge can be visualised within one blade passage time. The boundary layer separation behaviour can be seen near the blade trailing edge, which could indicate a source of profile loss that potentially can be improved by further redesign. It was notable that the movement of high-speed flow has almost no impact on the boundary layer thickness. This could mean this rotor design was turned effectively to generate thrust.

Due to the complexity of 3D MGT blade geometry, the flow field based on the velocity contour for the near-root and near-tip regions was also compared and analysed as shown in Figure 6.14.

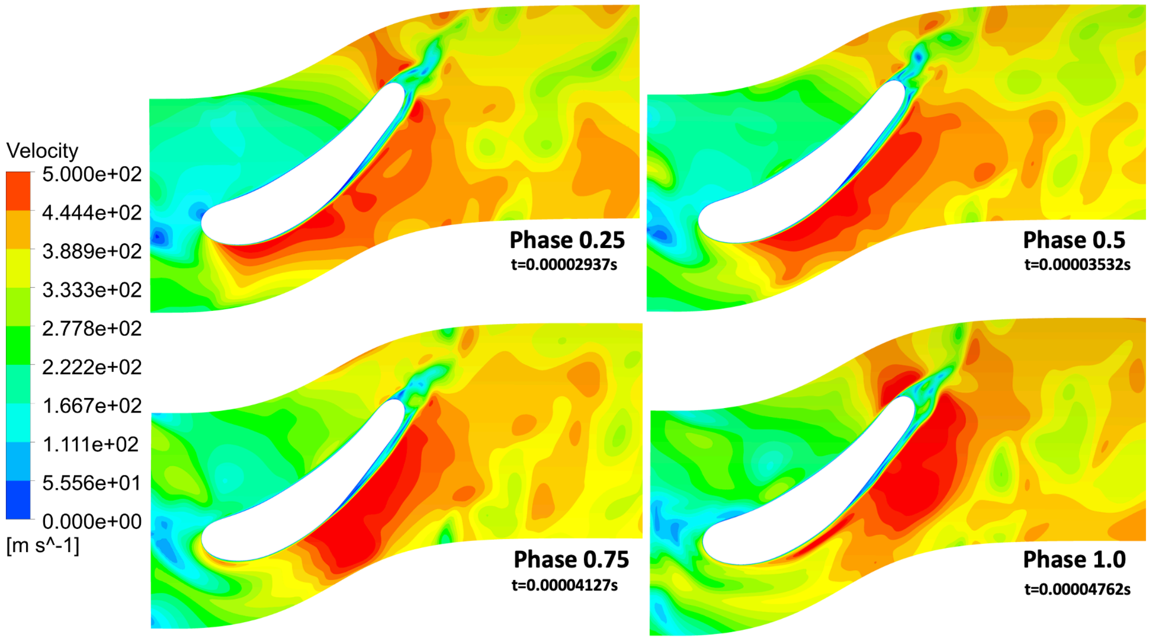

Figure 6.13: Wren100 Rotor (Discrete) Mean Profile Velocity Contour (120,000RPM)

Figure 6.14 presents the velocity contour for the Wren100 rotor blade at both the near-root and near-tip sections, offering insights into the local flow characteristics and potential aerodynamic losses. In the vicinity of the tip profile, a visual inspection of the velocity contour reveals discernible signs of flow separation. This is characterised by the periodic formation of a bubble of high-speed flow that progressively detaches from the suction side of the blade, subsequently fragmenting into smaller flow structures. The existence of lower velocity regions near the trailing edge of the suction side surface is indicative of flow recirculation. These recirculation zones are typically associated with increased profile losses due to the stagnation and subsequent reversal of the flow, leading to an effective reduction in the usable blade surface for energy extraction. However, the influence of the tip clearance effect renders the interpretation of the flow behaviour somewhat challenging. It is not immediately clear whether the observed flow characteristics, including flow separation are primarily a result of the geometrical configuration at the blade tip or the intricate flow dynamics within the shroud gap. Therefore, further investigation would be required to provide additional clarity on the flow behaviour at the tip regions.

For the root section, the velocity contour suggests that low-velocity regions are predominantly located near the pressure side, which is contrary to the mean and tip profiles. As the blade rotates downwards (Figure 6.14), the flow field remains well

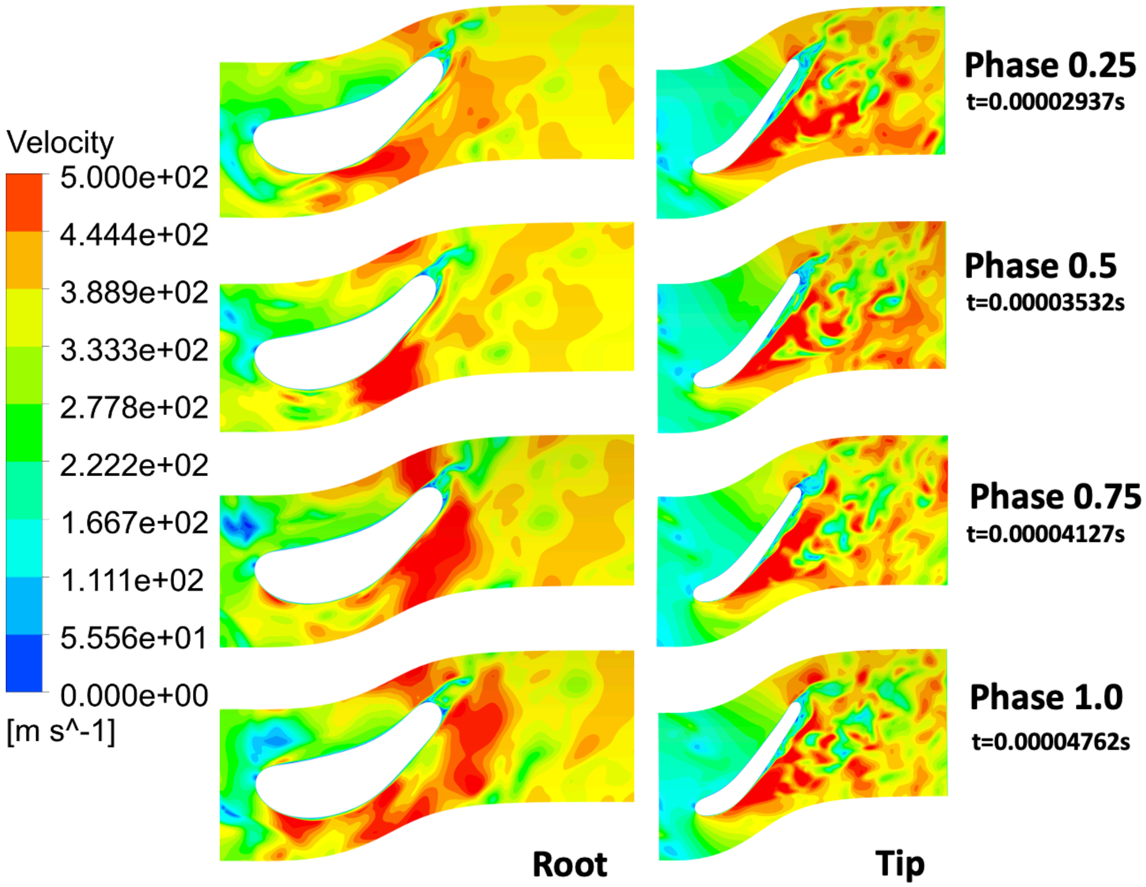

Figure 6.14: Wren100 Rotor (Discrete) Root & Tip Profiles Velocity Contour (120,000RPM)

attached to the blade pressure side and suction side surface. Relatively small flow separation behaviour can be seen near the leading edge of the root profile. While not as severe as the detachment noted at the mean and tip sections, any small flow separation could still contribute to blade total profile loss. Also, the red high-speed flow regions developed on the blade suction side of the root span are not as concentrated as the mean span for the final phase, which could be caused by several factors, such as the blade shape and endwall effect. Nevertheless, this behaviour could indicate the blade root can not be effectively turned by the flow to generate high thrust.

To better locate the sources of profile loss caused by the geometrical designs of the rotor profiles at different blade heights, the instantaneous skin friction coefficients were plotted as shown in Figure 6.15 for the near-root, mean and near-tip blade surface. These plots, especially when analysed in conjunction with the velocity and pressure contours at various operating conditions and phases, paint a comprehensive picture of the aerodynamic performance of the rotor blades.

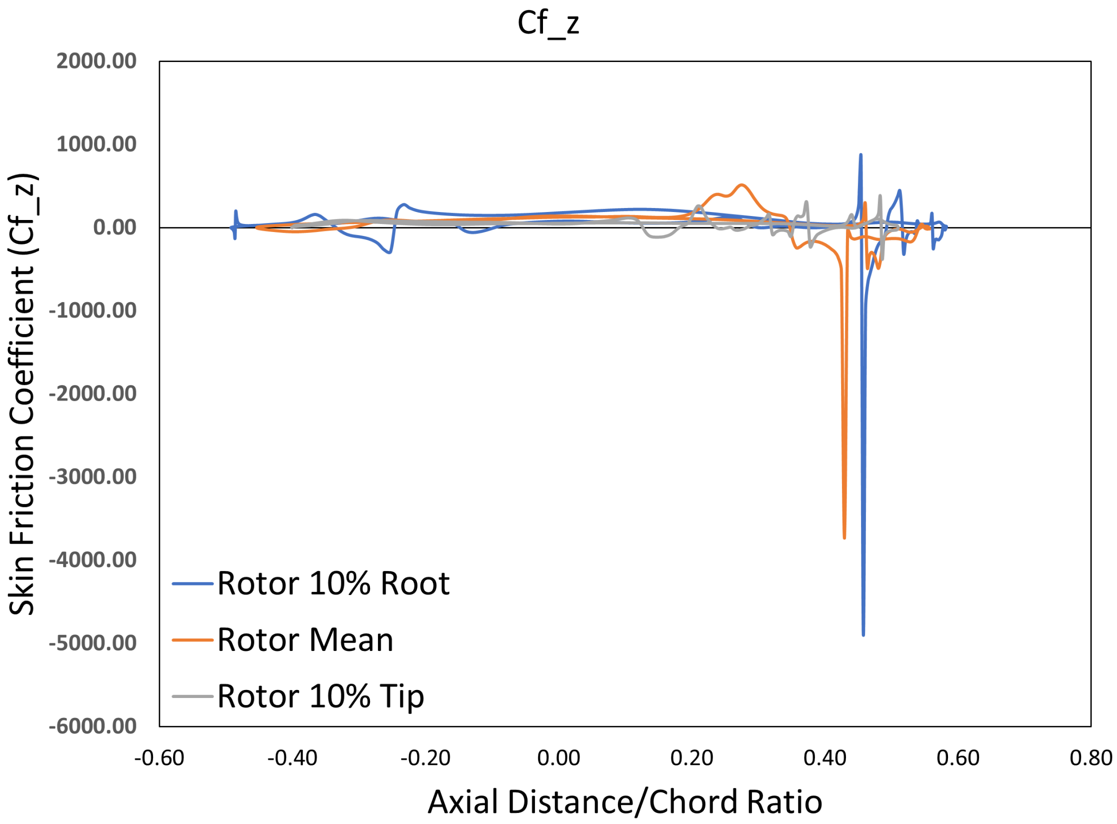

Figure 6.15: Instantaneous Skin Friction Coefficient of the Wren100 Rotor Blade at Main Flow (Cf_z) Direction (Rotor=120,000RPM)

From Figure 6.15, it can be seen that the skin friction coefficients near the leading edge of the rotor blade are relatively low for three different blade spans. This indicates relatively healthy and attached flow on the first half regions of the rotor blade. However, deviations from this can signal potential flow issues. In particular, regions of high skin friction could suggest that the boundary layer is becoming turbulent, which, while resistant to separation, can increase the viscous losses. Conversely, areas with negative values of Cf_z at the mean and near-root spans near the trailing edge are indicative of flow separation, which leads to an increase in profile loss.

Overall, the analysis of rotor blade profile loss indicates flow behaviour and profile losses are quite different along the blade span, meaning its profile loss behaviour is strongly influenced by both the profile design aspects, such as the shape of the blade and its surface finish, as well as the dynamic aspects, like the operating RPM and the unsteady flow phenomena.

6.3.1.2 Secondary & Tip Leakage Loss

In modern gas turbines, caused by the interaction between the endwall effect and the Horse-Shoe vortex, the spanwise motion of the flow often contributes to the majority portion of the secondary loss. Based on the Wren100 rotor blade mean profile, the development of local swirling flow structures was analysed by plotting the vorticity diagram at different phases as shown in Figure 6.16.

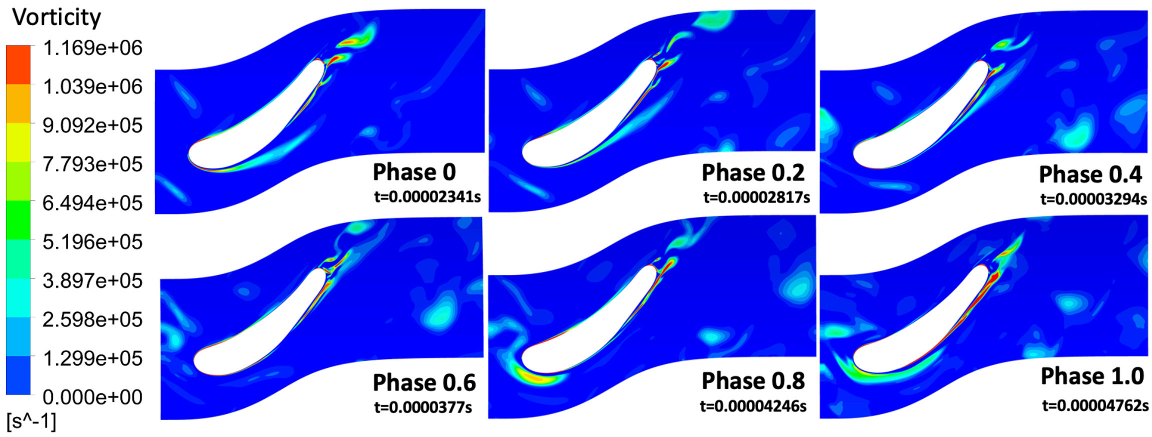

Figure 6.16: Wren100 Rotor Blade Vorticity Plots (120,000RPM)

According to the vorticity plot in one blade passage time, unsteady swirling flow structures can be visualised to be periodically generated from the leading edge, which remains attached along the suction side until dissipation after the trailing edge. While it is somewhat challenging to distinguish the development of high vorticity areas from flow separation (profile loss) and vortical structures such as leading edge vortex, trailing edge vortex, and passage vortex (secondary loss). However, based on the velocity and pressure plots as described before (Figure 6.12 and 6.13), it could be confirmed the formation and movement of the leading edge vortex. From Figure 6.16, the visualisation of unsteady swirling flow structures originating from the leading edge also points to this phenomenon. Hence, a potential leading edge redesign should be considered to improve the aerodynamic performance of the MGT rotor blade.

As described in previous subsections, another significant source of secondary flow could be caused by the existence of a small gap between the rotor blades and the outer shroud, known as the tip leakage loss. For the Wren100 rotor, the tip clearance was set to be 5% of the blade height, which is approximately 0.5mm. To visualise the impact of the tip clearance, the two-dimensional vorticities were plotted at the exit plane of the rotor blades as shown in Figure 6.17.

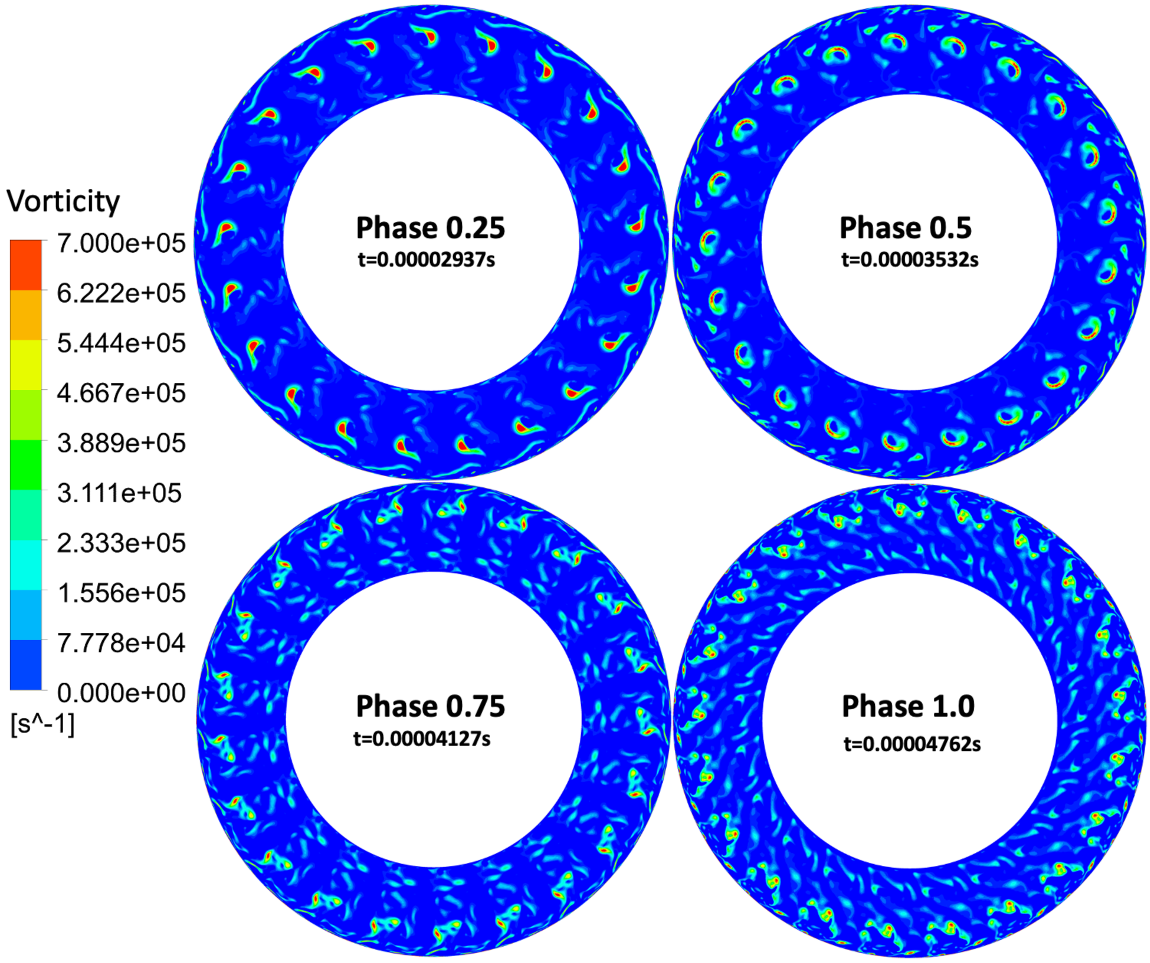

Figure 6.17: Wren100 Rotor Exit Entropy Contour (120,000RPM)

From Figure 6.17, the creation and movements of tip leakage vortex structures at different phases can be visualised. At phase 0.25, caused by the pressure difference between the pressure and suction side, the tip leakage flow rolls up into the vortex downstream of the blade, which leads to the red high vorticity regions. When mixed with the trailing edge vortices at phase 0.5, the circular formation of high vorticity regions slightly moves towards the mid span. However, the disintegration of the high vorticity regions from phase 0.75 to 1.0 suggests a more complex interaction. It seems that the well-defined vortices are becoming unstable and breaking down. The possible reason could be the complicated interactions between different flow structures or the inherent instability of the vortex. The development of trailing edge vortices is described in the next subsection. For the tip leakage loss, potential redesigns were suggested to focus on the optimisation of the tip clearance, which would reduce the complex mixture between different flow structures after the trailing edge.

6.3.1.3 Trailing Edge Loss

To investigate the impact of trailing edge geometrical designs at different blade heights, the flow field was analysed at the 10% root, mean and 10% tip profiles.

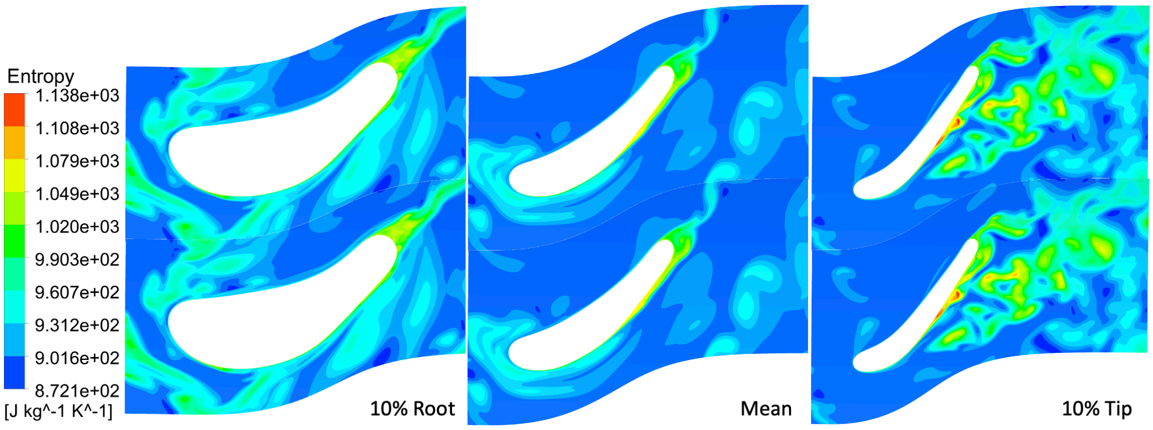

Figure 6.18: Wren100 Rotor Instantaneous Entropy Contour (120,000RPM)

Figure 6.18 plots the entropy generation contour around the Wren100 rotor near-hub, mean and near-shroud region. Similar to the velocity contours plotted before, the highlighted regions mostly come from the formation of flow separations and trailing edge vortices. For different rotor blade heights, vortex shedding can be visualised after the trailing edge, which is normally caused by the wake mixing and downstream effects.

To further understand and quantify the flow behaviours after the trailing edge, the phase-averaged spanwise total pressure at the near-root, mean and near-tip regions are calculated and plotted as shown in Figure 6.19.

Based on the downstream total pressure diagram, it was immediately noticed that the highest loss comes near the tip region. As described before in the secondary loss analysis section, it could be the generation of tip leakage flow propagated downstream that inhibits the recovery of total pressure outside the trailing edge wakes. The manifestation of the vortex shedding near the tip span results in the oscillation of

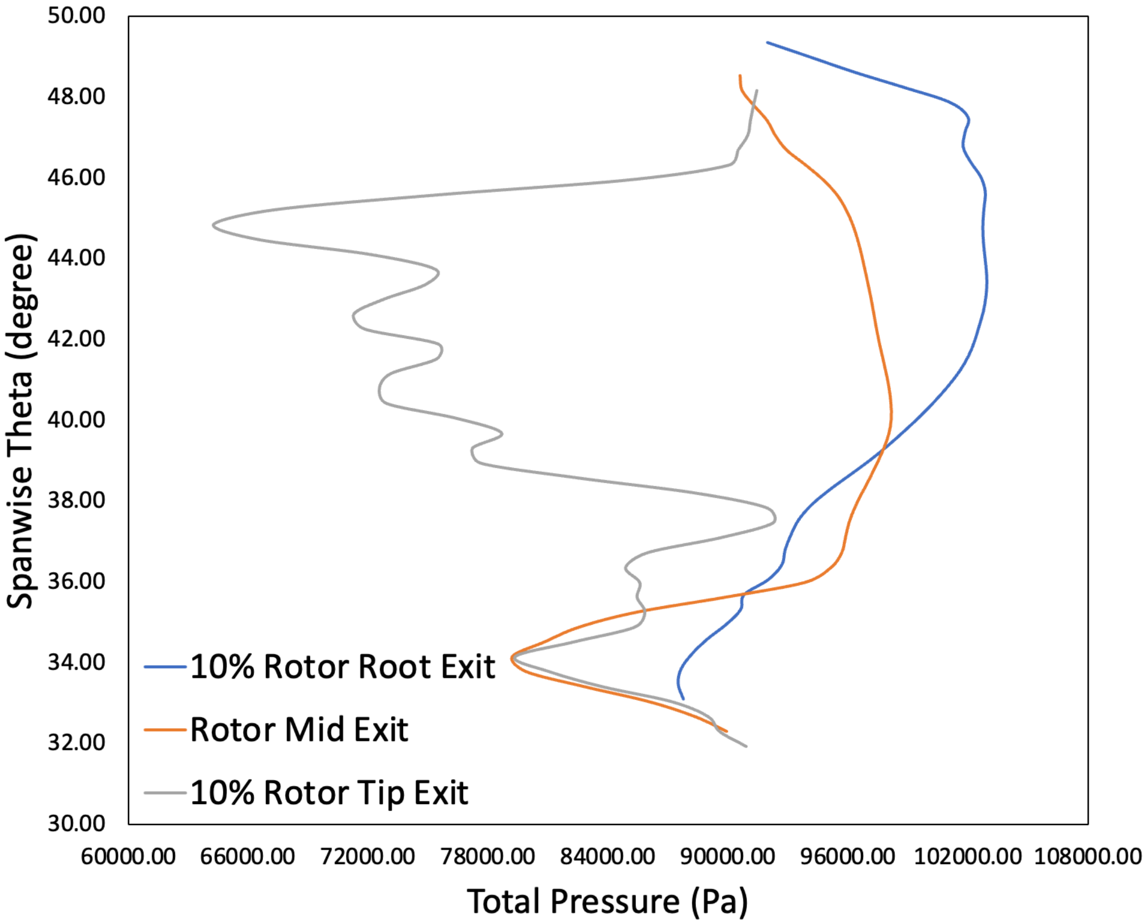

Figure 6.19: Phase-Averaged Total Pressure 10% Chord After Rotor TE (10% Root, Mid, 10% Tip)

an average 20.38% higher total pressure loss compared to its peak value outside the trailing edge wakes.

6.4 MGT Stator and Rotor Interaction

As presented in the previous sections, the results of the CFD simulations for the Wren100 micro gas turbine with only the stator and the combined stator-rotor system indicate a difference in the stagnation pressure loss coefficient (Yp) between the two cases, as demonstrated in Table 6.7.

Variable	**Case**	**Result**
Y_p	Only simulate stator vane	3.91%
Y_p	Stator vane in single stage stator-rotor system	9.25%

Table 6.7: Mass-Averaged MGT Stator Y_p For Different Fluids Domains

For the steady-state RANS simulations, the interface between the stator and rotor was modelled using the mixing-plane approach. This method efficiently averages the flow properties across the interface circumferentially, providing a simplified yet effective representation suitable for steady-state analysis. This approach captures the average effects of rotor-stator interactions without delving into the time-dependent behaviours of each blade passage, making it ideal for initial design evaluations and broader performance assessments [178]. Conversely, the LES simulations required a transient approach to capture the dynamic flow interactions and the temporal variations between the stator and rotor. A sliding mesh technique was utilised, enabling the physical rotation of the rotor relative to the stator. This setup, configured with profile transformation for blade geometry adaptation and a transient method of time integration, reflects the passing period of the rotor. Unlike the RANS setups, the interface type for LES was set to 'Fluid-Fluid' with a 'General Connection' model. The 'Transient Rotor Stator' frame change/mixing model, with an automatic pitch change option, dynamically adjusts the computational domain, ensuring that the simulation captures real-time effects of blade interactions on the flow field [179].

From Table 6.7, the only stator case exhibits a lower Yp of 3.91%, while the stator in the stator-rotor system has a higher Yp of 9.25%. This discrepancy could be attributed to the stator-rotor interaction, which is an essential aspect to consider when analysing the performance of a micro gas turbine system.

Many previous studies have shown that the interaction between stator and rotor occurs at all scales of gas turbines, which potential efficiency gain could be achieved based on more understanding behind the mechanism. Kozak et al. numerically investigated a single-stage high-pressure turbine stator rotor flow interaction at off-design conditions, which positive articulation of the rotor blades would enhance pressure loss and flow separation that reduce the stage efficiency as shown in Figure 6.20. The results also indicate an efficiency increment of 10% at off-design conditions can be achieved [180].

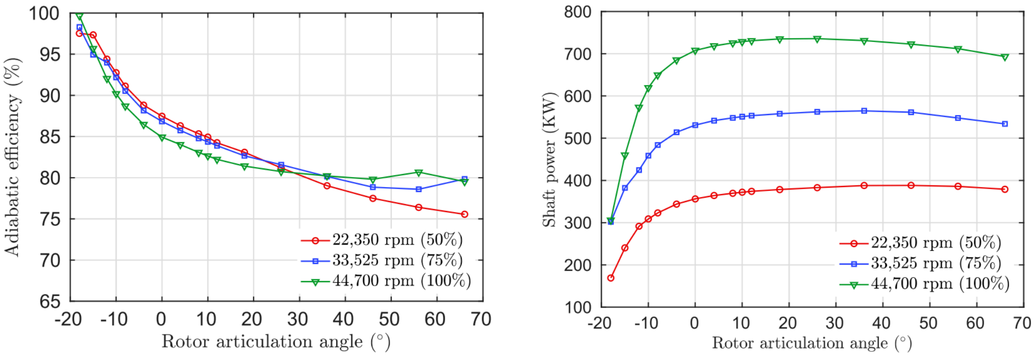

(a) Adiabatic efficiency (b) Shaft power

Figure 6.20: Gas Turbine Stage Performance With Different Rotor Articulation Angles [180]

6.4.1 Impact of Different RPMs on MGT Stator Flow Fields

A series of simulations were carried out for different RPMs to further investigate the effect of MGT rotor blades on the flow behaviour around the stator vanes. Initially, the distribution of stagnation pressure loss coefficient on the stator exit plane when the rotor is rotating at different RPMs was plotted as displayed in Figure 6.21. Also, the mass-averaged values of the stagnation pressure loss coefficients are listed in Table 6.8.

RPM	**110k**	**120k**	**130k**	**140k**	**150k**	**160k**
Y_p	8.76%	9.25%	6.65%	7.93%	9.81%	6.45%
η_{Rotor}	79.63%	79.89%	79.73%	76.46%	72.79%	75.33%

Table 6.8: Mass-Averaged MGT Stator Y_p and Rotor Isentropic Efficiency For Different Rotor RPMs

From Figure 6.21 and Table 6.8, it can be seen that the change of stagnation pressure loss coefficient seems to have no pattern and is relatively small as the rotor RPM increases from 110,000RPM to 160,000RPM. From the previous analysis, as the Reynolds number and mass flow rate increase from 110,000RPM to 120,000RPM,

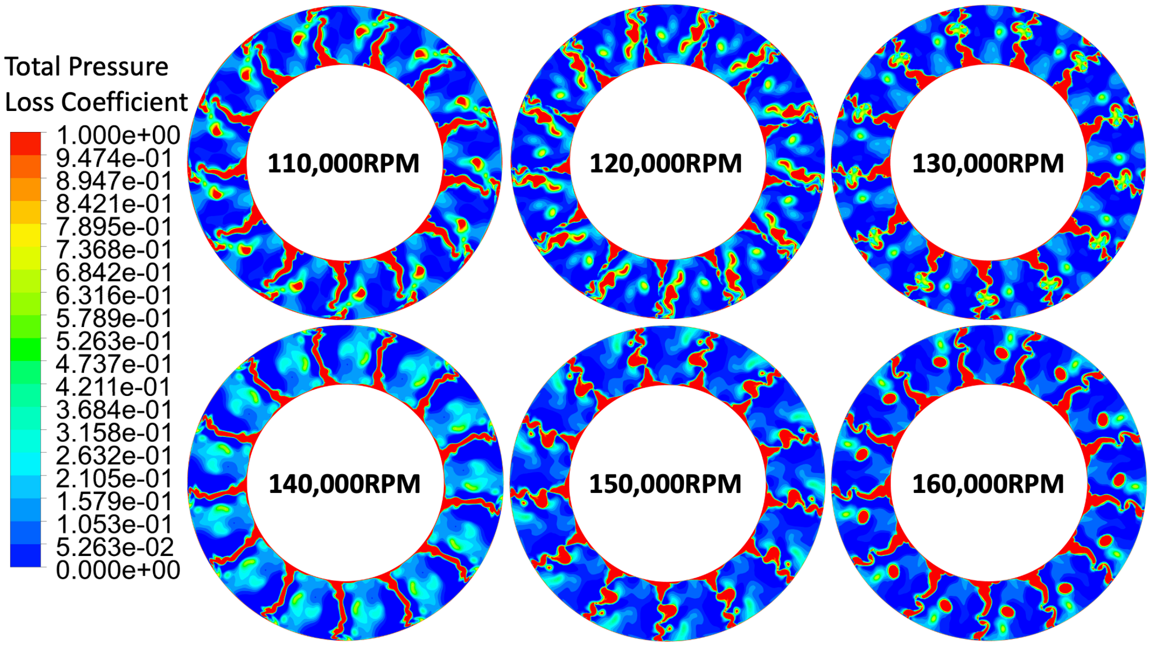

Figure 6.21: Instantaneous Stagnation Pressure Loss Coefficient Distribution on Wren100 Stator Exit Plane (LES Transient Phase 1.0)

a higher portion of transitional flow could lead to the increment of stagnation pressure loss. However, as flow gradually enters the fully turbulent regime from 150,000RPM to 160,000RPM, the interaction effect between the stator and rotor becomes smaller.

To further investigate the influence of the MGT rotor rotation on the stator flow field, the instantaneous Y_p around the stator vane at different RPMs were plotted as shown in Figure 6.22.

As the RPM increases from 110,000 to 160,000, several trends and potential implications can be observed in the rotor aerodynamic behaviour. Firstly, the red areas with high Y_p values, particularly around the trailing edge, are likely where boundary layer separation occurs, and where the flow expands and mixes turbulently with the surrounding fluid. This is indicative of increased aerodynamic losses, particularly as the RPM increases. Secondly, the wake regions, located near the mixing planes between the stator and rotor, appear to grow and shift with increasing RPM. This observation suggests that higher rotational speeds enhance the turbulent mixing in the wake or alter the vortex shedding frequency, both of which can contribute to increased aerodynamic losses.

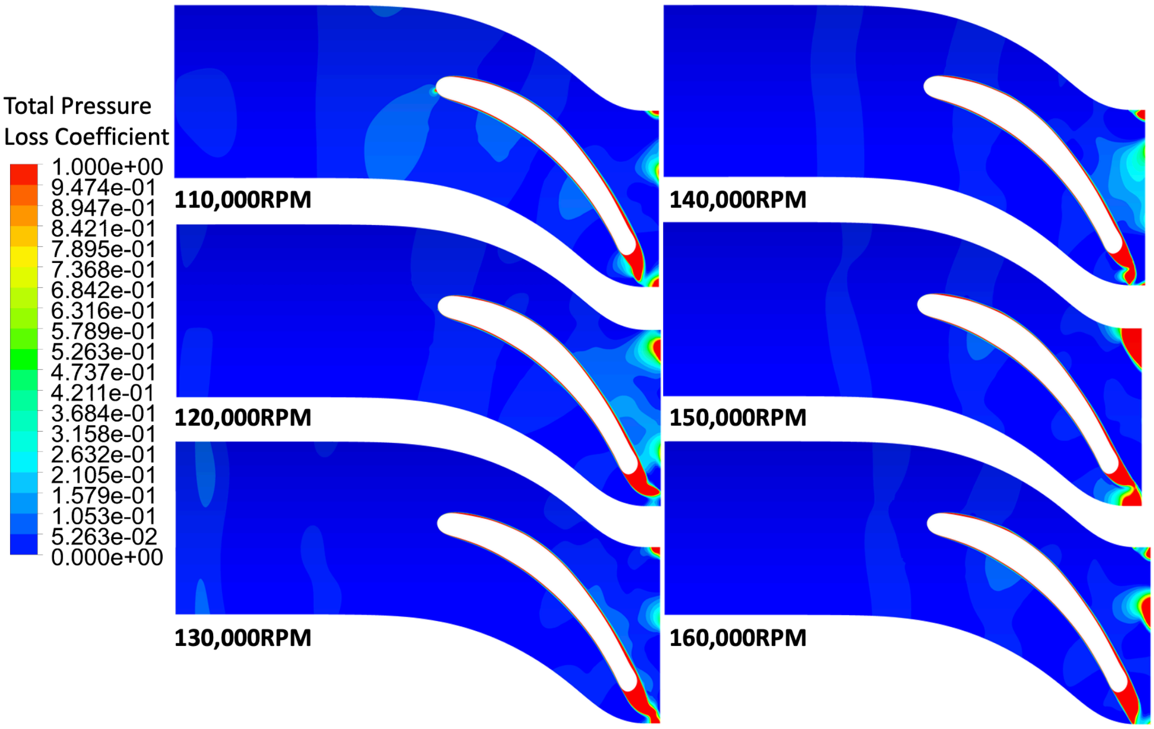

Figure 6.22: Instantaneous Stagnation Pressure Loss Coefficient Distribution on Wren100 Stator Mean Span (LES Transient Phase 1.0)

The provided plot of rotor isentropic efficiency under different RPMs in Figure 6.23 further supports these observations. The plot reveals a notable trend: as the RPM increases from 100,000 to around 130,000, the rotor isentropic efficiency initially remains stable or slightly increases, suggesting that the rotor design maintains its effectiveness up to a certain rotational speed. Beyond this point, particularly between 140,000 and 150,000 RPM, there is a sharp decline in efficiency, indicating that the rotor experiences significantly increased aerodynamic losses due to factors such as higher boundary layer separation and more intense vortex shedding. However, a slight recovery in efficiency is observed as the RPM approaches 160,000, which may suggest some adaptation of the flow structures or partial recovery of aerodynamic control at the peak RPM.

Overall, this analysis underscores the need for careful design and optimisation of stator vanes to manage the increased energy levels and mitigate the associated losses at higher RPMs. It also highlights the importance of understanding the dynamic interaction between the rotor and the stator, which becomes increasingly complex at higher RPMs. These insights are crucial for designing MGTs that can operate

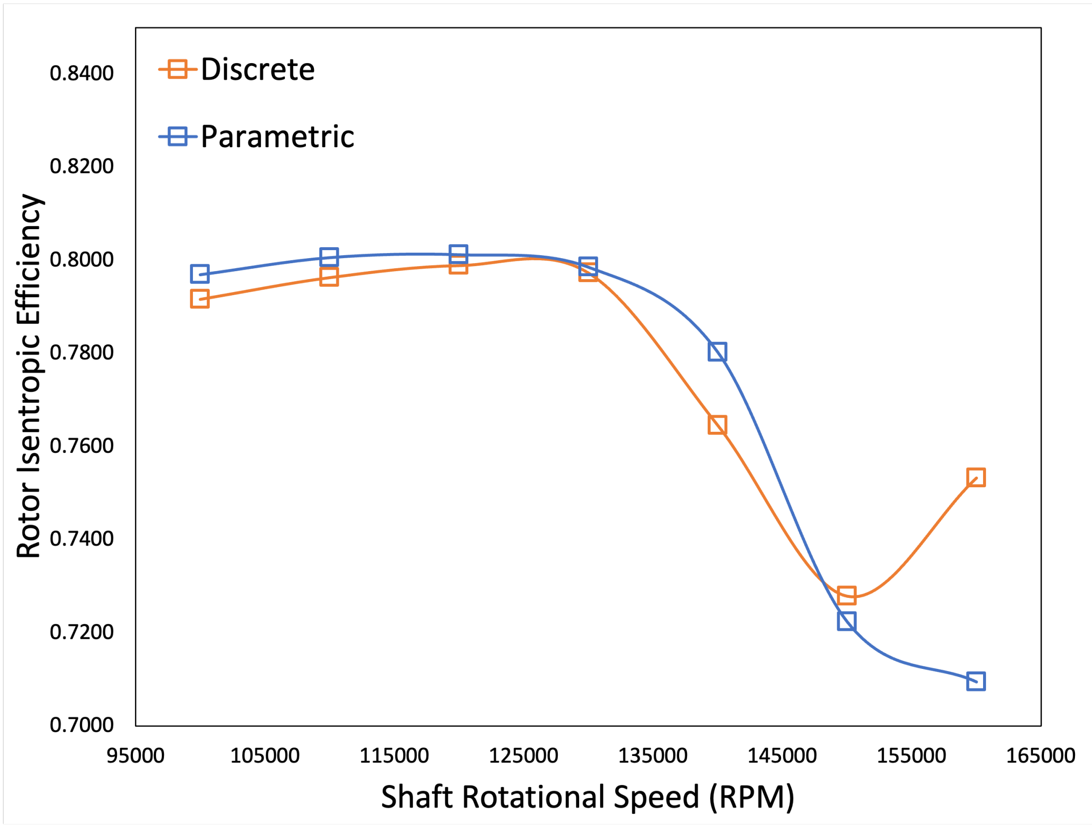

Figure 6.23: Overall Isentropic Efficiency of Wren100 Rotor Blade Under Different RPMs (RANS)

efficiently across a broad range of operational conditions.

6.5 Identification of Potential Design Enhancements through CFD Simulations

Based on dedicated CFD analysis, the potential design enhancements that could improve the Wren100 MGT aerodynamic performance are discussed in this section, which the goals were higher thrust and efficiency as requested by the engine manufacturer, Turbine Solutions Ltd. However, due to the complex 3D flow within the MGT passages, it is still uncertain whether those design changes could deliver the objectives. Hence, more parametric studies and a deeper understanding of the flow behaviours within micro turbo-machineries are required, which are also discussed in the next chapter (Chapter 8).

6.5.1 Wren100 Stator Vane

As the name suggests, the stator or nozzle guide vane (NGV), is an essential component inside the MGT to guide the flow to the correct angles before the rotor blades. However, it is inevitable for the existence of flow separation and secondary flows due to the viscous effect. The potential design enhancements for the stator vane are described as follows.

Firstly, based on the mean line predictions, it was found the secondary loss takes the greatest portion of the total loss. As demonstrated in Figure 6.24, the profile loss and trailing edge loss would gradually take smaller portions of the total loss as the Reynolds number rises.

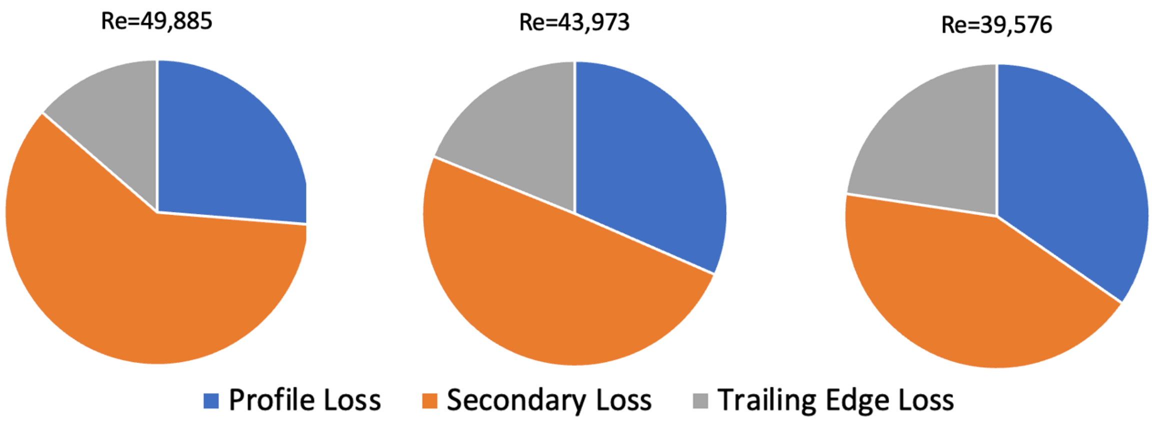

Figure 6.24: Wren100 Stator Mean Profile Loss Breakdown (Mean-Line Predictions)

From the mean profile performance, reducing the secondary loss could be the most effective way to optimise the overall stator performance, and one of the straightforward ways is by increasing the number of vanes. Theoretically, as the number of vanes rises, the blade loading for each vane would reduce, resulting in a lower secondary loss. However, with a higher number of vanes, the profile loss and base pressure loss would increase due to the greater surface area. Studies such as those by Kumar and Govardhan, and Ingram et al. have demonstrated that adjustments in vane numbers and configurations could significantly influence secondary flows and losses. These findings suggest a delicate balance and a compromise that require further parametric studies [181, 182], which the CFD analysis is also demonstrated in Subsection 8.2.1.

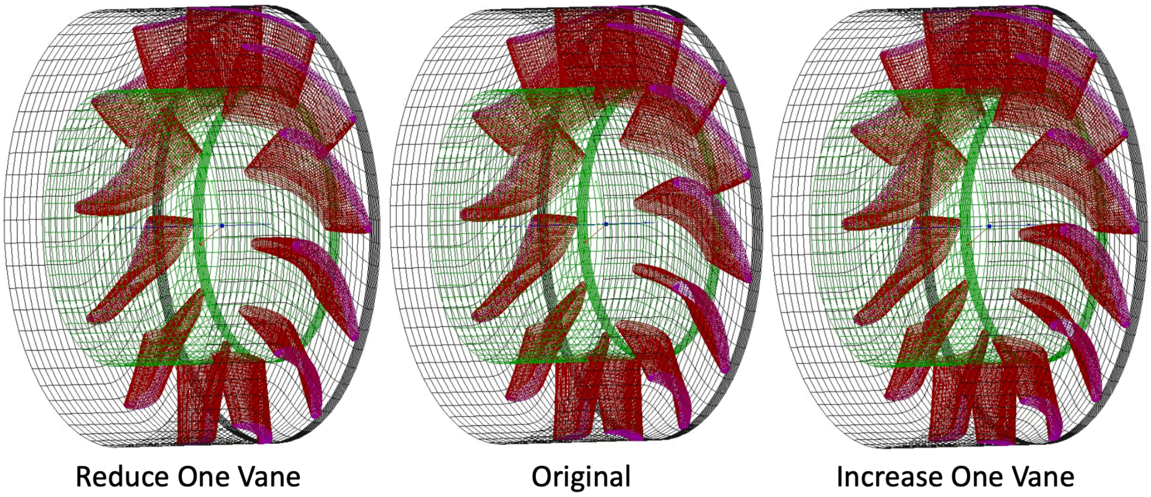

Figure 6.25: Wren100 Stator Number of Vanes Redesign

Secondly, as mentioned in the literature review chapter, another factor that could greatly affect the secondary flow is the blade aspect ratio. Adjusting the aspect ratio has been shown to significantly influence secondary flows and turbine performance, as detailed by Peters et al. and Hunt et al. These studies indicate that while higher aspect ratios can reduce secondary losses by distributing the flow more evenly along the blade span, they might also introduce complexities in flow behaviour that can adversely affect performance under certain conditions [183, 184]. To better visualise the design changes, both higher and lower aspect ratios were decided to be studied as illustrated in Figure 6.26. The detailed parametric study for this design change is described in Subsection 8.2.2.

Thirdly, based on the CFD results, one major source of loss is the profile loss due to the boundary layer separation on the suction side near the trailing edge. It was

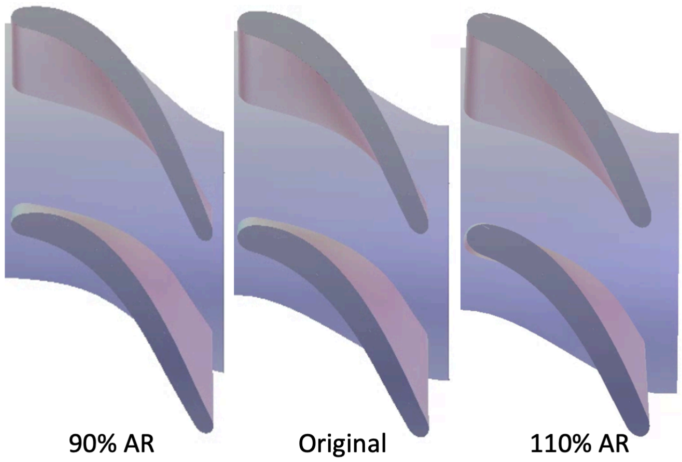

Figure 6.26: Wren100 Stator Aspect Ratio Redesign

found the trailing edge blade geometry or operating conditions might lead to a higher degree of flow separation, turbulence, or vortex shedding, especially near the root section, resulting in increased energy dissipation and aerodynamic losses. Hence, parametric studies were carried out (Subsection 8.2.3) to study how the trailing edge thickness affects the performance of the MGT as shown 6.27. Research by Gao et al. supports this investigation, demonstrating that variations in trailing edge thickness can significantly affect turbine blade performance, primarily through changes in flow behaviour and loss characteristics at the trailing edge [185].

6.5.2 Wren100 Rotor Blade

Compared to the stator vane, the potential redesign for the rotor blade based on the CFD analysis was much more difficult due to its unsteady transient nature. Hence, only two redesign recommendations came up according to the simulation results, which are summarised as follows.

Firstly, from the entropy plots, it is already known that a large portion of aerodynamic loss comes from the tip gap. To improve the efficiency, it was suggested that the tip clearance should be optimised.

Secondly, based on the analysis of the rotor flow vorticity contours at different phases (Figure 6.16), it was suggested the leading edge at the root and mean span should be optimised due to the formation of leading edge vortex as these vortices can be indicative of potential sub-optimal design features. Several published studies have also

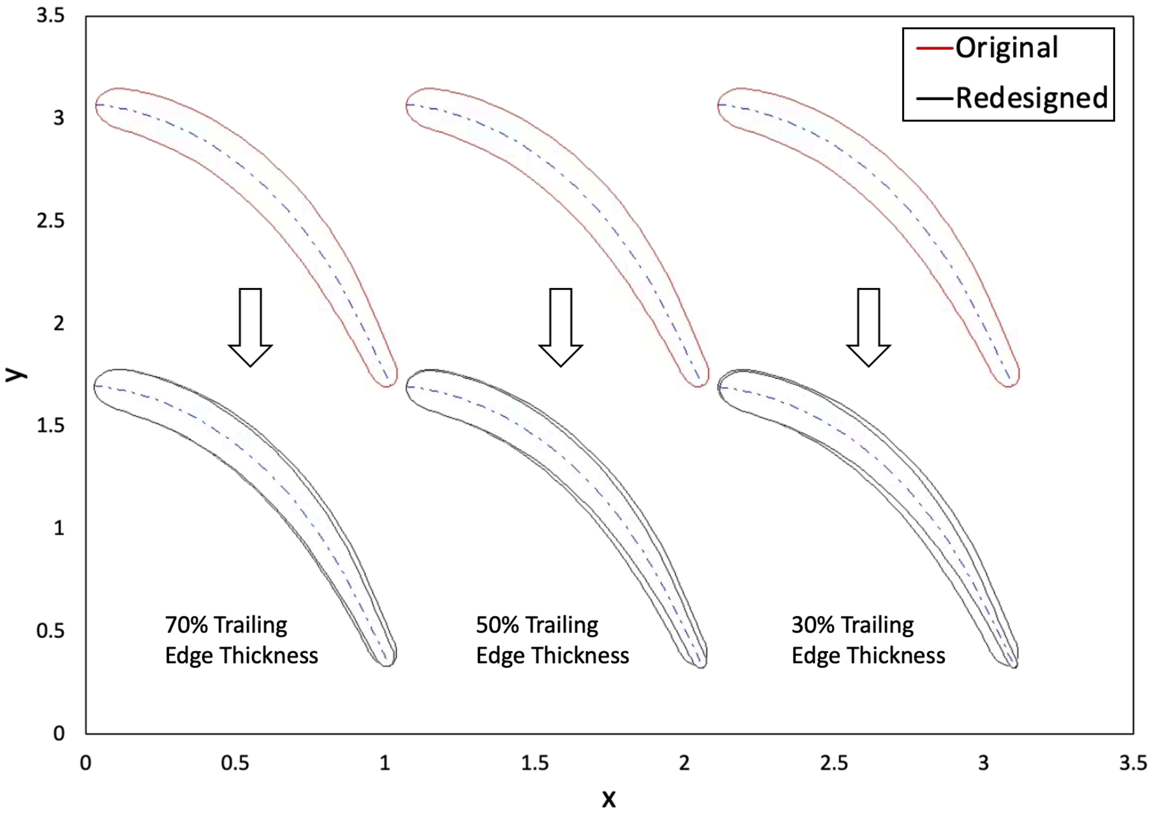

Figure 6.27: Wren100 Stator Trailing Edge Redesign

alluded to the important role of leading edge geometry in influencing the overall blade performance. Zhang et al. numerically studied the effect of blade leading edge redesign on the turbomachinery aerodynamic performance. With thinner leading edge thickness, reduced separation bubbles and 10% decreased profile loss at the design condition were discovered [186]. Thus, given the aforementioned insights from literature and CFD observations, there is a compelling rationale to carry out a parametric study focused on reducing the thickness of the leading edge, particularly in the root and mean span regions as shown in Figure 6.28.

From Figure 6.28, it can be seen the varying effects on the throat dimensions at different blade spans due to leading edge redesign. By reducing 30% of the leading edge thickness, the throat distance at the root section increased by around 10.5% while the mean span remained the same. The potential implications are described as follows. Firstly, enlarged throat areas typically allow for an increased mass flow rate, which can be advantageous as the rotor could extract higher overall work increasing the efficiency and thrust. Secondly, reduced flow separation could be achieved by

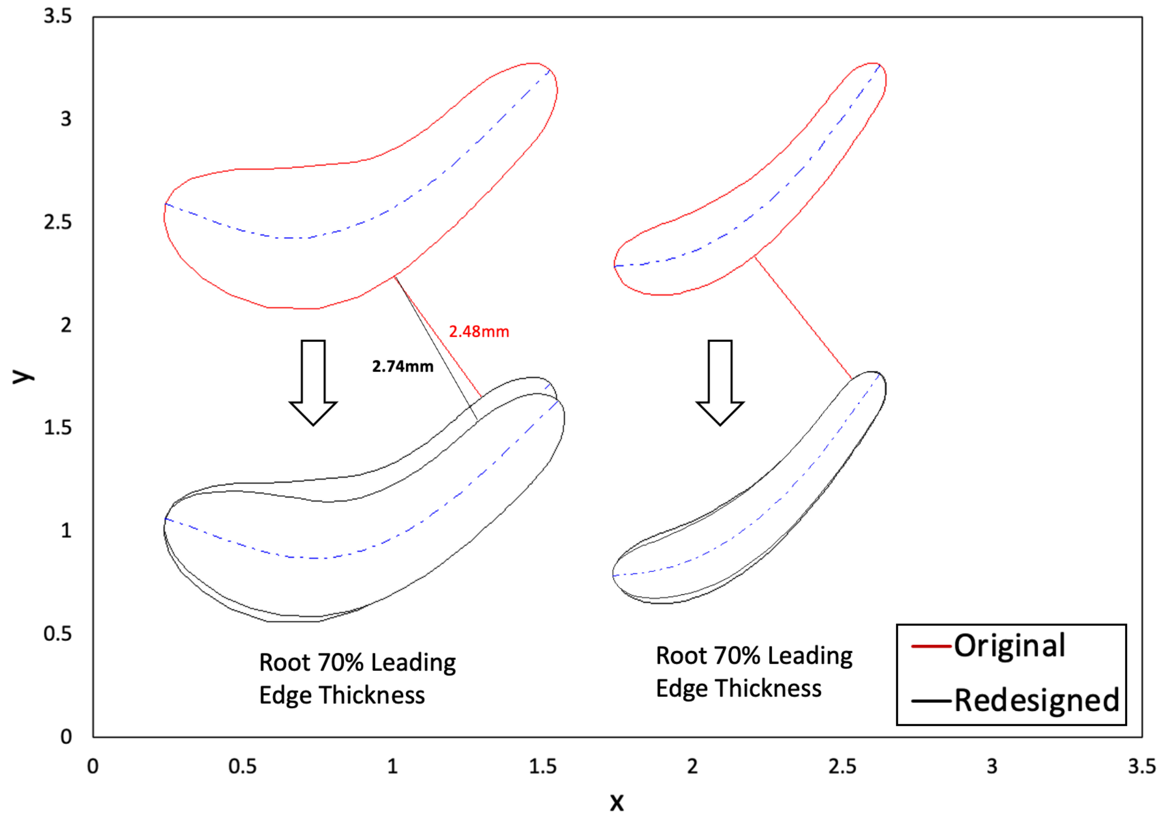

Figure 6.28: Wren100 Rotor Blade Root&Mean Leading Edge Redesign

the reduced flow acceleration due to the higher throat area. Thirdly, boundary layer development could be altered. Nonetheless, further explorations and analyses were also carried out to fully capture the impact of this design alteration on the turbine performance metrics and operational aspects (Chapter 8).

6.6 Summary

This chapter offers an exhaustive investigation into the aerodynamic characteristics of the Wren100 MGT stator vane and rotor blade. The methodological framework adopted incorporates insights from mean line predictions seamlessly integrated with findings from transient LES results.

The stator vane of the MGT predominantly showcases losses attributed to secondary flows. An in-depth scrutiny of entropy distributions ascertained a significant concentration of these losses in proximity to the hub wall. Such findings signify the amplifying influence of endwall effects on secondary losses. Additionally, given the relatively low Reynolds number characteristic of the MGT, there is an evident manifestation of laminar flow separations. These are most prominently observed on the suction side, proximate to the trailing edge of the stator vane, and are accompanied by pronounced trailing edge wakes, particularly intensified near the root span. A reduced rate of total pressure recovery observed at the mean span further corroborates the predominant influence of secondary flows in this region.

For the rotor blade, certain design peculiarities at the root span seem to preclude effective flow redirection. The periodic emergence of intense swirling flow structures near the rotor blade 'entry point' underscores potential aerodynamic inefficiencies and accentuates the exigency of a re-evaluation of the blade leading edge design. Beyond the analysis of individual components, there is a nuanced exploration of the symbiotic dynamics between the MGT stator and rotor, providing insights into their interactive intricacies.

In light of the findings regarding the aerodynamic behaviour of the existing design, a series of recommendations were proffered, and earmarked for detailed parametric evaluations in subsequent studies. Pertaining to the stator vane, key parameters delineated for further exploration encompass vane count, aspect ratio (AR), and trailing edge thickness. On the other hand, for the rotor blade, critical parameters identified for in-depth investigation include tip clearance and leading edge thickness. A comprehensive discourse on the simulation results, supplemented by a methodical analysis, is encapsulated in Chapter 8.

Chapter 7

Impact of Surface Roughness on Wren100 Turbine Stator Rotor System

7.1 Introduction

This chapter presents a comprehensive investigation of the impact of surface roughness on the aerodynamic performance of a single-stage micro gas turbine (MGT) stator-rotor system, encompassing both numerical and experimental studies. The CFD model assumes that the roughness is uniformly distributed across the surfaces of the stator vanes and rotor blades. The reason for this investigation is the potential significant influence of surface roughness on both stator and rotor components. The relative magnitude of surface roughness to the chord length, as indicated in Table 7.1, with ratios of 0.000955 for the stator and 0.00212 for the rotor, is considerably large. Such significant roughness could greatly disrupt the boundary layer flow over the blade surfaces.

The chapter begins by presenting the measured surface roughness data, accompanied by select numerical calculations. To gain an initial understanding of how surface roughness influences profile loss and trailing edge wakes, experimental data from a scaled wind tunnel cascade with rough surfaces are also discussed. Following this, a comparison of CFD results for smooth and rough turbine blades, with an original roughness of approximately 2.5 $\mu m R_a$, is presented, highlighting the effects of surface roughness on boundary layer behaviour and aerodynamic loss.

Subsequently, the chapter delves into CFD simulations conducted for various levels of roughness, ranging from 5 m Ra to 20 m Ra. These simulations aim to better understand the influence of surface roughness on the flow field within MGTs operating at relatively low Reynolds numbers. Additionally, by varying the RPMs, the impact of different Reynolds numbers with the same roughness on the MGT is also analysed.

The chapter concludes with a summary of the key findings and recommendations for future research in this area. This comprehensive analysis will contribute to a deeper understanding of the role of surface roughness in the aerodynamic performance of MGT stator-rotor systems and inform potential optimisations in their design and operation.

7.2 Presentation of Surface Roughness Data

As mentioned in the previous chapters, the surface roughness of the Wren100 stator vane and rotor blade was experimentally measured to investigate its effect on the turbine aerodynamic performance. The completed data of roughness are listed in Appendix B.1. Table 7.1 and Figure 7.1 show the average sand grain roughness data for the Wren100 stator vanes and rotor blades.

Samples	Ave. R_a (μm)	Ave. k_s (μm)	Roughness/Chord
Stator Vane	2.472	14.492	0.000955
Rotor Blade	2.606	15.279	0.00212

Table 7.1: Wren100 Average Sand Grain Roughness ($\overline{\varepsilon}$) Data

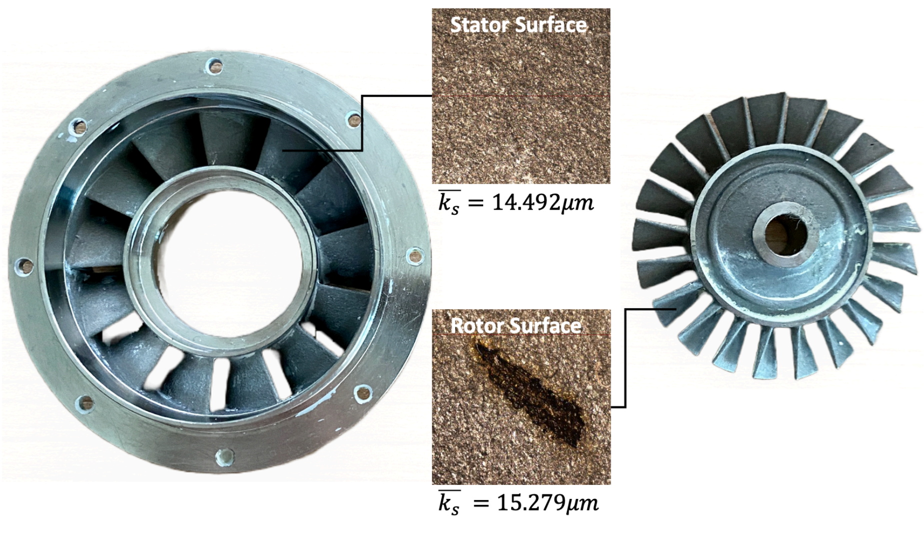

Figure 7.1: Wren100 Stator and Rotor Average Sand Grain Roughness ($\overline{k_s}$)

For typical gas turbines, it is known that the surface roughness has a significant impact on the flow structure within the blade passages as reviewed in Section 2.6.7. High surface roughness could lead to increased near-wall turbulence, which could then influence the shear stress and heat transfer. As shown in Table 7.1, compared to normal-size gas turbines, the roughness-to-chord ratio for the micro gas turbine is quite large. Thus, it was suspected that the roughness would have a huge impact on the aerodynamic performance of the MGT blades. However, due to the low Reynolds numbers of the MGTs, it is also possible that the potential thick boundary layer could offset the scale of the roughness.

7.3 Roughness Impact Tests Based on Wind Tunnel Cascade Experiments

7.3.1 Cascade Scale Study

In this section, the wind tunnel cascade scale study is presented for the Wren100 stator mean profile. One critical parameter to consider when scaling the blade profile is the roughness Reynolds number, a non-dimensional variable that characterises the flow behaviour and surface roughness effect on the blade surface. The aim was to match the original and scaled roughness based on CFD simulations. By doing so, it could be ensured that the flow characteristics within the scaled cascade experiments, such as boundary layer development and separation behaviour, remain consistent compared to the original blades.

$$k_{s,WT} = \frac{u_{\tau,o}}{u_{\tau,WT}} \cdot k_{s,o} = \sqrt{\frac{\tau_{w,o}}{\tau_{w,WT}}} \cdot k_{s,o} \tag{7.1}$$

In order to match the roughness Reynolds number, as depicted in Equation 7.1, obtaining the shear stress data on the scaled cascade blades is essential. However, this data can only be acquired through CFD simulations or experimental tests, which require prior knowledge of the surface roughness for the scaled model. To address this challenge, an iterative study was conducted using CFD simulations, as illustrated in the flow diagram (Figure 7.2).

Initially, a preliminary guess of the surface roughness for the scaled model was made by directly using the scaling factor (around 4.3), and this value was utilised to determine the shear stress data and a new surface roughness estimate. Subsequently, this updated surface roughness was employed to generate a refined rough model of the cascade blade for further simulations. This iterative process continued until the surface roughness data stabilised, indicating convergence.

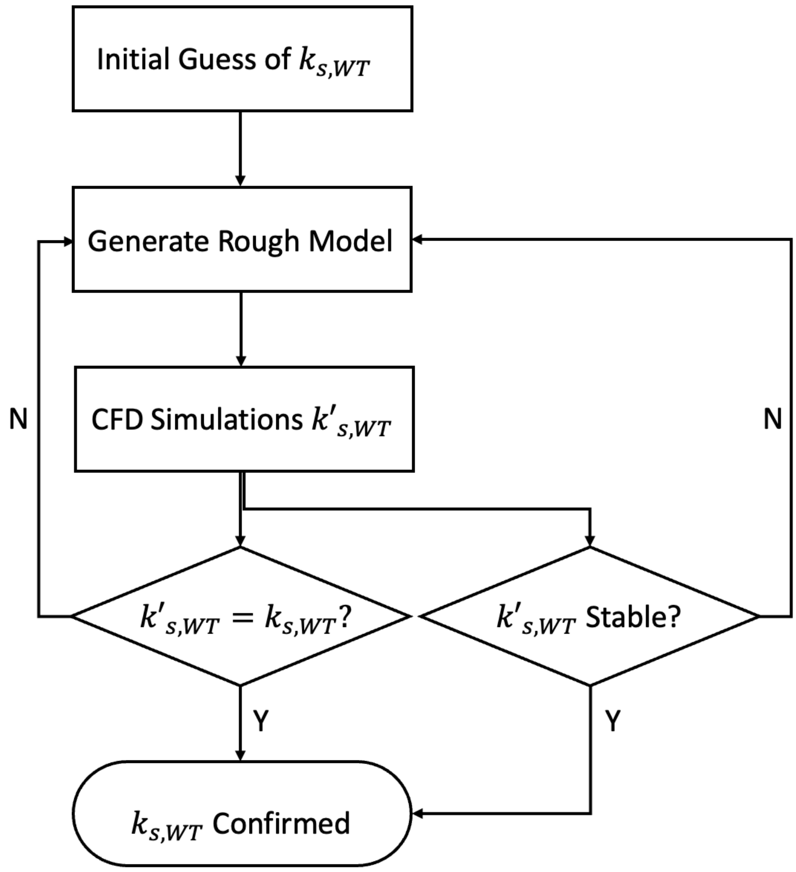

Figure 7.2: Flow Diagram of Iterative CFD Simulations to Acquire Surface Roughness of the Scaled Wind Tunnel Cascade Model

Upon completion of this iterative study, the final surface roughness for the scaled model was acquired, ensuring that the roughness Reynolds numbers were appropriately matched, which the arithmetic roughness and the sand grain roughness for the original and scaled Wen100 stator mean profile are listed in Table 7.2.

Samples	Ave. R_a (μm)	Ave. k_s (μm)
Original Profile	2.472	14.492
Scaled Cascade	8.447	49.518

Table 7.2: Original Stator Roughness Vs. Target Roughness for Scaled Wind Tunnel Cascade

According to the calculated data listed in Table 7.2, the roughness Reynolds number was calculated as shown in Equation 7.2.

$$5 < Re_k = \frac{u_\tau k_s}{\nu} = 6.234 < 70 \quad (7.2)$$

From the calculated Re_k, it was discovered the regime of roughness for the Wren100 stator blade is transitional rough, where the surface roughness elements start to have a noticeable impact on the flow field.

To match the Re_k for the wind tunnel cascade with the original MGT stator vane, the arithmetic roughness of the 3D printed blade surface was increased and measured by the professional roughness tester, Alicona InfiniteFocusSL.

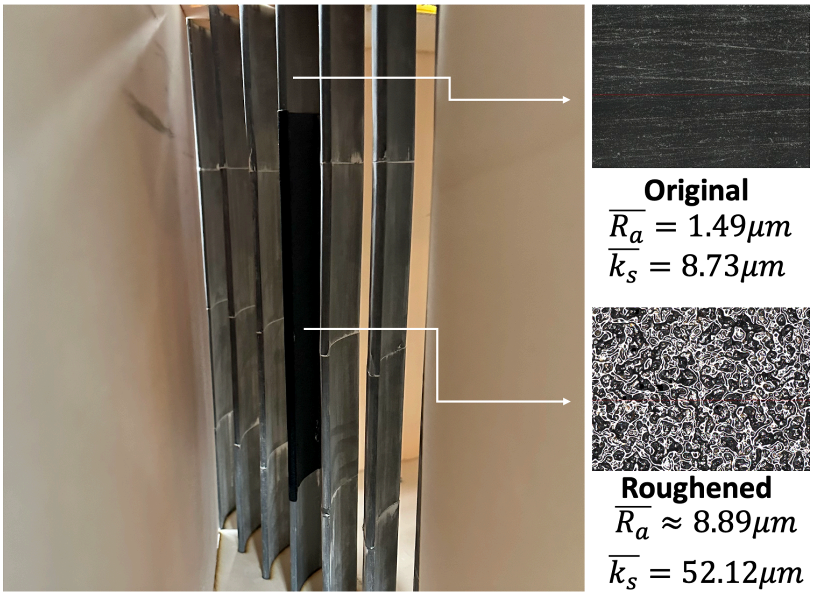

Figure 7.3: Sand-Roughened Wind Tunnel Cascade Middle Blade

As shown in Figure 7.3, the surface roughness of the middle blade was increased to near the required values ($k_s \approx 50\mu m$) by attaching a piece of rough paper on the blade surface.

7.4 CFX Roughness Model Validation Based on Cascade Data

The models used to investigate the impact of surface roughness on the Wren100 stator vane mean cascade models assume the same sand grain roughness is uniformly distributed. The fluid domain and detailed LES setups are the same as described in Subsection 5.4.3.1, except for the roughness factors. As shown in Figure 7.4, ANSYS

CFX does not modify the model surface directly; instead, it utilises the input sand grain roughness and user-selected wall function to mimic the flow behaviour influenced by the rough surface. This approach is a mathematical adjustment rather than a geometric modification, meaning no visual changes can be seen on the surface of the model (as seen in Figure 5.20). However, the effects of the surface roughness are subsequently analysed based on the changes in the simulated near-wall flow field.

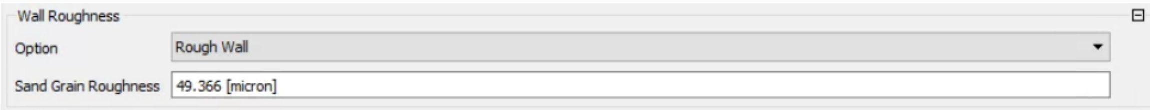

Figure 7.4: ANSYS CFX Input for Wall Roughness

The validation process for these roughness adjustments follows a similar methodology as outlined in Subsection 5.4.3.3, where the roughness factors were systematically tested. Results from this validation, including spanwise exit velocities and total pressures, were cross-referenced against wind tunnel data with matched roughness Reynolds numbers, ensuring the accuracy and reliability of our simulation approach as demonstrated in Figure 7.5.

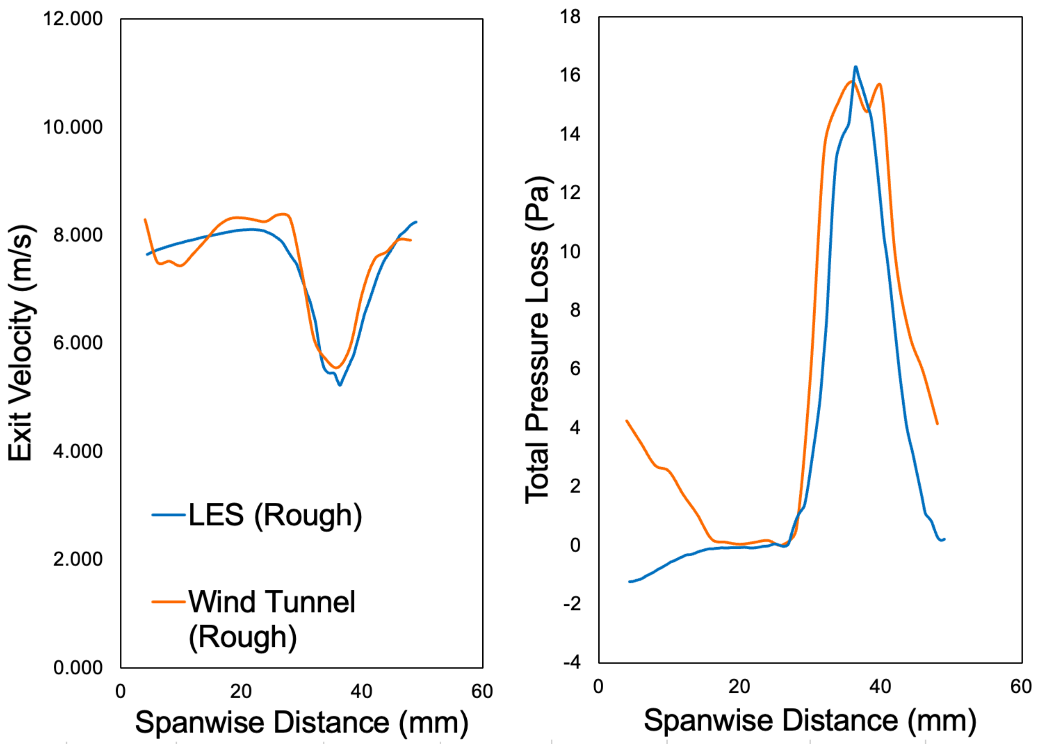

Figure 7.5: Spanwise Exit Velocity and Total Pressure Loss (LES vs. Wind Tunnel)

From Figure 7.5, it can be seen that the LES WALE model could capture the location and thickness of the trailing edge wake with high precision. Considering the limitations of the experimental measurements and the CFD model, it was confirmed that the LES WALE model could accurately predict the impact of surface roughness for the MGT stator. The following subsection describes how different levels of surface roughness influence the MGT aerodynamic performance.

7.5 Results & Discussion

Based on the validated LES model, a series of simulations were carried out for the original sand-grain (SG) roughness, $30\mu m$ SG and $60\mu m$ SG to study how different levels of roughness affect the flow field and the overall blade aerodynamic performance of the single stage MGT. Simulations based on two rotational speeds, including the 120,000RPM (normal Reynolds number) and 160,000RPM (peak Reynolds number), were conducted to investigate the influence of different low Reynolds numbers.

RPM	Original SG	$30\mu m$ SG	$60\mu m$ SG
$120k$ Stator	2.65	5.01	8.64
$120k$ Rotor	5.47	9.28	15.96
$160k$ Stator	1.73	3.17	5.39
$160k$ Rotor	5.34	9.16	15.06

Table 7.3: Wren100 Stator & Rotor Roughness Reynolds Number (Re_k)

The Re_k, thrust, efficiency and profile loss for the Wren100 micro gas turbine with and without the surface roughness are displayed in Table 7.3 and 7.4, which all the simulations were carried out at the design points of 120,000RPM and 160,000RPM. The results show both thrust and efficiency slightly change for the rough blade cases, in which the efficiency seems to be more sensitive to the change of surface roughness. It can be seen that most of the loss increment comes from the rise of profile loss with the rotor blades. On the contrary, despite the decline in total efficiency, the surface roughness would cause the decrement of profile loss in the MGT stator at a lower RPM of 120,000. The isentropic efficiencies, specifically the total-to-total efficiency, were calculated using the Turbo Macros feature in ANSYS CFD-Post. This tool automatically computes various performance metrics by applying industry-standard equations and methodologies tailored for turbomachinery. The total-to-total isentropic efficiency was derived using the formula 7.3.

$$\eta(\%) = \frac{h_{2t} - h_{1t}}{h_{2t,is} - h_{1t}} \times 100 \tag{7.3}$$

Where h_{1t} is the total enthalpy at the turbine inlet, h_{2t} is the total enthalpy at the turbine outlet, and $h_{2t,is}$ is the isentropic total enthalpy at the outlet, calculated assuming an isentropic process from the inlet to the outlet pressure.

Case	T_{02} (k)	Thrust (N)	η (%)	$Y_{p,stator}$ (%)	$Y_{p,rotor}$ (%)	RPM
Smooth	719.034	26.24	81.2	6.88	32.49	120k
Original SG	715.436	26.21	79.9	6.73	40.58	120k
30μm SG	717.272	26.45	80.0	8.41	37.78	120k
60μm SG	716.733	26.34	77.1	7.77	44.22	120k
Smooth	968.955	132.8	84.6	6.453	21.828	160k
Original SG	962.859	130.9	85.5	13.676	26.047	160k
30μm SG	973.490	129.9	81.8	10.437	25.211	160k
60μm SG	977.421	129.3	79.0	9.212	25.458	160k

Table 7.4: MGT Discrete Model Performance With Surface Roughness Based on LES WALE (120,000RPM)

As shown in Table 7.4, a noteworthy observation is the large influence of the increment of RPM and varying degrees of surface roughness on the loss behaviours of the MGT. The case of the MGT stator operating at 120,000 RPM exhibits marginal variations in the stagnation pressure loss coefficient (Y_p). Previous analysis of the flow field properties ascertains that at the rotational speed of 120,000RPM, the boundary layer exhibits a substantial thickness. Consequently, the original surface roughness may not be sufficiently pronounced to elicit any significant perturbations in the boundary layer flow dynamics as it is within the laminar sublayer ($Re_k < 5$). However, an increase in roughness to 30μm SG and 60μm SG causes an upward trend in aerodynamic loss, which suggests that the boundary layer might undergo disturbances which in turn intensify the turbulence and energy dissipation phenomena ($5 < Re_k < 70$). This inference finds support when examining the cases at 160,000 RPM, where the boundary layer could be markedly thinner. At this RPM, the impact of the original SG roughness on the MGT stator is considerably more pronounced than its counterpart at 120,000 RPM. Intriguingly, a further increment in roughness to 30μm SG and 60μm SG yields a decrement in MGT stator loss to approximately 10.437% and 9.212% respectively. This behaviour could be attributed to a multiplicity of factors contingent on the complexity of the flow field, including but not limited to roughness-induced flow structures or re-laminarisation. Further studies could be conducted to better understand this flow behaviour within MGTs.

For the MGT rotor, the ramifications of surface roughness on performance are marginally more acute compared to the stator, which can be attributed to the smaller chord sizes. Nonetheless, no discernible trend could be summarised as surface roughness progresses from a smooth surface to $60\mu m$ SG. It is noteworthy, however, that a general increase in rotor roughness is accompanied by an escalation in aerodynamic losses.

In summation, the impacts of surface roughness on the aerodynamic performance of both the MGT stator and rotor are imbued with complexity. A thorough understanding of the multifarious flow behaviours necessitates an in-depth analysis of the validated CFD results, which will be meticulously dissected in the subsequent subsections.

7.5.1 Impact on the MGT Stator Trailing Edge Wakes

7.5.1.1 Normal Operating Conditions - 120,000RPM

It is known that the surface roughness could potentially induce the transition from laminar to turbulent flow, which could enhance the mixing process after the gas turbine blade trailing edge increases the wake depth. However, no such studies have been carried out to analyse how the roughness influences the TE wake for MGTs. For the Wren100 stator vanes, the phase-averaged of the relative velocities for different levels of sand-grain (SG) roughness at the mean span was plotted spanwisely positions as shown in Figure 7.6.

From Figure 7.6, it can be seen that the relationship between the wake depth and the SG roughness for MGTs is not linear. As the roughness increases from the original to approximately $30\mu m$, the size and depth of the TE wake increase as expected. However, as the SG roughness rises from $30\mu m$ to $60\mu m$, the wake size and depth reduce around 20.46%. Based on the observation, it seems there exists an "optimal" roughness size (or optimum maintenance intervals) that induces the greatest turbulence and wake deepening, which in this specific MGT is around $30\mu m$ SG. However, when roughness exceeds this critical level of $60\mu m$, the turbulence induced by the roughness might be too intense, leading to a thicker, more resistant boundary layer.

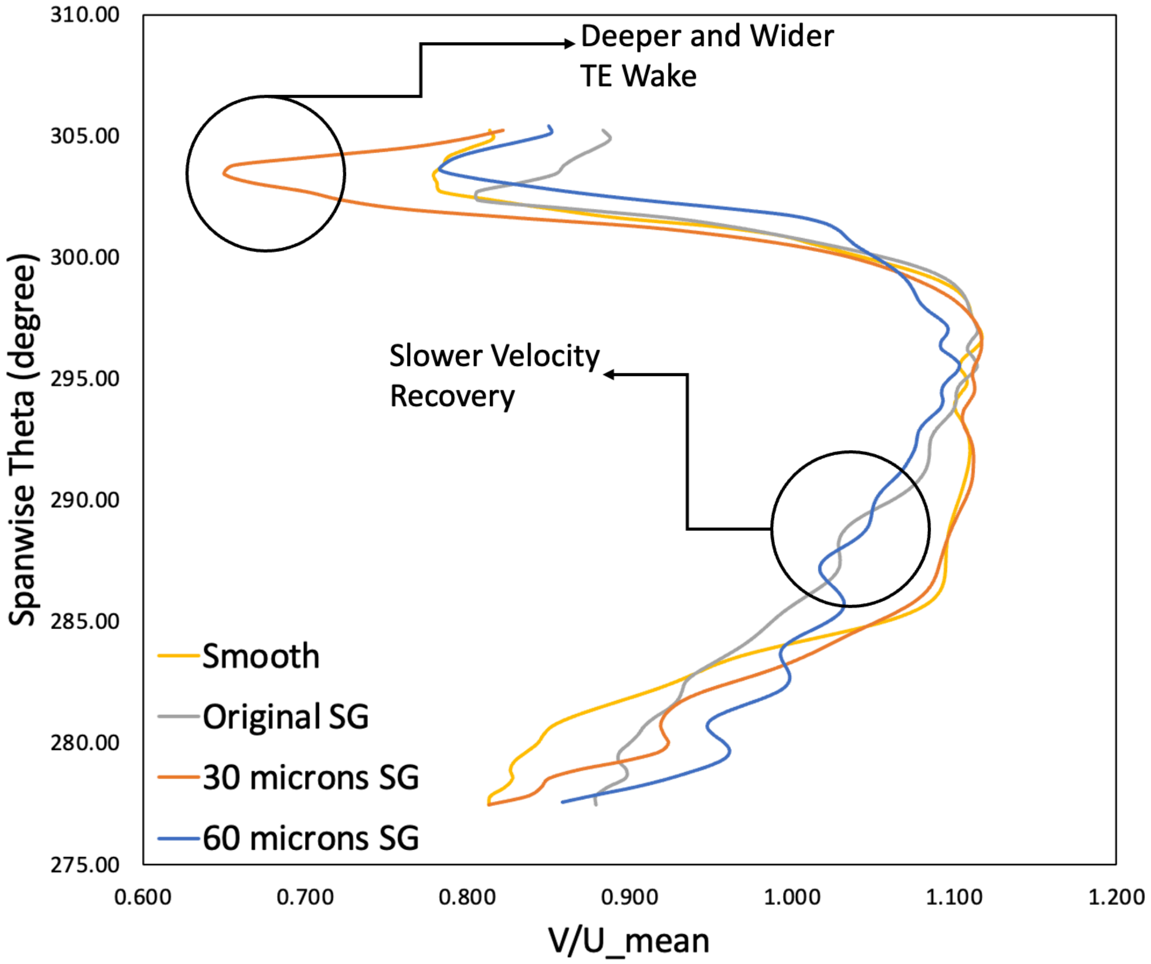

Figure 7.6: Phase-Averaged Spanwise Relative Velocities 10% Chord After the Wren100 Stator TE For Different Levels of Roughness (120,000RPM)

This could limit the formation of vortical structures (which happens from root to tip and affect the generation of secondary flows), thereby reducing the wake depth that reduces the mass-averaged stagnation pressure loss from 8.41% to 7.77% as listed in Table 7.4. The observation that the 30μm SG case has the highest stagnation pressure loss coefficient further substantiates this hypothesis. This unusual flow behaviour could be caused by the local flow features such as secondary flow and vortex shedding. At a certain level of SG roughness (30μm), those flow structures would enhance the wake deepening. However, for other roughness levels, the same flow structures could inhibit the wake formations. In addition, compared to the smooth and 30μm SG cases, the original SG and 60μm SG share similar velocity recovery behaviours outside the wake regions (slightly slower). This could be caused by several factors, including the enhanced strength of secondary flow structures due to the different boundary layer states or the altered transition location as the roughness level changes. Previous studies have also shown how rough-wall boundary layers cause big changes to secondary flow structures. Based on experimental studies, Vanderwel and Ganapathisubramani proved that secondary flows could be directly influenced by the spacing of surface roughness and developments of boundary layers [187]. Coull et al. numerically studied a turbine cascade, and they also discovered that larger secondary flow structures with higher SKE (secondary kinetic energy) could be caused by the thickening of the inlet boundary layer [188].

The intriguing finding and reveals the complexity and multidimensional nature of the aerodynamic effects of surface roughness. Therefore, to better visualise the impact of roughness on the TE wakes, the entropy creation downstream of the stator vane at different phases was plotted as shown in Figure 7.7.

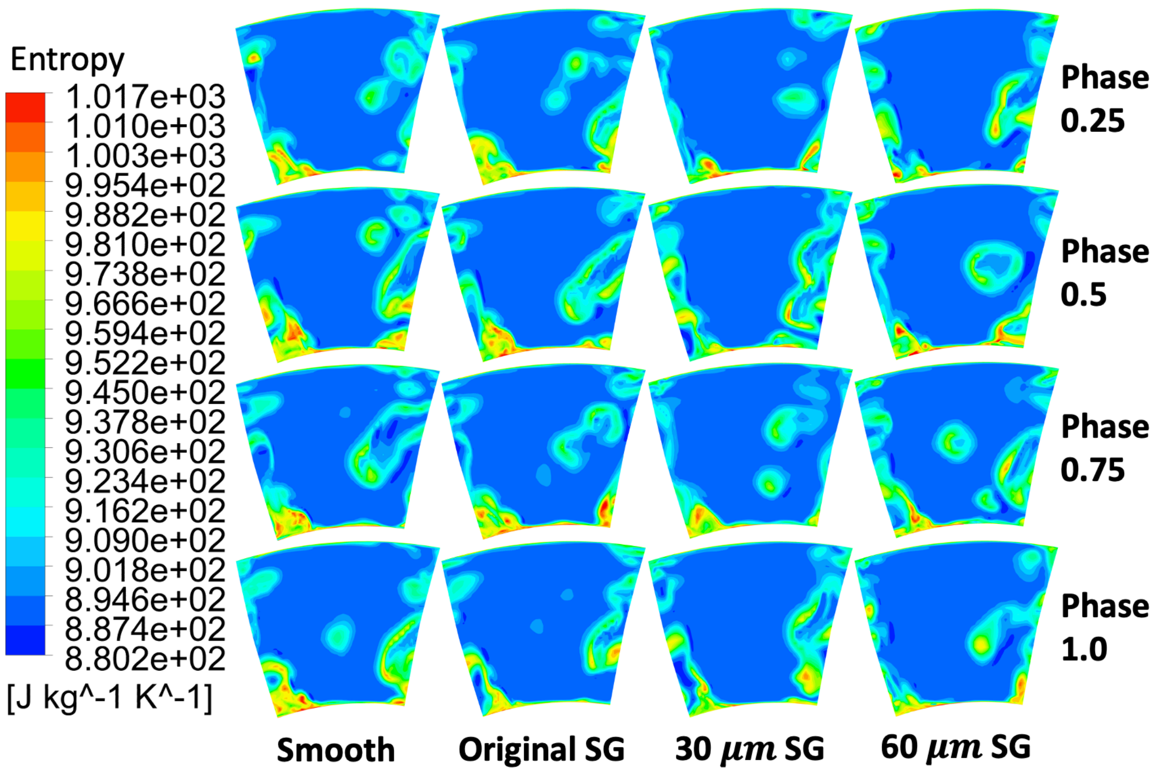

Figure 7.7: Wren100 Stator Exit Instantaneous Entropy Generation at Different Phases (120,000RPM)

The examination of the entropy contours sheds light on the intricate nature of loss generation mechanisms that transpire within the flow passage downstream of the MGT stator vanes. The manifestations of these processes are conspicuously influenced by variations in surface roughness. When the surface roughness is increased from a smooth configuration to the original SG roughness size of approximately $14.5\mu m$, a perceptible hastening in the migration and dissipation of trailing edge wakes can be visualised. With further increment in the roughness measure to $30\mu m$ SG, the dissipation of the wakes presents a higher degree of difficulty, which in turn escalates the overall stator loss. Strikingly, when the roughness level reaches the $60\mu m$ SG mark, the nature of the swirling flow patterns bears closer resemblance to the phenomena observed for the original SG case. This is corroborated by the phase-averaged spanwise relative velocities depicted in Figure 7.6. The augmentation of secondary flow activity seemingly attenuates the sizes and depths of wakes ensuing from the MGT stator vane trailing edge with elevated roughness levels.

A comprehensive assessment of the results indicates an "optimal" roughness value of approximately around $30\mu m$ SG for the Wren100 MGT stator. As the roughness ascends from the original SG to $30\mu m$ SG, the performance of the stator experiences degradation, which is ostensibly due to the growth of profile loss. Conversely, as the roughness is further increased from $30\mu m$ SG to $60\mu m$ SG, an amelioration in the aerodynamic performance of the stator is noticed. The enhanced performance at $60\mu m$ SG, as opposed to $30\mu m$ SG, can be partially attributed to the fact that the increased roughness could alter the turbulence behaviour in the boundary layer, leading to flow local transition to turbulence. This potential induced transition, in turn, might reduce the flow separation on the blade surface, thus decreasing the profile loss and enhancing the aerodynamic performance. Additionally, increased turbulence intensity caused by the higher roughness might disturb the formation and evolution of the vortical structures in the wake, reducing the wake-induced losses. Further analysis and visualisation of the flow field are presented in the following subsections.

7.5.1.2 Peak Operating Conditions - 160,000RPM

To investigate how the surface roughness at the peak Reynolds number conditions influences the trailing edge wakes of the MGT stator vanes, the mean span phase-averaged relative velocities for 160,000RPM conditions were plotted as shown in Figure 7.8.

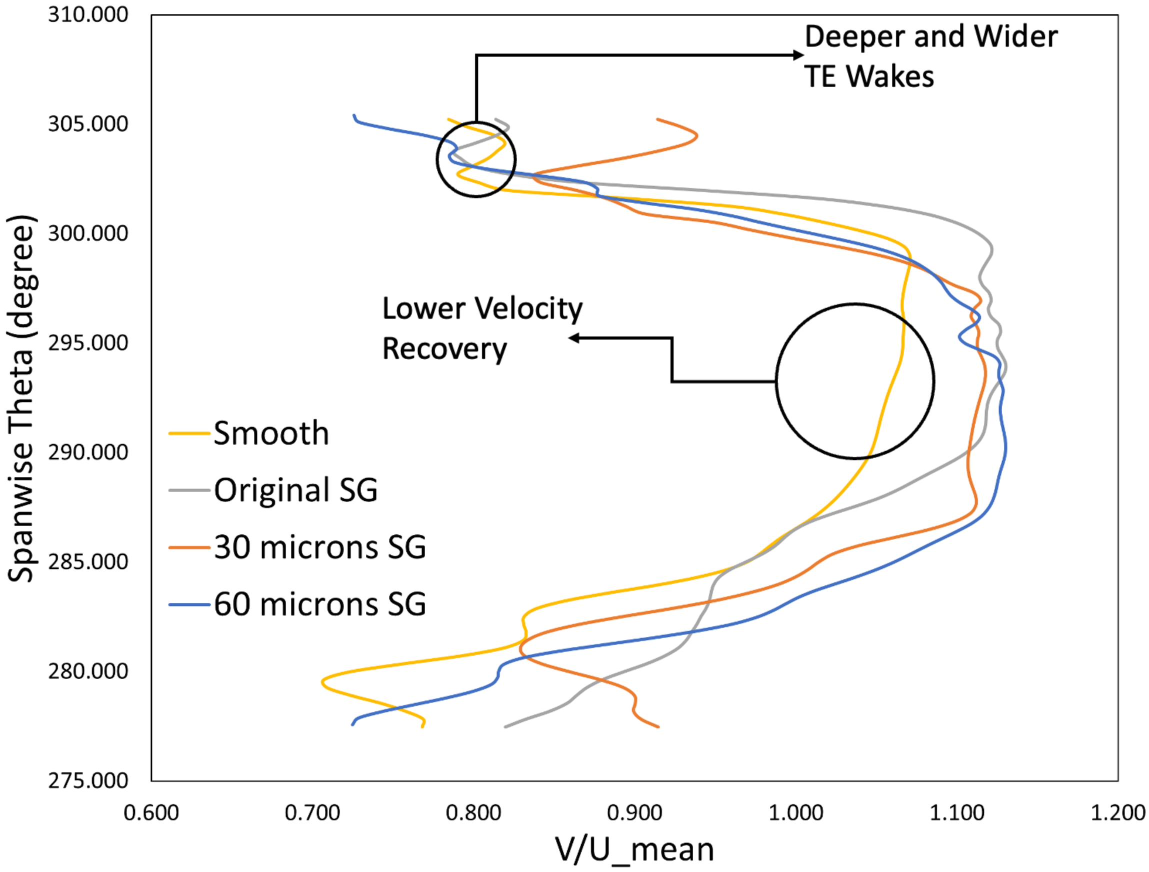

Figure 7.8: Phase-Averaged Spanwise Relative Velocities 10% Chord After the Wren100 Stator TE For Different Levels of Roughness (160,000RPM)

From the MGT stator mean exit spanwise relative velocities plot, it was found the wake behaviours are significantly different compared to the 120,000RPM conditions. The same levels of surface roughness seem to induce a different flow response due to the increased Reynolds number and reduced boundary layer thickness at this rotational speed. What stands out is the 30μm SG case, which resulted in the highest stator loss at 120,000RPM, and now exhibits the smallest wake.

For the spanwise positions outside the wakes regions, it can be noticed the smooth stator case has minimal recovered velocity. The velocity rates for different levels of roughness are quite similar, which is also different compared to the 120,000RPM conditions. This could indicate that the impact of roughness on the TE wake is less pronounced at the peak operating RPM. Compared to the 120,000RPM case, the 160,000RPM case could have higher turbine inlet total temperature and pressure, which would result in smaller average roughness Reynolds number Re_k with the same level of sand grain (SG) roughness as calculated in Table 7.3. Similar to the 120,000RPM case, to better visualise the impact of roughness on the trailing edge loss, the entropy creation at different phases under 160,000RPM operating conditions was also plotted.

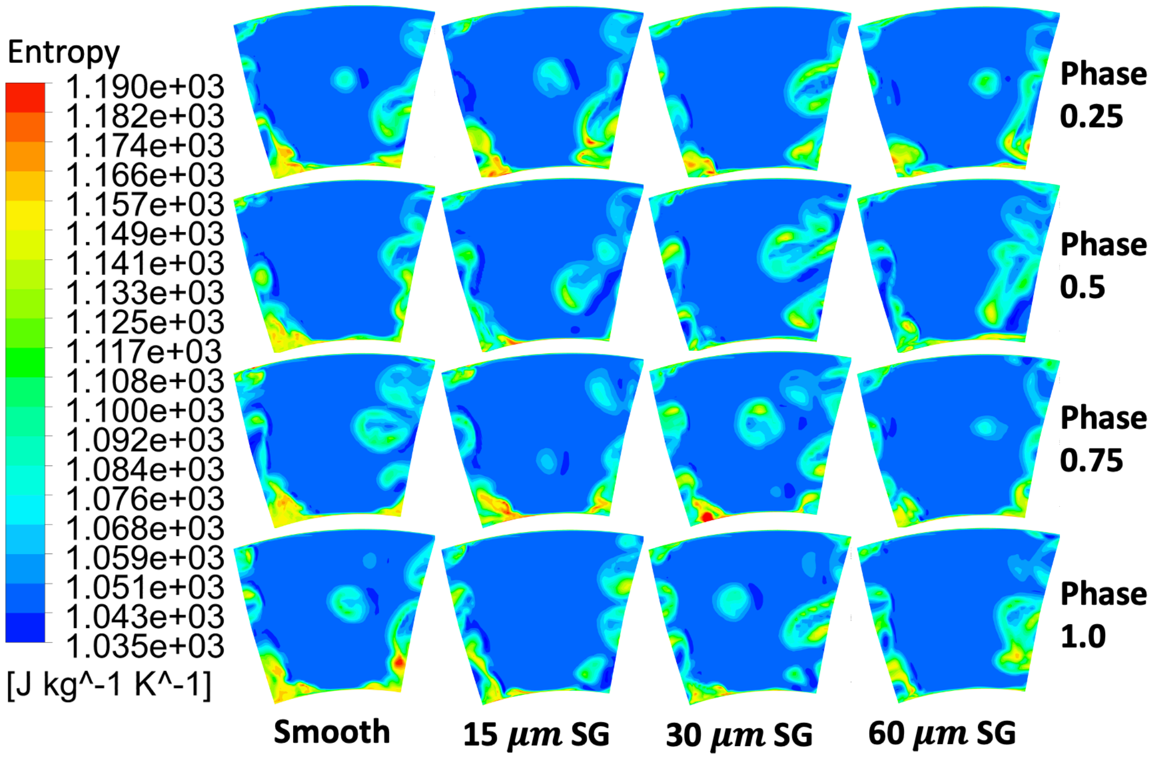

Figure 7.9: Wren100 Stator Exit Entropy Generation at Different Phases (160,000RPM)

As shown in Figure 7.9, it was observed the periodic formation of trailing edge wakes behaviours are similar for different levels of roughness. This could indicate the unsteady vortex shedding mechanism would not be greatly altered by the change of surface roughness under the peak operating conditions. However, the dissipation of trailing edge vortices as they propagate downstream of the trailing edge seems to be slower for the smooth and $30\mu m$ SG cases. This could be because the enhanced momentum exchange between the high-speed flow outside the wake and the low-speed flow within the wake might not be as effective in accelerating the wake dissipation as it would be in the cases with other roughness levels. Further studies of this interesting flow behaviour can be conducted to better understand its aerodynamics.

7.5.2 Impact on the MGT Stator Vane Boundary Layer & Efficiency Loss

7.5.2.1 Normal Operation Conditions - 120,000RPM

As displayed in Figure 7.10, the phase-averaged skin Friction coefficient magnitudes were plotted to highlight the influence of surface roughness on the wall shear stress, which also generally leads to a change in the overall vane profile loss. The use of phase-averaged wall shear magnitude for the computation of skin friction coefficients, despite transforming negative skin friction values into positive ones, remains a valuable approach. This approach is particularly informative when combined with phase-averaged data across all three axes Cf_x, Cf_y, and Cf_z as it encapsulates the comprehensive impact of viscous forces. Although this methodology may mask specific flow features such as laminar separation regions, the validation of flow separation has been supplemented by the visualisation of the Cf_z plots in Chapter 6 and the following velocity vectors, which can qualitatively confirm the presence of separation phenomena.

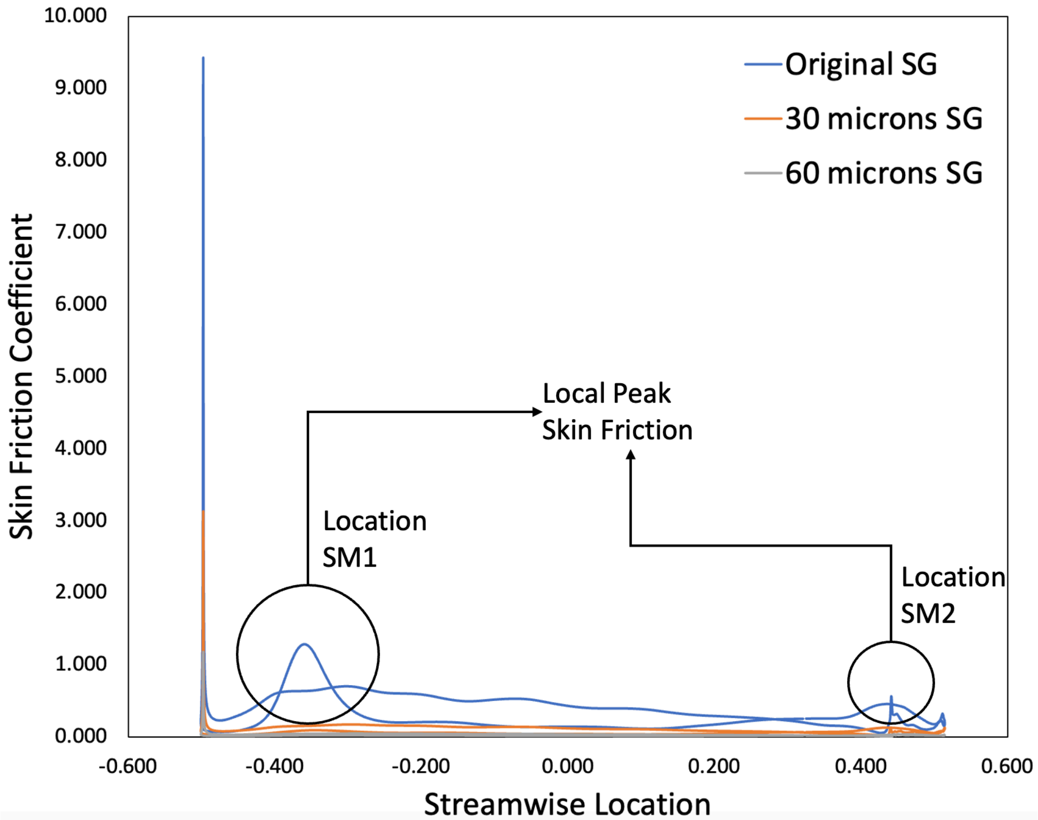

Figure 7.10: Phase-Averaged Wren100 Stator Mean Streamwise Skin Friction Magnitude For Different Levels of Roughness (120,000RPM)

According to the above plots, it was found that the skin friction for the MGT stator is quite sensitive to the change of surface roughness. For relatively low Reynolds number turbine blades, it is known that increased surface roughness tends to reduce laminar separation bubbles (thus reducing loss), which the flow transition could be delayed (as mentioned in Subsection 7.5.1.1) and cause the boundary layer to be thinner, thereby reducing the skin friction. Compared to the pressure side, the suction side could be more sensitive to the roughness level, which can visualised by the sudden increase of skin friction as seen in Location SM1 and SM2. The local peak of skin friction on the suction side positioned about 15% chord downstream of the leading edge is caused by the flow separation behaviour near the leading edge as displayed in Figure 7.11.

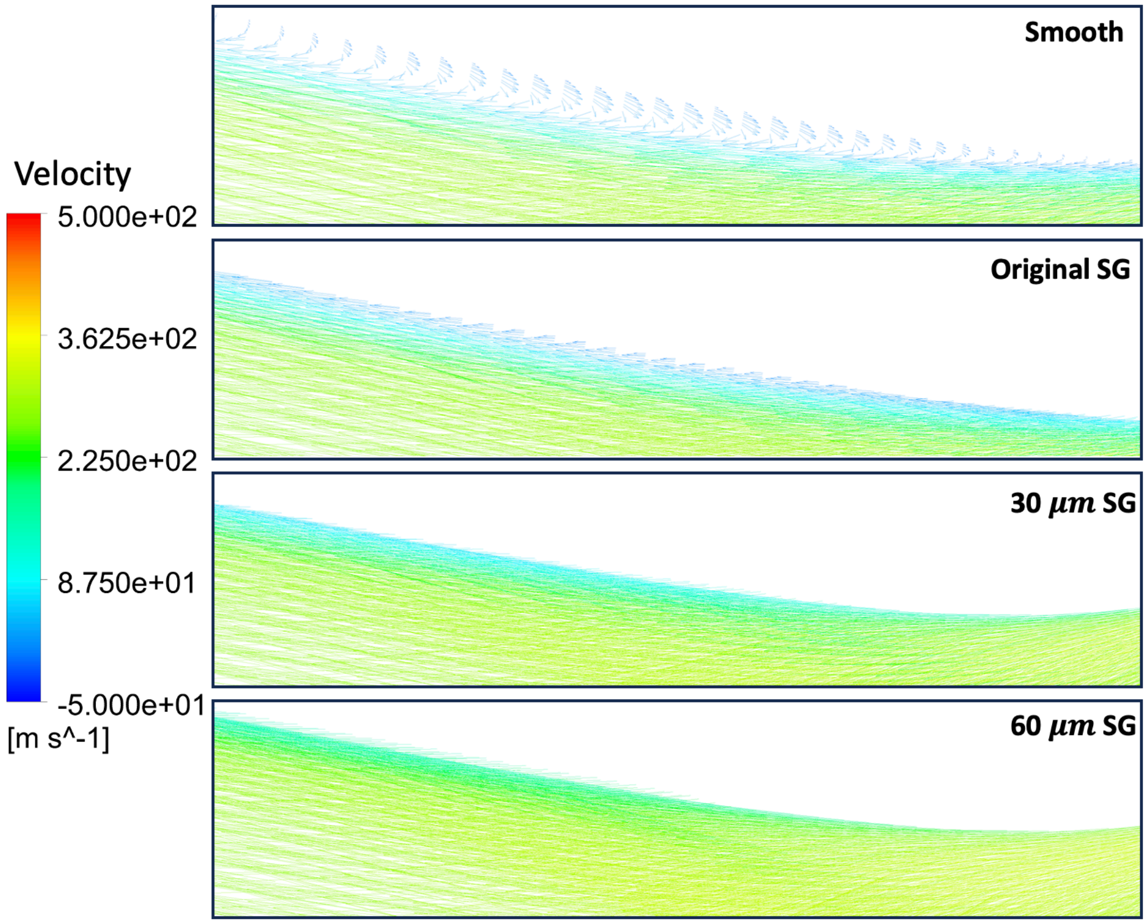

Figure 7.11: Velocity Vectors (SM1) Showing Flow Separation

It can be seen from the velocity vectors, that the flow separation reduces rapidly as surface roughness increases, which the changes in boundary layer development can also be visualised in Figure 7.12 and 7.13. To further investigate the impact of roughness on the boundary layer development, the U_{98} plots were created on the mean span. The values U_{98} were calculated based on Equation 7.4.

$$U_{98} = \frac{LocalVelocity}{FreeStreamVelocity} \approx 0.98 \tag{7.4}$$

At location 1, the thickening of the boundary layer (70.4 μm) is caused by the flow separation, in which the flow reattachments cause the regional sudden local increase of skin friction near position SM1. As flow separates, the boundary layer could also undergo transition, which then relaminarise at location 2. Notably, with the increase of roughness to 30μm SG and 60μm SG, the dampening effect of the local peak of skin friction after the leading edge can be observed. As higher roughness could potentially reduce laminar separations at low Reynolds number flows, thereby preventing flow transition at location 1 and reducing the boundary layer thickness (from 70.4μm to 2.2μm) as shown in Figure 7.12 and Figure 7.13.

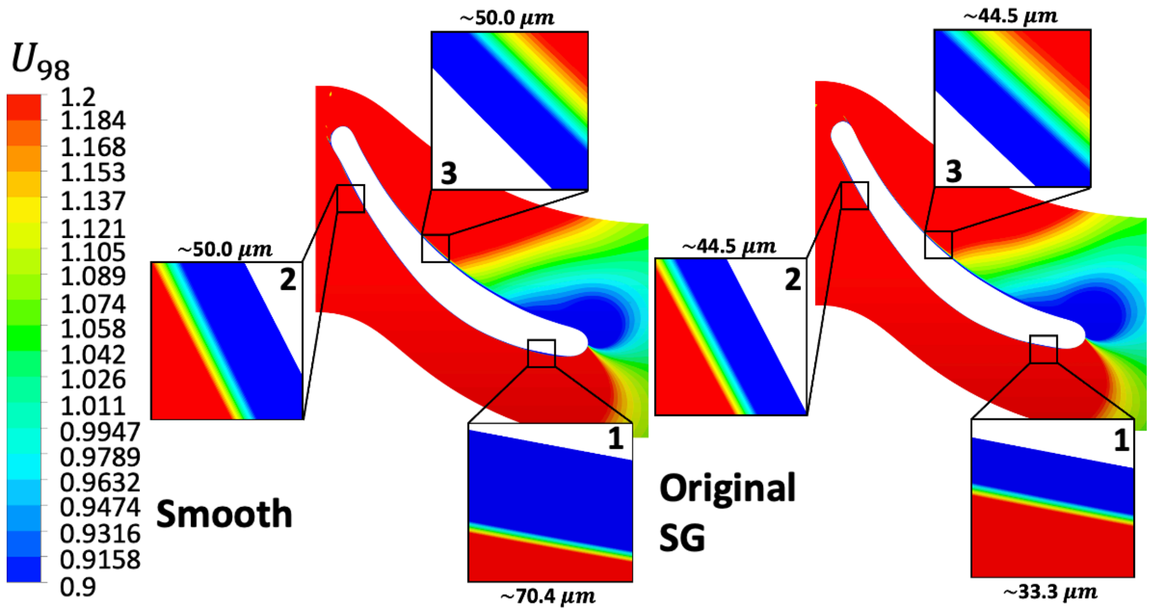

Figure 7.12: Wren100 MGT Stator Mean Span Boundary Layer Developments (Left: Smooth; Right: Original SG)

From Figure 7.12, the original SG roughness (14.5μm SG) would reduce the boundary layer thickness in all the monitored locations of the MGT stator vane. As mentioned earlier, the regional rapid thinning of the boundary layer at location 1 is caused by the reduction of the leading edge flow laminar separation, thus lowering the overall stator pressure loss compared to the smooth case in Table 7.4. This intriguing discovery has also been studied in several other previous researches. Hummel et al. investigated a higher exit Reynolds number range (around 560,000) in a linear rotor cascade, smaller profile loss increase was found for the roughened blade compared to the smooth ones. It was stated that the low Reynolds number benefit from surface roughness would only occur if the laminar separation on the smooth wall is prevented by roughness-induced transition [189]. For this Wren100 MGT stator with a Reynolds number of around 60,000, it can be clearly seen the laminar separation bubble at location 1 is eliminated by the increase of surface roughness.

At locations 2 and 3, by analysing the velocity vectors, it was found that the impact of surface roughness is relatively small compared to location 1, which could indicate more complex flow behaviours in these regions. For the smooth case, the boundary layer thicknesses at locations 2 and 3 are both thinner than location 1 due to the existence of laminar separation bubbles near the leading edge. However, as roughness increases from the original SG to 60μm SG in Figure 7.13, the thicker boundary layer can be discovered compared to the region on the suction side near the leading edge. This could indicate a flow transition from laminar to turbulence at downstream regions of the stator vane.

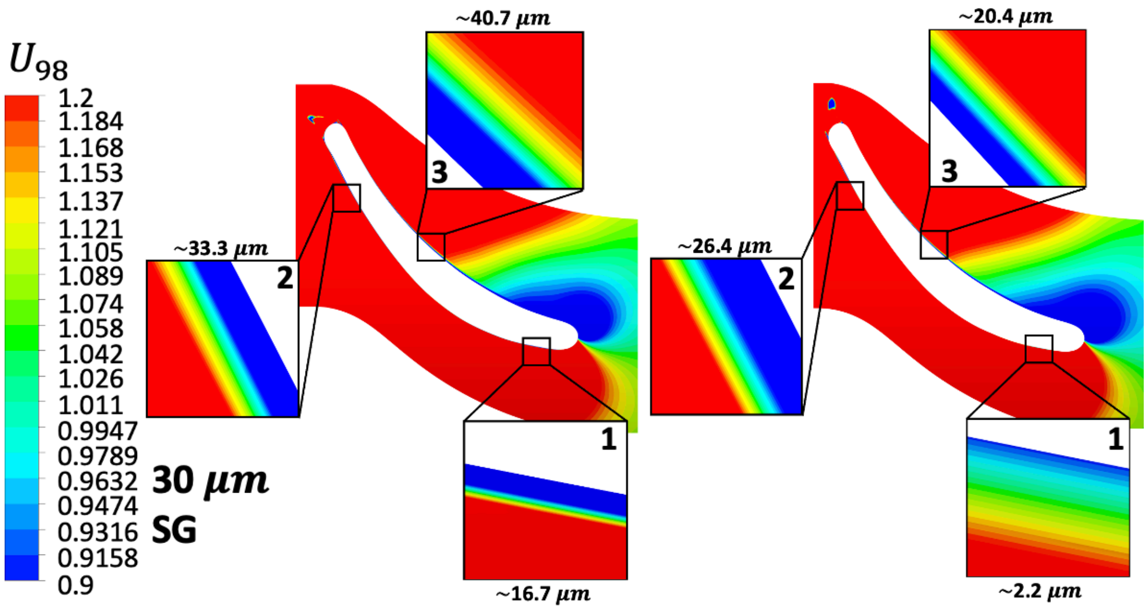

Figure 7.13: Wren100 MGT Stator Mean Span Boundary Layer Thickness (Left: 30 μm SG; Right: 60 μm SG)

However, an interesting finding is the boundary layer thinning at all monitored locations as the increase of surface roughness. As SG roughness increases from the original SG to 30μm SG and 60μm SG, the areas that previously exhibited relatively low thinning rates (Location 2 and 3) also begin to be more susceptible to the influence of higher roughness. The regional multifaceted behaviours also prove there could exist an "optimal" roughness near 30μm SG for the MGT stator vane under 120,000RPM operating conditions, as previously stated in the overall performance discussions.

Overall, for MGT stator vane mean span at low Reynolds number flows, the increase of surface roughness eliminates the laminar separation bubbles that originally occurred on the suction side near the leading edge in the smooth case. As the flow no longer separates, the flow remains laminar until it accelerates to a certain level near the trailing edge. However, as roughness further increases from the original SG to 60μm SG, the increase of roughness seems to stabilise the flow and delay the flow transition. This intriguing discovery also explains the loss reduction and increase around original SG (14.5μm SG) as listed in Table 7.4. The sudden change in the boundary layer thinning rates for the 30μm SG case also indicates the existence of an "optimal" roughness, which induces the greatest overall aerodynamic loss.

To further study the impact of surface roughness on the complex 3D flow across the vane heights, the phase-averaged skin friction coefficients at the near-root and near-tip regions were also plotted for different levels of roughness.

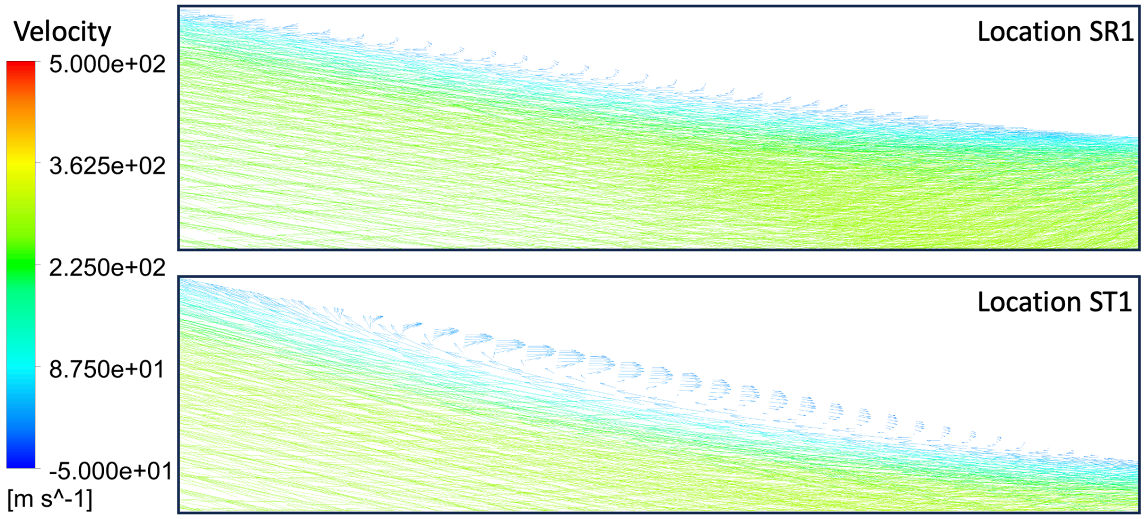

Figure 7.15: Velocity Vectors on the SS Near LE of MGT Stator Root (SR1) & Tip (ST1)

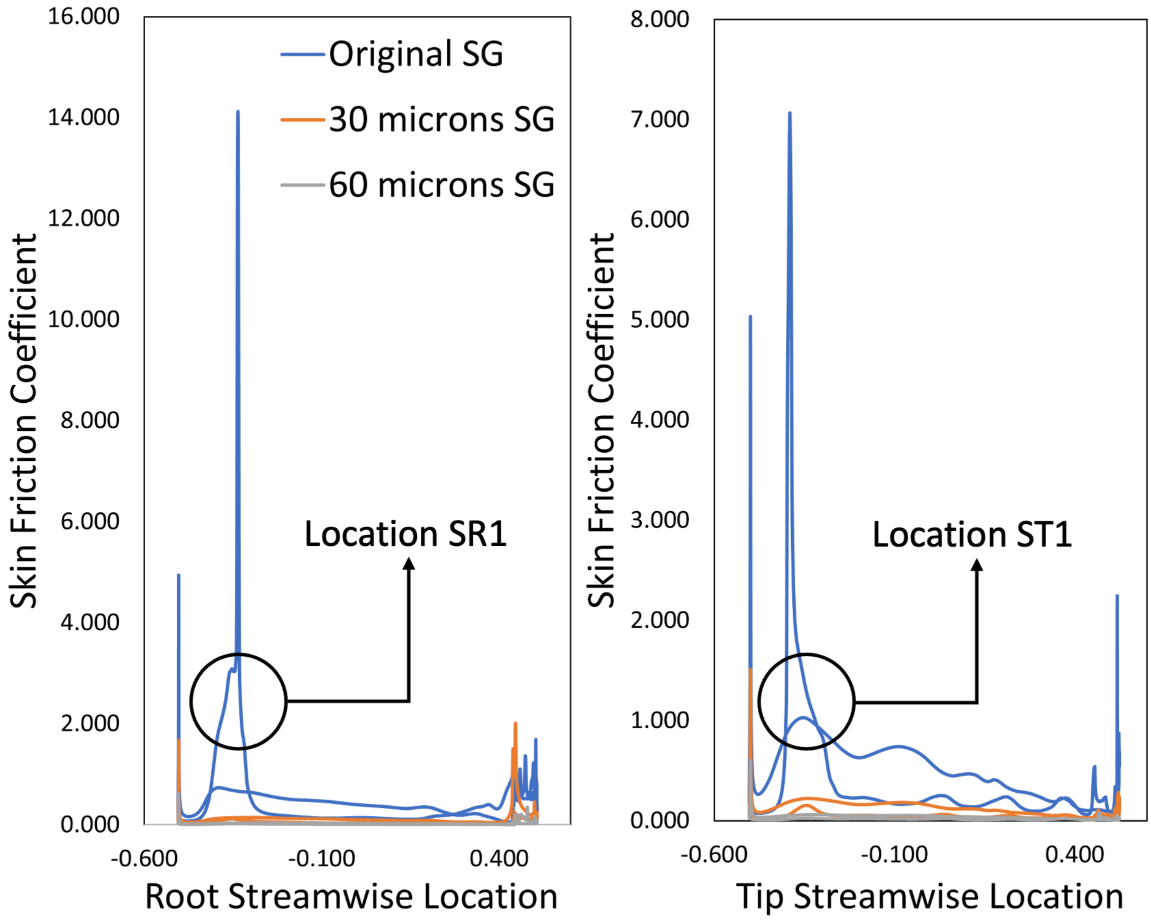

Figure 7.14: Phase-Averaged Wren100 Stator Root&Tip Streamwise Skin Friction Magnitude For Different Levels of Roughness (120,000RPM)

In Figure 7.14, a notable discrepancy between the root and tip regions compared to the mean span becomes evident: the downstream shift of peak skin friction locations from the leading edge. Specifically, peak skin frictions appear at approximately 15% chord streamwise on the suction side for the baseline surface roughness (original SG) case, as indicated by labels SR1 and ST1. Such behaviour implies the presence of complex 3D flow features in proximity to the root and tip regions. Previous examinations of the MGT stator vane suggest this could be a consequence of interactions between primary flow and secondary flow components, potentially involving hub and shroud vortex mechanisms.

However, with the increase of surface roughness to 30μm SG, an intriguing observation emerges: the peak skin friction repositions towards the vane leading edge, eradicating the previously noticed peak around the 15% chord downstream. The velocity vector illustrations for locations SR1 and ST1, depicted in Figure 7.15, show sizeable flow separation bubbles on the suction side proximal to the vane leading edge, more pronounced in the vicinity of the tip span (ST1). Drawing from prior analyses conducted on the mean span, it is evident that the increase of surface roughness notably mitigates the formation of laminar separation bubbles on the suction side adjacent to the leading edge. Nonetheless, contrasting the mean span, a distinct disparity arises in the pronounced influence of secondary flows in close quarters to the hub and tip domains, as discerned from wall shear vector diagrams in Figure 7.16. These alterations in local flow trajectories, inferred from wall shear vector diagrams, confirm the manifestation of substantial secondary flows at locations SR1 and ST1. Yet, intriguingly, with the increase of surface roughness, the dominance of hub and shroud vortex mechanisms appears to diminish, potentially attributed to the strengthened main flow with higher turbulence intensity caused by the increase in rough element sizes as shown in Figure 7.16.

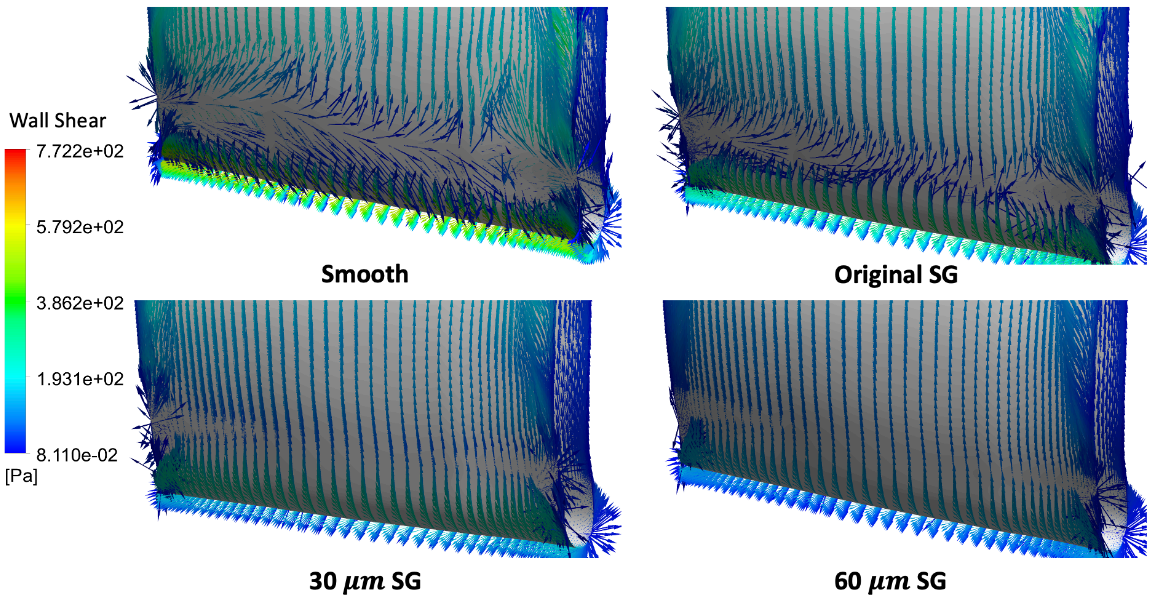

Figure 7.16: LE SS Wall Shear Vector Plots SR1 & ST1 (120,000RPM, Phase 1.0)

Near the trailing edge, additional skin friction peaks can also be observed in Figure 7.14, which could be caused by the boundary layer reattachment and greater ednwall effect near the hub and shroud regions. There also exists another local peak of skin friction for the 30μm SG case near the root trailing edge of 2.011, which is even higher than the leading edge (1.66). The higher friction loss for the 30μm SG at the root span could contribute to the higher stagnation pressure loss coefficient calculated in Table 7.4. This could be attributed to the secondary flow, and the boundary layer reattachment behaviour near the trailing edge is still not fully disrupted with $30\mu m$ SG roughness level, especially on the root span. As surface roughness further rises to $60\mu m$ SG, all the local peaks of skin friction except the leading edge are dampened, which aligns with the concept of flow being more stabilised by the enlarged rough elements. Additionally, despite the flow remaining at a laminar state with increased surface roughness, the strengthened main flow with higher turbulence intensity can disrupt the local secondary flow structures and separations that previously caused peaks of skin frictions, thereby leading to their dampening.

As mentioned earlier, the root span was considered to generate the highest loss, and the change of boundary development near the trailing edge area was also plotted to further investigate the sudden increase of skin friction coefficients.

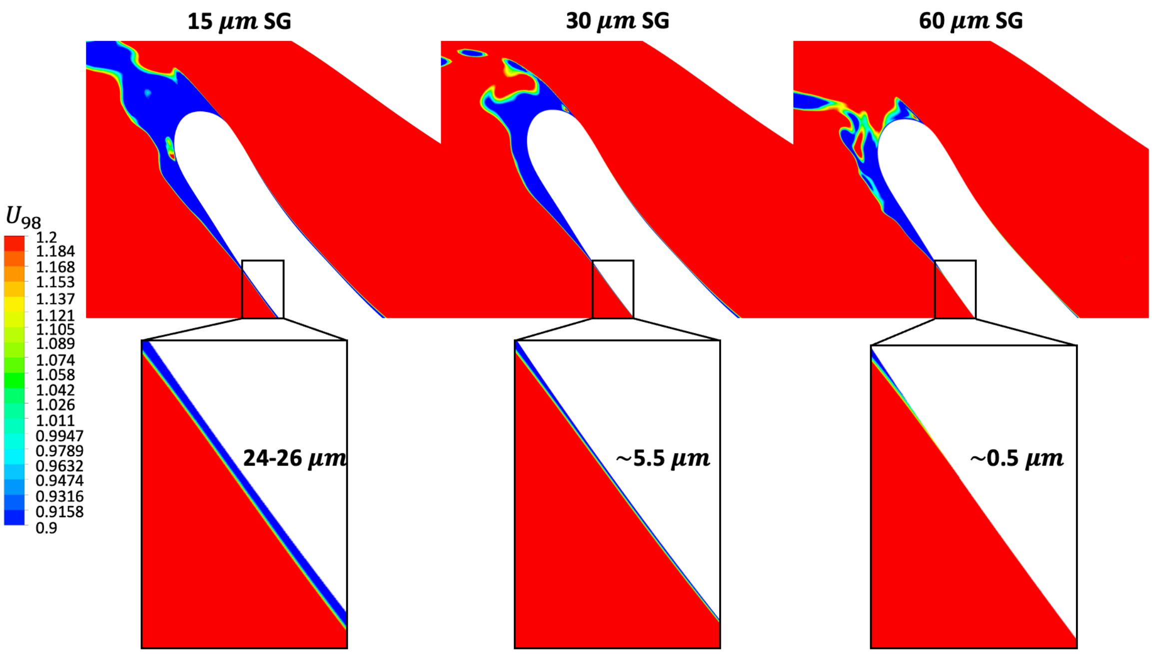

Figure 7.17: Rough MGT Stator Vane Root Section Boundary Layer Thickness (120,000RPM)

In Figure 7.17, a pronounced thick boundary layer is observed proximal to the MGT stator vane. With an escalation in surface roughness from 15 μm SG to 60 μm SG, a similar boundary layer reduction is discerned near the root trailing edge, analogous to the thinning behaviour in the mean span U_{98} previously delineated. This phenomenon can potentially be attributed to the flow being more laminarised and instigated by increased surface roughness levels, which later undergoes transition, culminating in a regionally denser boundary layer towards the trailing edge with enhanced wake mixing. Thus, it is possible that the laminarised state due to high roughness for the MGT vane is quite fragile, as the increased turbulence intensity in the outer flow can continually introduce new disturbances into the boundary layer, which can promote a rapid re-transition back to a turbulent state. This behaviour resonates with the local high skin friction values discerned on the suction side adjacent to the trailing edge as displayed in Figure 7.14. Moreover, as roughness increases, an expedited velocity recovery downstream of the trailing edge is evident. This recuperation can likely be ascribed to the augmented turbulence intensity, even as the flow reverts to its laminar state before the transition happens again. Overall, this complex behaviour is a result of the intricate and multifaceted interactions between the flow and the roughened vane surface, and understanding it in detail would likely require additional numerical simulations or experimental studies.

Efficiency Loss

To evaluate the impact of surface roughness on the MGT stator vane losses, the entropy contours on the suction side and pressure side were compared for original SG, 30 μm SG and 60 μm SG roughness. The areas on the suction side of the vane that generate the most significant loss under 120,000RPM are also highlighted.

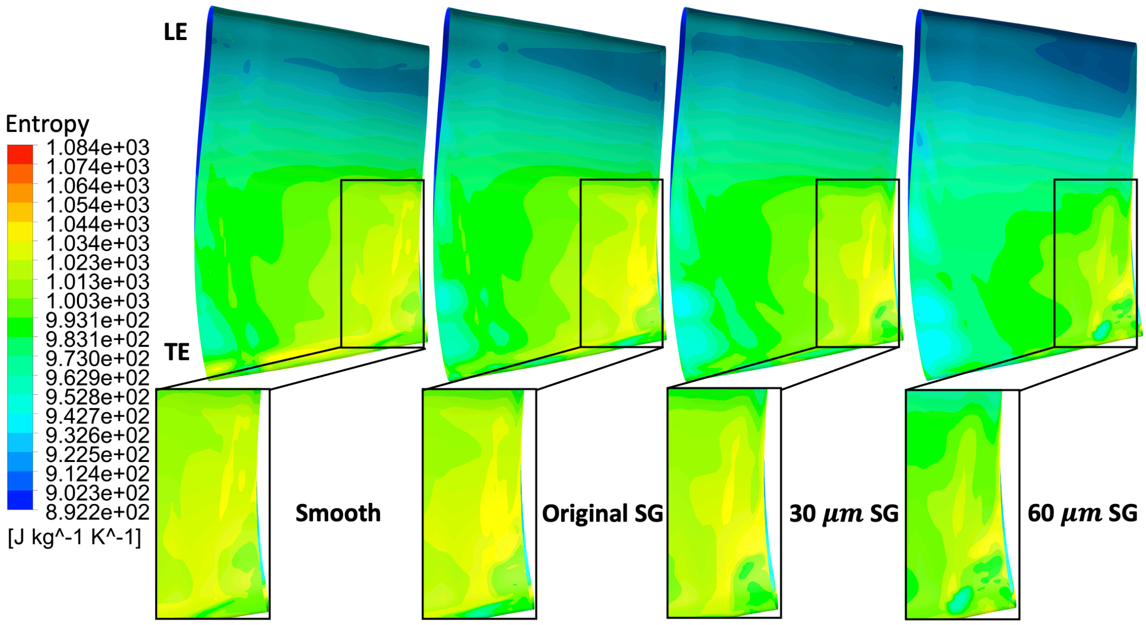

Figure 7.18: Wren100 Stator Suction Side Instantaneous Entropy Creation (Phase 1.0)

In analysing the data depicted in Figure 7.18, it is clear that adjustments in surface roughness significantly influence the entropy dynamics in the MGT stator system, especially near the suction side trailing edge at the root section. In the initial phase, with an increase in roughness up to 30 μm SG, the entropy generation remains relatively constant at about $1034J/kg \cdot K$. This could indicate a certain resilience for the MGT stator when there are moderate increases in the surface roughness.

However, a further increment in surface roughness to 60 μm SG initiates a noticeable reduction in entropy generation, reaching values around $993.1J/kg \cdot K$. This decline can be attributed to an amplified turbulence intensity fostered by the enlarged roughness elements. This increased turbulence, in turn, seems to strengthen the main flow, making it more resilient against the disturbances caused by secondary flows, which were previously marked as significant sources of energy loss in the system. These flow behaviours can also be visualised by the wall shear diagrams in Figure 7.16, which also leads to the change in skin friction in those areas.

To sum up, this phenomenon indicates that the flow dynamics adapt positively to increased surface roughness levels, with the enhanced turbulence facilitating a more robust and streamlined main flow. This adaptation successfully mitigates the disruptive effects of secondary flows, resulting in a decrease in entropy generation and, consequently, energy loss in critical areas. This reduction in entropy hints at an opportunity to improve the thermodynamic efficiency of the MGT system, emphasising the need for further research to comprehend the complex relationship between surface roughness, turbulence intensity, and secondary flow patterns in shaping the efficiency parameters of MGT stator vanes. It beckons a deeper investigation, both experimentally and computationally, to refine the design and operational strategies for achieving optimised performance in MGT setups.

7.5.2.2 Peak Operation Conditions - 160,000RPM

Similar to the normal operating conditions analysis, the phase-averaged skin friction coefficients across the MGT stator vane at 160,000RPM were also plotted to study how the surface roughness affects the engine performance at higher Reynolds numbers.

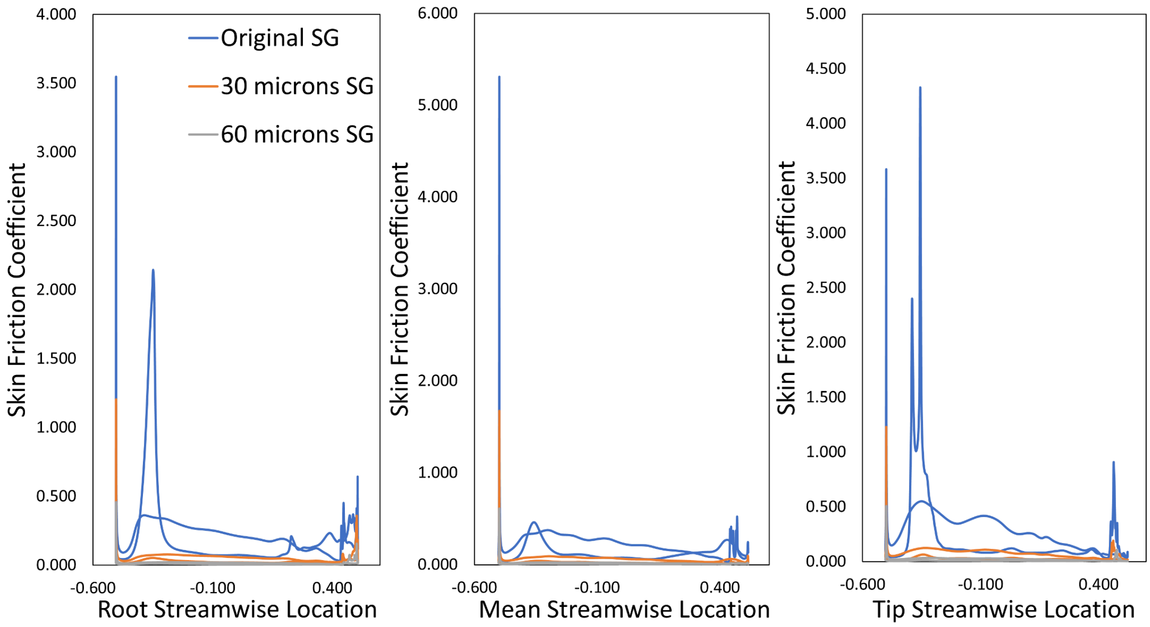

Figure 7.19: Phase-Averaged Wren100 Stator Streamwise Skin Friction Magnitude For Different Levels of Roughness (160,000RPM)

Analysing the data from Figure 7.19 in the context of the MGT stator vane at a higher Reynolds number corresponding to 160,000RPM rotor speed, several key observations emerged. Primarily, the trend in skin friction at the peak rotor rotational speed (Reynolds number around 86,000) mirrors that observed at the 120,000RPM condition (Reynolds number around 63,000). Notably, at the mean span with an original roughness of 14.5μm SG, laminar flow separation behaviours persist at both the higher and lower RPM conditions. This flow separation can be recognised by the distinctive local peak in skin friction, positioned on the suction side approximately 15% downstream of the leading edge in terms of axial chord length. Also, an intriguing distinction arises when comparing the magnitudes of this peak across the two rotational speeds. The skin friction value at this specific location is considerably reduced for the higher Reynolds number case, registering at around 0.46, in contrast to the considerably higher value of approximately 1.28 observed for the 120,000RPM condition. This pronounced reduction in the magnitude of skin friction indicates a potential increase in the extent of flow laminar separation for the higher Reynolds number case compared to its 120,000RPM counterpart. The enlarged separation bubble can also be seen in the velocity vector diagrams as shown in Figure 7.20. This extended separation region could potentially mitigate the shear stresses exerted on the surface, resulting in a reduced coefficient of skin friction.

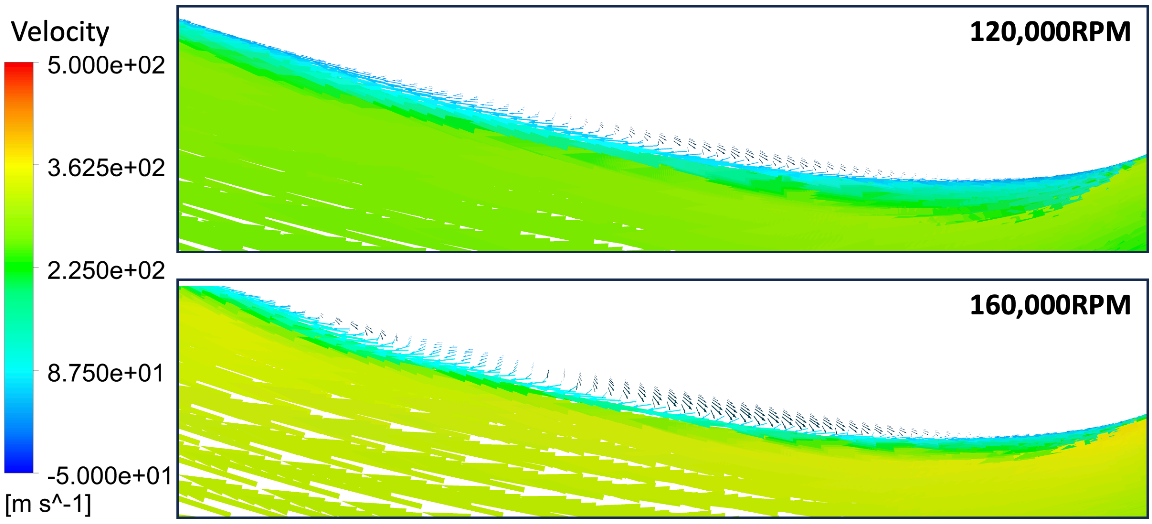

Figure 7.20: Mean Span Velocity Vectors on the SS Near LE (120,000RPM vs. 160,000RPM)

It was clearly observed that the higher rotor speed initiates an escalated degree of flow separation on the stator vane. For the root span, a greater second surge of skin friction at about 15% chord downstream of the leading edge was found, which could be caused by the combined effect of flow separation and the influence of secondary flows similar to the 120,000RPM case. With higher Reynolds number flows, the higher peak skin friction at the leading edge as compared to the 120,000 RPM case (where the highest skin friction is downstream of the LE) could be emblematic of a thinner boundary layer for a higher RPM case. For both operating conditions, the original roughness can eliminate the laminar separation on the suction side near the leading edge. Further analysis of Figure 7.19 revealed additional changes in the boundary layer dynamics for the 160,000RPM case, characterised by multiple minor escalations in skin friction coefficients in the proximity of the trailing edge, with values fluctuating between 0.4 and 0.45. This pattern seems to underline the emergence of more intricate boundary layer behaviours at this higher RPM, possibly hinting at a series of intermittent transitions from laminar flow to turbulent states, which is a hallmark of complex fluid dynamics with higher Reynolds number flows. In a comparative lens with the lower Reynolds number scenario at 120,000RPM, it is apparent that the skin friction coefficients at the root suction side, near the trailing edge, remain elevated for the 160,000RPM conditions. This sustained elevation might be indicative of a scenario that the flow maintains a turbulent character throughout the trailing edge at 160,000RPM. This could be because the flow becomes more prone to instability and susceptible to disruptions due to the higher Reynolds number. Moreover, the thinner boundary layer associated with the 160,000 RPM case might be a contributing factor to the distribution of skin friction peaks, in which the influence of the original SG has a greater impact to induce an earlier onset of flow transition.

For the tip span, the major difference for the higher Reynolds number case compared to the 120,000RPM one is the two distinct skin friction increases following the leading edge. The first local peak of around 2.5 is lower than the skin friction at the leading edge, but the second local peak of about 4.5 surpasses the leading edge skin friction. This two-peak pattern suggests a more complex boundary layer development with possibly flow separation followed by strong secondary effects at a later peak C_f location. With a higher Reynolds number, the influence of secondary flow near the shroud area is expected to be smaller. With the same original SG roughness, the thinner boundary layer near the leading edge could lead to an earlier transition that results in an additional local peak of skin friction. Furthermore, the skin friction distribution near the trailing edge also varies between the two rotor rotational speeds. At 160,000RPM, a small peak in skin friction (about 0.901) arises at a small distance upstream of the trailing edge, whereas at 120,000 RPM, a small peak appears directly at the trailing edge (about 2.245). This could imply a shift in flow reattachment or increased turbulence activity near the trailing edge as the rotational speed increases from 120,000RPM to 160,000 RPM. As the surface roughness increases, the reduction of the secondary effect near the tip area was also visualised from the 3D wall shear vectors in Figure 7.21.

Similar to the 120,000RPM case, the U_{98} plots were also calculated and plotted for the higher Reynolds number conditions (160,000RPM) to study the influence of different levels of roughness on the boundary layer development. Initially, the smooth and the original SG roughness cases were compared as shown in Figure 7.22.

According to the initial comparison of U_{98} plots, it can be visualised that not all regions of the boundary layer reduce as the Reynolds number increases with the original SG roughness for the higher Reynolds number conditions. Similar to the 120,000RPM

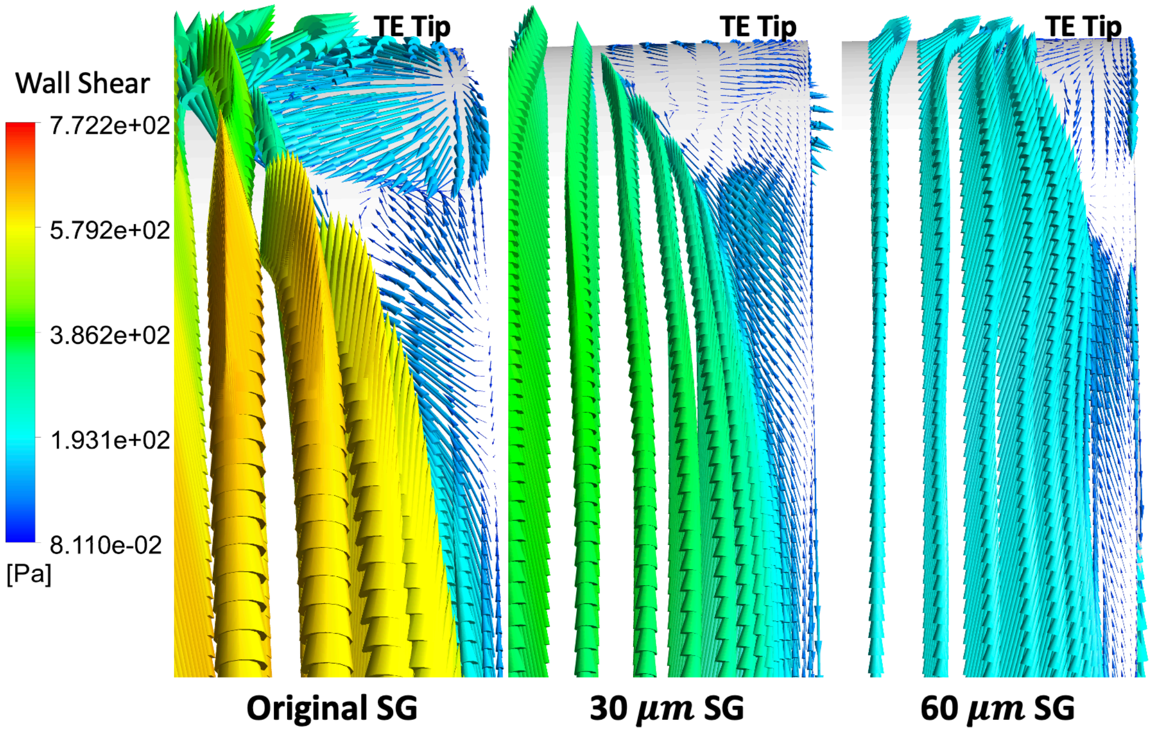

Figure 7.21: Wall Shear Vector Vane Suction Side Near Tip Region for Different Levels of Surface Roughness

case, the rapid reduction of boundary layer thickness at location 1 is caused by the elimination of flow laminar separation bubbles due to the existence of the original surface roughness. However, the regional thickening of the boundary layer at location 2 ($38.2\mu m$ to $48.2\mu m$) could suggest flow transition behaviour induced by the roughness elements. For the smooth case, the flow experiences separation and transition at location 1, which then relaminarises at location 2, which leads a drop in boundary layer thickness. As the original SG roughness was added to the vane surface, the laminar separation was eliminated, which delayed the flow transition towards location 2 closer to the trailing edge. For the 160,000RPM case, the enhanced sensitivity to roughness is likely due to the increased turbulence levels associated with the higher Reynolds number, which small roughness elements could trigger early transition to turbulence.

As the roughness elements sizes further increase, the change of boundary layer behaviours are also analysed in Figure 7.23. At 160,000RPM, it was observed that the boundary layer continues to thin as roughness increases to $60\mu m$ SG, but again with a decreasing rate. Similar as the 120,000RPM case, this could indicate a different

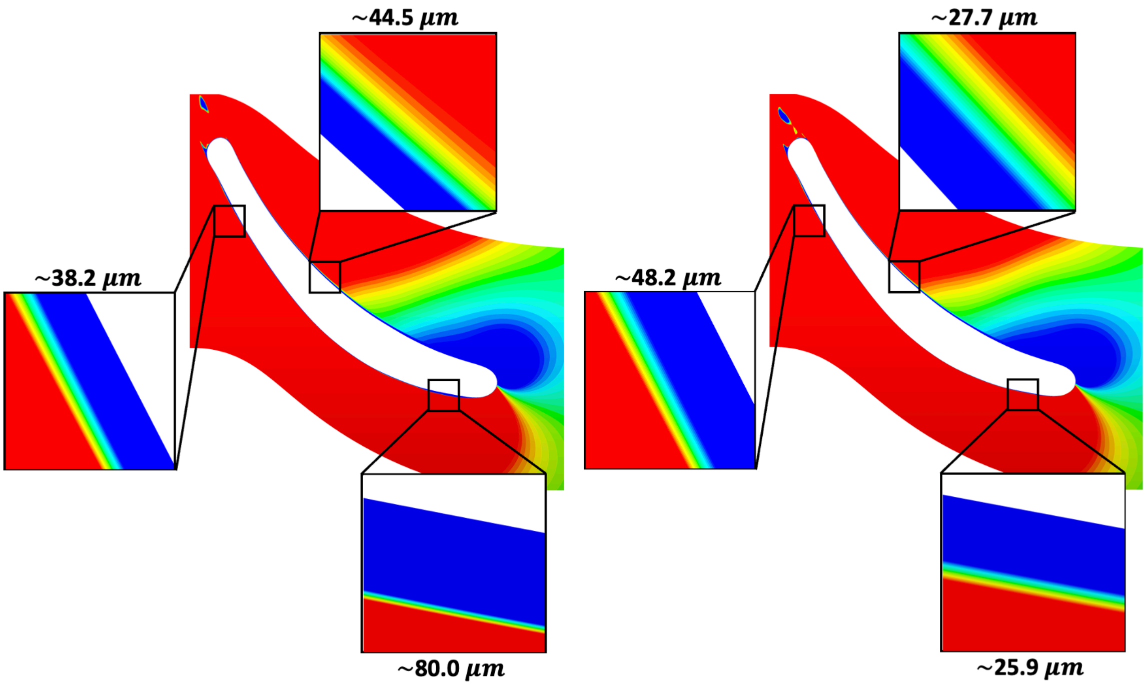

Figure 7.22: Wren100 MGT Stator Mean Span Boundary Layer Thickness (Left: Smooth; Right: Original SG) (160,000RPM)

"optimal roughness" at a lower roughness level close to 15 μm SG due to the higher Reynolds number.

To sum up, the fact that the rate of boundary layer thinning ($\Delta\delta$) appears to be decelerating at a higher RPM also supports the idea that the optimal roughness ($k_{s,optimal}$) is a function of the Reynolds number (Re) and local boundary layer thickness (δ_{Local}). The related function are summarised in Equation 7.5 and 7.6.

$$k_{s,optimal} \propto \{\Delta\delta, Re, \delta_{Local}\} \tag{7.5}$$

$$\Delta\delta \propto \{Re, \delta_{Local}\} \tag{7.6}$$

For the Wren100 MGT stator, at 120,000RPM, the boundary layer thinning effect seems to peak at around 30μm SG of surface roughness, whereas at 160,000RPM, the most significant thinning occurs when the roughness is increased to original SG. Further investigations of more accurate values of the optimal roughness at different RPMs can be carried out in the future.

Efficiency Loss

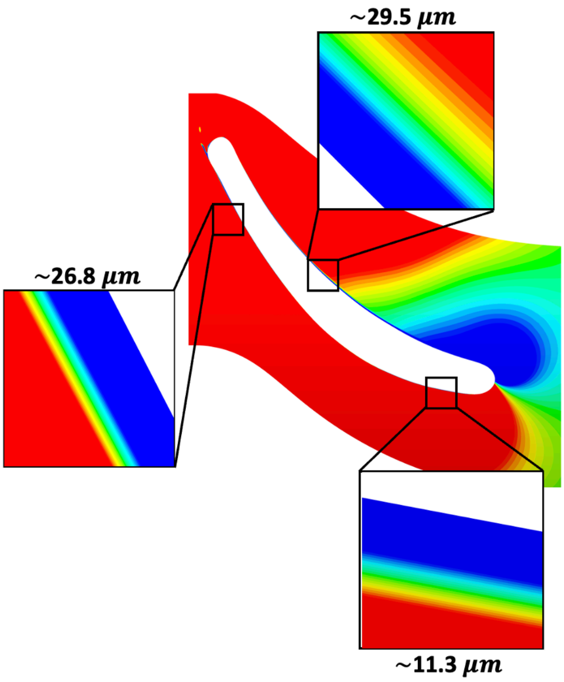

Figure 7.23: Wren100 MGT Stator Mean Span Boundary Layer Thickness (Left: Smooth; Right: Original SG) (160,000RPM)

The changes of the MGT stator vane losses at peak operating conditions for the different levels of surface roughness were also visualised in Figure 7.24.

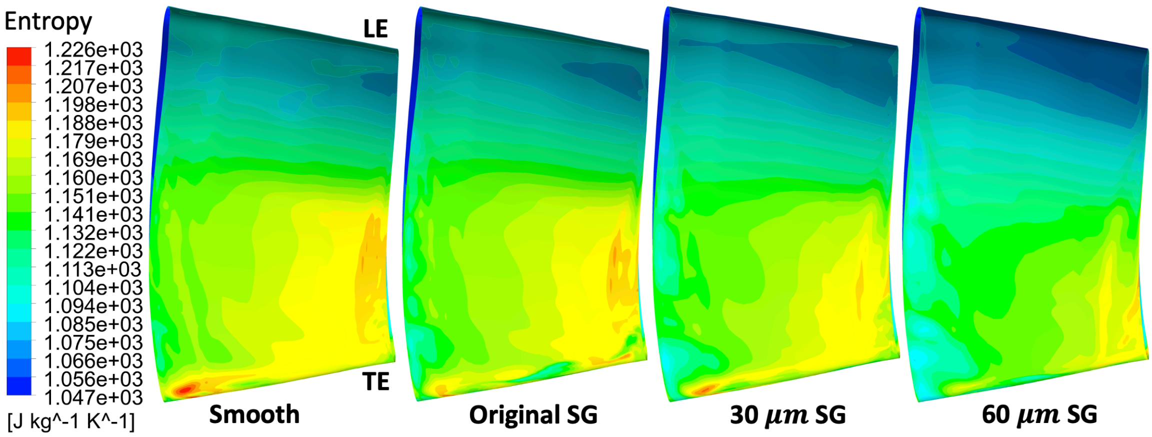

Figure 7.24: Wren100 Stator Suction Side Instantaneous Entropy Creation (160,000RPM) (Phase 1.0)

From the entropy creation plots, it can be seen that the entropy creation diminishes as the roughness levels increase, especially near the root and tip regions. At the root and tip regions near the trailing edge, the flow is extremely complex due to the presence of endwall effects and secondary flows. For MGT stator vanes, the changes in roughness might have a particularly pronounced impact in these regions by modifying these flows and potentially reducing losses. Additionally, compared to the 120,000RPM case, the drop in entropy generation is more significant for the MGT stator at 160,000RPM conditions. This suggests that the higher Reynolds number might be amplifying the effects of surface roughness on flow separation and boundary layer transition. It also further emphasises that the overall entropy changes due to roughness are dependent on a complex interplay of multiple factors, including Reynolds number, roughness size, and the specific flow characteristics and geometries involved.

7.5.3 Impact on the MGT Rotor Blade Boundary Layer

7.5.3.1 Normal Operation Conditions - 120,000RPM

To study the influence of surface roughness on the MGT rotor blade, similar to the stator vanes, the skin friction coefficient magnitude was initially plotted on the mean span under 120,000RPM operating conditions.

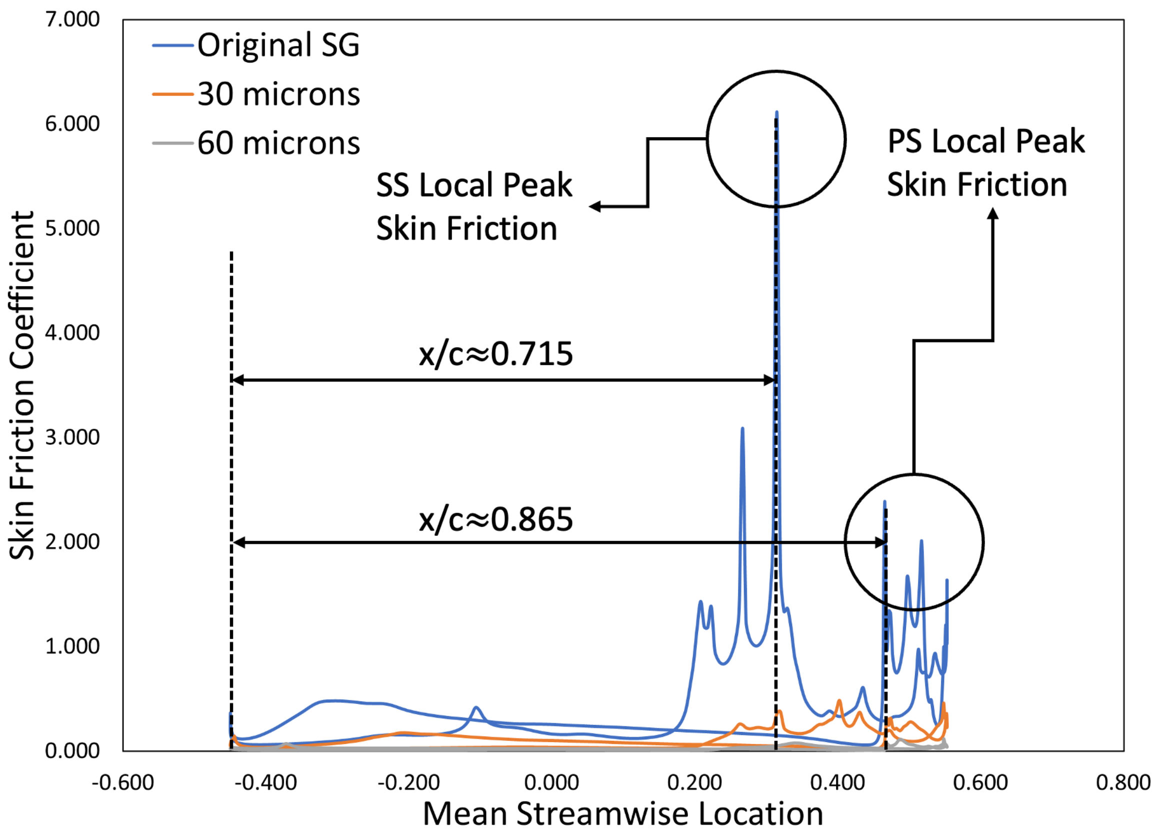

Figure 7.25: Phase-Averaged Wren100 Rotor Mean Streamwise Skin Friction Magnitude For Different Levels of Roughness (120,000RPM)

As displayed in Figure 7.25, the average skin friction coefficients across the rotor blade mean span drop rapidly as the surface roughness level increases from original SG to $60\mu m$ SG. With the original SG roughness, multiple sudden increases of skin friction coefficient magnitudes on the suction side ($x/c \approx 0.715$) could be caused by the flow separation and reattachments at those surge locations. In addition, turning effects due to the highly cambered geometrical shape near the trailing edge could also be a contributing factor for the delayed flow separation (compared to the stator vane). These flow separation behaviours can also be visualised in Figure 7.26, where the cross-passage flow causes the thickening of the boundary layers on the suction side of the blade (SS). As the roughness level increases to 30μm SG and 60μm SG, the boundary layer near the trailing edge becomes less obvious, resulting in the dampening effects of the local peaks of skin friction.

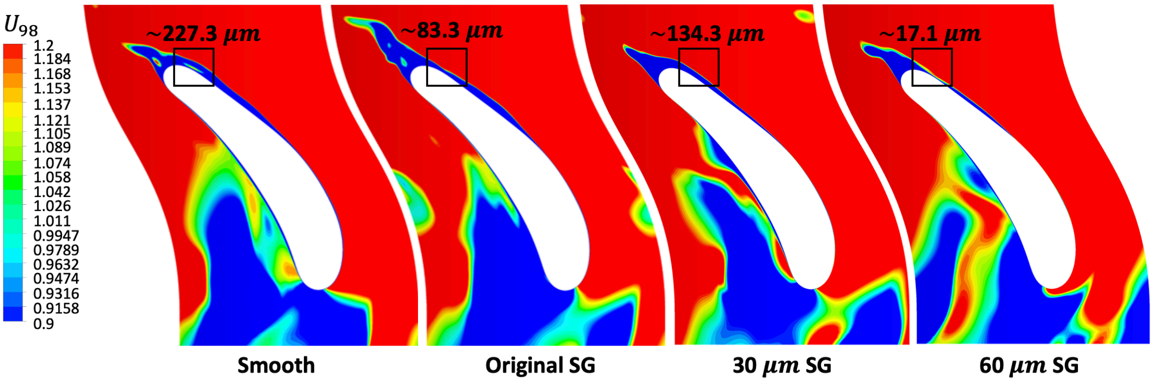

Figure 7.26: Wren100 MGT Rotor Mean Span Instantaneous Boundary Layer Thickness (120,000RPM, Phase 1.0)

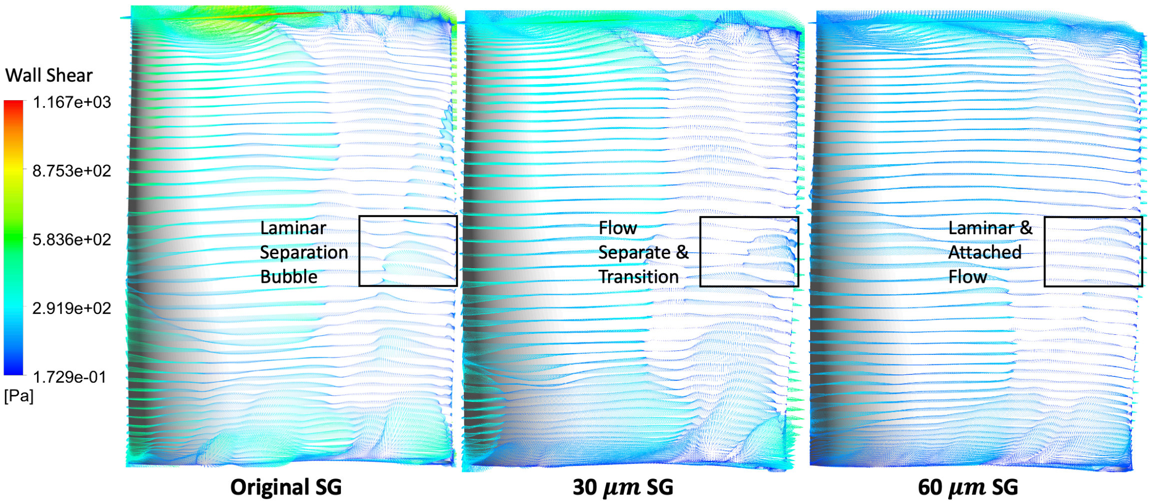

Figure 7.27: Wall Shear Blade Suction Side for Different Levels of Roughness

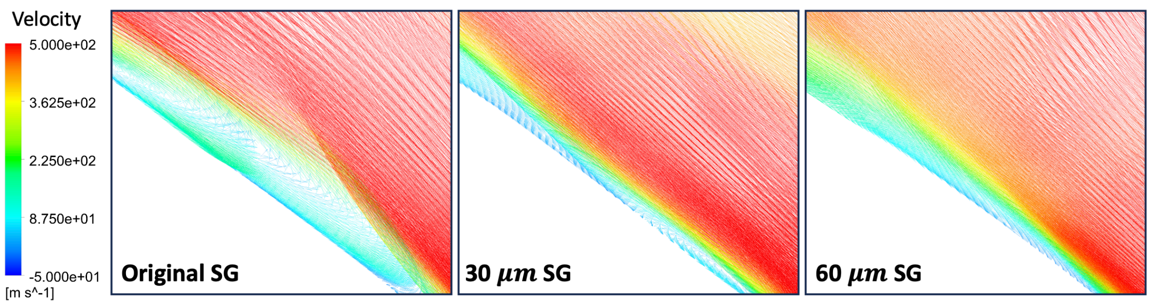

Figure 7.28: Velocity Vectors on the SS Near TE of MGT Rotor Mean

Upon reviewing the U_{98}, wall shear and velocity vector diagrams, it is evident that there is an increase of secondary flow as surface roughness changes from original SG to $30\mu m$. At $30\mu m$ SG, the increased secondary effect and roughness-induced flow transition could very likely be the cause for the observed thickening of boundary layer on the mean span at the examined location. However, as the roughness further increases to $60\mu m$ SG, a different scenario unfolds, with a rapid reduction of boundary layer thickness and more streamlined flow. From the velocity vector diagrams in Figure 7.28, almost no flow separation is visible. This could be due to the fact that the $60\mu m$ SG roughness elements height exceeds the thickness of the viscous sublayer. With greater influence on the flow field and reduced separation, the boundary layer for the $60\mu m$ SG at the monitored location could remain largely laminar, which results in more attached flow near the blade trailing edge as displayed in the U_{98} plots.

On the pressure side (PS), several local increases of skin friction can be observed from $x/c \approx 0.865$ upstream the blade trailing edge. A similar dampening effect can be visualised with higher surface roughness levels on the suction side. For the original roughness case, the surges of skin friction are likely to be caused by the potential transition behaviour before the flow leaves the blade trailing edge. As the surface roughness further increases, the flow seems to become more stabilised, resulting in a more flattened skin friction coefficient distribution.

According to the previous analysis, it is certain that the increased roughness levels could have great influences on the secondary effects due to the escalated turbulence intensity, especially for MGT blades with relatively low Reynolds number flows. Due to the large spanwise shape changes of the MGT rotor blade, the influence of the surface roughness on the near-hub and near-shroud endwall regions was also studied by analysing the skin friction magnitudes and boundary layer developments.

The skin friction magnitudes diagrams for the root and tip regions show a similar reduction trend as the increment of surface roughness. For the root section, it is notable that the leading edge skin friction for the $30\mu m$ SG case is higher than the Original SG. This could be attributed to the more attached flow near the leading edge that results from the increased surface roughness, which can also be visualised from the U_{98} plots as shown in 7.30. As roughness increases from the original SG to $30\mu m$ SG, the peak of skin friction shifts from the trailing edge to the leading edge, also evident in the presence of potential earlier transition. When the surface roughness

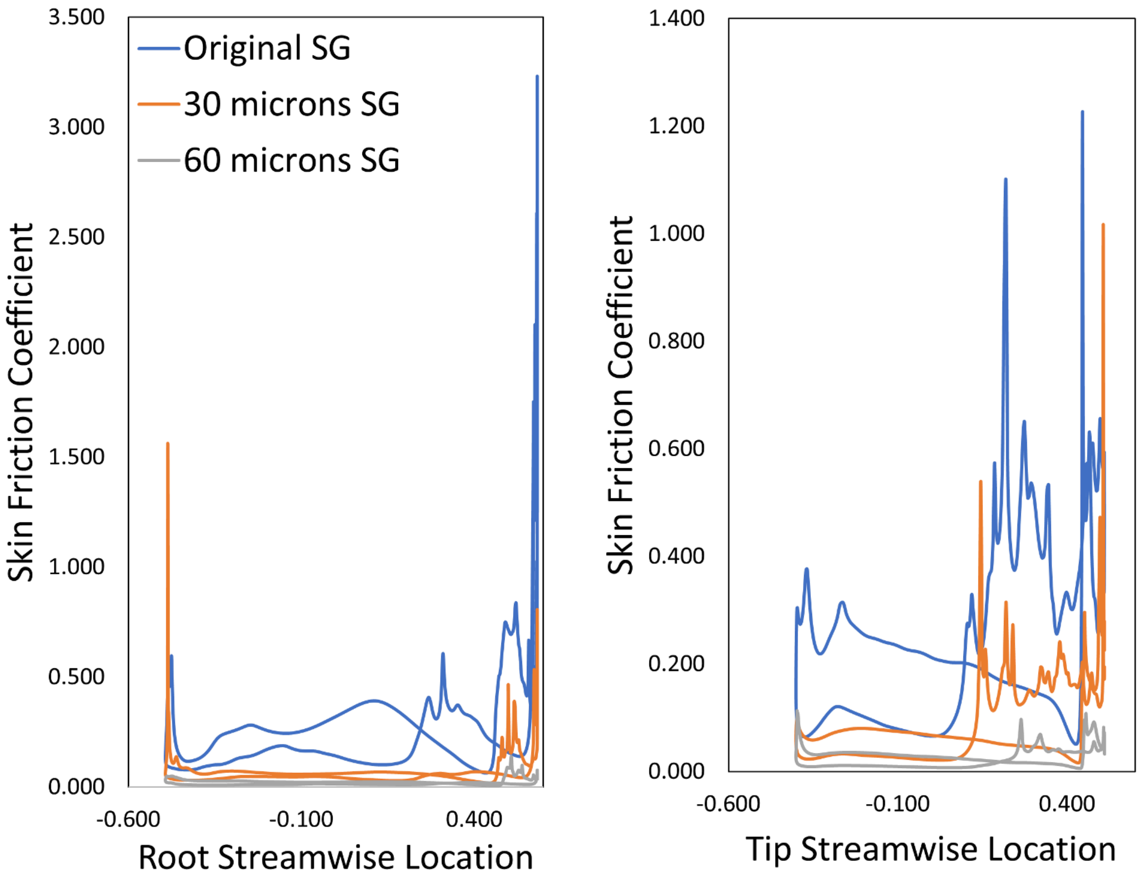

Figure 7.29: Phase-Averaged Wren100 Rotor Root&Tip Streamwise Skin Friction Magnitude For Different Levels of Roughness (120,000RPM)

further increases to $60\mu m$ SG, all abrupt increments of skin friction are dampened. This could be attributed to the fact that despite increased turbulent intensity and fluctuations, the boundary layer remains a laminar state as it passes from the leading edge to the trailing edge.

From the U_{98} diagrams, it can be seen that the wake on the pressure side grows bigger near the leading edge. This depicts the possible development of a highly disturbed boundary layer across the chord, instigated by the increased roughness level. In addition, the increase of surface roughness could potentially enhance wake propagation and mix from the stator to the rotor, which not only carries velocity defects but also induces additional turbulence in the flow field.

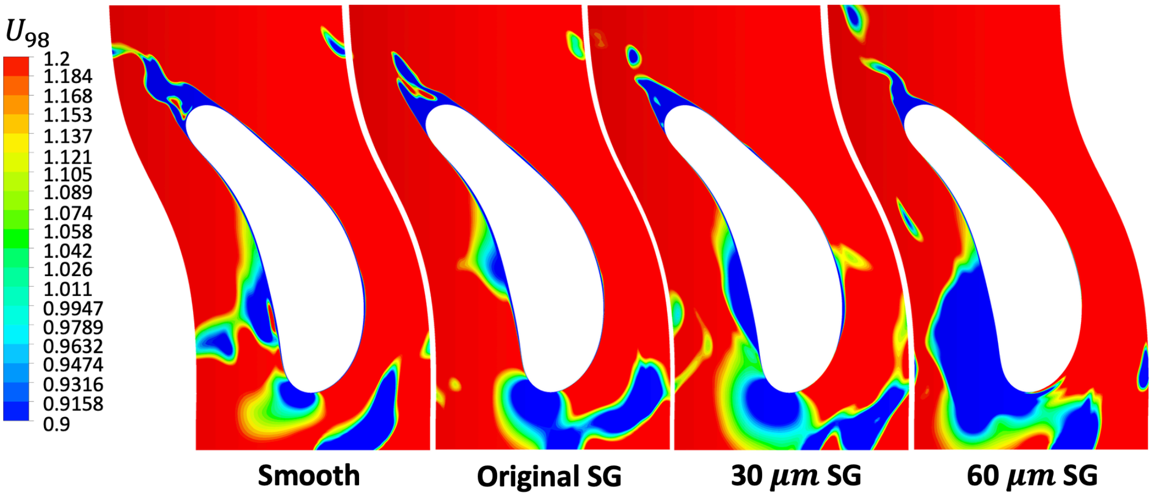

Figure 7.30: Wren100 MGT Rotor Root Span Instantaneous Boundary Layer Thickness (120,000RPM, Phase 1.0)

For the near tip span, the flow behaviour becomes highly complex due to the presence of the tip gap, which introduces additional secondary flows, such as tip leakage vortex and corner vortex, into the mainstream flow. As surface roughness increases, the overall skin friction decreases as the boundary layer becomes thinner (Figure 7.31). However, the observation of numerous local increases of skin friction in the after-half of the blade with less apparent dampening of these peaks with increased roughness from original SG to 30μm SG is intriguing. This can also be noticed from the U_{98} boundary layer plots, in which the thinning effect from original SG to 30μm SG is slightly less obvious compared to the mean span.

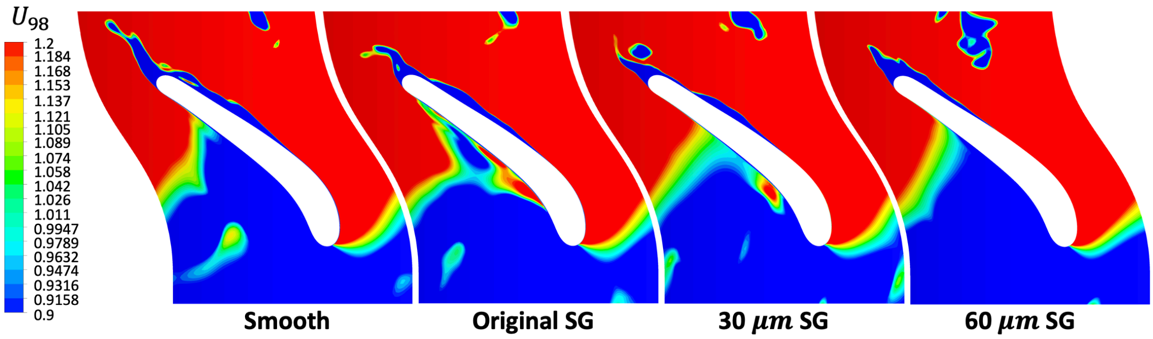

Figure 7.31: Wren100 MGT Rotor Tip Span Instantaneous Boundary Layer Thickness (120,000RPM, Phase 1.0)

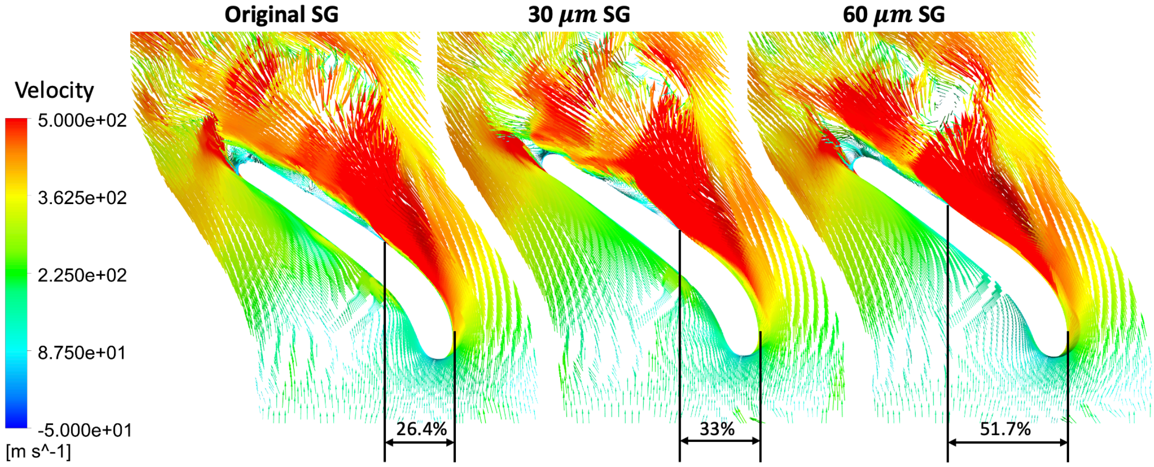

Figure 7.32: Instantaneous Velocity Vectors MGT Rotor Blade Near Tip Span (120,000RPM, Phase 1.0)

From the velocity vectors diagrams in Figure 7.32, the wake formed after the blade trailing edge becomes smaller as the roughness increases to 30μm SG. However, the wake grows bigger when the blade surface is roughened to 60μm SG. Based on the performance evaluated in Table 7.4 and the velocity vectors, it could highlight that the roughness elements can potentially alter the wake structure and the loss generation in the MGT blades. A similar influence due to the increased roughness was discussed in the MGT stator case. Additionally, it can be clearly seen that the maximum height and length of the separation bubble decrease as the roughness level increases from the original SG to 30 and 60μm SG. Interestingly, the separation bubble onset location would also be delayed by the roughened blade (as listed in Table 7.5). On the near-tip span, the interaction between the rough surface and the tip leakage flow can potentially modify the characteristics of the tip leakage vortex, influencing the onset and extent of separation bubbles.

	Original SG ($\sim 14.5\mu m$)	30 μm SG	60 μm SG
Separation Onset Distance/Axial Chord	26.4%	33%	51.7%

Table 7.5: MGT Rotor Blade Near Tip Separation Onset Locations for Different Levels of Surface Roughness

To sum up, for the MGT rotor blade at 120,000RPM, the increase of surface roughness could dampen the local surges of skin friction caused by the secondary flow and separation bubbles. On the mean span, the height and length of the separation bubble reduce with a higher roughness level, but the separation onset location remains unchanged. As the roughness increases, the wake mixing and propagation from the upstream stator to the rotor could be enhanced, which potentially results in the non-linear change in boundary layer thickness at the monitored location on the blade suction side near the trailing edge. For the hub and shroud areas, the flow fields are highly complex due to the existence of the endwall effects. The interaction between the main passage boundary layer and regions of high shear stress on the blade surface near the tip leads to multiple local peaks of skin friction. For the near tip span, not only does the size of the separation bubble decrease as the roughness increases, but the onset of the separation would also be delayed. Below $30\mu m$ SG, the tip leakage vortex and corner vortices seem to be quite robust against the increased turbulence level induced by the enlarged roughness elements, resulting in a relatively persistent boundary layer and local peaks of skin friction. As the roughness level reaches $60\mu m$ SG, the much higher turbulence level from the main passage flow overwhelms these secondary flow features. While maintaining a laminar state, the strengthened primary flow leads to a more uniform turbulence distribution, increased boundary layer mixing, and thereby a reduction in the overall phase-averaged skin friction.

7.5.3.2 Peak Operation Conditions - 160,000RPM

For the 160,000RPM operating conditions of the Wren100 MGT, the phase-averaged skin friction coefficients on the MGT rotor blade root, mean and tip spans were initially generated to further evaluate the potential influence of different levels of roughness at the peak operating conditions.

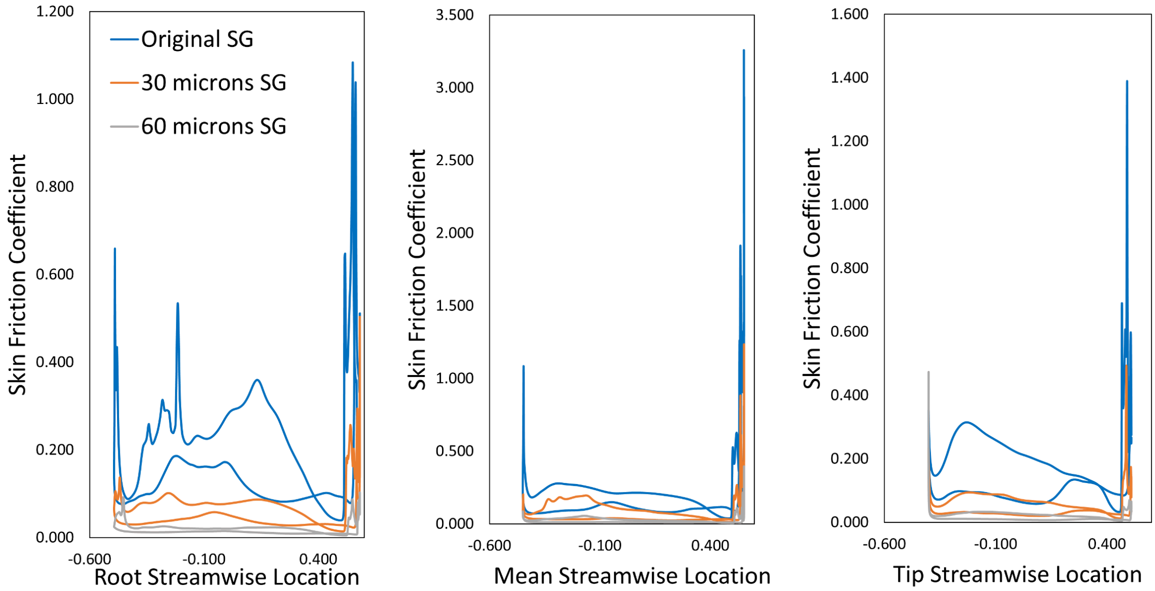

Figure 7.33: Phase-Averaged Wren100 Rotor Blade Streamwise Skin Friction Magnitude For Different Levels of Roughness (160,000RPM)

As shown in Figure 7.33, as the rotational speeds increase, corresponding drops in overall skin friction at different blade heights were observed, suggesting a modification of the boundary layer aerodynamics due to higher loading and potentially increments of the turbulent intensity of the flow.

The analysis starts from the root section with different levels of surface roughness. On the near root span, the peaks of the skin friction are primarily located at the trailing edge, which is different compared to the 120,000RPM case due to the potential thinner boundary layer with a higher Reynolds number. As roughness increases to 30μm SG and 60μm SG, the discernible dampening effect of the local peaks of skin friction is also more pronounced at higher RPM cases.

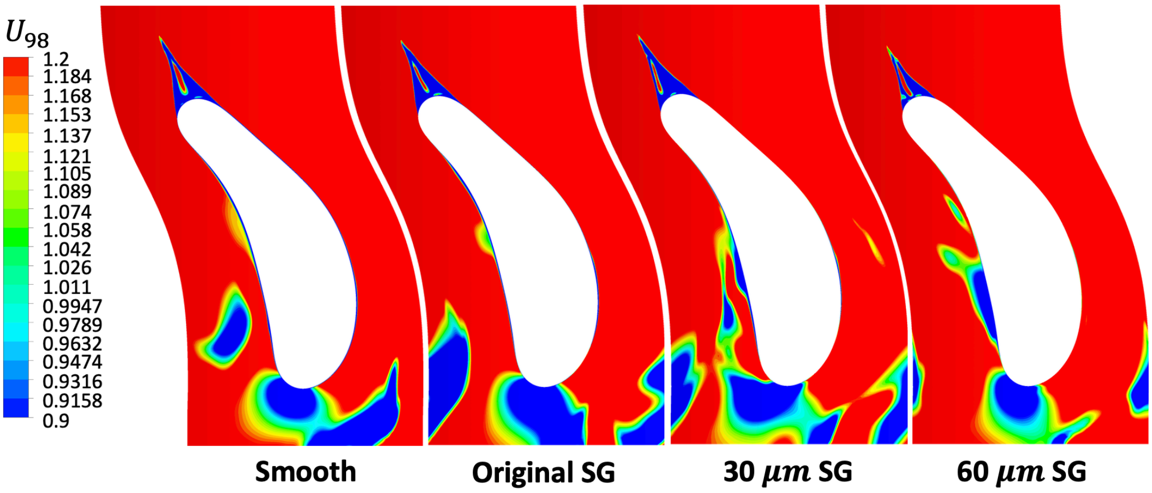

Figure 7.34: Wren100 MGT Rotor Root Span Instantaneous Boundary Layer Thickness (160,000RPM, Phase 1.0)

An in-depth inspection of the U_{98} plot, as showcased in Figure 7.34, shows a discernible augmentation in boundary layer thickness on the pressure side proximate to the blade leading edge with increasing surface roughness. This amplification is hypothesised to be a result of two interconnected phenomena. Firstly, the boundary layer thickening can be attributed to the interaction with wakes disseminating from the upstream stator stage. The reduced blue zones observed for the higher RPM configuration indicates less velocity defects being carried from the stator vane trailing edge. As analysed in Subsection 7.5.2.2, the escalated rotational speeds and higher Reynolds number decrease the formation and propagation of the vane trailing edge wakes. This results in a more uniform flow incidence onto the rotor compared to the 120,000RPM case, thereby reducing the velocity defects and rendering a slightly consistent momentum profile across the blade span. Secondly, as surface roughness increases, it could indicate localised flow transition phenomena, especially near the leading edge. The cumulative effect of this flow regime shift and the wake interactions elucidated above manifest as the observed variations in boundary layer dynamics with the different roughness levels.

Contrarily, for the cases revolving at 160,000 RPM, the increased interplay between the leading edge and endwall vortices due to the augmentation of roughness on the suction side is not as discernible as it is for the 120,000 RPM scenarios. A possible explanation for this phenomenon could be that at these higher rotational speeds while maintaining a laminar state, the resultant elevated Reynolds number instigates

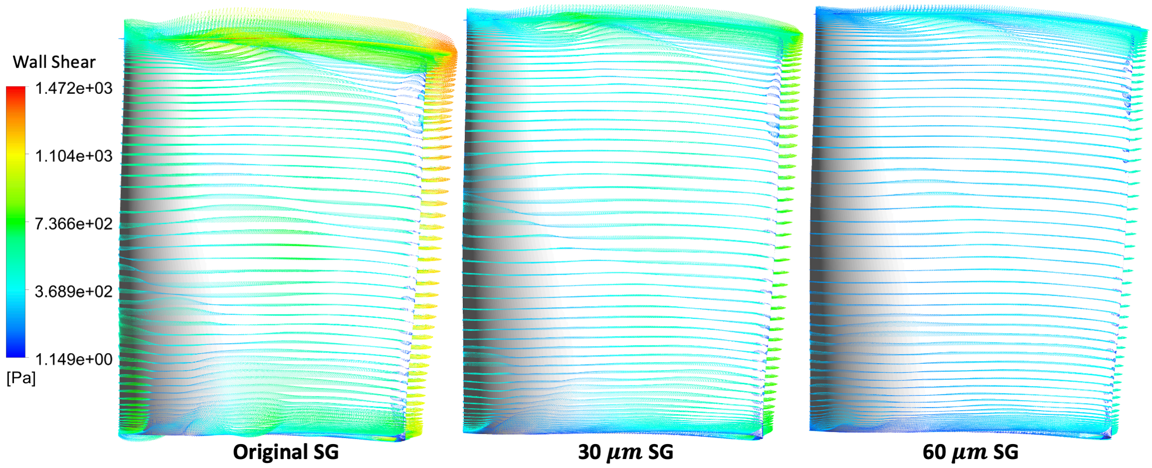

Figure 7.35: Wall Shear Blade Suction Side for Different Levels of Roughness (160,000RPM, Phase 1.0)

an increase in turbulence intensity. This higher turbulence intensity is assumed to outweigh the secondary effects, culminating in a lesser regional thickening of the boundary layer as the roughness increases, in contrast to the cases at 120,000 RPM. This behaviour can also be visualised in the wall shear vector displayed in Figure 7.35. By comparing the wall shear vector diagrams for two RPMs, it is evident that these secondary flows are less pervasive and tend to be directed more towards the trailing edge for the higher Reynolds number case.

For the mean span skin friction distribution of the MGT rotor blade at 160,000RPM, several notable distinctions can be observed compared to 120,000RPM attributable to higher Reynolds number. Firstly, under 160,000RPM operating conditions, local peaks of skin friction at the leading edge could indicate premature transition due to the higher Reynolds numbers. As a result, the skin friction distribution along the chord exhibits a more uniform or "dampened" behaviour for higher RPMs with less pronounced sudden increases. Secondly, another important feature observed in the mean span of the MGT rotor blade is the prominence of the peak skin friction at the trailing edge, which contrasts markedly at 120,000RPM. The difference can also be visualised in the U_{98} diagrams as shown in Figure 7.36.

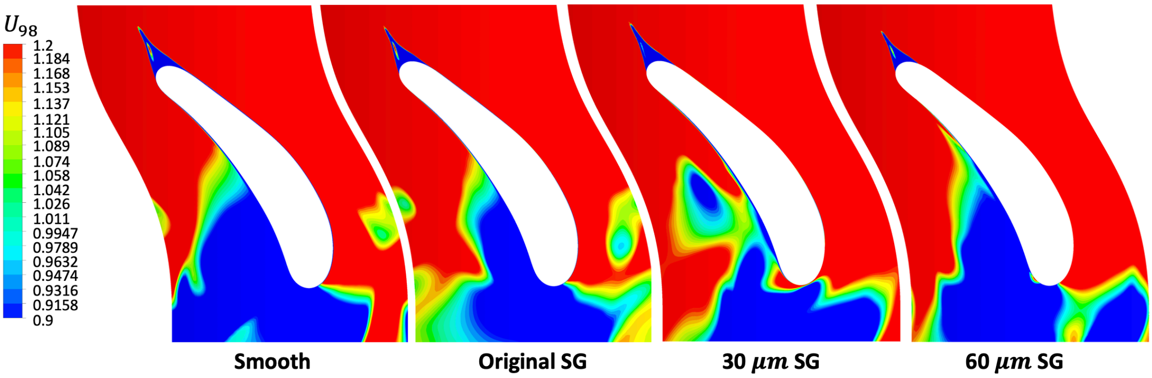

Figure 7.36: Wren100 MGT Rotor Mean Span Instantaneous Boundary Layer Thickness (160,000RPM, Phase 1.0)

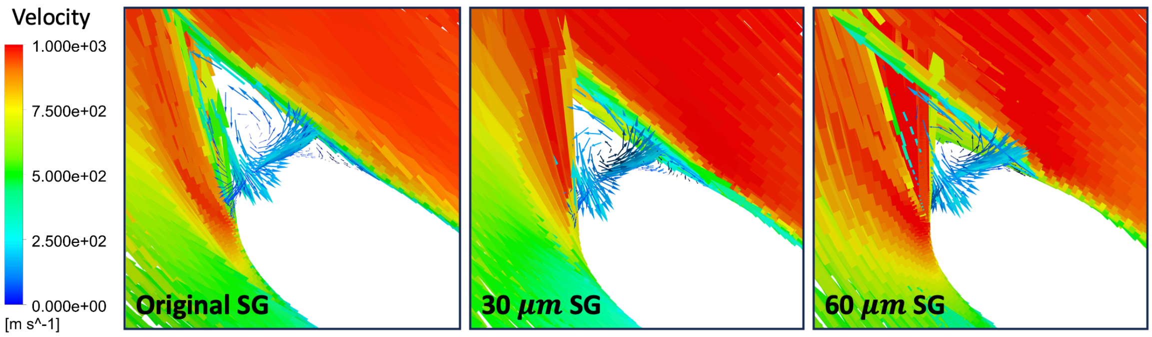

Figure 7.37: Instantaneous Velocity Vectors MGT Rotor Blade Mean Span TE Wake (160,000RPM, Phase 1.0)

For higher rotational speeds, the flow remains predominantly attached to the blade surface near the trailing edge. This reduced boundary layer thickness at the heightened RPM could be attributed to the increased momentum in the main flow due to higher rotational speeds and Reynolds number, which can suppress the boundary layer growth, leading to enhanced aerodynamic performance. In addition, as roughness rises from the original SG to 60μm SG, a contraction of the trailing edge wake can be visualised from the velocity vector diagrams in Figure 7.37. This shrinking of the blade downstream wake could suggest a mitigation of trailing edge loss. A plausible reason for this flow behaviour is the strengthened momentum in the primary flows stemming from both the pressure and suction sides of the blade as roughness increases.

An evaluation of the MGT rotor blade tip span operating at 160,000RPM further reveals significant insights into the flow dynamics under different levels of roughness. As shown on the right-hand side of Figure 7.33, the skin friction distribution for the near tip span exhibits similar trends to that of the mean span. It features minor increases in skin friction at the leading edge and peak skin friction at the trailing edge. This pattern is notably different from the flow behaviours seen at 120,000RPM, where multiple local peaks of skin friction can be found in the after-half of the rotor blade due to tip leakage and corner vortex effects. A more uniform skin friction distribution along the rotor blade chord for various levels of roughness can also be observed in Figure 7.33 and 7.38.

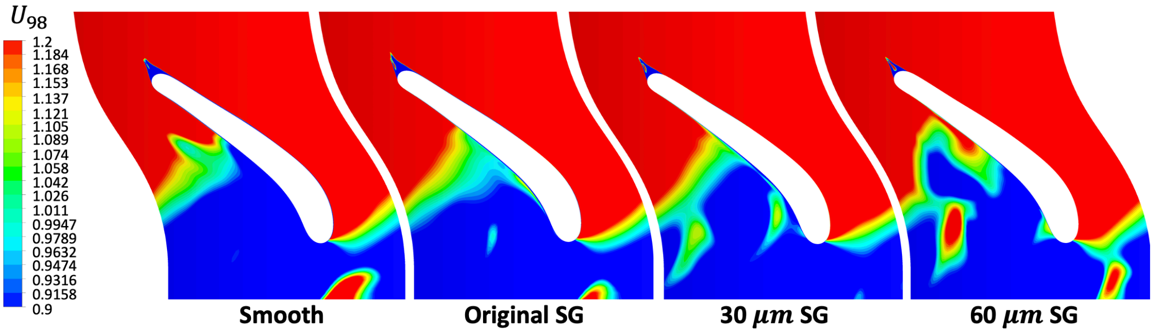

Figure 7.38: Wren100 MGT Rotor Tip Span Instantaneous Boundary Layer Thickness (160,000RPM, Phase 1.0)

As shown in the U_{98} plots for the mean and near tip span, what stands out is the similarities of its boundary layer developments as the roughness increases. For the higher RPM case, the separation bubble on the suction side of the tip span is completely eliminated. Compared to the 120,000RPM conditions, the higher RPM and corresponding turbulence intensity can serve to overpower the secondary flow effects that reduce the overall blade boundary layer thickness under the peak operating conditions (as also discussed on the near root span).

7.6 Summary

This chapter delineates the consequences of surface roughness on the aerodynamic performance of the MGT single-stage stator vane and rotor blade. The findings based on the numerical data analysed before are summarised in the following subsections. Overall, the discoveries gleaned from this investigation not only bolster the understanding of MGT aerodynamics but also furnish invaluable insights for future redesign and optimisation ventures in the realm of turbomachinery.

7.6.1 MGT Stator Vane

Boundary Layer Measurements: As surface roughness increases, the changes in boundary layer developments and the average roughness Reynolds numbers were acquired from the CFD results, which are also listed in Table 7.6.

Case	Location 1 (μm)	Location 2 (μm)	Location 3 (μm)	Re_{ks} (Stator)	Re_{ks} (Rotor)
120k Smooth	70.4	50.0	50.0	0	0
120k Original	33.3	44.5	44.5	2.65	5.47
120k 30 μm SG	16.7	33.3	40.7	5.01	9.28
120k 60 μm SG	2.2	26.4	20.4	8.64	15.96
160k Smooth	80.0	38.2	44.5	0	0
160k Original	25.9	48.2	27.7	1.73	5.34
160k 30 μm SG	11.3	26.8	29.5	3.17	9.16
160k 60 μm SG	~ 0.2	18.3	24.9	5.39	15.06

Table 7.6: Changes in Boundary Layer Developments for Different Roughness Levels

Overall & Local Effects: In the multifaceted aerodynamic landscape of the MGT stator vane, surface roughness exhibits nuanced effects across varied operational speeds. At the peak 160,000RPM conditions, identical roughness levels demonstrate an amplified influence on average pressure loss coefficients (Y_p) compared to the 120,000RPM regime. Despite a majority of the vane exhibiting a thick boundary layer at the standard 120,000RPM, surface roughness below certain thresholds, as seen in the original SG case, tends to minimally affect overall aerodynamic losses. However, the complex, three-dimensional flow around the stator vane means that the same roughness can elicit diverse local responses. For instance, even with average roughness Reynolds numbers (Re_{ks}) for the original SG cases under 5 (typifying hydraulically smooth conditions) at both rotor operating RPMs, these roughness elements can still reduce and eliminate laminar separation bubbles, especially near the vane leading edge on the suction side. This underscores the importance of considering both global and localised aerodynamic interactions when assessing roughness impacts.

Elimination of Separation Bubble & Transition Delay: Upon analysing the MGT stator vane aerodynamics under two distinct operational conditions, it becomes evident that elevating surface roughness can effectively mitigate and eliminate laminar separation bubbles proximate to the leading edge on the suction side. This results in flow becoming more attached along the vane surface, subsequently delaying the onset of transition from the proximal section near the leading edge (referred to as location 1) to a more downstream location closer to the trailing edge (termed as location 2). Notably, the aerodynamic sensitivity to variations in surface roughness was accentuated at the higher RPM scenario, underscoring its pronounced responsiveness to rough element perturbations.

Turbulent Flow and Secondary Structures: Despite the flow been mostly laminar due to the low Reynolds numbers, it was found that the augmented roughness would engender a strengthened primary flow with increased turbulent intensity against the potential secondary effects. This enhanced turbulence has been observed to perturb local secondary flow structures and separation zones, which were erstwhile sources of high skin friction. Such disturbances also culminate in the dampening effects of these local skin friction peaks.

Impact on TE Wake & Determination of 'Optimal Roughness': The study revealed a phenomenon termed 'optimal roughness' that varies according to rotor operating RPMs, which the MGT stator would generate the highest loss. For the Wren100 turbine operating at 120,000 RPM, this 'optimal roughness' for the stator vane is approximated at 30 microns SG. However, at an RPM of 160,000, this value diminishes to around 15 microns SG. The reduced 'optimal roughness' at higher RPMs indicates that there may exist an inverse relationship between RPM and optimal roughness. Thus, two heuristic formulae have been derived that encapsulate observations related to the rate of boundary layer thinning as roughness escalates, its relationship with Reynolds number, and the aforementioned 'optimal roughness' (Equation 7.5 and 7.6).

7.6.2 MGT Rotor Blade

Separation Reduced and Delayed Onset: The increment in surface roughness has been observed to mitigate flow separation, particularly on the suction side proximal to the rotor blade trailing edge under normal operating conditions (120,000RPM). What stands out is on the near tip span, the increased surface roughness not only leads to the maximum length and height reduction of the laminar separation bubble, but also affects its onset location. For the two different operating conditions, increased roughness could enhance wake and turbulent mixing in the separated shear layer, which potentially decreases the influence of stator-rotor interaction.

Flow Field Alterations with RPM: The broader flow field enveloping the rotor blade exhibits sensitivity to surface roughness, exhibiting variances between normal operational speeds (120,000RPM) and peak operational speeds (160,000RPM). At the former speed and for roughness under 30 microns SG, secondary flow features, such as the tip leakage vortex and corner vortex, demonstrate resilience against escalating turbulence levels, culminating in persistent boundary layer formations and localised skin friction peaks. At a heightened roughness of 60 microns SG, the predominant turbulence from the primary flow appears to eclipse these secondary structures, yielding a more homogeneous turbulence profile and swift boundary layer thinning. At the peak RPM of 160,000, the elevated Reynolds number results in flow predominantly adhering to the blade surface. The nuanced effects of surface roughness on boundary layer thinning become less discernible due to the inherently thin boundary layer at such RPMs. This phenomenon also elucidates the consistent rotor stagnation pressure loss coefficient across varied surface roughness levels at these conditions.

7.6.3 Final Remarks

In summary, the interplay of surface roughness with the aerodynamic performance of gas turbine blades presents a complex paradigm, predominantly attributed to the inherently three-dimensional nature of the flow and fluctuating operating conditions. Particularly in MGTs that operate at relatively low Reynolds numbers, investigating the potential impacts of different roughness magnitudes becomes pivotal. Such analysis, grounded in rigorously validated CFD models, offers invaluable insights for turbine design practitioners. An important revelation from the current study, especially pertinent for the Wren100 turbine stator, is the demarcation of an "optimal" roughness threshold (or optimum maintenance intervals). Under standard operational parameters, roughness configurations at or below the original Sand Grain (SG) magnitude need not warrant undue concern. Yet, should roughness exceed this optimal threshold, the inherent low Reynolds number dictates a strategic increase in roughness to instigate heightened turbulence, thereby mitigating prevailing secondary flow effects. Contrarily, the MGT rotor blade exhibits amplified sensitivity to surface anomalies, warranting recommendations from the authors to minimise roughness deviations.

Despite these insights, it is imperative to acknowledge the constraints posed by the current investigative tools and commercial CFD platforms. Several nuances of the MGT flow dynamics remain elusive. Future research endeavours could greatly benefit from deploying advanced flow visualisation methodologies, such as Particle Image

Velocimetry (PIV). Such techniques could shed light on intricate flow phenomena, encompassing flow separations, vortex dynamics, and nuanced turbulence interactions caused by different roughness scales.

Chapter 8

Wren100 Turbine Redesign

8.1 Aerofoil Shape Redesign and Comparison With Baseline Performance

Based on previous experimental and numerical studies of the Wren100 turbine stator and rotor system, the base aerodynamic performance and potential sources of loss are acquired. With all the information, a redesign was carried out with validated CFD models to optimise the turbine thrust and efficiency, which is also the interest of the company (Turbine Solutions Ltd.) that initially developed the micro engine. In the context of micro gas turbine blade design optimisation, the process of implementing design modifications was carried out manually. The main reason behind this approach is the complex and unconventional geometries of the Wren100 turbine blades, which make it challenging for automated optimisation algorithms to efficiently explore the design space.

8.1.1 Wren100 Micro Turbine Base Performance

In this study, a verified CFD model (described in Chapter 5) was employed to conduct iterative simulations to accurately determine the boundary conditions of the Wren100 turbine. As previously discussed, two reverse-engineered models were generated: the discrete model and the parametric model. A comparison between the simulation and experimental data in the earlier chapter demonstrated that the discrete model closely resembled the actual turbine. However, the parametric model, while still predicting results within the error range and following the same trend of thrust as RPM increased, was deemed to be acceptable but slightly less accurate.

Despite the superior performance of the discrete model, it posed a challenge in terms of modification, making redesign based on this model problematic. Conversely, the parametric model was constructed using a series of parameters, allowing for easier manual adjustments. Given that the parametric model adequately represents the performance of the Wren100 stator-rotor system, the redesign process was carried out based on this model. This approach facilitated a more efficient and effective redesign process, paving the way for improved understanding and optimisation of the Wren100 turbine's aerodynamic performance.

The final base performance iterated based on the jet engine test data and the parametric model with the 4-eq. transitional turbulence models are shown in Table 8.1.

T_{01} (K)	P_2 (bar)	P_{02} (bar)	$\dot{m}$ (kg/s)	F (N)	RPM
1114.2	0.66	1.19	0.184	89.5	160,000
1015.8	0.73	1.13	0.177	68.1	150,000
913.4	0.70	0.98	0.149	48.2	140,000
829.2	0.74	0.90	0.136	35.4	130,000
807.3	**0.80**	**0.87**	**0.117**	**24.3**	**120,000**
754.9	0.82	0.84	0.102	17.1	110,000
718.1	0.82	0.81	0.090	13.2	100,000

Table 8.1: Wren100 Turbine Based Performance (Parametric Model)

As previously noted, the impact of COVID-19 and the temporary out-of-service status of the Wren100 turbine limited its operational capacity to a maximum of 120,000 RPM during the first three years of this project. Although data at higher RPMs were eventually obtained in the final year of the project, the turbine redesigns were primarily conducted based on the flow conditions at 120,000 RPM. This constraint was taken into account during the redesign process, ensuring that the parametric model would still provide valuable insights and optimisations for the aerodynamic performance under these specific flow conditions of the Wren100 turbine. It is also highly likely the turbine with the redesigned components would have better performance at higher RPMs.

The following subsections show some of the parameter changes that could potentially achieve the redesign goals (increase efficiency and thrust) in this research project. Initially, the simulations were conducted based on the validated 4-eq. transitional turbulence model for rapid change of design parameters and lower computational resource requirements. When the optimised blade parameters were acquired, high-fidelity LES simulations were carried out to better visualise how the flow field is changed compared to the base performance.

8.2 Parametric Redesign Part 1: Stator Vane

8.2.1 Influence of Vanes Number Adjustments

As a preliminary investigation based on the transitional SST model, the rough impact of the MGT stator vanes number on the stator stagnation pressure loss coefficient and rotor efficiency were calculated and plotted in Figure 8.1.

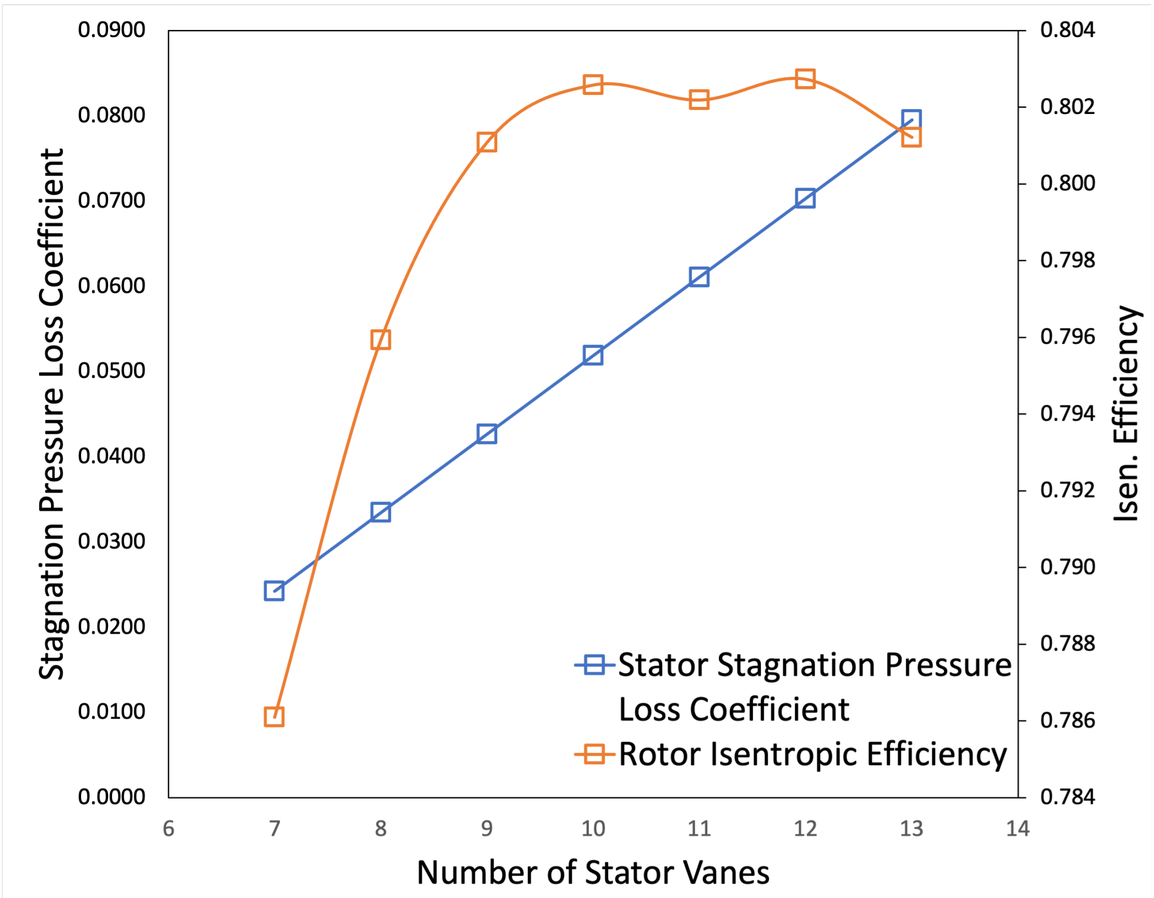

Figure 8.1: Impact of MGT Stator Vanes Number (120,000RPM)

Initially, the stator vane count was reduced from the original configuration of 13 to 10, which yielded promising outcomes with a substantially reduced stagnation pressure loss coefficient from 8.87% to 5.19%. Concurrently, the rotor remains the same efficiency and the thrust exhibited an increment from 22.77N to 29.54N, indicating a potential enhancement in propulsion capabilities. However, further investigations by reducing the vane count below 10 to 7 suggested an adverse trend, with rotor efficiency declining rapidly, which emphasised the complexity of the stator rotor interaction and the delicate balance requirements to optimise performance in both MGT components simultaneously.

Based on the findings, a decision was made to fine-tune the stage performance by moderating the change in vane count from 13 to 12. This intermediate stator redesign configuration provides an opportunity to explore the potential performance enhancement without triggering rapid changes in stator rotor interactions that reduce the rotor efficiency. To evaluate the 12 vanes configuration, comprehensive aerodynamic performance analyses were carried out based on high-fidelity LES WALE simulations.

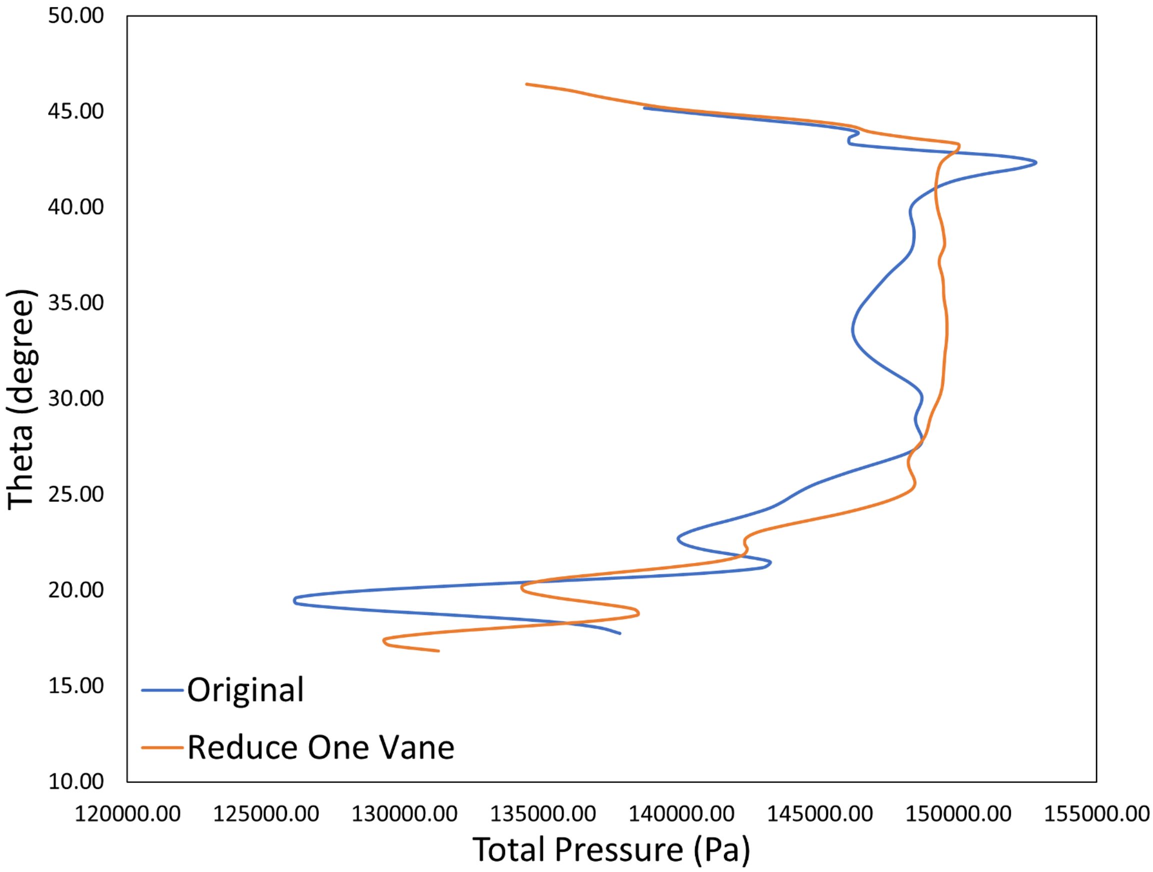

Figure 8.2: Phase-Averaged Stator Mean Downstream Total Pressure (Original Vs. Redesigned)

Figure 8.2 displays the phase-averaged spanwise total pressure results derived from the LES simulations, which slight performance improvements could be observed from the modification of MGT stator vane count from 13 to 12. Primarily, the reduction in vane count demonstrated a considerable decrease in wake depth, with values altering from 126107 Pa for the original 13-vane configuration to 134358 Pa for the 12-vane setup. As discussed earlier, the wake depth is a critical determinant of turbine performance, and reducing one vane could potentially reduce the base pressure loss and enhance the flow quality before entering the rotor domain. Additionally, an apparent stabilisation in the spanwise total pressure distribution outside the wake region can be observed for the reduced vane case. Higher total pressure stability downstream of the stator vane is likely indicative of a less turbulent and more uniform flow field, which could also lead to reductions in base pressure loss or trailing edge loss. Thus, potential higher thrust could be achieved for a greater proportion of flow kinetic energy being effectively converted to useful work with lower aerodynamic loss.

For the profile loss and secondary loss, it is known reducing vane count invariably increases the blade loading, which results in the profile loss reduction due to the smaller surface area and unchanged blade shape. However, potential escalation of secondary loss is also expected due to the larger passage area and augmented flow complexity. In this case, the interplay between two losses was visualised based on the entropy creation diagram.
According to the entropy plots, it was observed the instantaneous entropy creation reduces for the 12-vane setup, which indicates the potential increase in secondary losses has not been significant enough to offset the decrease in profile losses.

Overall, based on the comprehensive analyses, the redesigned 12-vane configuration emerges as a favourable redesign point for the MGT stator for higher thrust.

8.2.2 Influence of Aspect Ratio (AR) Redesign

According to previous mean line prediction and comprehensive performance analysis of the MGT stator vane, one particular observation is the presence of a high secondary loss, which has significant implications for the overall efficiency of the MGT stage. Previous studies have suggested the potential of optimising the secondary loss by increasing the stator aspect ratio. Therefore, the MGT stator vane axial chord was reduced by 10% of its original value, which effectively increased the aspect ratio by around 11%.

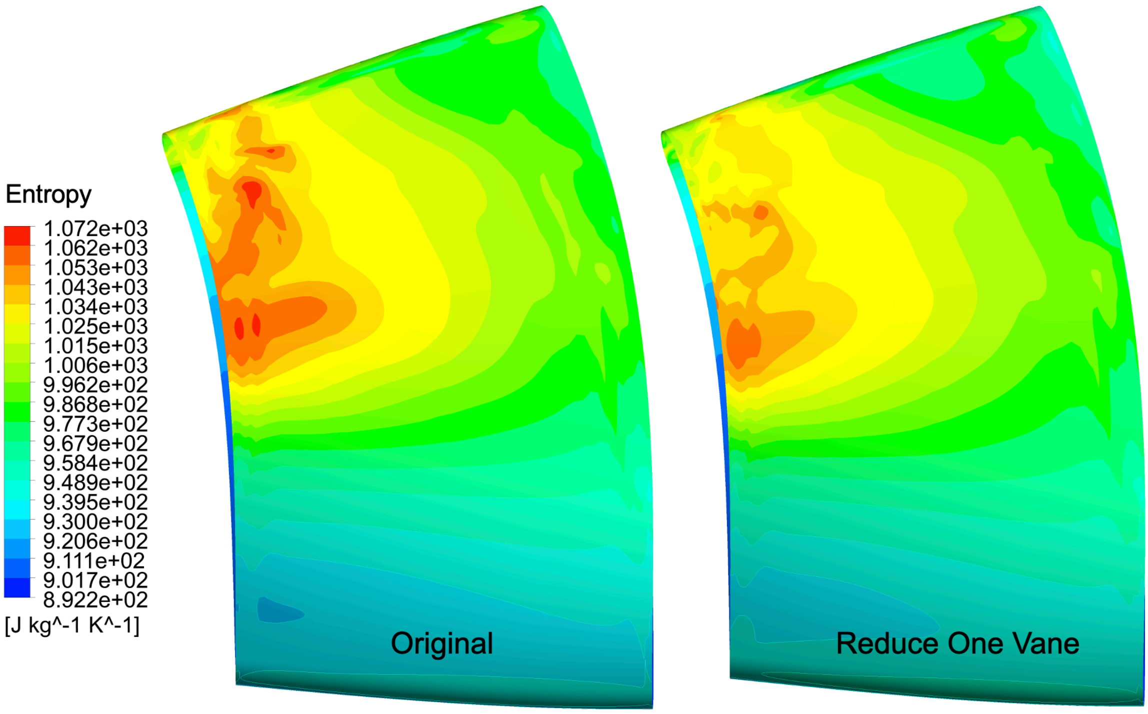

Figure 8.3: Instantaneous Stator Surface Entropy Generation Contour (Original Vs. Redesigned)

	P_{02} (bar)	T_{02} (k)	Thrust (N)	η (%)	$Y_{p,stator}$ (%)	$Y_{p,rotor}$ (%)
Base	0.866	713.30	24.25	80.1	7.95	24.55
90% Axial-Chord	0.900	721.646	27.14	79.1	8.80	23.30

Table 8.2: Wren100 MGT Redesigned Performance Comparison (Parametric Model)

From Table 8.2, preliminary evaluations based on the transitional SST model show promising improvements in the performance of the MGT stage. The thrust was increased from 24.25N to 27.14N and the rotor stagnation pressure loss coefficient was reduced from 24.55% to 23.3%, suggesting an enhanced energy extraction from the working fluid and improved aerodynamics. This could also mean that the secondary flow structures introduced by the stator have a lesser adverse impact on the rotor blade performance in the increased AR case To further investigate the influence of the increased AR on the development of secondary flows, the wall shear vector plots were compared as shown in Figure 8.4.

From the wall shear comparison diagrams, it was evident misalignment and more

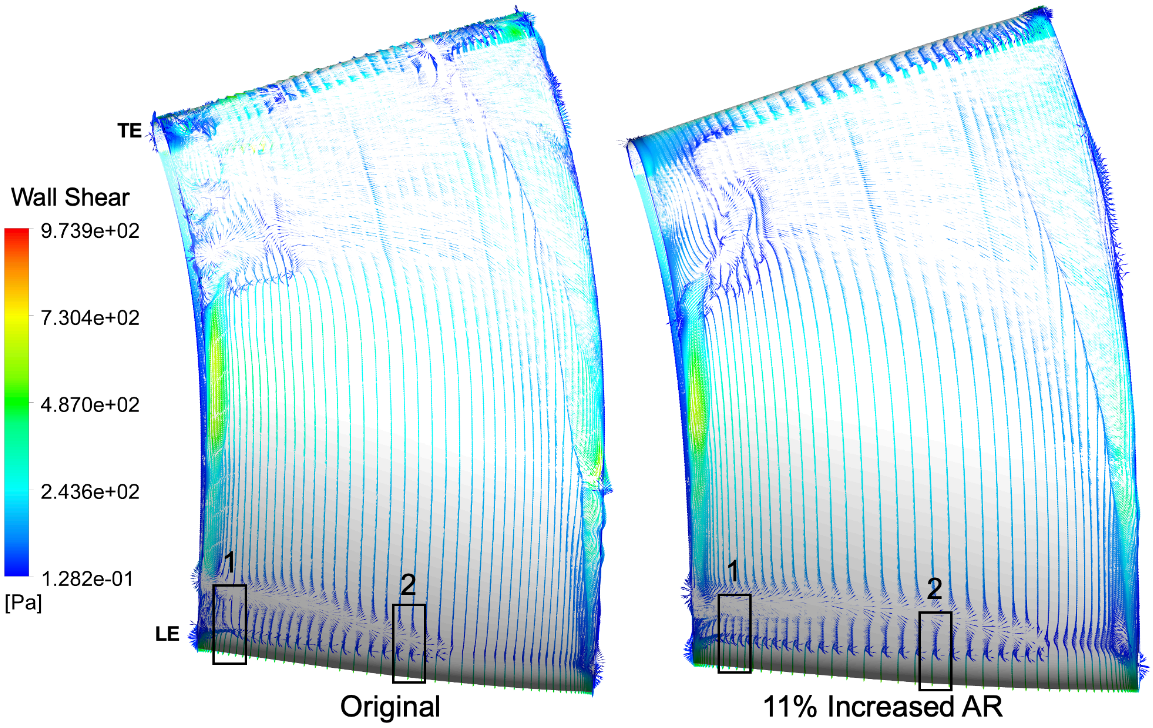

Figure 8.4: Instantaneous Wall Shear Vector On Vane Suction Side (Original Vs. Redesigned)

pronounced swirl flow patterns close to the vane trailing edge for the original design, which is also the high entropy creation region as analysed before in Figure 8.3. By reducing the axial chord, the passage vortex, a common secondary flow structure, becomes less intense. In addition, the overall wall shear vectors become slightly more aligned with the primary flow direction for the majority of the vane surface.

Overall, despite the passage vortex is a significant secondary flow feature visible in both designs, its intensity appears less pronounced in the increased AR case. The reduced intensity of the passage vortex could lead to the observed reduction in downstream rotor losses, resulting in the observed efficiency improvements. While the increased AR vane exhibits a marginally higher pressure loss coefficient (Y_p) for the stator, the benefits it offers in terms of rotor performance and overall thrust generation seem to outweigh this increase in loss. It could imply that the secondary flows introduced by the stator in the increased AR case might be less detrimental to the rotor performance.

An additional finding is the increased AR design could potentially enhance the flow laminar separation bubbles formed on the suction side near the leading edge, especially at location 2 on the mean span that slightly raises the regional flow velocity as displayed in Figure 8.5.

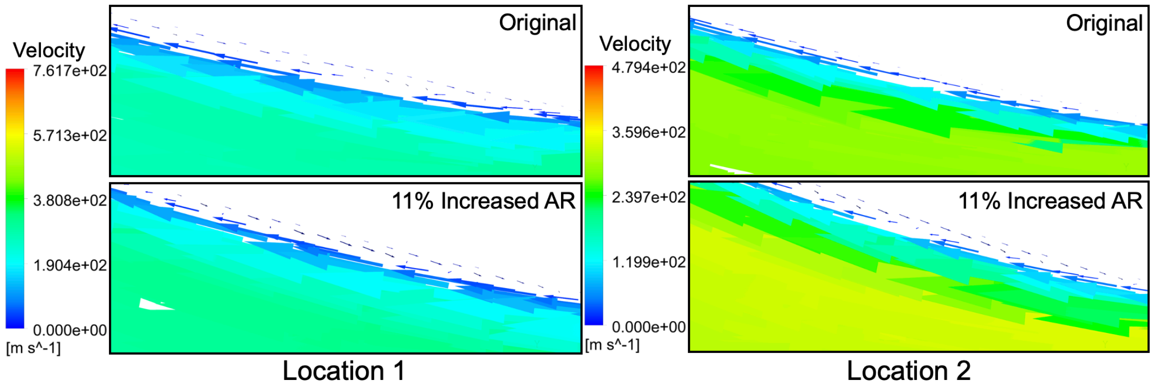

Figure 8.5: Instantaneous Velocity Vectors at Monitored Location 1&2 (Original Vs. Redesigned)

In conclusion, the increased aspect ratio design seems to mitigate some of the adverse secondary flow effects for the MGT turbine stage, especially near the trailing edge, leading to improved downstream rotor performance and increased thrust. This suggests that while secondary flow effects are still present, their overall impact on the MGT stage performance is reduced in the increased aspect ratio case.

8.2.3 Influence of Trailing Edge Thickness Redesign

According to the aerodynamic performance analysis of the MGT stator vane in Section 6.2, it was known that most of the entropy generation is from the suction side near the trailing edge and the downstream wake region. Thus, the second parametric study was conducted by adjusting the vane trailing edge thickness. This study was aimed at reducing the associated profile loss and trailing edge loss. Figure 8.6 displays the change of profile loss and isentropic efficiency as the reduction of trailing edge thickness.

According to the initial simulation results, it can be seen that the stator stagnation pressure loss coefficient gradually decreases as the trailing edge becomes thinner. The change of trailing edge thickness also has a positive effect on the rotor efficiency, which the 90% reduction of trailing edge thickness would result in a 3.2% increment of rotor efficiency compared to the base performance. However, due to the tiny sizes of the

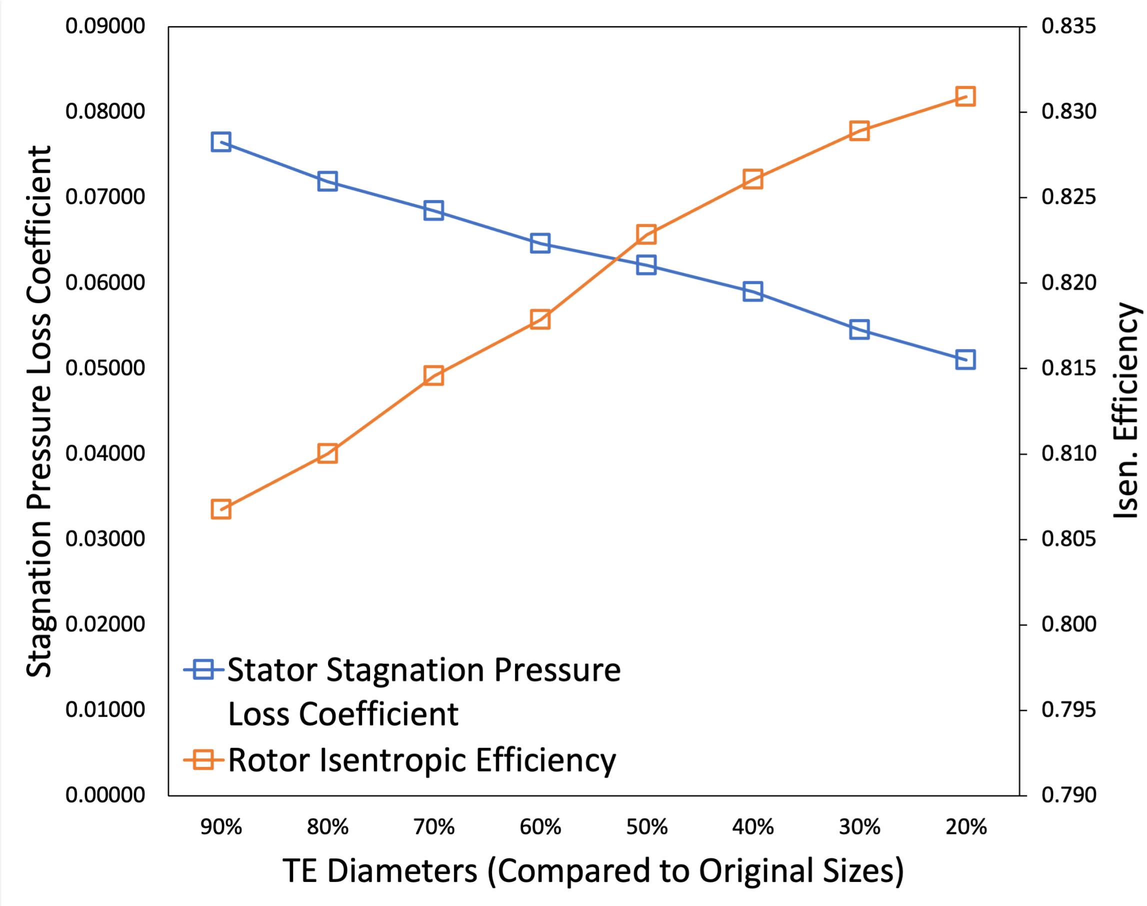

Figure 8.6: Trailing Edge Thickness Reduction of Wren100 Stator Vanes

MGT parts, achieving 10% of the original blade thickness is somewhat difficult with the current manufacturing technique. Thus, the initial redesign recommendation is half the trailing edge thickness of the stator (50%), which the detailed comparison between the 50% trailing edge thickness case and the base design are shown in Table 8.3.

	P_{02} (bar)	T_{02} (k)	Thrust (N)	η (%)	$Y_{p,stator}$ (%)	$Y_{p,rotor}$ (%)
Base	0.866	713.30	24.25	80.1	7.95	24.55
50% TE	8.896	716.13	26.20	82.3	6.21	23.58

Table 8.3: Wren100 MGT Redesigned Performance Comparison for TE Thickness Reduction (Parametric Model)

Based on the initial redesign recommendation, the LES simulations were carried out to better visualise the flow behaviour changes within the MGT passages. According

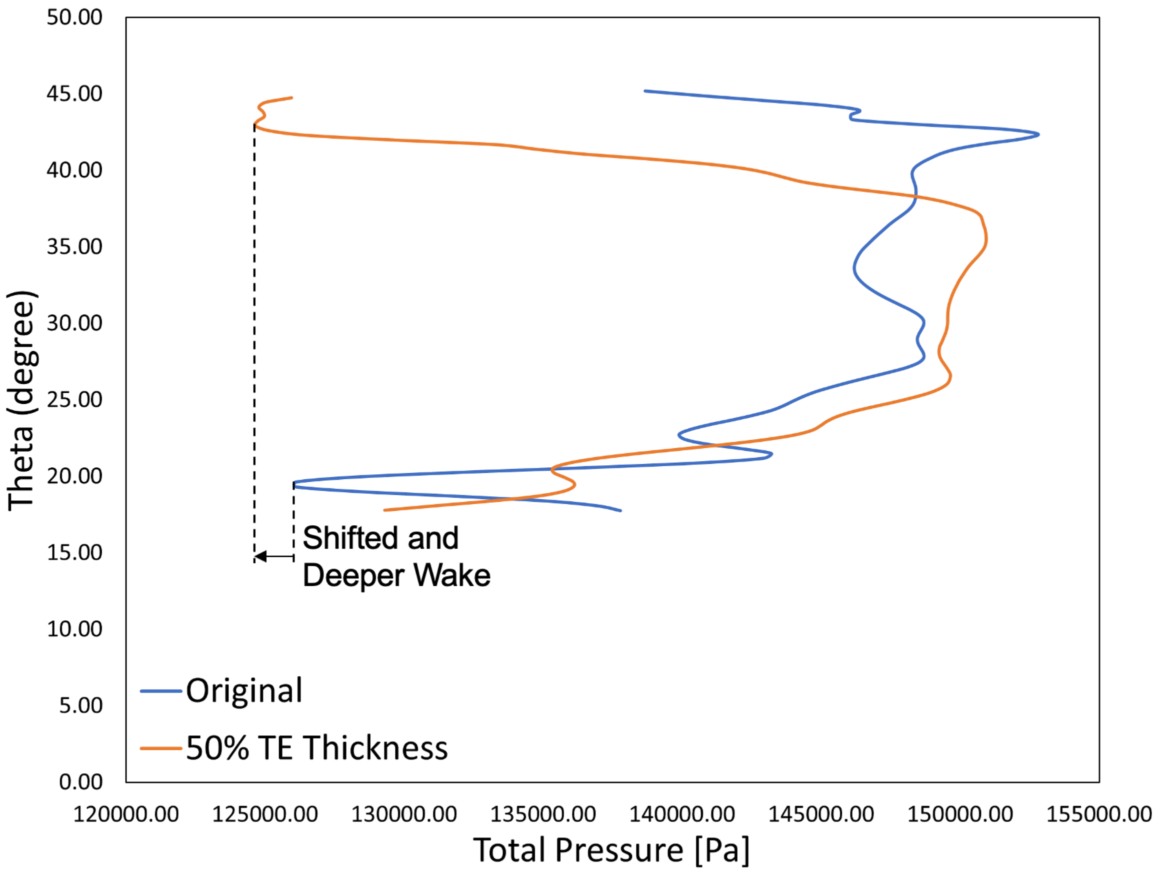

Figure 8.7: Phase-Averaged Stator Mean Downstream Total Pressure (Original Vs. Redesigned)

to the phase-averaged stator downstream total pressure distributions comparison, an immediate observation is the relocation of the wake for the 50% TE thickness moves away from the trailing edge relative to the original vane shape. This displacement of the wake can be attributed to a reduction in flow blockage due to the thinner trailing edge, leading to a delay in the development of the downstream wakes. Furthermore, the wake depth has increased from 126107Pa in the original design to 124665Pa in the thinner 50% TE thickness design. This increased wake depth indicates a slightly higher trailing edge loss, which is associated with increased mixing and turbulence intensity due to the thinner trailing edge. However, the thinner TE design exhibits a higher and slightly steadier base total pressure downstream of the stator outside the wake region compared to the original configuration.

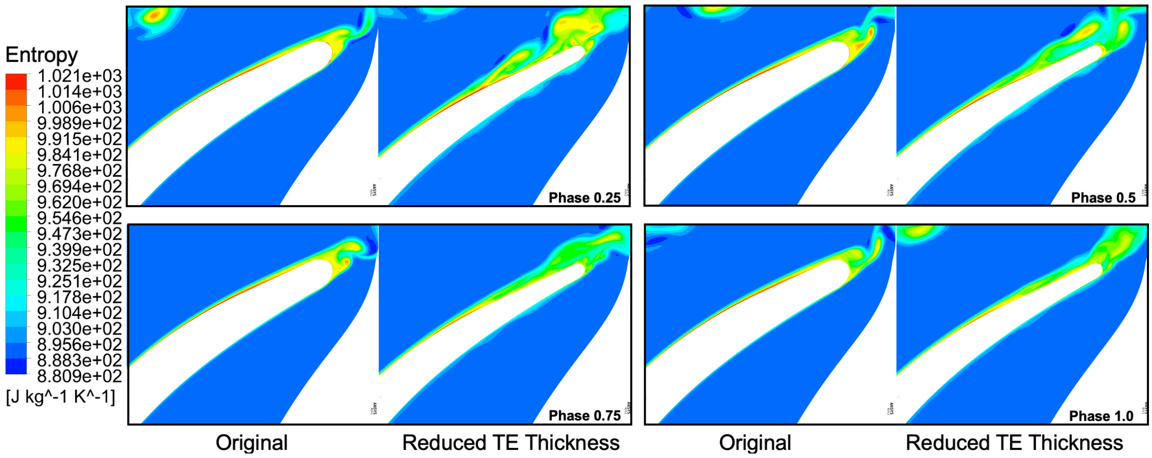

Figure 8.8: MGT Stator Mean Downstream Entropy Generation (Original Vs. Redesigned)

To better understand the influence of a 50% thinner TE on the performance of the MGT stator vane, an evaluation of entropy contours at the vane mean span was conducted based on LES data at varying phases within one rotor passage time. At phase 0.25, relatively high entropy on the suction side for the thinner TE configuration was thicker and displayed more chaotic behaviour than the original design. This heightened entropy region, as revealed by the vorticity contours in Figure 8.9, was primarily due to an increased flow separation occurring on the suction side near the trailing edge in the thinner TE configuration. The 50% thinner TE induces a much stronger mixing and interaction effect in the flow, leading to a more rapid conversion of turbulence energy into thermal energy, thus increasing the regional entropy creation.

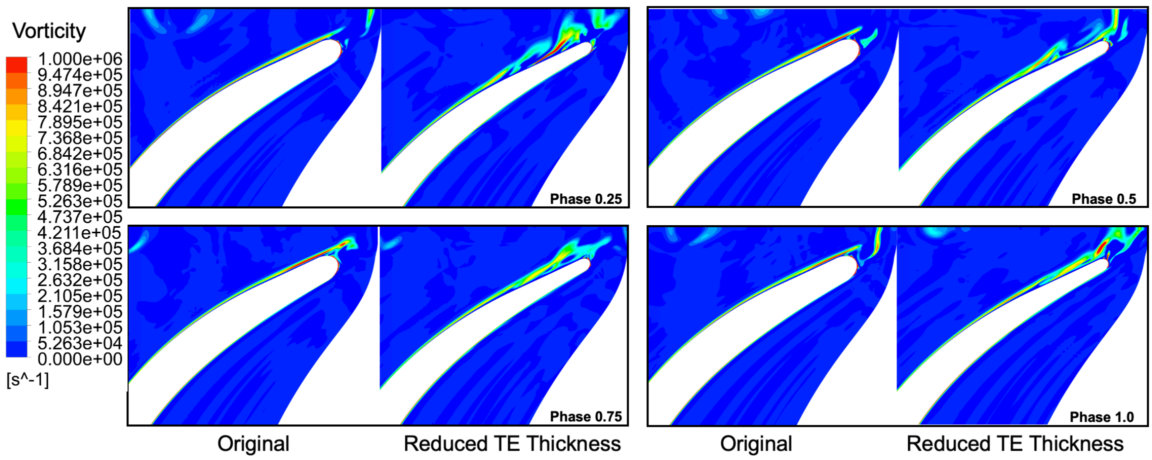

Figure 8.9: MGT Stator Mean Downstream 2D Vorticity (Original Vs. Redesigned)

For phase 0.25 to phase 0.75, the region of red heightened entropy rapidly dissipates downstream for the thinner TE design, as evidenced by the diminishing vorticity contours. This is caused by the following two factors. Firstly, the thinner TE enhances the mixing of the wake with the free stream flow, which leads to quicker dissipation of the vortical structures and, thus, quicker reduction of the wake size and intensity. Secondly, as shown in 8.9 (phase 1.0), the wake production for the thinner TE case has different characteristics that convect and dissipates more quickly due to the interaction with the surrounding flow and downstream blades. By phase 1.0, the entropy creation contours indicate the smaller region of extremely high entropy (red region) in the thinner TE design. The more extensive areas of highlighted entropy downstream of the trailing edge in the thinner TE design suggest a continuous dissipation process of the initially formed high-entropy region.

Overall, despite the transient increase in entropy, the rapid dissipation and the smaller extent of the high-entropy region at phase 1.0 suggest a more effective conversion of kinetic energy to work within the rotor passage time for the thinner TE configuration. This underpins the observed increase in thrust and rotor efficiency despite the broader wake. As a result, the thinner TE design appears to be a promising configuration for improving the performance of the MGT stator vane.

8.3 Parametric Redesign Part 2: Rotor Blade

8.3.1 Influence of Tip Clearance Reduction

In the process of seeking potential improvements for the rotor blade, the role of tip clearance in the single-stage MGT has been brought into scrutiny as analysed in Section 6.3. Similar to the stator vane redesign, parametric studies were carried out based on the validated RANS transitional SST model by considering a gradual reduction in tip clearance from 5% to 2% in increments of 0.5% as displayed in Figure 8.10.

From the initial RANS results, an intriguing trend was discovered. As the tip clearance was reduced, the efficiency of the rotor blade increased steadily from 80.1% at 5% clearance to 84.2% at 2% clearance. However, this was accompanied by a decline in thrust from 24.25N to 22.61N. Weighing the trade-offs between these two target performance parameters, a compromise approach is always necessary for the design of a gas turbine component [190]. While higher efficiency is a desirable goal, manufacturing constraints and the objective of increased thrust necessitate a balanced approach. Taking these considerations into account, a tip clearance of 2.5% was deemed to be an appropriate balance between increased efficiency and manageable manufacturing complexities while also providing acceptable thrust levels. Further LES simulations were also conducted to capture the transient flow physics in detail and compare the performance difference between the original and redesigned rotor blades with half the tip gap.

To comprehensively assess the flow field changes around the rotor blade for the reduced tip gap case, it is apparent that the alteration of the rotor blade tip gap imparts significant modifications to the flow characteristics, especially in the vicinity of the tip. By examining the velocity contours at multiple spans in proximity to the blade tip (6%, 8%, 16% and 18%) as shown in Figure 8.11 and 8.12, the reduction of the tip gap was found to have a notable impact on the flow separation behaviour close to the shroud. For the flow structures, there are distinct high-velocity streaks near the blade tips for the original tip clearance case. These are indicative of massive separation bubbles and tip leakage flows. The swirling patterns and vortical structures observed, especially towards the later phases, also indicate the presence of secondary flows. From the data at different phases for the 6% and 8% tip, the flow separation

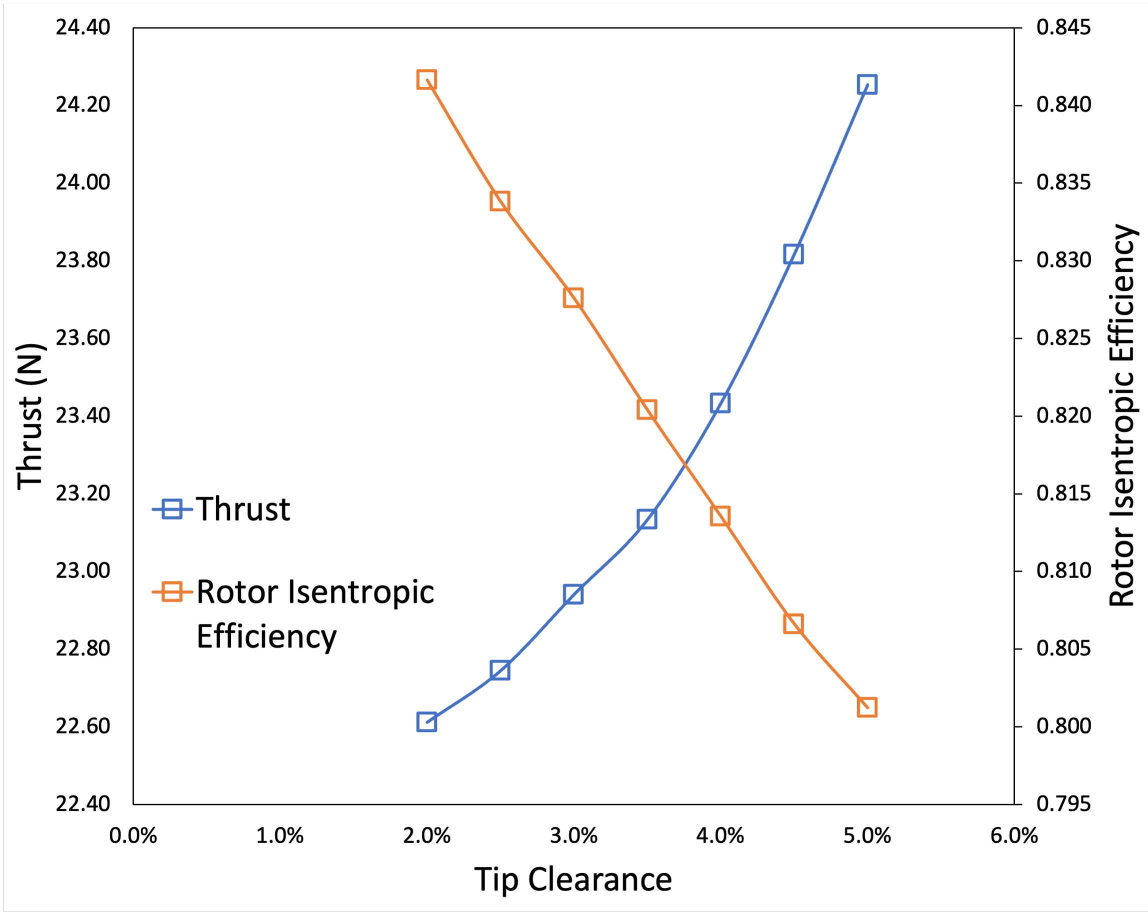

Figure 8.10: Tip Clearance Reduction of Wren100 Rotor Blades

behaviour observed on the suction side in the original design (left) is significantly suppressed in the case with the reduced tip gap (right). The high-speed flow (depicted in red) for the reduced tip gap case exhibits a higher degree of attachment to the blade suction side, which suggests improved flow quality with a more efficient aerodynamic profile close to the rotor tip. In addition, the reduction of the tip gap does not affect the onset of the separation bubble.

Overall, for the spans closer to the tip, the impact of tip clearance is more pronounced. The reduction in high-velocity regions is evident when comparing these diagrams, showcasing the efficiency gains achieved by the redesign.

When moving away from the shroud, the effects of tip leakage become less dominant. Instead, the flow is more influenced by the blade camber and overall geometry. At these spans, the velocity distributions appear more uniform, suggesting a well-

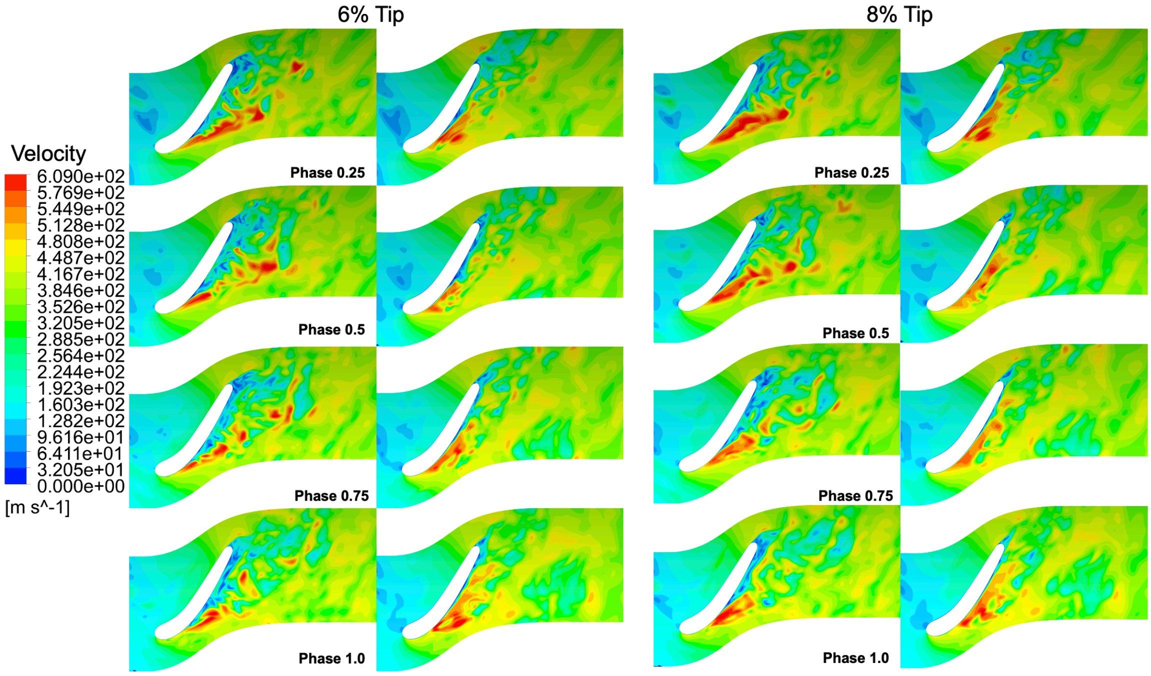

Figure 8.11: Near-Tip Sectional Velocity Contour (6% & 8% Tip) (Original Vs. Redesigned)

behaved flow with reduced secondary effects. For the 16% and 18% tip spans, it can be seen the influence of the tip gap on the flow field is less pronounced. However, even at these distances away from the shroud, differences between the original and reduced tip gap designs persist. The velocity contours for the original tip gap design show a broader area of flow separation and a thicker boundary layer on the suction side near the trailing edge compared to the reduced tip gap case.

To sum up, reducing the tip gap exhibits considerable promise in enhancing the overall aerodynamic efficiency of the rotor blade, principally through improved flow attachment and suppression of leakage flows and laminar separation at critical regions near the blade tip. However, the uniform velocity distribution, especially near the blade tips, can result in a reduced pressure differential across the blade. This, in turn, can explain the observed reduction in thrust.

8.3.2 Influence of Leading Edge Redesign

As suggested in Chapter 6, parametric studies were carried based on the RANS simulations with a gradual reduction in blade leading edge thickness to 70% of its original value at root and mean spans to reduce the unsteady LE vortex. The initial

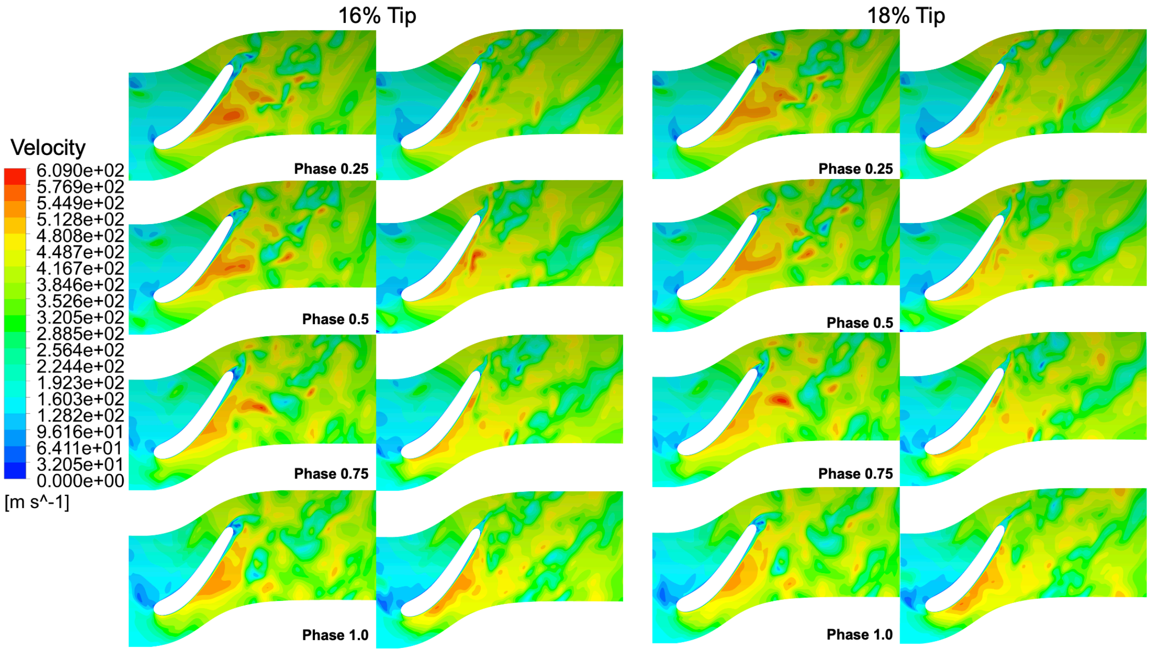

Figure 8.12: Near-Tip Sectional Velocity Contour (16% & 18% Tip) (Original Vs. Redesigned)

calculation results based on the steady RANS transitional simulations were compared in Table 8.4.

	P_{02} (bar)	T_{02} (k)	Thrust (N)	η (%)	$Y_{p,stator}$ (%)	$Y_{p,rotor}$ (%)
Base	0.866	713.30	24.25	80.1	7.95	24.55
90% LE	0.863	712.73	24.40	80.0	8.06	24.48
80% LE	0.860	712.09	24.56	80.0	8.08	24.60
70% LE	0.858	711.53	24.72	79.9	8.04	24.72

Table 8.4: Wren100 MGT Redesigned Performance Comparison (Parametric Model)

Upon studying the modifications to the MGT rotor blade leading edge root and mean span thickness, it was observed that reductions result in a consistent, although slight, decrease in exit total pressure and temperature. Interestingly, there is an improvement in thrust with each decrement, hinting at enhanced flow alignment around the leading edge. This might be because a sharper leading edge can better delay or reduce the size of the leading edge vortex, translating to slightly higher thrust. However, isentropic efficiency shows a different trend, with a minor decline when the thickness is reduced aggressively. Additionally, both stator and rotor stagnation pressure loss coefficients exhibit subtle increases with decreased leading edge thickness, implying potential secondary flow enhancements or altered boundary layer dynamics. It also suggests that the leading edge modifications of the MGT rotor blade might have enhanced its aerodynamics while introducing challenges for the stator.

To further explore the unsteady flow phenomena, high-fidelity LES results were generated for the 70% LE case to compare with the base performance.

For the mean span of the MGT rotor blade, the vorticity contours at different phases were compared between the original and redesigned profiles.

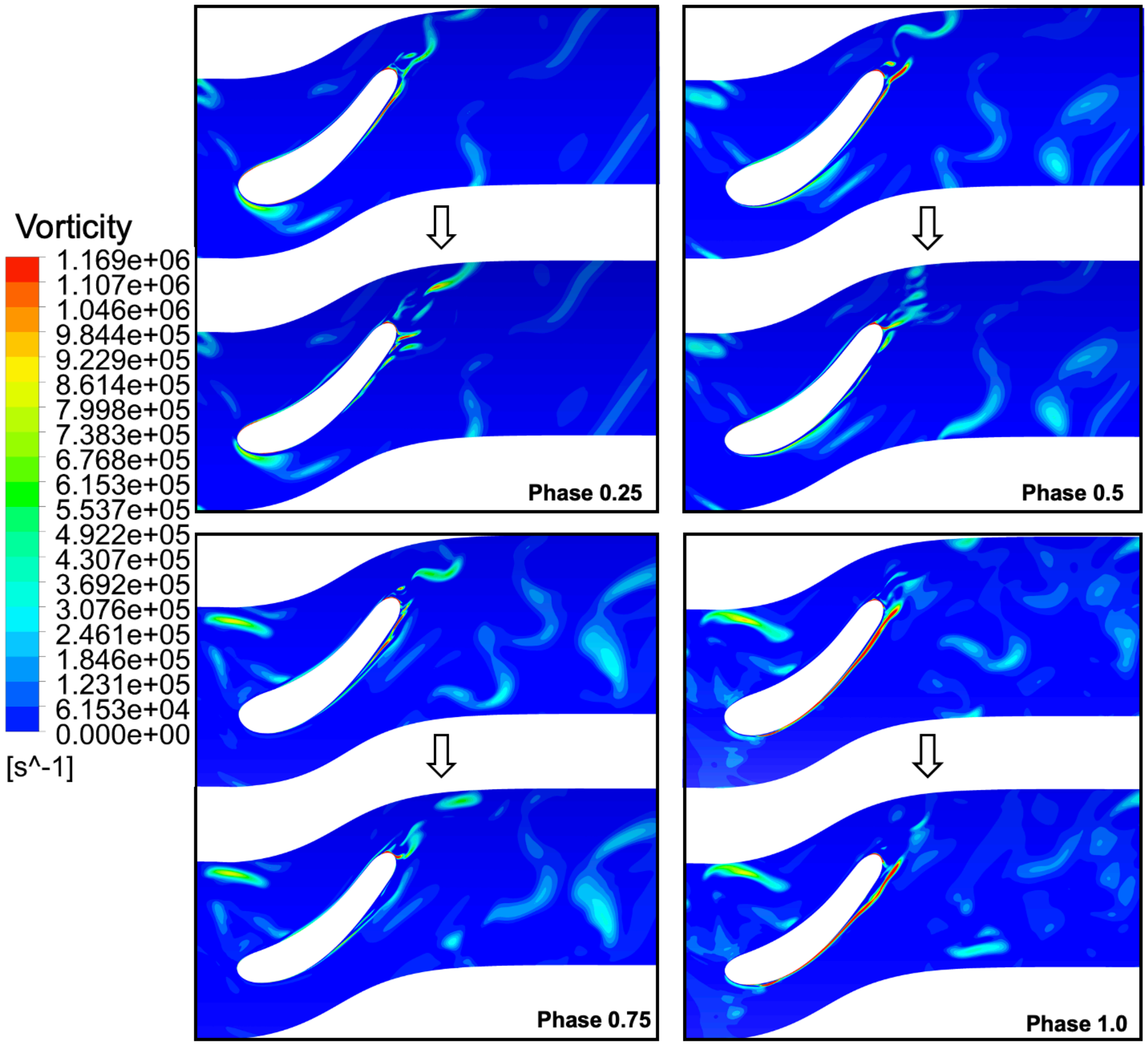

Figure 8.13: MGT Rotor Mean Vorticity For Different Phases (120,000RPM) (Original Vs. Redesigned)

From Figure 8.13, similar formation and propagation of leading-edge vortex can be observed for the redesigned rotor blade. At the onset, it is evident that the reduction in the LE thickness has an appreciable effect on the evolution and strength of the leading edge vortex at the mean span. The findings underscore a somewhat attenuated vortex strength on the suction side for the rotor blade with diminished LE thickness as compared to the original design. This attenuation in vortex strength is indicative of a slightly more streamlined flow structure around the modified blade profile, suggesting that the thinner leading edge is less prone to forming strong vortical structures. The reduced vortex strength can be attributed to a variety of reasons including altered pressure gradients, reduced stagnation zones, or smoother boundary layer transition regimes due to the redesigned leading edge profile.

However, a notable observation comes forth at phase 1.0. The modified design, with the reduced LE thickness, exhibits increased flow separation on the suction side, especially proximate to the trailing edge. These phenomena might be a consequence of the interaction between the altered leading edge vortex dynamics and the boundary layer. A diminished leading edge vortex might be influencing the pressure distribution on the suction side in such a way that it promotes adverse pressure gradients towards the trailing edge, thus fostering flow separation. The resultant flow separation could be directly linked to the subtle escalation in the stagnation pressure loss coefficient for the rotor blade with reduced LE thickness. Flow separation, especially near the trailing edge, can introduce additional turbulent structures into the wake of the blade, leading to increased mixing losses. Consequently, these losses are captured as a rise in the stagnation pressure loss coefficient listed in Table 8.4.

For the root span, the reduced LE thickness case reveals similar overall vorticity contours as the original design. However, the reduced LE thickness case seems to have greater flow separation on both the pressure and the suction side. Considering the endwall and strong secondary flow effect near the hub plane, the velocity vector diagrams for the leading edge redesigned blade are compared against the original case. In the redesigned blade with reduced leading edge thickness of the root and mean span, the first discovery is the velocity distribution appears to be smoother, especially around the root region. Secondly, the redesigned blade seems to show a reduced magnitude and concentration of high-velocity regions near the root span, particularly on the suction side. This suggests a potential reduction in secondary flows near the root. The flow appears more streamlined, especially close to the leading edge, which could mean a reduction in the inception and strength of vortices. Thirdly, both the original and redesigned diagrams display different flow behaviours near the leading and

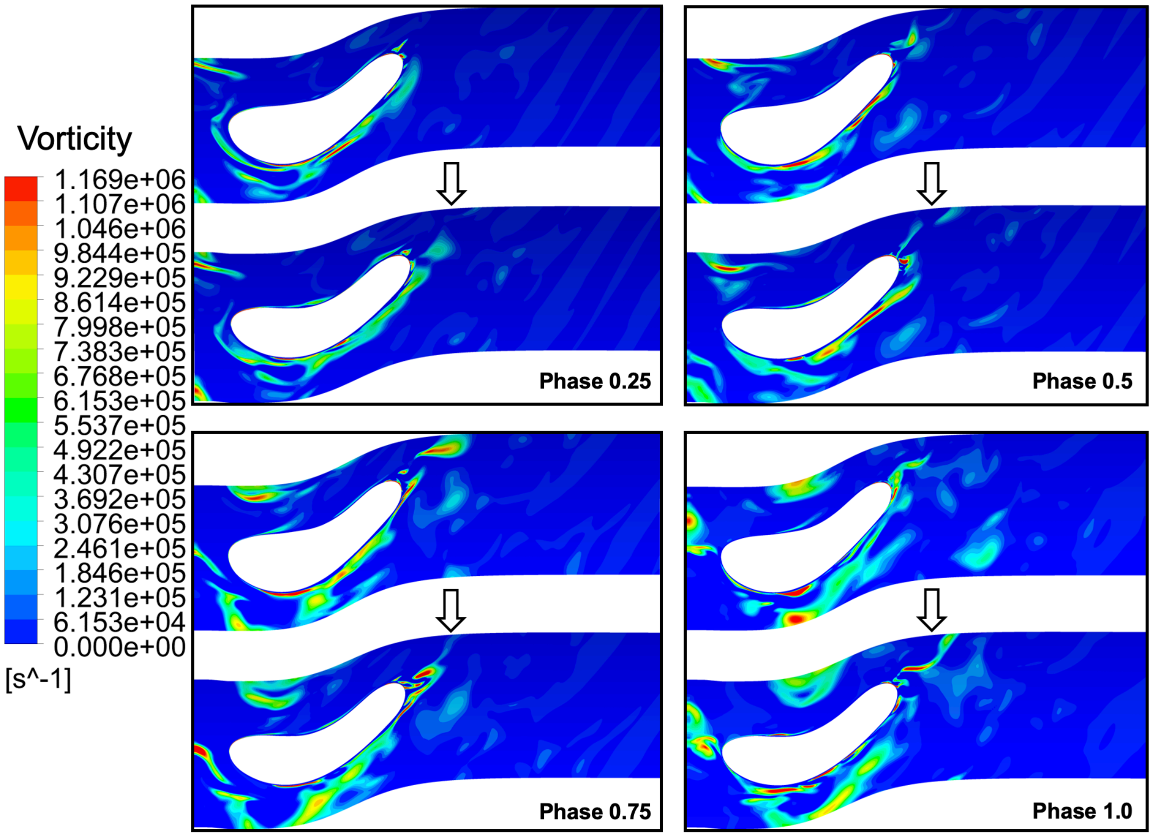

Figure 8.14: MGT Rotor Root Vorticity For Different Phases (120,000RPM)

trailing edges. While it is clear that the leading edge in the redesigned blade appears to manage the incoming flow slightly more effectively (leading to reduced secondary flows as discussed), the trailing edge in both designs still shows some complexities.

In Figure 8.16 and 8.17, the Q-Criterion plots provide a visual confirmation of these observations. They show slightly more pronounced and concentrated vortex structures in the redesigned rotor, particularly near the leading edge of the redesigned case. This indicates that while the leading edge redesign may enhance the initial handling of the incoming flow, it also alters the vortex dynamics significantly. This change could potentially improve the blade aerodynamic efficiency by reducing undesirable vortex activity.

However, both the original and redesigned rotor blades display differing flow behaviours near the leading and trailing edges. While the redesigned blade appears to manage the incoming flow slightly more effectively at the leading edge, reducing secondary flows as initially hypothesised, the complexities observed at the trailing

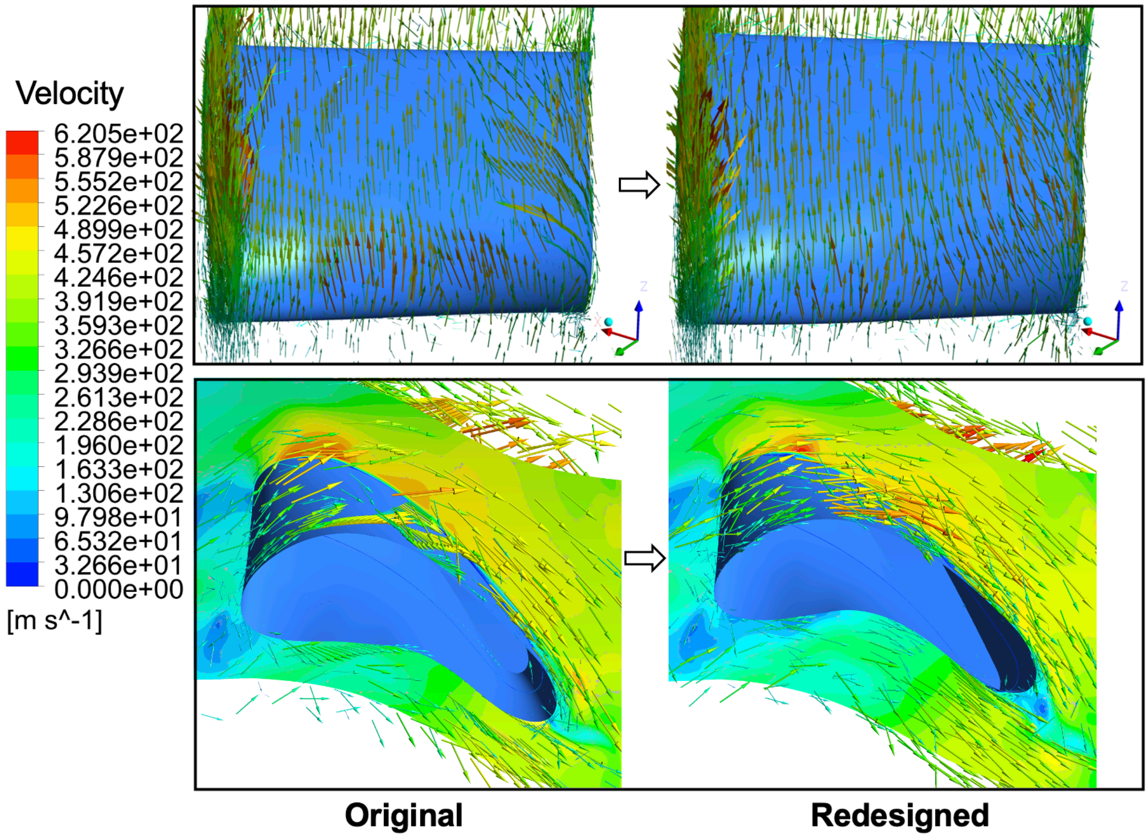

Figure 8.15: MGT Rotor Velocity Vectors (120,000RPM, Phase 1.0)

edge in both designs remain significant. These complexities, evident from the persistent presence of intense vortices and turbulent flow patterns at the trailing edge, underscore the need for higher fidelity data to thoroughly analyse these areas. The Q-Criterion plots particularly highlight the dynamic and transient interactions at the blade trailing edge, suggesting that any improvements at the leading edge might be offset by aerodynamic challenges at the trailing edge. Such findings highlight the delicate balance required in rotor blade design, where modifications to one section of the blade can have unintended consequences on other sections.

In summary, the CFD analysis supplemented by the Q-Criterion visualisation reveals that the redesigned blade with reduced leading edge thickness results in less pronounced leading-edge vortices, potentially leading to decreased aerodynamic losses and thus improved thrust. The redesigned blade also seems to offer improvements in flow management, particularly in reducing secondary flows on the suction side near the root span. However, while there are noticeable benefits in terms of thrust augmentationfrom 24.25N to 24.72Nthe gains are not significant enough to justify

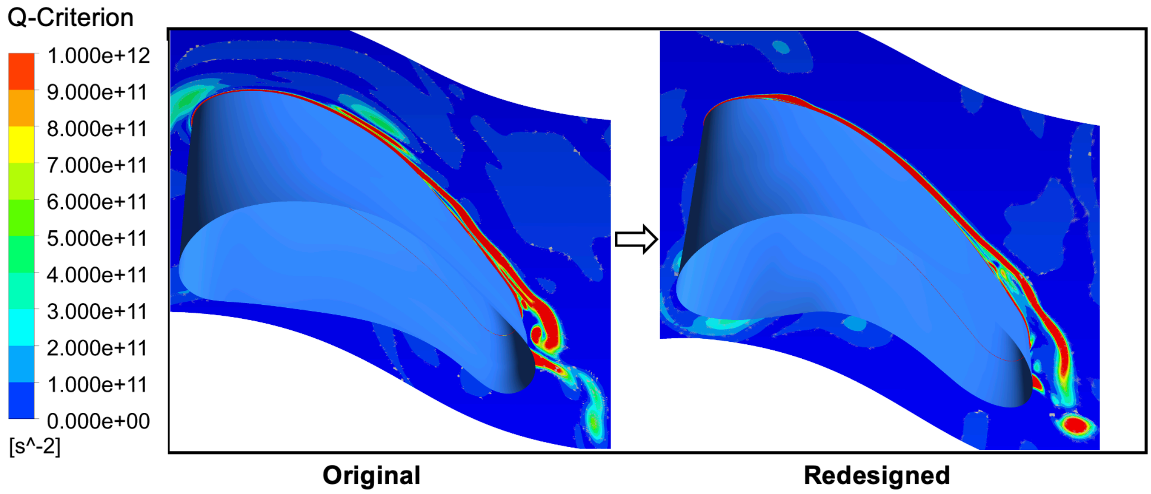

Figure 8.16: MGT Rotor Mid Span Q-Criterion (120,000RPM, Phase 1.0)

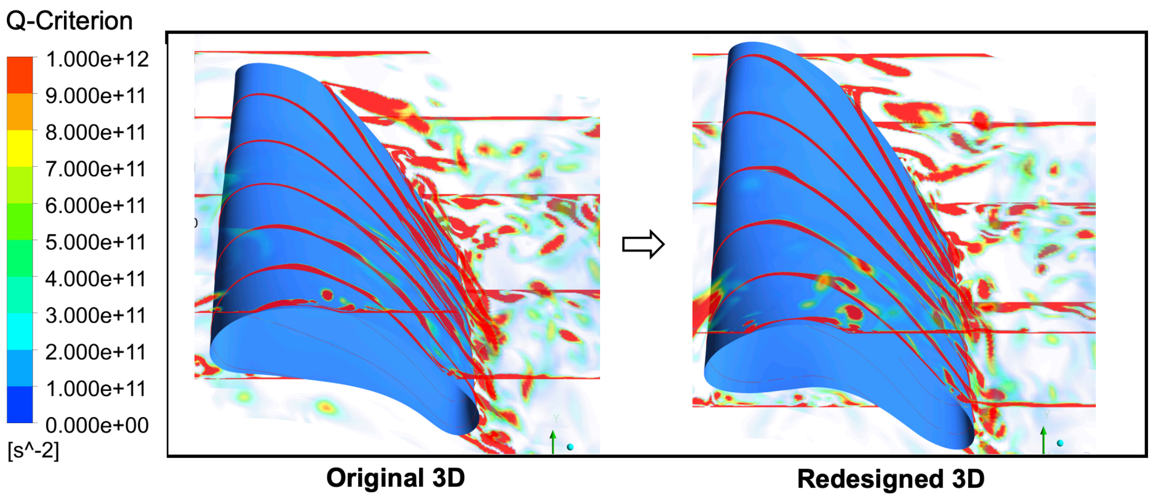

Figure 8.17: MGT Rotor Domain Q-Criterion (120,000RPM, Phase 1.0)

the accompanying drop in isentropic efficiencyfrom 80.1% to 79.9%. Consequently, given these findings, the decision was to discard this particular redesigned rotor blade. This decision emphasises the critical need for a balanced approach in rotor blade design, aiming to enhance thrust while maintaining or improving overall aerodynamic efficiency.

8.4 Results and Discussion

8.4.1 Rebuilt Wren100 Stator & Rotor Display

In the pursuit of redesigning the aerodynamic performance of the Wren100 MGT, a series of CFD parametric studies were undertaken to critically assess the MGT stator and rotor configurations. Based on the insights drawn from these studies, a refined design for the MGT stator and rotor was proposed and subsequently realised using the advanced SLM280 metal 3D printing technique, as elaborated in Chapter 3.2.3. The modifications for the redesigned MGT stator vane encompassed:

- A reduction by one vane, thereby potentially influencing the flow characteristics through the stator;
- A 50% decrement in the trailing edge thickness, aiming to enhance the flow exit and minimise potential aerodynamic losses;
- A 10% reduction in the axial chord, effectively elevating the aspect ratio (AR), potentially influencing the secondary flows of the MGT vanes.

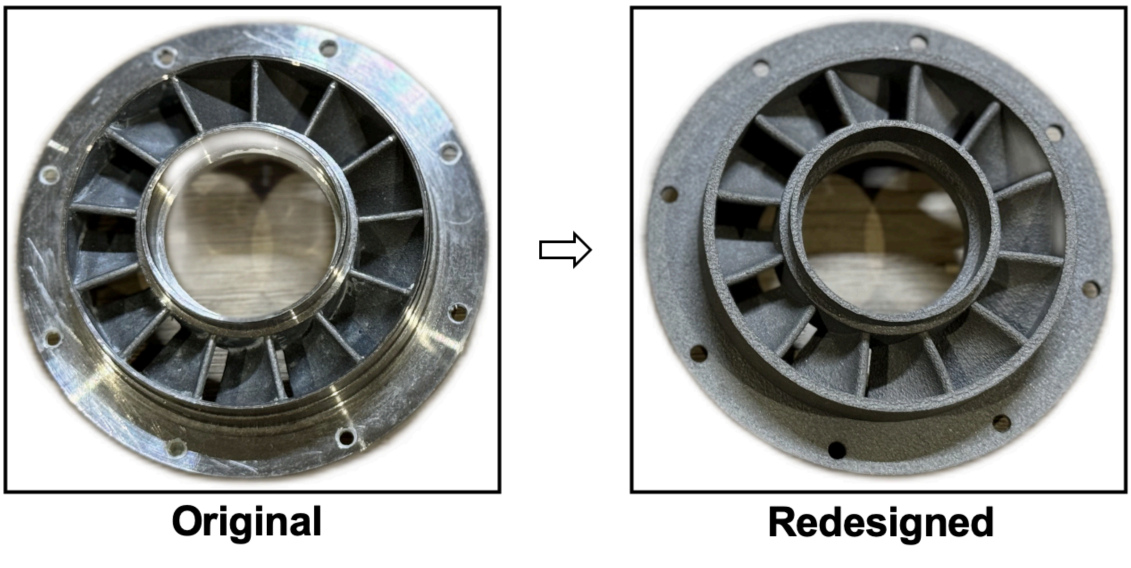

Figure 8.18: Manufactured Redesigned Wren100 Stator Vanes

For the MGT rotor blade, the design alterations were:

- Halving the tip clearance, which could potentially influence the tip leakage flow and the associated aerodynamic losses;

- Implementing linear stagger angles, potentially ensuring a more consistent flow path and reducing complexities associated with varying stagger.

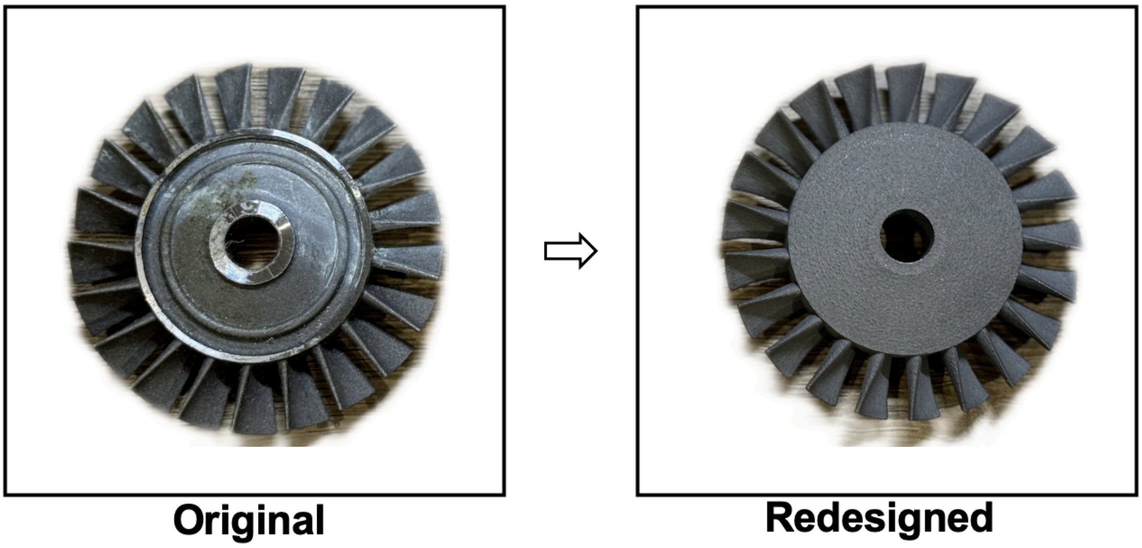

Figure 8.19: Manufactured Redesigned Wren100 Stator Vanes

The resultant manufactured components are illustrated in Figures 8.18 and 8.19. While the original intent was to incorporate these redesigned components into the MGT engine for additional experimental validations, unforeseen technical constraints precluded the realisation of this plan. Nonetheless, it is anticipated that these components offer a fertile ground for future aerodynamic investigations. It remains a promising avenue for subsequent researchers to harness these components in their studies to further unravel the nuances of MGT aerodynamics.

8.4.2 Potential Problems for the Redesigned Components

8.4.2.1 Increased Mass Flow Rate

During the simulation process, it was noticed that the redesigned MGT components would result in an increase in mass flow rate. Based on the CFD data, the changes in mass flow rate for different parametric redesigns are listed in Table 8.5.

	Mass Flow Rate (kg/s)	Changes
Original	0.117	
Stator Reduce One Vane	0.121	+3.42%
Stator 50% TE Thickness	0.122	+4.27%
Rotor 50% Tip Clearance	0.116	-0.85%
Rotor Linear Stagger	0.119	+1.71%

Table 8.5: Potential Changes in Mass Flow Rate With the Redesigned MGT Components

Several existing studies have investigated how the increased mass flow rate would influence the gas turbine performance. In 2022, Kamranpey numerically studied the impact of increased mass flow rate and different compressor pressure ratios. It was found that the increase of mass flow rate would lead to the rise of the cycle net work, which could potentially improve the overall performance of the turbine [191]. Despite potential aerodynamic performance gains, the increased mass flow rate observed in the redesigned Wren100 stator vane and rotor blade configurations could potentially cause some problems based on engineering turbine design principles, which are listed as follows.

- **Thermal overload and Higher Mechanical Stress:** A higher mass flow rate can result in increased heat input to the turbine, especially for the combustion-driven Wren100 MGT. This can lead to excessive temperatures in certain components, potentially exceeding their material limits and reducing their lifespan.

- **Alteration in Operating Points:** An increased mass flow rate can shift the operating point of the turbine on its performance map. This can lead to conditions that the turbine was not originally designed for, potentially affecting its performance and reliability.

- **Operational Challenges:** Control systems of the Wren100 MGT might need recalibration or redesign to cope with the altered flow characteristics, especially if the increase in mass flow rate was not initially accounted for in the design phase.

Thus, while these redesign points have led to higher efficiency and thrust, for future researchers to experimentally test the redesigned components, it is crucial to consider these potential mass flow problems to ensure the overall structural integrity and durability of the MGT.

8.4.2.2 Aerodynamic Flow Matching Problem Between MGT Stator and Rotor

In the domain of turbomachinery design and operation, the aerodynamic interaction between stator and rotor components is paramount, especially when applying design modifications to the entire MGT stage. For future researchers aspiring to utilise the redesigned MGT stator and rotor components, careful consideration of aerodynamic flow matching is essential to ensure optimal performance and reliability. The key considerations based on existing studies in the field of gas turbine redesign are summarised as follows.

- **Stage Loading & Velocity Triangles:** Although the MGT stator vane exit angles remain unchanged, ensuring a matched velocity triangle at the stator exit and rotor inlet is still crucial for future experimental or numerical studies. This involves confirming that the absolute, relative, and whirl velocities are in harmony to prevent off-design conditions and maintain the intended operational performance.

- **Pressure Distribution:** When applying design changes to both stator and rotor, a consistent pressure gradient could ensure a reduced potential for boundary layer separation.

- **Wake Interactions:** As discussed earlier, the wake generated by the stator vanes directly impacts the rotor blades. With the stator vane modifications, the wake characteristics might have been altered. A proper understanding and management of this wake are essential to mitigate rotor performance penalties, such as increased aerodynamic loss.

In conclusion, while the redesigned MGT stator and rotor components offer promising prospects, meticulous attention to aerodynamic flow matching is indispensable. Future research endeavours should incorporate comprehensive numerical and experimental studies, ensuring that the redesigned components, when integrated, operate cohesively and efficiently. Such an approach will ensure that the full potential of the redesigned components is realised while maintaining system reliability and longevity.

8.5 Summary

In this chapter, a thorough analysis of the effect of the process and results associated with the redesigned Wren100 MGT stator and rotor components has been presented based on the performance evaluated in Chapter 6. The investigation was conducted for the Wren100 MGT stator and rotor with chord length under 10mm and under the normal operating conditions of 120,000RPM. These modifications were conceptualised based on the validated RANS and LES data acquired from parametric studies.

The utilisation of the SLM280 metal 3D printer ensured precision in the replication of the design modifications. However, it is imperative to mention that the planned replacement of the redesigned components in the Wren100 MGT engine for empirical tests could not achieved due to the project time limits and technical contingencies.

8.5.1 Redesign Highlights

The observed trends of the parametric studies for the MGT stator and rotor are summarised as follows.

1. MGT Stator Vane

- **Base Pressure Loss Reduction (Number of Vanes):** In the course of refining the MGT stator vane, particularly in terms of vane count and trailing edge thickness, a noticeable influence on the base pressure at the trailing edge was observed. By moderately reducing one stator vane, a decline in base pressure loss was achieved, leading to enhanced flow stabilisation beyond the wake region. While a reduction in trailing edge thickness did result in marginally elevated trailing edge losses, the redesigned MGT stator vane showcased a more consistent and elevated base pressure distribution.

- **Wake Mixing Enhancement (Trailing Edge Thickness):** The parametric investigations into the reduced trailing edge thickness revealed improved wake mixing characteristics. While initially, the thinner trailing edge caused a temporary increase in entropy compared to the original blade design, this high-entropy condition was quickly dissipated. As a result, the thinner trailing edge led to an overall increase in thrust, confirming the benefits of this design change.

- **Enhanced Flow Acceleration & Separation (Aspect Ratio):** Increasing the aspect ratio of the MGT stator vane was observed to potentially amplify flow acceleration and separation, predominantly on the suction side proximate to the leading edge. Notably, while the elevated aspect ratio appeared to influence the peak dimensions of the separation bubble, its onset point was found to remain unaffected.

2. MGT Rotor Blade

- **Optimised Tip Behaviour (Tip Clearance):** The strategic reduction of the MGT rotor tip clearance brought about a marked improvement in the aerodynamic behaviour near the blade tip. Specifically, there was a noticeable decline in the flow separation tendencies within this region. Such flow alterations can significantly influence blade performance. In this instance, by mitigating these separation bubbles, the rotor blade showcased an enhanced isentropic efficiency, which is paramount for higher turbine performance and achieving better energy conversion rates.

- **Root Secondary Effects Mitigation (Leading Edge Redesign):** A significant reduction of 30% in the leading edge thickness of the MGT rotor blade, both at the root and mean span, notably decreased the pronounced secondary effects previously observed near the root span. Intriguingly, despite this decrease in secondary losses, the overall aerodynamic performance of the rotor blade remained largely unaffected. This suggests a potential compensatory increase in other forms of losses, like profile and trailing edge losses, effectively neutralising the advantages gained from the reduced secondary effects. The interplay between these various losses underscores the intricate balance needed in future rotor blade redesign.

In conclusion, the redesign journey of the MGT stator and rotor offered invaluable insights into the complexities and nuances of turbomachinery performance optimisation. While some design changes did not yield the desired outcomes, they paved the way for future iterative refinements

Chapter 9

Conclusions and Recommendations

9.1 Introduction

This study delved into an in-depth analysis of single-stage micro gas turbines (MGT), with a focus on the Wren44 and Wren100 engines provided by Turbine Solutions Ltd. Due to the extremely small sizes of the MGT blades (chord less than 10mm), two reverse-engineering (RE) methods were developed and assessed using detailed CFD models. The research used the Wren100 jet engine test unit and a wind tunnel setup for experiments. As mentioned in Chapter 1, while MGTs have a range of uses, they have not been as extensively researched as larger-scale gas turbines. These small turbines often face challenges that lower their efficiency and require more thrust. Given the limited existing research on this topic, the following key findings emerged from this study.

- Two unique reverse-engineering (RE) strategies based on laser-scanning and novel iterative CFD techniques have been developed and compared. The direct scan approach was found to be unsuitable for MGT components due to its lack of fidelity. It was found both RE strategies have unique strengths and limitations. The discrete ("what the part really is") is better for high-quality aerodynamics analysis, while the parametric ("what the part could be") could capture the blade overall performance with a few parameters, suitable for rapid design modifications with numerical tools.

- The complete MGT gas path was simulated employing the renowned CFX software suite, utilising both RANS and LES modelling techniques. Ensuring fidelity, the CFD models underwent rigorous verification and validation against empirical data from jet engine tests and wind tunnel cascade experiments. The baseline performance of the MGT, analysed using these RANS and LES models at various RPMs, is presented in Figure 5.23 and Table 8.1 with an error margin of ±4.45% from the thrust sensor specifications.

- By applying the transient LES WALE model, a detailed aerodynamic performance analysis was conducted for the Wren100 MGT under standard operational conditions (120,000RPM). It was discovered for both the MGT stator vane and rotor blade, and the secondary losses are the biggest issue. Insights gleaned from this analysis informed actionable redesign recommendations.

- Based on the parametric studies conducted, various modifications were suggested for the MGT stator vane and rotor blade, leading to the manufacturing of redesigned components. For the Wren100 stator, it was determined that reducing the number of vanes, halving the trailing edge (TE) thickness, and increasing the aspect ratio (AR) by 11% could significantly enhance performance. These changes boosted the thrust from 24.25N to 29.95N, with an increase in rotor isentropic efficiency from 80.1% to 81.1%. Additionally, for the MGT rotor paired with the redesigned stator, halving the tip clearance was found to potentially further elevate the isentropic efficiency to 83.4%, while still maintaining the improved thrust levels.

- Investigations into different levels of surface roughness and their effects were conducted through wind tunnel cascade experiments and LES WALE model simulations, focusing on the Wren100 MGT performance from normal to peak operational conditions. These studies led to recommendations for optimal surface roughness maintenance. For the Wren100 stator, under two different operational scenarios, it was observed that surface roughness could eliminate laminar separation bubbles near the leading edge on the suction side, potentially delaying the onset of flow transition. This roughness could also enhance the turbulence intensity in the main flow, mitigating the effects of secondary losses. For the MGT rotor blade tip, increased surface roughness was found to not only reduce the size of the separation bubble but also delay its onset. Additionally, the heightened turbulence intensity resulting from increased roughness could further diminish secondary effects such as tip leakage flows and corner vortices.

These objectives, detailed in earlier chapters, underscore the achievements of this study. This concluding chapter aims to summarise the findings and offer directions for future research in this area.

9.2 Conclusions from Reverse-Engineering Strategies

The thesis detailed the reverse-engineering (RE) techniques applied to the Wren44 stator and Wren100 single-stage MGT. During the RE of the Wren44 stator, it was observed that the direct scanning method fell short of capturing the intricate details of the MGT components. As a result, for the Wren100 stator and rotor, the research shifted towards utilising silicone rubber moulds and EP resin tooling in the RE process. Surface roughness tests revealed a negligible difference, with the maximum roughness variance between the EP resin models and the original turbine parts being approximately $2.79\mu m$.

Two distinct RE approaches were adopted to construct the 3D geometrical representation of the MGT stator and rotor. These models underwent performance assessments using a validated CFD solver. To establish initial conditions for iterative CFD simulations and to corroborate the findings, experimental evaluations were conducted at varied rotational speeds, ranging from 100kRPM to 140kRPM.

In the comparative assessment, it was found that simulations rooted in both RE methods provided reliable predictions of engine performance. However, when contrasting the simulation outcomes derived from the two RE models with experimental data, the discrete model displayed a slight advantage over the parametric model. This difference can be understood by realising that solely depending on a limited number of parameters for the RE of MGT blades might omit various blade attributes.

In conclusion, the study suggests a two-pronged approach. If there is only limited blade information available for RE of MGTs or if redesigns are on the horizon, the emphasis should be on "what the part could be" (Parametric Model). Conversely, for a detailed and precise representation, the focus should shift to "what the part really is" (Discrete Model), encompassing all blade attributes in the RE models. Adopting the latter approach implies leveraging the mould and resin method, which, while ensuring accuracy, might add to the duration and cost of the reverse-engineering endeavour.

9.3 Impact of Surface Roughness on MGT Blades

In this thesis, the intricate interactions between surface roughness and the aerodynamic performance of the MGT stator and rotor have been extensively investigated based on numerical and experimental methods in this study. Based on the comprehensive analysis, the following conclusions can be drawn.

- Based on the validated CFD models, the boundary layer thickness at various locations and the average roughness Reynolds number for the Wren100 MGT stator and rotor under normal and peak operating conditions were measured and calculated.
- The flow fields around the Wren100 stator vane and rotor blade are inherently 3D. Thus, the influence of the same roughness height can vary across different spatial regions of the blade, leading to diverse local effects even if the global performance metrics appear similar.
- For the Wren100 MGT stator vane, roughness up to the original Sand Grain (SG) magnitude does not pose significant aerodynamic concerns under standard operational conditions. Beyond this threshold, due to the prevalent low Reynolds number environment, there is a nuanced interplay where strategically increasing roughness can be leveraged to foster increased turbulence, which may help in offsetting the pronounced secondary flow effects.
- The rotor blade of the MGT demonstrates heightened sensitivity to surface irregularities. Hence, maintaining minimal roughness is paramount to safeguard its aerodynamic efficiency. This is especially critical given the blade intricate flow dynamics, where even slight roughness variations can markedly alter the flow behaviour, including laminar-to-turbulent transition and wake dynamics.
- The MGT response to roughness is also influenced by its operational RPM. At peak RPMs, such as 160,000 RPM, the system exhibits an increased sensitivity to roughness changes. This can be attributed to the higher Reynolds numbers, leading to a thinner boundary layer and hence, a more pronounced reaction to surface roughness.
- The stator wake behaviour significantly impacts the downstream rotor. At increased RPMs, the wake dissipating from the stator and propagating towards

the rotor diminishes, leading to a more uniform flow incidence onto the rotor. This modulation in wake behaviour, along with roughness variations, jointly affects the rotor aerodynamic performance.

In light of these findings, it is clear that while surface roughness is a seemingly minute detail, its implications on the aerodynamic performance of MGTs are profound. Careful consideration of roughness levels, in conjunction with other operational parameters, is pivotal in optimising turbine efficiency and longevity.

9.4 Experimental & CFD Analysis of the MGT Turbine Aerodynamics and Parametric Redesign

The analysis undertaken in this thesis encompassed both experimental and computational methodologies to assess the aerodynamic performance of the Wren100 MGT stator and rotor components, subsequently guiding the potential redesign suggestions and parametric studies.

- Utilising validated CFD models, a profound understanding of flow characteristics within the MGT blade passages was achieved. By leveraging both RANS and LES models, the research provided intricate flow data. In particular, the LES WALE model was instrumental in the transient analysis of the Wren100 MGT aerodynamic performance under various operating conditions.

- Initial findings highlighted several areas of inefficiencies in the original turbine design. Aspects such as stator vane count, trailing edge thickness, aspect ratio (AR), rotor tip clearance, and leading-edge thickness were identified as focal points that could benefit from potential modifications.

- Based on the acquired aerodynamic data, a series of redesign suggestions were proposed. The objective of these modifications was to enhance specific performance parameters of the turbine. Adjustments to the stator vane count and rotor tip clearance emerged as promising solutions to improve wake mixing, flow acceleration, and separation behaviour. Similarly, considerations regarding the leading edge thickness at the blade root and mean span were deemed pivotal in tackling issues related to secondary aerodynamic effects.

- The combination of the CFD simulation results with experimental data underscored the reliability of the former. The detailed representation in simulations, utilising the parametric, proved invaluable in the field of MGT redesign. The new version of the Wren100 stator and rotor were also manufactured for future studies.

In conclusion, this in-depth exploration of MGT stator and rotor aerodynamics has not only deepened the comprehension but also provided actionable redesign recommendations. These insights represent a significant stride forward in improving turbine performance and present a solid foundation for future advancements in this domain.

9.5 Recommendations for Future Research

The conducted research in this study has delved deeply into the intricate flow dynamics within the MGT blade passages, revealing the challenges inherent in enhancing engine aerodynamic thrust and thermal efficiency. As stated in Chapter 1, MGTs, when compared with larger turbines, are characterised by their low Reynolds numbers, distinct aspect ratios, high RPMs, and notable tip gaps. Additionally, a void exists in the literature pertaining to the influence of surface roughness on MGTs, especially those with an extremely small chord length of approximately 10mm. While this dissertation has made strides in addressing these issues, certain constraints, including the impacts of the COVID pandemic and engine unavailability, have underscored the necessity for further research. Numerous avenues remain unexplored, emphasising the need for a continued deep dive into MGT component aerodynamics.

9.5.1 MGT Whole Stage Modelling and Analysis

- While this study has successfully compared novel strategies for reverse-engineering MGT components in Chapter 4 and 5, there is an avenue to refine these techniques. Advanced imaging and scanning technologies could provide more precise geometrical recreations and thus a more accurate starting point for aerodynamic analysis and redesign.

- The simulations carried out in this thesis use RANS 4-equations transitional SST and LES WALE models. However, more advanced turbulence models and transient simulations could be adopted to capture intricate flow features more accurately. This can provide a deeper understanding of the aerodynamics and further refine design alterations.

- The interaction between the stator wake and downstream rotor, especially under varying roughness and RPM scenarios, warrants a more exhaustive study. It would be beneficial to develop new numerical models that capture this interplay with higher fidelity, ensuring a deeper understanding of the MGT aerodynamics.

- In Chapter 8, the parametric redesign efforts based on potential bottlenecks primarily concentrated on a series of fundamental blade attributes. To further enhance performance, exploration into advanced blade optimisation methods, including blade lean and tip gap sealant, is recommended.

9.5.2 Experimental Methods

- For the current wind tunnel tests, fully controlled experimental environments could not be achieved due to the project time and equipment limitations. Thus, it is suggested to rebuild a bigger and more robust blade cascade lifting mechanism with additional sensors for better data quality.

- To dive deeper into the complex flow structures and turbulence dynamics, especially in regions of surface roughness, more advanced experimental techniques like Particle Image Velocimetry (PIV) should be employed. This can provide a granular insight into flow separations, vortical structures, and turbulence interactions across varied roughness spectra.

- For the redesigned Wren100 stator and rotor, the new components were manufactured and ready to be tested at the Propulsion lab of the University of Sheffield. However, due to technical problems with the engine emission rig, these experiments could not be conducted. It is thus recommended that such tests are conducted to create a reference database for the numerical model validation.

Appendix A

CFD Model Reviews

A.1 Mathematical Equations

The Navier-Stokes equations, a set of nonlinear, second-order partial differential equations, provide the core mathematical framework for addressing various fluid dynamics problems. These equations can assume different forms depending on the specific problem being investigated. The conservation form of the Navier-Stokes equations, as shown in Equations A.1, A.2, and A.3, assumes a Newtonian fluid, with both momentum and energy conserved [100, 102].

$$\frac{\partial \rho}{\partial t} + \frac{\partial (\rho u_i)}{\partial x_i} = 0 \tag{A.1}$$

$$\frac{\partial (\rho u_i)}{\partial t} + \frac{\partial [\rho u_i u_j]}{\partial x_j} = -\frac{\partial p}{\partial x_i} + \frac{\partial \tau_{ij}}{\partial x_j} + \rho f_i \tag{A.2}$$

$$\frac{\partial (\rho e)}{\partial t} + (\rho e + p)\frac{\partial u_i}{\partial x_i} = \frac{\partial (\tau_{ij} u_j)}{\partial x_i} + \rho f_i u_i + \frac{\partial (\dot{q}_i)}{\partial x_i} + r \tag{A.3}$$

A.1.1 RANS Turbulence Models

The Reynolds-Averaged Navier-Stokes (RANS) equations resemble the Navier-Stokes equations in form, with the primary distinction being the use of mean velocities in the RANS equations, as demonstrated in Equation A.4 and A.5 [100].

$$\frac{\partial \rho}{\partial t} + \frac{\partial U_i}{\partial x_i} = 0 \tag{A.4}$$

$$\rho(\frac{\partial U_i}{\partial t} + U_j\frac{\partial U_i}{\partial x_j}) = -\frac{\partial P}{\partial x_i} + \frac{\partial}{\partial x_j}(\mu\frac{\partial U_i}{\partial x_j} - \rho\overline{u_i\prime u_j\prime}) + \rho F_i \tag{A.5}$$

As evident from Equations A.4 and A.5, the non-linearity of the $\frac{\partial}{\partial x_j}$ operation results in the creation of new unknown terms on the right-hand side of Equation A.5 when they are derived (the closure problem) [110]. In these equations, $\mu\frac{\partial U_i}{\partial x_j}$ represents the laminar stress, while $\rho\overline{u_i\prime u_j\prime}$ corresponds to the turbulent stress, which accounts for the production of fluctuating velocities.

Consequently, the RANS equations cannot be directly resolved and necessitate the development of empirical turbulence models to approximate the additional unknown variables [105]. Several standard turbulence models can be applied within the scope of this research project, including the $k-\epsilon$ model, the $k-\omega$ model, and the Shear Stress Transport (SST) model, among others.

A.1.1.1 $k-\epsilon$ Turbulence Model

The transport equations for k and ϵ are displayed in Equations A.6 and A.7, with the modelled constants listed in Table A.1.

$$\frac{Dk}{Dt} = -\overline{u_i\prime u_j\prime}\frac{\partial U_i}{\partial x_j} - \epsilon + \frac{\partial}{\partial x_j}[(\upsilon + \frac{\upsilon_t}{\sigma_k})\frac{\partial k}{\partial x_j}] \tag{A.6}$$

$$\frac{Dk}{Dt} = -\overline{u_i\prime u_j\prime}\frac{\partial U_i}{\partial x_j}c_{\epsilon 1} - c_{\epsilon 2}\frac{\epsilon^2}{k} + \frac{\partial}{\partial x_j}[(\upsilon + \frac{\upsilon_t}{\sigma_\epsilon})\frac{\partial \epsilon}{\partial x_j}] \tag{A.7}$$

Table A.1: Model Constants $k-\epsilon$

C_μ	C_1	C_2	σ_k	σ_ϵ
0.09	1.44	1.92	1.0	1.3

The model constants in Table A.1 are based on empirical approaches and have been progressively refined over time to enhance the accuracy of CFD predictions. In 1994, Menter posits that even minor alterations to these constants can significantly influence the model outcomes, necessitating extensive testing and comparisons between well-documented research flows and turbulence models. Additional studies have further emphasised the importance of selecting appropriate constants for specific applications, such as in the context of gas turbine blade simulations [114].

A.1.1.2 $k - \omega$ Turbulence Model

The $k - \omega$ turbulence model, as modified by Wilcox in 1988, can be expressed by Equations A.8 and A.9.

$$\frac{Dk}{Dt} = P_k - \beta^* \omega k + \frac{\partial}{\partial x_j}[(\upsilon + \sigma_k \frac{k}{\omega})\frac{\partial k}{\partial x_j}] \tag{A.8}$$

$$\frac{D\omega}{Dt} = \frac{\gamma\omega}{k} P_k - \beta^* \omega^2 + \frac{\partial}{\partial x_j}[(\upsilon + \sigma_\omega \frac{k}{\omega})\frac{\partial \omega}{\partial x_j}] \tag{A.9}$$

The turbulent eddy viscosity (υ_t) can be calculated using the relation $\upsilon_t = k/\omega$, which implies that ω is associated with the turbulent timescale. The model constants are presented in Table A.2.

Table A.2: Model Constants $k - \omega$

σ_k	σ_ω	β^*	β	γ
0.5	0.5	0.09	3/40	5/9

A.1.1.3 Transitional SST ($\gamma - \overline{Re_{\theta,t}}$) Turbulence Model (4 Equations)

The transport equations for k (turbulence kinetic energy) and ω (dissipation rate) in the four-equation transitional SST ($\gamma - \overline{Re_{\theta,t}}$) turbulence model are similar to those in the $k - \omega$ turbulence model. However, additional terms, such as the production (P_k) and dissipation (D_k) of kinetic energy and the blending function (F_1), are incorporated into the transitional model as described in Equations A.10 and A.11.

$$\frac{\partial(\rho k)}{\partial t} + \nabla \cdot (\rho \mathbf{U} k) = \nabla \cdot ((\mu + \frac{\mu_t}{\sigma_k})\nabla k) + P_k - D_k \tag{A.10}$$

$$\frac{\partial(\rho w)}{\partial t} + \nabla \cdot (\rho \mathbf{U} w) = \nabla \cdot ((\mu + \frac{\mu_t}{\sigma_k})\nabla w) + \frac{\gamma}{\nu_t} P_k - \beta \rho \omega^2 + 2(1 - F_1)\frac{\rho \sigma_{\omega 2}}{\omega}\nabla k : \nabla w \tag{A.11}$$

As shown in Equation A.10, the production of turbulent energy (P_k) is multiplied by the turbulence intermittency (γ), which indicated the flow state locally. Thus, the intermittency factor (γ) decides whether the term P_k exists or not, meaning if the turbulence fluctuation always present, the γ is equal to one. The intermittency factor (γ) is equal to zero when the flow is completely laminar. Physically, knowing the value of γ means the information of the time percentage of the turbulence fluctuations exists locally in the flow boundary layer. The dissipation term (D_k) also depends on the intermittency factor (γ), which D_k would be replaced by $0.1D_k$ if the boundary layer is laminar. Thus, the third equation of this transition model is the transport equation for γ shown in Equation A.12, where the P_γ and D_γ are the production and dissipation terms.

$$\frac{\partial(\rho\gamma)}{\partial t} + \nabla \cdot (\rho \mathbf{U} \gamma) = \nabla \cdot ((\mu + \frac{\mu_t}{\sigma_\gamma})\nabla\gamma) + P_\gamma - D_\gamma \tag{A.12}$$

For the blending function (F_1) in Equation A.11, it controls whether the $k-\epsilon$ or the $k-\omega$ turbulence model is used, which F_1 would either be unit (near-wall) or zero (free-stream). Previous research have shown that the $k-\epsilon$ turbulence model cannot predict the near-wall regions accurately as described in the last subsection. Therefore, it would be better for the CFD user to avoid the turbulence model being switched from $k-\omega$ to $k-\epsilon$. Finally, the fourth equation of the $\gamma - \overline{Re_{\theta,t}}$ turbulence model is shown as Equation A.13, which is the transport equation for a newly introduced variable $\overline{Re_{\theta,t}}$.

$$\frac{\partial(\rho\overline{Re_{\theta,t}})}{\partial t} + \nabla \cdot (\rho \mathbf{U} \overline{Re_{\theta,t}}) = \nabla \cdot [(\mu + \frac{\mu_t}{\sigma_{\theta,t}})\nabla\overline{Re_{\theta,t}}] + P_{\theta,t} \tag{A.13}$$

Where the $\overline{Re_{\theta,t}}$ is a distance variable from the leading edge to the point that flow transition occurs, which empirical relationships can only calculate its local values. There are many shreds of evidence to suggest that the $\gamma - \overline{Re_{\theta,t}}$ turbulence model gives superior predictions for engineer applications that involve transitional flow.

A.1.2 LES Models

From the textbook definition, the governing equations for LES simulations are derived from the filtered NS equations, where the filtering operation separates the flow field into resolved large-scale ($\overline{U}(x,t)$) and unresolved small-scale ($u'(x,t)$) eddies. According to Leonard in 1974, the general filtering operation is shown in Equation A.14 and A.15 [121].

$$\overline{U}(x,t) = \int G(r,x)U(x-r,t)dr \tag{A.14}$$

$$\int G(r,x)dr = 1 \tag{A.15}$$

The closure is normally achieved by applying eddy viscosity models. To calculate the eddy viscosity related to the unresolved small-scale turbulence in the flow, subgrid-scale (SGS) models are commonly applied, and the governing equations for the typical models are illustrated as follows.

A.1.2.1 The Smagorinsky Model

The Samagorinsky model was proposed by Samagorinsky in 1963, which is the most basic LES subgrid scale (SGS) model to close the equations for the filtered velocity. The model can be treated as two components, which are the SGS stress tensor and the eddy viscosity model by analogy to the mixing length hypothesis as shown in Equation A.16 and A.17 [105].

$$\tau = -2\nu_r \overline{S_{i,j}} \tag{A.16}$$

$$\nu_r = l_s^2 \overline{S} = (C_s \Delta)^2 \overline{S} \tag{A.17}$$

Where τ is the SGS stress tensor, ν_r is the eddy viscosity of the residual motion, $\overline{S}$ is the resolved characteristic filtered rate of strain, l_s is the Samgorinsky length scale, Δ is the filter width (computational grid size), and C_s is the model constant (normally around 0.1-0.2) [105].

A.1.2.2 The Wall-Adapting Local Eddy-viscosity (WALE) Model

The Wall-Adapting Local Eddy-viscosity (WALE) model is also an SGS model commonly used in Large Eddy Simulation (LES) for simulating turbulent flows near walls. Compared to the Smagorinsky model, a more complex equation to calculate the SGS eddy viscosity is used by the WALE model as shown in Equation A.18 [122].

$$\nu_t = (C_w \Delta)^2 \frac{\overline{OP_1}}{\overline{OP_2}} = (C_w \Delta)^2 \cdot \overline{\varpi} \tag{A.18}$$

Where C_w is the WALE model constant, $\overline{OP}$ is the spatial operator. The WALE model incorporates both the shear stress and the rotation tensor, with the underlying operators derived from the square of the velocity gradient tensor. These operators are defined in Equations A.19 and A.20 [122].

$$\overline{\varpi} = \frac{(g_{i,j}^d g_{i,j}^d)^{3/2}}{(S_{i,j} S_{i,j})^{5/2} + (g_{i,j}^d g_{i,j}^d)^{5/4}} \tag{A.19}$$

$$g^d_{i,j} = S_{i,k}S_{k,j} + \Omega_{i,k}S_{k,j} - \frac{1}{3}\delta_{i,j}(S^2 - \Omega^2) \tag{A.20}$$

Appendix B

Wren100 MGT Data & Interpolation

B.1 Roughness Data

The measured roughness data for the Wren100 MGT original and rebuilt stator-rotor system are shown in the following tables.

Samples	R_a (μm)	R_z (μm)
Vane 1	2.236	14.471
Vane 2	2.153	12.474
Vane 3	2.395	12.888
Vane 4	2.170	12.179
Vane 5	2.140	11.919
Vane 6	2.480	14.515
Vane 7	1.755	11.456
Vane 8	2.491	14.350
Vane 9	2.773	16.898
Vane 10	3.274	19.631
Vane 11	3.218	18.762
Vane 12	2.510	17.329
Vane 13	2.538	14.512
Average	**2.472**	**14.722**

Table B.1: Original Stator Vane Roughness Measurements

Samples	R_a (μm)	R_z (μm)
Vane 1	1.191	10.940
Vane 2	1.788	11.603
Vane 3	2.619	15.858
Vane 4	2.126	10.441
Vane 5	1.918	11.200
Vane 6	1.926	10.749
Vane 7	2.371	14.090
Vane 8	1.888	11.733
Vane 9	2.137	12.188
Vane 10	2.473	14.047
Vane 11	1.939	10.843
Vane 12	1.740	9.316
Vane 13	1.951	12.107
Average	**2.005**	**11.932**

Table B.2: Rebuilt EP Resin Stator Vane Roughness Measurements

Samples	R_a (μm)	R_z (μm)
Blade 1	2.272	12.735
Blade 2	2.879	16.432
Blade 3	2.569	15.525
Blade 4	3.119	16.629
Blade 5	2.441	13.197
Blade 6	2.137	12.192
Blade 7	2.754	18.447
Blade 8	3.072	18.312
Blade 9	2.775	16.986
Blade 10	2.736	15.580
Blade 11	2.521	14.155
Blade 12	2.509	13.734
Blade 13	2.592	15.620
Blade 14	2.571	16.655
Blade 15	2.443	15.390
Blade 16	2.862	15.881
Blade 17	2.455	14.936
Blade 18	2.115	10.915
Blade 19	2.781	15.325
Blade 20	2.809	16.734
Blade 21	2.313	13.725
Average	**2.606**	**15.195**

Table B.3: Original Rotor Blade Roughness Measurements

Samples	R_a (μm)	R_z (μm)
Blade 1	1.783	10.525
Blade 2	1.854	10.312
Blade 3	2.591	15.345
Blade 4	2.756	16.325
Blade 5	2.486	15.380
Blade 6	1.943	12.184
Blade 7	3.067	20.933
Blade 8	3.411	21.082
Blade 9	2.159	14.091
Blade 10	2.951	17.867
Blade 11	2.116	13.160
Blade 12	2.813	14.903
Blade 13	2.353	13.671
Blade 14	2.123	12.127
Blade 15	1.829	12.036
Blade 16	2.695	16.895
Blade 17	1.948	14.031
Blade 18	2.868	20.345
Blade 19	2.163	14.216
Blade 20	2.665	16.487
Blade 21	2.512	16.744
Average	**2.433**	**15.174**

Table B.4: Rebuilt EP Resin Rotor Blade Roughness Measurements

B.2 Higher RPMs Iterpolation Code

The data interpolation tool that utilised simple Python codes is illustrated as follows.

Python Codes:

import numpy as np

# Lower RPM Data
rpm_values = [rpm_1, rpm_2, ..., rpm_i]
monitored_variable_values = [y_1, y_2, ..., y_i]

Function to interpolate

```
def interpolate(rpm):
if rpm < rpm_values[0] or rpm > rpm_values[-1]:
return None # Theta value is out of range
else:
for i in range(len(rpm_values) - 1):
if rpm_values[i] < = rpm < = rpm_values[i + 1]:
# Linear interpolation formula
return monitored_variable_values[i] + (monitored_variable_values[i + 1] -
monitored_variable_values[i]) * (rpm - rpm_values[i]) / (rpm_values[i + 1] - rpm_values[i])

# New rpm values to find variable values for
rpm_to_find = [rpm'_1, rpm'_2, ..., rpm'_i]

# Calculate monitored variable values
monitored_variable_values = [ ]
for rpm in rpm_values:
monitored_variable_results.append(interpolate(theta))

# Print the results
for i in range(len(rpm_to_find)):
print(f"Theta: rpm_to_find[i],
Pressure: monitored_variable_results[i]")
```

Bibliography

[1] E. Benini, Progress in Gas Turbine Performance, Rijeka: InTech, 2013.

[2] NBC News, "This jet pack lets you live your Iron Man fantasies but you'll need Tony Stark money," NBC News, 2018. [Online]. Available: https://www.nbcnews.com/mach/science/jet-pack-lets-you-live-your-iron-man-fantasies-you-ncna893661. [Accessed: May 02, 2022].

[3] L. Rentzos, "Extending Electric Car Range," Turbomachinery Blog, 2018. [Online]. Available: https://blog.softinway.com/micro-turbines-for-extending-electric-car-range/. [Accessed: May 02, 2022].

[4] L. Ren, R. Zhu, L. Liao, and Y. Zhou, "Analysis on the development of micro gas turbine generation technology," Journal of Physics: Conference Series, vol. 1983, no. 1, p. 012006, 2021.

[5] Turbine Power Solutions Ltd., "Wren Engine Sales and Service, Fuel Tubing, Pneumatic Fittings, RC Jets - Turbine Solutions," 2020. [Online]. Available: https://www.turbinesolutions.co.uk/. [Accessed: Oct. 22, 2020].

[6] AMT Netherlands, 2022, *AMT Netherlands Mercury HP*, Amtjets.com, See also URL http://www.amtjets.com/MercuryHP.php. [Accessed: Oct. 22, 2020]

[7] Bf-turbines, 2022, *Turbine B100F*, Bf-turbines.de, See also URL http://www.bf-turbines.de/. [Accessed: Oct. 22, 2020]

[8] Jetcat Company, 2022, *P100-RX - JetCat*, Jetcat.de, See also URL https://www.jetcat.de/en/productdetails/produkte/jetcat/produkte/hobby/Engines/p100_rx. [Accessed: Oct. 23, 2020]

[9] Hawkturbine, 2022, *Hawk 100R*, Hawkturbine.com, See also URL `http://www.hawkturbine.com/Hawk100R1.htm`. [Accessed: Oct. 23, 2020]

[10] P. Newton et al., *Aerothermal Investigations of Tip Leakage Flow in Axial Flow TurbinesPart III: TIP Cooling*, Journal of Turbomachinery, vol. 131, no. 1, 2008.

[11] J. Alqallaf and J. Teixeira, *Blade Roughness Effects on Compressor and Engine PerformanceA CFD and Thermodynamic Study*, Aerospace, vol. 8, no. 11, p. 330, 2021.

[12] R. Taylor, *Surface Roughness Measurements on Gas Turbine Blades*, Journal of Turbomachinery, vol. 112, no. 2, pp. 175-180, 1990.

[13] G. Walker, *The Role of Laminar-Turbulent Transition in Gas Turbine Engines: A Discussion*, Journal of Turbomachinery, vol. 115, no. 2, pp. 207-216, 1993.

[14] Rani, S., Agrawal, A. and Rastogi, V., *Failure investigation of a first stage Ni based super alloy gas turbine blade*, Material Today: Proceedings, 5(1), pp.477-486, 2018.

[15] W. J. R. Thomas, A. J. Higson, *An Intercooled Regenerative Rolls-Royce Spey Gas Turbine*, ASME Paper 85-IGT-59, 1985.

[16] S. Choi, S. Choi, H. Park and H. Cho, *Effect of Aspect Ratio on Heat Transfer of Triangular Internal Cooling Channel of Gas Turbine Blade*, Transactions of the Korean Society of Mechanical Engineers - B, vol. 45, no. 3, pp. 135-143, 2021.

[17] Saravanamuttoo, H., *Gas Turbine Theory* 7th ed. London: Licensing Agency Ltd. 2017.

[18] M. Murugan, D. Booth, A. Ghoshal, D. Thurman, *Concept study for adaptive gas turbine rotor blade*, The International Journal of Engineering and Science (IJES), vol. 4, no. 9, pp. 1-7, 2015.

[19] P. Zhu, L. Song, J. Li, Z. Feng, *Effects of upstream slot geometry on the endwall aerothermal performance of a gas turbine blade under different ejection angle conditions*, International Journal of Heat and Mass Transfer, vol. 113, pp. 780-794, 2017.

[20] H. Hasemann, G. Weser, D. Hagelstein, and M. Rautenberg, *Investigation of the solidity and the blade vibration behaviour of unshrouded centrifugal compressor impellers with different aerodynamic design*, Volume 4: Manufacturing Materials and Metallurgy; Ceramics; Structures and Dynamics; Controls, Diagnostics and Instrumentation; Education; IGTI Scholar Award, 1997.

[21] M. Anderson, *Reaction Versus Impulse Type Turbomachinery*, 2020. [Online]. Available at: `https://www.conceptsnrec.com/blog/reaction-versus-impulse-type-turbomachinery`. [Accessed: 14 Sep. 2020]

[22] S. Yoon, *The Effect of the Degree of Reaction on the Leakage Loss in Steam Turbines*, Journal of Engineering for Gas Turbines and Power, vol. 135, no. 2, 2013.

[23] J. Lee, S. Kang, T. Kim, S. Park and G. Hong, *The effect of hub leakage on the aerodynamic performance of high-pressure steam turbine stages*, Journal of Mechanical Science and Technology, vol. 31, no. 1, pp. 445-454, 2017.

[24] Smith, and M. H., *A simple correlation of turbine efficiency*, Journal of Royal Aeronautical Society, 1965.

[25] Y. Liu, P. Hendrick, Z. Zou, and F. Buysschaert, *A reliable update of the Ainley and Mathieson profile and secondary correlations*, International Journal of Turbomachinery, Propulsion and Power, vol. 7, no. 2, p. 14, Apr. 2022.

[26] C. R. Day, M. L. Oldfield, G. D. Lock, and S. N. Dancer, *Efficiency measurements of an annular nozzle guide vane cascade with different film cooling geometries*, Volume 4: Heat Transfer; Electric Power; Industrial and Cogeneration, 1998.

[27] S. Ito, E. R. Eckert, and R. J. Goldstein, *Aerodynamic loss in a gas turbine stage with film cooling*, Journal of Engineering for Power, vol. 102, no. 4, pp. 964970, 1980.

[28] R. Pichler, R. D. Sandberg, G. Laskowski, and V. Michelassi, *High-fidelity simulations of a linear HPT vane cascade subject to varying inlet turbulence*, Proceedings of ASME Turbo Expo, Volume 2A: Turbomachinery, 2017.

[29] R. J. Howell, *Wake-separation bubble interactions in low Reynolds number turbomachinery*, Ph.D. thesis, Whittle Laboratory, Univ. of Cambridge, Cambridge, UK, 1999.

[30] M. J. Kim, J. H. Kim, and T. S. Kim, *The effects of internal leakage on the performance of a Micro Gas Turbine*, Applied Energy, vol. 212, pp. 175184, 2018.

[31] J. E. LaGraff and D. E. Ashpis, *Minnowbrook II, 1997 workshop on Boundary Layer Transition in turbomachines*, Cleveland, OH: National Aeronautics and Space Administration, Lewis Research Center, 1998.

[32] H. P. Hodson and R. J. Howell, *Bladerow interactions, transition, and high-lift aerofoils in low-pressure turbines*, Annual Review of Fluid Mechanics, vol. 37, no. 1, pp. 7198, 2005.

[33] R. Brachmanski and R. Niehuis, *About the distribution of the Mach number and losses under consideration of the diffusion factor: Profile distribution and losses for low pressure turbine profiles with high diffusion factors under steady flow conditions*, Volume 2B: Turbomachinery, 2016.

[34] A. D. Rossiter, G. Pullan, and A. P. Melzer, *The influence of boundary layer state and trailing edge wedge angle on the aerodynamic performance of Transonic Turbine Blades*, Journal of Turbomachinery, vol. 145, no. 4, 2022.

[35] V. Nagabhushana Rao, P. G. Tucker, R. J. Jefferson-Loveday, and J. D. Coull, *Large eddy simulations in low-pressure turbines: Effect of wakes at elevated free-stream turbulence*, International Journal of Heat and Fluid Flow, vol. 43, pp. 8595, 2013.

[36] V. Michelassi, Liwei. Chen, R. Pichler, and R. Sandberg, *Compressible direct numerical simulation of low-pressure turbines: Part II effect of inflow disturbances*, Volume 2D: Turbomachinery, 2014.

[37] M. M. Opoka and H. P. Hodson, *Transition on the T106 LP turbine blade in the presence of moving upstream wakes and downstream potential fields*, Journal of Turbomachinery, vol. 130, no. 4, 2008.

[38] U. K. SINGH, *The effect of viscosity on the flow past aerofoils in cascade*, PhD thesis, Liverpool University, June 1974.

[39] G. J. Walker, *The Boundary Layer Behaviour on the Blading of a Single-Stage Axial-Flow Compressor*, PhD thesis, University of Tasmania, Hobart, Tasmania, Nov. 1972.

[40] A. B. Turner, *Local heat transfer measurements on a gas turbine blade*, Journal of Mechanical Engineering Science, vol. 13, no. 1, pp. 112, 1971.

[41] Hodson, H. P., *The Development of Unsteady Boundary Layers on the Rotor of an Axial-Flow Turbine*, AGARD CP 351, Sept. 1983.

[42] G. J. Walker, *Transitional flow on axial turbomachine blading*, AIAA Journal, vol. 27, no. 5, pp. 595602, 1989.

[43] D. Lengani, D. Simoni, M. Ubaldi, P. Zunino, and F. Bertini, *Experimental study of free-stream turbulence induced transition in an adverse pressure gradient*, Experimental Thermal and Fluid Science, vol. 84, pp. 1827, 2017.

[44] B. Niebles Atencio, V. Chernoray, and M. Jahanmiri, *An experimental study on laminar-turbulent transition at high free-stream turbulence in boundary layers with pressure gradients*, EPJ Web of Conferences, vol. 25, p. 01029, 2012.

[45] G. I. Ilieva, *On turbulence and its effects on aerodynamics of flow through turbine stages*, Turbulence Modelling Approaches - Current State, Development Prospects, Applications, 2017.

[46] L.S. Kovasznay, *Turbulence in supersonic flow*, Journal of the Aeronautical Sciences, 20(10), pp.657-674, 1953.

[47] E. R. Van Driest and C. B. Blumer, *Boundary layer transition- freestream turbulence and pressure gradient effects*, AIAA Journal, vol. 1, no. 6, pp. 13031306, 1963.

[48] B. J. Abu-Ghannam and R. Shaw, *Natural Transition of Boundary LayersThe Effects of Turbulence, Pressure Gradient, and Flow History*, Journal of Mechanical Engineering Science, vol. 22, no. 5, pp. 213228, Oct. 1980.

[49] L. Wang, S. Fu, A. Carnarius, C. Mockett, and F. Thiele, *A modular rans approach for modelling laminarturbulent transition in turbomachinery flows*, International Journal of Heat and Fluid Flow, vol. 34, pp. 6269, 2012.

[50] Morkovin M. V., Reshotko E., Herbert T., *Transition in open flow systemsa reassessment*, Bull. Am. Phys. Soc. 39:1882., 1994.

[51] R. Govindarajan and R. Narasimha, *The role of residual nonturbulent disturbances on transition onset in two-dimensional boundary layers*, Journal of Fluids Engineering, vol. 113, no. 1, pp. 147149, 1991.

[52] J. Frst, P. Straka, and J. Phoda, *Modelling of natural and bypass transition in aerodynamics*, EPJ Web of Conferences, vol. 67, p. 02030, 2014.

[53] Kenndal, James M., *xperiments on Boundary Layer Receptivity to Free stream Turbulence*, AIAA, Aug. 2012.

[54] Z. Yang, *On bypass transition in separation bubbles: A Review*, Propulsion and Power Research, vol. 8, no. 1, pp. 2334, 2019.

[55] J. Holman and J. Frst, *Numerical simulation of separation induced laminar to turbulent transition over an airfoil*, Journal of Computational and Applied Mathematics, vol. 394, p. 113530, 2021.

[56] Gaster M., *The structure and behavior of laminar separation bubbles*, AIAA, Aeronautical Research Council. Reports and Memoranda no. 3595, SBN 11 470192 X. Norwich: Her Majestys Stationery Office.

[57] A. Hatman and T. Wang, *A Prediction Model for Separated-Flow Transition*, Journal of Turbomachinery, vol. 121, no. 3, pp. 594-602, 1999.

[58] A. Minot, X. de Saint Victor, J. Marty, and J. Perraud, *Advanced numerical setup for separation-induced transition on high-lift low-pressure turbine flows using the γ-R_{θ_t} model*, Proceedings of ASME Turbo Expo, Volume 2B: Turbomachinery, 2015.

[59] J. R. Graveline and S. A. Sjolander, *A spectral study of a moderately loaded low-pressure turbine airfoilpart I: Identifying frequencies affecting bypass transition*, Journal of Turbomachinery, vol. 135, no. 4, 2013.

[60] L. M. Segu, L. Y. Gicquel, F. Duchaine, and J. de Laborderie, *Importance of boundary layer transition in a high-pressure turbine cascade using Les*, Volume 2C: Turbomachinery, 2018.

[61] C. Sieverding, H. Richard and J. Desse, *Turbine Blade Trailing Edge Flow Characteristics at High Subsonic Outlet Mach Number*, Journal of Turbomachinery, vol. 125, no. 2, pp. 298-309, 2003.

[62] . A. Rodrguez-Sevillano, M.J. Casati-Calzada, C. Gonzlez-Gutirrez, *Exploring the Effectiveness of Visualization Techniques for NACA Symmetric Airfoils at Extremely Low Reynolds Numbers*, Fluids, vol. 8, no. 7, p. 207, Jul. 2023.

[63] E. M. Curtis, H. P. Hodson, M. R. Banieghbal, J. D. Denton, R. J. Howell, and N. W. Harvey, *Development of blade profiles for low-pressure turbine applications*, Journal of Turbomachinery, vol. 119, no. 3, pp. 531538, 1997.

[64] P. Lampart, *Tip leakage flows in turbines*, TASK QUARTERLY. 10., pp 139-175, 2006.

[65] Denton, J., *The 1993 IGTI Scholar Lecture: Loss Mechanisms in Turbomachines*, Journal of Turbomachinery, 115(4), pp.621-656, 1993.

[66] A. Yamamoto, *Interaction mechanisms between tip leakage flow and the passage vortex in a linear turbine rotor cascade*, Journal of Turbomachinery, vol. 110, no. 3, pp. 329338, 1988.

[67] C. Bringhenti and J. R. Barbosa, *Effects of turbine tip clearance on gas turbine performance*, Volume 6: Turbomachinery, Parts A, B, and C, 2008.

[68] P. Lampart, *Tip leakage flows in turbines*, Journal of Theoretical and Applied Mechanics, 44(1), 3-22, 2006.

[69] Z. Wei, W. Qiao, P. Shi, P. Chen, and L. Zhao, *Tip-leakage flow loss reduction in a two-stage turbine using axisymmetric-casing contouring*, Chinese Journal of Aeronautics, vol. 27, no. 5, pp. 11111121, 2014.

[70] N. L. Key and T. Arts, *Comparison of turbine tip leakage flow for flat tip and squealer tip geometries at high-speed conditions*, Volume 2: Turbo Expo, 2004.

[71] S. K. Krishnababu, P. J. Newton, W. N. Dawes, G. D. Lock, H. P. Hodson, J. Hannis, and C. Whitney, *Aerothermal investigations of tip leakage flow in axial flow turbinespart I: Effect of tip geometry and tip clearance gap*, Journal of Turbomachinery, vol. 131, no. 1, 2008.

[72] R. E. Chupp, R. C. Hendricks, S. B. Lattime, and B. M. Steinetz, *Sealing in Turbomachinery* ARC, 2023.

[73] C. H. Sieverding, *Recent progress in the understanding of basic aspects of secondary flows in turbine blade passages*, Journal of Engineering for Gas Turbines and Power, vol. 107, no. 2, pp. 248257, 1985.

[74] L. S. Langston, M. L. Nice, and R. M. Hooper, *Three-dimensional flow within a turbine Cascade Passage*, Journal of Engineering for Power, vol. 99, no. 1, pp. 2128, 1977.

[75] LD. G. Gregory-Smith, C. P. Graves, and J. A. Walsh, *Growth of secondary losses and vorticity in an axial turbine cascade*, Journal of Turbomachinery, vol. 110, no. 1, pp. 18, 1988.

[76] R. J. Adrian, K. T. Christensen, and Z.-C. Liu, *Analysis and interpretation of instantaneous turbulent velocity fields*, Experiments in Fluids, vol. 29, no. 3, pp. 275290, 2000.

[77] J. Denton and G. Pullan, *A numerical investigation into the sources of endwall loss in axial flow turbines*, Volume 8: Turbomachinery, Parts A, B, and C, 2012.

[78] S. Harrison, *The influence of blade stacking on turbine losses*, PhD thesis, University of Cambridge, 1989.

[79] M. W. Benner, S. A. Sjolander, and S. H. Moustapha, *The influence of leading-edge geometry on secondary losses in a turbine cascade at the design incidence*, Journal of Turbomachinery, vol. 126, no. 2, pp. 277287, 2004.

[80] J. D. Denton and L. Xu, *The trailing edge loss of transonic turbine blades*, Volume 1: Turbomachinery, 1989.

[81] A. D. Rossiter, G. Pullan, and A. P. Melzer, *The influence of boundary layer state and trailing edge wedge angle on the aerodynamic performance of Transonic Turbine Blades*, Journal of Turbomachinery, vol. 145, no. 4, 2022.

[82] A. P. Melzer and G. Pullan, *The role of vortex shedding in the trailing edge loss of transonic turbine blades*, Journal of Turbomachinery, vol. 141, no. 4, 2019.

[83] C. H. Sieverding and H. Heinemann, *The influence of Boundary Layer State on vortex shedding from flat plates and Turbine Cascades*, Journal of Turbomachinery, vol. 112, no. 2, pp. 181187, 1990.

[84] C. H. Sieverding, M. Stanislas, and J. Snoeck, *The base pressure problem in Transonic Turbine Cascades*, Journal of Engineering for Power, vol. 102, no. 3, pp. 711718, 1980.

[85] Ainley and Mathieson, *A Method of Performance Estimation for Axial-Flow Turbines*, ARC Reports and Memoranda No. 2974, 1957.

[86] J. Dunham and P. M. Came, *Improvements to the Ainley-Mathieson Method of turbine performance prediction*, Journal of Engineering for Power, vol. 92, no. 3, pp. 252256, 1970.

[87] Denton, J., *Entropy Generation in Turbomachinery Flows*, SAE Transactions, 99, 2251-2263, 1990. [Online]. Available: `ttp://www.jstor.org/stable/44473181`. [Accessed: Oct. 23, 2021]

[88] A. B. Ennil, R. Al-Dadah, S. Mahmoud, K. Rahbar, and A. AlJubori, *Minimization of loss in small scale axial air turbine using CFD modeling and evolutionary algorithm optimization*, Applied Thermal Engineering, vol. 102, pp. 841848, 2016.

[89] X.-D. Zhang, J.-J. Liu, and C. Li, *A cooled turbine airfoil performance prediction method with two-dimensional CFD computation and loss models*, International Journal of Turbo & Jet-Engines, vol. 0, no. 0, 2023.

[90] S.-M. Li, T.-L. Chu, Y.-S. Yoo, and W. F. Ng, *Transonic and low supersonic flow losses of two steam turbine blades at large incidences*, Journal of Fluids Engineering, vol. 126, no. 6, pp. 966975, 2004.

[91] P. Rajeevalochanam, R. Senthil Kumaran, S. N. Sunkara, N. Kalita, and P. P. Sharath, *Experimental and numerical studies on a curved back transonic airfoil*, Volume 1: Compressors, Fans and Pumps; Turbines; Heat Transfer; Combustion, Fuels and Emissions, 2017.

[92] V. Raja and K. Fernandes, *Reverse Engineering*, London: Springer, 2010.

[93] T. Vrady, R. Martin, and J. Cox, "Reverse engineering of geometric modelsan introduction," *Computer-Aided Design*, vol. 29, no. 4, pp. 255-268, 1997.

[94] F. C. Langbein, "Beautification of reverse engineered geometric models," Ph.D. dissertation, Dept. of Computer Science, Cardiff University, 2003.

[95] M. Mahboubkhah, M. Aliakbari, and C. Burvill, "An investigation on measurement accuracy of digitizing methods in turbine blade reverse engineering," *Proceedings of the Institution of Mechanical Engineers, Part B: Journal of Engineering Manufacture*, vol. 232, no. 9, pp. 1653-1671, 2016.

[96] K. Mohaghegh, M. Sadeghi, and A. Abdullah, "Reverse engineering of turbine blades based on design intent," *The International Journal of Advanced Manufacturing Technology*, vol. 32, nos. 9-10, pp. 1009-1020, 2006.

[97] C. She and C. Chang, "Study of applying reverse engineering to turbine blade manufacture," *Journal of Mechanical Science and Technology*, vol. 21, no. 10, pp. 1580-1584, 2007.

[98] Y. Li, X. Huang, C. Gong, and Kelvin Wang, "An engineering rules based parameterisation approach for turbine blade reverse engineering," *Journal of Mathematical Analysis and Applications*, vol. 292, no. 1, pp. 311-315, 2004.

[99] Abid, M. A. R. et al., *Gas turbine blade flow analysis comparison using CFD and Wind Tunnel*, in Proceedings of 2012 9th International Bhurban Conference on Applied Sciences & Technology (IBCAST). IEEE. 2012.

[100] J. Anderson, *Computational fluid dynamics* New York, NY: McGraw-Hill, 2010.

[101] Fred Stern, Robert V. Wilson, Hugh W. Coleman*, and Eric G. Paterson, *Verification and Validation of CFD Simulations*, Iowa Institute of Hydraulic Research, College of Engineering, The University of Iowa, Iowa City IA 52242, IIHR Report No. 407, Sept. 1999.

[102] NASA, *Navier-Stokes Equations*, Grc.nasa.gov, 2020. [Online]. Available at: `https://www.grc.nasa.gov/www/k-12/airplane/nseqs.html`. [Accessed: 11 Oct. 2020]

[103] Hermann Schlichting, Klaus Gersten *Boundary-Layer Theory* 9th ed. Springer-Verlag Berlin Heidelberg 2017. [Online]. Available: `https://doi.org/10.1007/978-3-662-52919-5`. [Accessed: 11 Oct. 2020]

[104] P. G. Hill and C. R. Peterson, *Mechanics and thermodynamics of propulsion* New Delhi: Dorling Kindersley, 2014.

[105] S. B. Pope, *Turbulent flows* Cambridge: Cambridge University Press, 2000.

[106] P. A. Davidson, *Turbulence: An introduction for scientists and Engineers* Oxford, United Kingdom: Oxford University Press, 2015.

[107] Frisch, U., *Turbulence: The legacy of A. n. kolmogorov*, Cambridge, England: Cambridge University Press, 1995.

[108] *Turbulence models in CFD - RANS, DES, LES and DNS*, IdealSimulations, 2020. [Online]. Available at: `https://www.idealsimulations.com/resources/turbulence-models-in-cfd/`. [Accessed: 20 Oct. 2020]

[109] Y. Zhiyin, *Large-eddy simulation: Past, present and the future*, hinese Journal of Aeronautics, vol. 28, no. 1, pp. 11-24, 2015.

[110] D. C. Wilcox and D. C. Wilcox, *Solutions manual turbulence modeling for CFD* La Caada: DCW Industries, Inc., 2006.

[111] Z. Yang and T. Shih, *New time scale based k-epsilon model for near-wall turbulence*, AIAA Journal, vol. 31, no. 7, pp. 1191-1198, 1993.

[112] SimScale, *K-epsilon turbulence model: Global settings*, SimScale.com, 2021. [Online]. Available at: `https://www.simscale.com/docs/simulation-setup/global-settings/k-epsilon/`. [Accessed: 20 Oct. 2021]

[113] L. R. Heather, *Application of a modified k-[epsilon] turbulence model to gas turbine combustor geometries*, PhD diss., Virginia Tech, 1993.

[114] F. Menter, *Two-equation eddy-viscosity turbulence models for engineering applications*, AIAA Journal, vol. 32, no. 8, pp. 1598-1605, 1994.

[115] David M. Driver and H. Lee Seegmiller, *Features of a Reattaching Turbulent Shear Layer in Divergent Channel Flow*, AIAA Journal, vol. 23, no. 2, pp. 163-171, 1985.

[116] R. B. Langtry and F. R. Menter, *Correlation-based transition modeling for unstructured parallelized computational fluid dynamics codes*, AIAA Journal, vol. 47, no. 12, pp. 28942906, 2009.

[117] F. R. Menter and Y. Egorov, *The scale-adaptive simulation method for unsteady turbulent flow predictions. part 1: Theory and model description*, Flow, Turbulence and Combustion, vol. 85, no. 1, pp. 113138, 2010.

[118] G.B. Schubauer and P.S. Klebanoff, *Contributions on the mechanics of boundary-layer transition*, Washington, D.C.: NASA, Report No.: NACA TN 3489, 1955. [Online]. Available: `https://www.semanticscholar.org/paper/Contributions-on-the-Mechanics-of-Boundary-Layer-Schubauer-Klebanoff/f6926c79d1d862326cc7688912e7f5ac6767cf80?p2df`. [Accessed: 20 Oct. 2021]

[119] C. Xia and W. Chen, *FBoundary-layer transition prediction using a simplified correlation-based model*, Chinese Journal of Aeronautics, vol. 29, no. 1, pp. 66-75, 2016.

[120] K. Menzies, *Large eddy simulation applications in gas turbines*, Philosophical Transactions of the Royal Society A: Mathematical, Physical and Engineering Sciences, 2009.

[121] K. J. Leonard and E. G. Suggs, *Setosphaeria prolata, the ascigerous state of Exserohilum prolatum*, Mycologia, vol. 66, no. 2, p. 281, 1974.

[122] F. Nicoud and F. Ducros, *Subgrid-scale stress modelling based on the square of the velocity gradient tensor*, Mycologia, Flow, turbulence and Combustion, 62(3), 183-200, 1999.

[123] D. Lakehal, *Near-Wall Modeling of Turbulent Convective Heat Transport in Film Cooling of Turbine Blades With the Aid of Direct Numerical Simulation Data*, Journal of Turbomachinery, vol. 124, no. 3, pp. 485-498, 2002.

[124] M. Karczewski and J. Baszczak, *Performance of three turbulence models in 3D flow investigation for a 1.5-stage turbine*, Task Quarterly, 12(3-4), 185-195, 2008.

[125] M. Dave and J. A. Franck, *Comparison of rans and Les for a cross-flow turbine in confined and unconfined flow*, Journal of Renewable and Sustainable Energy, vol. 13, no. 6, p. 064503, 2021.

[126] P. Dong and R. S. Amano, *High-pressure gas turbine vane turbulent flows and heat transfer predicted by Rans/Les/des*, Volume 5B: Heat Transfer, 2017.

[127] B. Mandal and H. Mazumdar, *The Importance Of The Law Of The Wall*, International Journal of Applied Mechanics and Engineering, vol. 20, no. 4, pp. 857-869, 2015.

[128] Jousef Murad, *What is y+ (yplus)?*, SimScale CAE Forum, 2020. [Online]. Available at: `https://www.simscale.com/forum/t/what-is-y-yplus/82394`. [Accessed: 31 Oct. 2020]

[129] B.E. Launder and D.B. Spalding, *The Numerical Computation of Turbulent Flows*, Computer Methods in Applied Mechanics and Engineering 3, pp. 269-289, 1973.

[130] D. Spalding, *A Single Formula for the Law of the Wall*, Journal of Applied Mechanics, vol. 28, no. 3, pp. 455-458, 1961.

[131] G. Kalitzin, G. Medic, G. Iaccarino and P. Durbin, *Near-wall behavior of RANS turbulence models and implications for wall functions*, ournal of Computational Physics, vol. 204, no. 1, pp. 265-291, 2005.

[132] manchestercfd, *All there is to know about different mesh types in CFD!*, Grc.nasa.gov, Manchestercfd.co.uk, 2020. [Online]. Available at: `https://www.manchestercfd.co.uk/post/all-there-is-to-know-about-different-mesh-types-in-cfd`. [Accessed: 19 Oct. 2020]

[133] C. Tth, J. O'Rourke and J. Goodman, *Handbook of discrete and computational geometry*, North Holland, 2000.

[134] Ansys, C. F. X., *ANSYS CFX-solver theory guide*, Ansys CFX Release, 15317, 724-746. 2009.

[135] R. Alldieck, H. Seehausen, F. Herbst, and J. R. Seume, *The effect of rough-wall boundary conditions on RANS-based transition prediction*, roceedings of Global Power & Propulsion Society, 2020.

[136] B. Blocken, T. Stathopoulos, and J. Carmeliet, *CFD simulation of the atmospheric boundary layer: Wall function problems*, Atmospheric Environment, vol. 41, no. 2, pp. 238252, 2007.

[137] J. Nikuradse, *Laws of flow in rough pipes*, digital.library.unt.edu, 1950.

[138] Y.-S. Kang, J.-C. Yoo, and S.-H. Kang, *Numerical predictions of roughness effects on the performance degradation of an axial-turbine stage*, Journal of Mechanical Science and Technology, vol. 20, no. 7, pp. 10771088, 2006.

[139] Lutum, E., Cottier, F., Crawford, M. E., Laveau, B., and Abhari, R. S., *A computational investigation of the effect of surface roughness on heat transfer on the stator endwall of an axial turbine*, Proceedings of the Institution of Mechanical Engineers, Part A: Journal of Power and Energy, 229(5), 454-464. 2015.

[140] A. A. Gamil, T. Nikolaidis, J. A. Teixeira, S. H. Madani, and A. Izadi, *Assessment of Surface Roughness Effects on micro axial turbines*, Volume 8: Industrial and Cogeneration; Manufacturing Materials and Metallurgy; Marine; Microturbines, Turbochargers, and Small Turbomachines, 2020.

[141] Omega *Wire color codes and limits of error* Omega Engineering, 2021. [Online]. Available: `https://www.omega.com/en-us/colorcodes`. [Accessed: 28 Mar. 2021]

[142] H. GOLCHIN, F. OMMI, and Z. SABOOHI, *Assessment of converting approach to efficient design of micro-turboprop engines*, Chinese Journal of Aeronautics, vol. 33, no. 2, pp. 572588, 2020.

[143] B. Martin, F. Duchaine, L. Gicquel, N. Odier, and J. Dombard, *Accurate inlet boundary conditions to capture combustion chamber and turbine coupling with large-eddy simulation*, Journal of Engineering for Gas Turbines and Power, vol. 144, no. 2, 2021.

[144] SLM Solutions, *SLM280 2.0* SLM Solutions, 2023. [Online]. Available: `https://www.slm-solutions.com/products-and-solutions/machines/slm-280/`. [Accessed: 28 Mar. 2023]

[145] Furness Controls, *FCO510 Low Pressure Microprocessor Micromanometer*, furness.com, See also URL `https://www.bissistem.com/furness/files/FCO510-Laboratuvar-Tipi-Akis-Olcer.pdf`. [accessed May 26, 2023]

[146] Bruker Alicona, *InfiniteFocusSL*, Alicona.com, 2022, See also URL `https://www.alicona.com/en/products/infinitefocussl/`. [Accessed: 28 Mar. 2023]

[147] D. A. Macdonald, *The application of focus variation microscopy for lithic use-wear quantification*, Journal of Archaeological Science, vol. 48, pp. 2633, 2014.

[148] T. Adams, C. Grant, and H. Watson, *A simple algorithm to relate measured surface roughness to equivalent sand-grain roughness*, International Journal of Mechanical Engineering and Mechatronics, 2012.

[149] I. Capasso, A. Langella, G. Brando, *D-printed metals: Process parameters effects on mechanical properties of 17-4 PH stainless steel*, Heliyon, vol. 9, no. e07376, 2023.

[150] B. Prawara, E. Martides, E. Junianto, *First-rate manufacturing process of primary air fan (PAF) coal power plant in Indonesia using laser powder bed fusion (LPBF) technology*, Journal of Materials Processing Technology, 2022.

[151] T. Lieneke, T. Knneke, F. Schlenker, V. Denzer, *Manufacturing accuracy in additive manufacturing: a method to determine geometrical tolerances*, Joint Special Interest Group meeting between euspen and ASPE on Dimensional Accuracy and Surface Finish in Additive Manufacturing, 2019.

[152] D. Jia, F. Li, Y. Zhang, *3D-printing process design of lattice compressor impeller based on residual stress and deformation*, Scientific Reports, vol. 10, Article no. 57131, 2020.

[153] A. Ahmed, A. Majeed, Z. Atta, G. Jia, *Dimensional quality and distortion analysis of thin-walled alloy parts of AlSi10Mg manufactured by selective laser melting*, Journal of Manufacturing and Materials Processing, vol. 3, no. 2, Article 51, 2019.

[154] O. N. Eid, *The Design of a Rolling Road for the Bob Wind Tunnel at the University of Manchester, to Implement Boundary Layer Control and Removal*, School of Mechanical, Aerospace and Civil Engineering, University of Manchester, Manchester, UK, 2016.

[155] Y. Zhang, P. Cardiff, J. Keenahan, *Wind-induced phenomena in long-span cable-supported bridges: a comparative review of wind tunnel tests and computational fluid dynamics modelling*, Applied Sciences, vol. 11, no. 4, 1642, 2021.

[156] R. A. Catarelli, P. L. Fernndez-Cabn, et al., *Automation and new capabilities in the university of Florida NHERI Boundary Layer Wind Tunnel*, Frontiers in Built Environment, vol. 6, article 558151, 2020.

[157] Cadence, *CFD meshing methods* Cadence, 2022. [Online]. Available: `https://resources.system-analysis.cadence.com/blog/msa2021-cfd-meshing-methods`. [Accessed: 01 Mar. 2023]

[158] Cadence, *Combining structured and unstructured meshes: The holy grail for CFD Engineers* Cadence, 2022. [Online]. Available: `https://resources.system-analysis.cadence.com/computational-fluid-dynamics-articles/combining-structured-and-unstructured-meshes-the-holy-grail-for-cfd-engineers`. [Accessed: 01 Mar. 2023]

[159] Moldex3D, *Mesh Quality Definition* Moldex3D, 2023. [Online]. Available: `http://support.moldex3d.com/r16/en/modelpreparation_reference-pre_meshqualitydefinition.html`. [Accessed: 01 Mar. 2023]

[160] Cadence, *Hexahedral mesh vs. tetrahedral: Comparing high-quality meshing* Cadence, 2023. [Online]. Available: `https://resources.system-analysis.cadence.com/blog/`

msa2022-hexahedral-mesh-vs-tetrahedral-comparing-high-quality-meshing. [Accessed: 01 Mar. 2023]

[161] S. Yang, S. Luo, F. Liu, and H.-M. Tsai, *Subsonic flow over unstalled pitching airfoil computed by euler method*, 36th AIAA Fluid Dynamics Conference and Exhibit, 2006.

[162] CFD Online, *Skin friction coefficient* Cfd-online.com, 2020. [Online]. Available: https://www.cfd-online.com/Wiki/Skin_friction_coefficient. [Accessed: 26 Oct. 2020]

[163] P. Sagaut, *Large Eddy Simulation for Incompressible Flows: An Introduction*, Springer Science & Business Media, 2010.

[164] U. Piomelli, *Large-eddy simulation: Achievements and Challenges*, Progress in Aerospace Sciences, vol. 35, no. 4, pp. 335362, 1999.

[165] Rory Douglas Stieger, *The Effects of Wakes on Separating Boundary Layers in Low Pressure Turbines*, Ph.D. thesis, Cambridge University Engineering Department, Cambridge, UK, 2002. [Online]. Available: http://www-g.eng.cam.ac.uk/whittle/T106/T106A_cascade/T106A_cascade_publications/RStieger_PhD.pdf. [Accessed: 26 Oct. 2020]

[166] Grnman, A, Sallinen, P, Honkatukia, J, Backman, J, Uusitalo, A, Nerg, J, & Jaatinen-Vrri, A. *Experimental and Analytical Analysis of Aero-Derivative Micro Gas Turbine Heat Transfer and Performance* Proceedings of the ASME Turbo Expo 2019: Turbomachinery Technical Conference and Exposition, Phoenix, Arizona, USA. June 1721, 2019.

[167] D. Verstraete, P. Hendrick, V. Djanali, C. Gonzalez, J. Ling, K. C. Wong, and S. Armfield, *Micro Propulsion Activities at the University of Sydney*, PowerMEMS 2010 Conference, pp. 14, 2010.

[168] V. Djanali, K.C. Wong and S. Armfield, *Numerical Simulations of Transition and Separation on a Small Turbine Cascade*, WSEAS Transactions on Fluid Mechanics, 9(1), pp. 879-884, 2006.

[169] F. Afshari, H. Dehghanpour and A. Khanlari, *A Basic Comparison Between Numerical Methods Provided By ANSYS CFX, ANSYS Fluent AND ABAQUS Standard*, in 2018 Conference Uluslararasi Mesleki Ve Teknik

Bilimler Kongresi (UMTEB-4), Erzurum, Turkey, pp.1802-1811. [Online]. Available: `https://www.researchgate.net/publication/329586623_A_BASIC_COMPARISON_BETWEEN_NUMERICAL_METHODS_PROVIDED_BY_ANSYS_CFX_ANSYS_Fluent_AND_ABAQUS_Standard`. [Accessed: 26 Nov. 2020]

[170] Gauri V. Thorat and Laxmikant D. Mangate, *Comparison of Ansys CFX and Ansys Fluent solver for compressor assembly*, Journal of Emerging Technologies and Innovative Research, vol. 5, no. 7, pp. 315318, 2018.

[171] L. N. Zhang, D. H. Zhang, and Y. P. Liu, "Research on modeling turbine blade in reverse engineering," *Materials Science Forum*, vol. 532-533, pp. 777-780, 2006.

[172] Technovent, *Technical/User Data Sheet: Platinum Cure Rubber-Z004*, Technovent.com, 2022. See also URL `http://www.technovent.com/Z004\%20Instructions\%20and\%20MSDS.pdf`.

[173] Bondmaster, *Two Part Epoxy Resin Technical Information Sheet*, Farnell.com, 2022. See also URL `http://www.farnell.com/datasheets/316730.pdf`. [Accessed: 26 Oct. 2021]

[174] SHINING 3D, *EinScan Pro 2X Plus-Handheld Industrial Scanner*, EinScan, 2022. See also URL `https://www.einscan.com/handheld-3d-scanner/2x-plus/`. [Accessed: 26 Oct. 2021]

[175] P. Amornvit and S. Sanohkan, "The accuracy of digital face scans obtained from 3D scanners: An in vitro study," *International Journal of Environmental Research and Public Health*, vol. 16, no. 24, pp. 5061, 2019.

[176] J. H. T. Daemen, T. G. J. Loonen, A. C. Verhulst, T. J. J. Maal, J. G. Maessen, Y. L. J. Vissers, K. W. E. Hulsew and E. R. de Loos, "Three-dimensional imaging of the chest wall: A comparison between three different imaging systems," *Journal of Surgical Research*, vol. 259, pp. 332-341, 2020.

[177] S. Simone, F. Montomoli, F. Martelli, K. Chana, I. Qureshi, and T. Povey, "Analysis on the effect of a nonuniform inlet profile on heat transfer and fluid flow in turbine stages," *Journal of Turbomachinery*, vol. 134, no. 1, 2011.

[178] A. Fhring, D. Kozulovic, M. FTanke, *Quasi-Unsteady Wake Effect Modeling in Steady State Mixing Plane Simulations of Turbines*, Proceedings of DLRK, 2019.

[179] T. Sipil, *Propeller flows: quasi-steady, mixing plane, and time-accurate approaches*, Ene-39.4052, Post Graduate Seminar on Heat and Fluid Flow, 2008.

[180] N. Kozak et al., *High-fidelity finite element modeling and analysis of adaptive gas turbine stator-rotor flow interaction at off-design conditions*, Journal of Mechanics, vol. 36, no. 5, pp. 595606, 2020.

[181] K. N. Kumar and M. Govardhan, *Secondary flow loss reduction in a turbine cascade with a linearly varied height streamwise endwall fence*, International Journal of Rotating Machinery, vol. 2011, Article ID 352819, 2011.

[182] G. Ingram, D. Gregory-Smith, and D. B. I. Harvey, *The effect of end-wall profiling on secondary flow and loss development in a turbine cascade*, Proc. ASME Turbo Expo 2002: Power for Land, Sea, and Air, vol. 3, 2002.

[183] M. Peters, T. Schmidt, P. Jeschke, *Influence of blade aspect ratio on axial compressor efficiency*, Journal of the Global Power and Propulsion Society, 2019.

[184] A. Hunt, C. Stringer, B. Polagye, *Effect of aspect ratio on cross-flow turbine performance*, Journal of Renewable and Sustainable Energy, vol. 12, no. 5, 054501, 2020.

[185] W. Gao, L. Li, Z. Yue, H. Li, G. Xie, and F. Tong, *Research on the influence of guide blade trailing edge structure on turbine performance*, Journal of Thermal Science, vol. 28, no. 1, pp. 1826, 2019.

[186] W. Zhang, Z. Zou, and J. Ye, *Leading-edge redesign of a turbomachinery blade and its effect on aerodynamic performance*,Applied Energy, vol. 93, pp. 655667, 2012.

[187] C. Vanderwel and B. Ganapathisubramani, *Effects of spanwise spacing on large-scale secondary flows in rough-wall turbulent boundary layers*, Journal of Fluid Mechanics, vol. 774, 2015.

[188] J. Coull, C. Clark, and R. Vazquez, *The sensitivity of turbine cascade endwall loss to inlet boundary layer thickness*, Journal of the Global Power and Propulsion Society, vol. 3, 2019

[189] F. Hummel, M. Ltzerich, P. Cardamone, and L. Fottner, *Surface roughness effects on turbine blade aerodynamics*, Journal of Turbomachinery, vol. 127, no. 3, p. 453, 2005.

[190] Todd Alhart, *GE Integrating AI to Enable Performance-Informed Gas Turbine Inverse Design*, GE Reports, 2023. [Online]. Available: https://www.ge.com/research/newsroom/ge-integrating-ai-enable-performance-informed-gas-turbine-inverse-design. [Accessed: 01 Mar. 2023]

[191] Kamranpey, Ali, *A study on effects of mass flow rate and compressor pressure ratio on gas turbine cycle performance*, International Journal of IC Engines and Gas Turbines, 8.2, 2022.